CRANFIELD INSTITUTE OF TECHNOLOGY

SCHOOL OF MECHANICAL ENGINEERING

Ph.D. Thesis

K. J. Syed

Soot and Radiation Modelling in Buoyant Fires

Supervisor: Professor J. B. Moss

October 1990

This thesis is submitted for the degree of
Doctor of Philosophy

ABSTRACT

This study seeks to advance present modelling capabilities in respect of soot and thermal radiation emission from fires. Such developments are crucial to the improved estimate of the hazard potential of accidental fires.

Radiation calculation requires the prediction of temperature and the concentrations of all radiatively important species. In hydrocarbon combustion, the key species are carbon dioxide, water vapour, carbon monoxide and particulate soot. In large hydrocarbon fires the latter is usually the dominant radiator. The detailed prediction of the gaseous species in turbulent combustion has previously been shown to be successfully achieved using laminar flamelet modelling in the fast chemistry limit. Soot, however, is governed by relatively slow formation processes which as yet remain poorly understood.

The present study proposes a model for soot formation in turbulent non-premixed combustion which aims to address both the slow chemistry and turbulence interaction. In order to circumvent uncertainties in soot formation processes the model relies on empiricism, through the experimental investigation of a sooting laminar diffusion flame.

The soot formation model is used to predict soot levels in a jet diffusion flame. Subsequent comparison with experimental data suggests the satisfactory performance of the model, but highlights soot oxidation to be a more significant problem. This stems from uncertainties associated both with instantaneous soot oxidation rate and the highly intermittent nature of this process in turbulent non-premixed flames.

The soot formation model is also applied to the prediction of soot levels in a simulated buoyant methane fire, which supplement temperature and gaseous species predictions using a flamelet approach. Detailed predictions of spectrally resolved radiative intensity are then performed and compared with similarly detailed experimental data. The encouraging agreement with experiment allows the assessment of the effect of turbulence-radiation interaction. This is shown to be particularly important in buoyancy-driven fires and is most evident for the luminous radiation. This arises from the soot which is largely confined to narrow sheets that typically lie close to peak temperature zones. A strategy in which more representative soot-temperature correlations may be realised is also described.

ACKNOWLEDGEMENTS

The author would like to express his sincere thanks to Professor J. B. Moss, whose support, guidance and patience have been greatly appreciated; to Mr. C. D. Stewart for the use of his experimental rig and for many stimulating discussions.

British Gas and The Science and Engineering Research Council are to be acknowledged for their financial support during this study and in particular the author is indebted to Dr. M. Fairweather and Mr. P. Docherty of Midland Research Station, British gas, for their help and guidance in aspects of radiation modelling.

Finally the author is grateful to Mr. G. Cox and Dr. S. Kumar of the Fire Research Station, Building Research Establishment, for the interest shown in the present work and many discussions related to fire phenomena.

CONTENTS

NOMENCLATURE

a_c, a_d	Collision and Doppler fine structure parameters
B	Blackbody radiative intensity (=E/π)
B	Beta function
C_f	Rate coefficient
C_i	Molar concentration of species i
Cp	Specific heat at constant pressure
$C_\alpha, C_\beta, C_\gamma, C_\delta$	Constants in soot formation model
C_{g1}, C_{g2}	Constants in the source term of ξ''^2
$C_{\varepsilon 1}, C_{\varepsilon 2}$	Constants in source term of ε
C_μ, C_v, C_d	Constants in turbulence model
C_1, C_2	Planck's first and second constants
d_e	Mean line spacing
D	Diffusion coefficient
E	Blackbody radiation
f_v	Soot volume fraction
F	Cumulative distribution function (CDF)
g	Gravitational acceleration
G_{bk}	Buoyancy source in turbulent kinetic energy equation
h	Enthalpy
h	Heat transfer coefficient
H_a	Activation energy
H_{f0}	Enthalpy of formation
I	Intermittency
I	Radiative intensity
k	Turbulent kinetic energy
K	Absorption coefficient
K	Reaction rate constant
l_e	Mixing length
L_e	Length of characteristic eddy
m	Soot mass density
mm_α	Molecular mass of species α
n	Soot number density
n,m	Terms in refractive index of soot

N	Normalised soot number density ($=n/N_0$)
N_0	Avogadro's number ($6x10^{26}$)
P	Pressure
P	Probability density function (PDF)
Pr	Prandtl number
P_α	Partial pressure of species α
R_0	Universal gas constant
R_j, R_{-j}	Forward and reverse reaction rate
Re	Reynolds number
s	Distance
Sc	Schmidt number
S_e	Mean line strength
S_ϕ	Volumetric source term of ϕ
t	Time
t_p	Soot formation plug flow residence time
T	Temperature
T_α, T_γ	Activation temperatures in soot formation model
u	Velocity
v	Velocity
w	Chemical source term
x	Distance
X	Mole fraction
X	Optical depth
X^*	Optical depth in the weak line limit
X_c, X_d	Pure collision and Doppler optical depths
Y	Mass fraction
Y	Combined collision and Doppler broadened optical depth

Greek symbols

$\alpha'_{ij}, \alpha''_{ij}$	Stoichiometric coefficients for species i
α, β	Exponents of beta function
α	Term in soot nucleation
β	Term in soot coagulation
β	Thermal expansion coefficient

γ	Term in soot surface growth
γ_c, γ_d	Collision and Doppler half-widths
ε	Turbulence dissipation rate
ε	Emissivity
ε	Soot oxidation parameter
λ	Wavelength
Γ_ϕ	Transport coefficient of ϕ
μ	Dynamic viscosity
ν	Kinematic viscosity
ξ	Mixture fraction
ρ	Gas phase density
ρ_s	Density of soot
σ	Stefan-Boltzmann constant
σ_ϕ	Prandtl/Schmidt number of ϕ
σ_i	Mole number of species i
σ_m	Reciprocal of mixture molecular mass
τ	Time constant
τ	Transmissivity
τ_{ij}	Viscous stress tensor
ϕ	General variable
ϕ_m	Soot mass fraction ($=m/\rho$)
ϕ_n	Soot particle number per unit mass of gas ($=N/\rho$)
Φ	Soot concentration parameter
χ	Scalar dissipation rate
ψ	Stream function
ω	Normalised stream function
ω	Wave number
ω	Soot oxidation per unit area

Subscripts

c	Soot coagulation
f	Fuel stream
g	Soot surface growth
HC	Hydrocarbon

n	Soot nucleation
o	Oxidant stream
st	Stochiometric
t	Turbulent
t	Thermophoresis
0	Reference conditions
λ,ω	Spectral property

Superscripts

–	Time (or Reynolds) average
′	Time (or Reynolds) fluctuation
~	Density weighted (or Favre) mean
″	Density weighted (or Favre) fluctuation

CHAPTER 1

Introduction

The detailed prediction of the hazards presented by both open fires and fire within buildings has attracted increasing attention in recent years. The concern in open fires is, by and large, restricted to the heating of neighbouring structures which may be subsequently drawn into the fire and thus contribute to fire spread. Fires in buildings raise additional concerns related to emission of combustion products, in particular smoke which is often the major cause of fatalities. Soot is formed in large concentrations in hydrocarbon fuelled fires. This reflects both the highly sooting nature of the complex hydrocarbons comprising typical fuels, and the favourable conditions offered by the flame flow field - fires exhibit relatively poor fuel-air mixing and long residence times, which allows soot to be formed at high temperatures in fuel rich regions. Subsequent heatloss then freezes the process of soot combustion and leads to its emission as smoke.

Thermal radiation plays a key role in the development of fire hazards since, in open fires, it is the only mode of heat transfer to neighbouring structures. It is also significant in enclosure fires, where radiative heating of remote bodies may cause them to release combustible vapours and subsequently ignite. If ignition does not occur immediately, such vapours are released into the ambient atmosphere and an explosive flash-over may result.

It is the modelling of radiation from buoyant fires to which the present work is directed. Such modelling requires the detailed prediction of the temperature and the concentrations of thermally radiating species, the most significant of which, in hydrocarbon

combustion, are CO_2, H_2O, CO and particulate soot. Given the large-scale fluctuating nature of fires, turbulence-chemistry interaction must be incorporated in the prediction of the scalar field.

Fires generally fall within the category of non-premixed combustion, where the fuel and oxidant are initially separate and combustion takes place at the interface where they mix. These flames exhibit a range of mixture states ranging from pure fuel to pure air. Non-premixed combustion also occurs in many practical situations, for example in gas turbine combustors, diesel engines and furnaces. Some common elements may therefore be identified between the combustion process in practical devices and in hazardous fires. The alternative burning mode is that of premixed combustion, where the fuel and oxidant are intimately mixed prior to combustion. Such flames are characterised by a single mixture state given by the reactant equivalence ratio. This may give rise to hazard in relation to explosive mixtures but falls outside the scope of this thesis.

Computationally-based models of the combustion process have found increased application across a wide range of industries, prompting the investigation of a number of theoretical approaches. Recent years have seen the development, in particular, of conserved scalar-based approaches to turbulent non-premixed combustion which allow turbulence-chemistry interaction to be considered with comparative ease. Such approaches are typically applicable in the fast chemistry limit (ie. when chemistry time scales are much shorter than mixing time scales). This condition is generally met by the processes that govern the overall heat release and the formation of the major gaseous products.

One of the most readily applicable conserved scalar methods is the laminar flamelet approach (cf. Liew (1981)). This considers a turbulent flame to comprise an ensemble of microscopic laminar flamelets which may be stretched, contorted and transported by the fluctuating turbulent motion, whilst their structure remains essentially laminar-like. The method is particularly attractive in

that it permits the incorporation of detailed chemical kinetics without major penalty computationally. This is possible because such calculation is restricted to the 'exact' computation of representative laminar flames that are free of the statistical uncertainties introduced in turbulent flows. The laminar flamelet model is used in the present study.

The formation of soot is governed by complex physical and heterogeneous chemical processes, which are relatively slow and to which the conserved scalar approaches do not directly apply. In addition, our current understanding of soot formation is fairly limited and accurate prediction even in laminar flames is not possible from first principles.

The present study proposes a model for soot formation which is developed empirically, through small-scale laminar flame experiment, and capitalises on key features of the laminar flamelet approach in its application to turbulent flows. The empirical basis avoids many of the issues related to uncertain details of the soot formation mechanism.

Buoyancy-driven fires are characterised by large scale fluctuations in scalar properties which, given the non-linear dependence of radiation on scalar properties, results in substantial turbulence interaction. Such interaction, if ignored, can lead to significant underestimates in emitted radiative fluxes. A scheme for the calculation of both luminous and non-luminous radiation from fires that incorporates turbulence-radiation interaction is described.

The thesis has the following broad structure.

In chapter 2 we review the literature associated with the modelling of turbulent combustion, soot and radiation. The chapter also provides an introduction to the theoretical background to the present study.

Chapter 3 describes the development of the soot formation model. This also involves the measurement of soot concentration in a laminar diffusion flame. The soot formation rate is deduced from these measurements through detailed numerical simulation of the flame. A methane-air flame is investigated which reflects the interests of the sponsoring body (British Gas) which is interested in the scenario, amongst others, in which a tank of liquefied natural gas (LNG) ruptures and the resulting spillage ignites. Given the semi-global nature of the soot modelling approach, the deduced formation rate is unlikely to be directly applicable to other fuels. The strategy, however, may be applied to a range of fuels and related work, for example, is aimed towards the prediction of soot levels in gas turbine combustors and investigates kerosene flames (cf. Stewart et al (1990).

Chapter 4 demonstrates the application of the soot model in a turbulent jet diffusion flame, where predicted soot levels are compared with the data of Kent and Honnery (1987). Kent and Honnery have investigated ethylene flames, and their data is used for validation and demonstration in the absence of detailed soot measurements in turbulent methane flames. The predictions therefore use the soot formation rate determined by Moss et al (1988) who apply the presently described strategy to the investigation of laminar ethylene flames. Though this does not test the formation rate derived in chapter 3, the overall strategy is assessed.

Chapter 5 presents the prediction of a simulated buoyant methane fire, where the soot formation rate derived in chapter 3 is used to predict soot levels. These together with the predicted gaseous field (obtained using the laminar flamelet approach) provides a full scalar representation for subsequent radiation calculation. The predicted temperature and velocity fields are compared with the data of Crauford (1984).

Chapter 6 utilises the scalar field predicted in chapter 5 to predict spectrally-resolved luminous and non-luminous radiation intensities. These are compared with the measurements of Charnley (1986) which

allows the investigation of the soot prediction and turbulence-radiation interaction.

Finally chapter 7 presents the overall conclusions and highlights the important findings. Some recommendations for further development are also made.

CHAPTER 2

Turbulent Reacting Flows

2.1 Modelling of turbulent reacting flows

2.1.1 The governing equations

Low Mach number, non-reacting fluid flow may be described by the conservation principle applied to mass and momentum. The former gives rise to the continuity equation and the latter to the Navier-Stokes equations. If the flow is reacting, further equations are required to describe the conservation of energy and chemical species. It is common practice to assume that the diffusion of heat and mass are adequately described by the laws of Fick and Fourier (cf. Reid et al (1977)) in which case the governing conservation equations take the following forms (cf. Libby and Williams (1980)) :-

mass continuity

$$\frac{\partial \rho}{\partial t} + \frac{\partial \rho u_i}{\partial x_i} = 0 \qquad \ldots \quad (2.1)$$

momentum conservation

$$\frac{\partial \rho u_i}{\partial t} + \frac{\partial \rho u_i u_j}{\partial x_i} = - \frac{\partial P}{\partial x_i} + \frac{\partial \tau_{ij}}{\partial x_j} + B_i \qquad \ldots \quad (2.2)$$

energy conservation

$$\frac{\partial \rho h}{\partial t} + \frac{\partial \rho u_i h}{\partial x_i} = \frac{\partial P}{\partial t} + \frac{\partial}{\partial x_i}\left(\frac{\mu}{Pr}\frac{\partial h}{\partial x_i} + \left[\frac{\mu}{Sc} - \frac{\mu}{Pr} \right] \sum_{\alpha=1}^{ns} h_\alpha \frac{\partial Y_\alpha}{\partial x_i} \right) + Q_r \qquad \ldots \quad (2.3)$$

species conservation

$$\frac{\partial \rho Y_\alpha}{\partial t} + \frac{\partial \rho u_i Y_\alpha}{\partial x_i} = \frac{\partial}{\partial x_i}\left(\frac{\mu}{Sc_\alpha}\frac{\partial Y_\alpha}{\partial x_i} \right) + w_\alpha \quad , \; \alpha = 1 \text{ to } ns \qquad \ldots \quad (2.4)$$

The left-hand-side of all the above equations represents rate of change with time and convection. The terms on the right-hand-side of equation 2.2 represent pressure, viscous and body forces respectively. τ_{ij} is the viscous stress tensor and is given by

$$\tau_{ij} = \mu \left\{ \frac{\partial u_i}{\partial x_j} + \frac{\partial u_j}{\partial x_i} - \frac{2}{3}\delta_{ij}\frac{\partial u_k}{\partial x_k} \right\} \qquad \ldots \quad (2.5)$$

where δ_{ij} is the Kronecker delta ($\delta_{ij}=1$ for $i=j$ and $\delta_{ij}=0$ for $i \neq j$). The body force, B_i, may refer to gravitational influences.

Equation 2.3 considers the rate of change of mechanical energy per unit volume, heat transfer due to molecular processes and radiative heat transfer (Q_r).

The terms on the right-hand-side of equation 2.4 represent molecular diffusion and chemical formation respectively. The latter is generally described by the Arrhenius expression and is a highly non-linear function of temperature and species concentration (cf. Williams (1985)).

Closure of the above equations requires additional auxiliary relationships. These take the form of the equation of state, cf.

$$\rho = \frac{p}{R_0 \; T \; \sum_{\alpha=1}^{ns} Y_\alpha / mm_\alpha} \qquad \ldots \quad (2.6)$$

and a thermodynamic relationship between enthalpy and temperature, cf.

$$h = \sum_{\alpha=1}^{ns} Y_\alpha \left(H_{f0} + \int_{T_0}^{T} Cp_\alpha(T) \; dT \right) \qquad \ldots \quad (2.7)$$

where H_{f0} is the enthalpy of formation of species α referenced at temperature T_0. The above equations may be solved provided Q_r is prescribed and there is a model for the reaction scheme from which w_α may be derived. The equation set is, however, difficult to solve owing to the strong coupling between species and temperature. Furthermore, such systems exhibit time scales that range over several orders of magnitude since typical chemical time scales are much shorter than those associated with mixing. Mathematical equations exhibiting this type of behaviour are termed "stiff" (cf. Oran and Boris (1981)). Examples of suitable algorithms for simultaneous chemical kinetic and transport problems are CRECK (cf. Pratt (1977)) and that developed by Warnatz (cf. Warnatz (1981)). A version of the former is used in chapter 4 to solve for a laminar, adiabatic ethylene-air diffusion flame.

The system of species conservation equations (cf. eqn 2.4) may be greatly simplified if the diffusion coefficient of all species is the same. This allows balance equations of conserved scalars to be derived. Such scalars may be Shvab-Zeldovitch coupling functions, atomic species mass fraction and mixture fraction (cf. Williams (1985)). A conserved scalar is defined as a quantity which is conserved through chemical reaction and therefore obeys the following balance equation:

$$\frac{\partial \rho\phi}{\partial t} + \frac{\partial \; \rho u_i \phi}{\partial x_i} = \frac{\partial}{\partial x_i}\left(\frac{\mu}{\sigma} \frac{\partial \phi}{\partial x_i} \right) \qquad \ldots \quad (2.8)$$

It is useful to note that if Q_r is negligible and the Lewis number is unity, enthalpy becomes a conserved scalar.

If it is further assumed that the chemistry is fast compared to the mixing, any chemistry dependent scalars (eg. species concentration and temperature) can be shown to be algebraically related to conserved scalars (cf. Bilger (1976a)). This allows great simplification in the modelling of laminar flames, since only one conserved scalar balance equation need be considered to describe the entire scalar field.

The above simplification is utilised in chapter 3 where the prediction of a laminar methane-air diffusion flame is reported. The simplification, however, has greater impact on the prediction of turbulent diffusion flames, as will become apparent in section 2.1.3 when conserved scalar approaches to turbulent non-premixed combustion are described.

It is timely to introduce mixture fraction which is the most widely used conserved scalar, reflecting the usefulness of a mixing property which is naturally bounded between zero and unity. Mixture fraction, ξ, is defined as the fraction of mass originating from the fuel stream, in a two-stream mixing system where fuel and oxidant diffuse into one another. Bearing this in mind mixture fraction may be expressed in terms of local fuel to air ratio (f/a), cf.

$$\xi = \frac{f/a}{1 + f/a} \qquad \ldots \quad (2.9)$$

Mixture fraction may also be defined in terms of any conserved scalar, ϕ, by

$$\xi = \frac{\phi - \phi_o}{\phi_f - \phi_o} \qquad \ldots \quad (2.10)$$

where the subscripts o and f refer to the oxidant and fuel streams, respectively.

More will be said about mixture fraction in section 2.1.3.

The governing balance equations (eqns. 2.1 to 2.4) are applicable to both laminar and turbulent flows. Turbulence, however, is characterised by length and time scales that range from the Kolmogorov scale to the integral scale (cf. Tennekes and Lumley (1972)). The ratio between these scales can be several orders of magnitude in flows of practical interest. Fortunately, however, it is often only the characteristics of the mean flow that are of interest, the time scales of which are typically much longer than those associated with the turbulence. This has led to a statistical view of the governing equations, where they are averaged over the turbulence scales to yield mean flow properties. The strategy was proposed by Reynolds (cf. Tennekes and Lumley (1972)), and entails decomposing the instantaneous value of a property into a mean and a fluctuation about that mean, cf.

$$\phi = \overline{\phi} + \phi' \qquad \ldots (2.11)$$

This is termed Reynolds decomposition. $\overline{\phi}$ is defined as a time (or Reynolds) average, cf.

$$\overline{\phi} = \lim_{\Delta T \to \infty} \frac{1}{\Delta T} \int_{T}^{T+\Delta T} \phi(t)\, dt \qquad \ldots (2.12)$$

The mean flow equations are of a similar form to their instantaneous counterparts except that turbulent correlations are introduced. These include the Reynolds stresses and turbulent scalar fluxes (cf. Tennekes and Lumley (1972)). Both result from non-linearities in convection terms and represent transport due to the fluctuating motion. The evaluation of these correlations is the goal of turbulence modelling which is described in section 2.1.2.

In turbulent flows that exhibit variable density, additional correlations involving density fluctuations arise. The resulting mean equations are then substantially more complex than their constant-

density counterparts (cf. Bray (1973)). The equations can, however, be simplified by introducing the concept of density weighted (or Favre) averaging (cf. Bilger (1976a)). Here, prior to time averaging the instantaneous balance equations, variables are decomposed into Favre (or density weighted) mean and fluctuating components, cf.

$$\phi = \tilde{\phi} + \phi'' \qquad \ldots (2.13)$$

where

$$\tilde{\phi} = (1/\bar{\rho}) \lim_{\Delta T \to \infty} \frac{1}{\Delta T} \int_{T}^{T+\Delta T} \rho(t)\ \phi(t)\ dt \qquad \ldots (2.14)$$

The resulting Favre mean balance equations are similar to those for constant density flow and may attract similar modelling strategies.

In the present work the Favre averaged equations are used and are shown in appendix A. Closure of the turbulent fluxes is achieved using the k-ε turbulence model (cf. Jones and Launder (1972)). This amongst other models is reviewed in the next subsection. Following that, the issue of the chemical source term closure is discussed in section 2.1.3.

The closure of mean balance equations will always require modelling assumptions. Although balance equations for third (or higher) order correlations may be introduced, these will inevitably involve terms of yet higher order. Statistical approaches that are an alternative are the probability density function (PDF) methods (cf. Lundgren (1969) and Pope (1985)). These allow full closure since a PDF, in principle, can contain all the necessary statistical information. Their use in non-reacting flows has not been widely adopted, since they introduce substantial computational complexity. Also, for most practical situations, mean flow closures have proved adequate. PDF methods will be discussed further in section 2.1.3 where chemical source term closure is introduced. Their use in reacting flows is promoted by the

inadequacy of mean closure assumptions to the highly non-linear source term.

Until recently, statistical approaches to turbulent flows have been the only option. However, advances in computer technology have allowed the solution of the time-dependent governing equations (cf. eqns. 2.1-2.4) where the turbulence scales are resolved. These methods are called direct numerical simulation (DNS) and have been recently reviewed by Givi (1989). DNS is attractive since the equations are exact, given adequate representation of the molecular transport and chemistry, and require no closure assumptions. Computational limitations, however, have restricted such calculations to low Reynolds numbers, simple geometry and simple reactions which are unrepresentative of practical problems (cf. Givi (1989)). The usefulness of DNS is therefore limited to the understanding of the physics of turbulent reacting flows and to the development and assessment of modelling assumptions used in the statistical approaches.

A compromise between DNS and the statistical approaches is large eddy simulation (LES) (cf. Schumann and Friedrich (1986)). The governing equations are filtered to remove the small scales and DNS is applied to the large scales only. The small scales are usually closed by modelling akin to that required in mean flow closures - this is called sub-grid scale modelling. LES is presently unsuitable for reacting flows since the source term closure issue is not resolved.

2.1.2 Turbulence modelling

Early turbulence models relied heavily on intuition and analogy with molecular motion, rather than on any sound physical basis. The turbulent flux appears as a redistribution term in the mean balance equations, in which respect it is similar to the molecular transport term. By analogy, this turbulent transport was thought to result from the Brownian motion of macroscopic eddies rather than of molecules.

Therefore, just as molecular transport of a property can be shown to be related to its gradient, it was postulated that turbulent transport may be related to the gradient of the mean. This leads to the following representation of the Reynolds stress and turbulent scalar flux:

$$\bar{\rho}\,\widetilde{u_i'' u_j''} = \delta_{ij}\frac{2}{3}\left(\bar{\rho}\,k + \mu_t \frac{\partial \tilde{u}_k}{\partial x_k}\right) - \mu_t\left(\frac{\partial \tilde{u}_i}{\partial x_j} + \frac{\partial \tilde{u}_j}{\partial x_i}\right) \qquad \ldots (2.15)$$

$$-\bar{\rho}\,\widetilde{u_i''\phi''} = \frac{\mu_t}{\sigma_t}\frac{\partial \tilde{\phi}}{\partial x_i} \qquad \ldots (2.16)$$

where σ_t is the turbulent Prandtl/Schmidt number and μ_t is the turbulent (or eddy) viscosity which, unlike its molecular counterpart, is dependent on local flow properties.

In order to define μ_t, analogy is again sought with molecular motion. Molecular viscosity can be shown to be dependent on the average molecular velocity and on the average distance a molecule travels between collisions (cf. Hirschfelder et al (1967)). Turbulent viscosity was therefore thought to be dependent on a velocity associated with the turbulent motion and and a length scale, termed the "mixing length".

An excellent text describing the development of eddy viscosity models (and beyond) is given by Launder and Spalding (1972) and is therefore not provided here. One such model that will be described is the two-equation k-ε model (cf. Jones and Launder (1972)), since it is used in the present work.

The k-ε model is one of the most advanced of the eddy viscosity models, since both the turbulent velocity and length scale are obtained through solution of balance equations. The latter allow the transport, as well as the generation and dissipation of these properties, to be considered.

The turbulent kinetic energy, k, is defined as the kinetic energy of the fluctuating motion per unit mass, cf.

$$k = \frac{1}{2} \left(\widetilde{u''^2} + \widetilde{v''^2} + \widetilde{w''^2} \right) \qquad \ldots (2.17)$$

where u,v and w are the three velocity components.

A turbulent velocity may therefore be defined by $k^{1/2}$, leading to the following description of turbulent viscosity :-

$$\mu_t = \rho \, C_v \, k^{1/2} \, l_e \qquad \ldots (2.18)$$

where C_v is a universal constant and l_e is the length scale.

The distribution of k throughout the domain may be deduced through solution of its balance equation. The latter is derived by mathematical manipulation of the momentum equations as described by Launder and Spalding (1972). The modelled form of the equation is shown in appendix A and contains terms representing transport, extraction of energy from the mean flow and viscous dissipation. The concept of eddy viscosity allows closure of all terms within this equation except the last. This is modelled in terms of the turbulent kinetic energy and the mixing length, cf.

$$\overline{\mu \left(\frac{\partial u_i''}{\partial x_j} \, \frac{\partial u_i''}{\partial x_j} \right)} = \bar{\rho} \, \varepsilon = \bar{\rho} \, C_d \, k^{3/2} / l_e \qquad \ldots (2.19)$$

where ε is the turbulent kinetic energy dissipation rate and C_d is a universal constant. Though the dissipation term that appears in the balance equation for k is due to molecular (or small scale) dissipation (ie. transfer of turbulence energy into heat), it is modelled in terms of the breakup of macroscopic eddies. The latter, however, is thought to be the rate limiting step.

The length scale is determined through solution of a balance equation for ε (cf. appendix A). The turbulent viscosity may then be defined in terms of k and ε, cf.

$$\mu_t = \bar{\rho}\, C\mu\, k^2 / \varepsilon \qquad \ldots (2.20)$$

where C_μ is an empirical constant.

The k-ε model was devised in constant density flows; however, its suitability to reacting flows represented by Favre averaged equations has been demonstrated by several studies (cf. e.g. Lockwood and Naguib (1975) and Liew (1983)).

Models that use a scalar eddy viscosity cannot adequately represent the normal Reynolds stresses. This can lead to errors in the prediction of the mean flow if these stresses play a direct role. Such regimes include flow in a non-circular pipe and recirculatory flow (cf. Speziale (1987)).

In the present study we are interested in the prediction of an axi-symmetric fire which exhibits non-isotropic behaviour, in that the vertical fluctuating velocity is greater than the horizontal components. The fire is represented by a two-dimensional parabolic formulation and hence the normal Reynolds stresses are thought to have limited effect on the mean flow. There would, however, be implications for the fluctuating field. This is of concern since the fluctuating scalar field influences the radiative emission through turbulent media (cf. chapter 6). In view of this, it is useful to review some of the more elaborate turbulence models that are suited to non-isotropic flow.

Second order closures (cf. Launder et al (1975)) do not rely on the eddy viscosity concept, in that balance equations are set up for the Reynolds stresses and turbulent scalar fluxes themselves. Closure of the equations requires modelling of third order correlations in terms

of computed second order correlations. This requires a turbulent length scale and hence a balance equation for ε.

Second order closures are expensive to implement since, for three-dimensional flow, six Reynolds stress equations are required in addition to those for the scalar fluxes. This has promoted the development of algebraic stress models (ASM) (cf. Chen and Rodi (1975)). These are capable of addressing non-isotropic turbulence and in some applications are computationally more tractable in that the second order differential equations are approximated comparatively simply by algebraic expressions. Chen and Rodi (1975) suggested that the Reynolds stress balance equations could be replaced by algebraic expressions by simply neglecting the convective and diffusive terms. The stresses are then expressed simply in terms of k and ε. Later, Rodi (1976) proposed a refinement whereby the transport may be approximated, by assuming the Reynolds stresses to be proportional to the turbulent kinetic energy.

The k-ε turbulence model which was developed in inert flows has been successfully implemented in the prediction of high Reynolds number reacting jets (cf. Lockwood and Naguib (1975) and Liew (1983)). Fire prediction offers a sterner test to the models since the flow is substantially influenced by buoyancy and exhibits laminar to turbulent transition. Both these have implications on the development of turbulence.

The detailed evaluation of turbulence modelling in fires has not been performed. The effect of buoyancy on turbulence has however been studied through the investigation of inert thermal plumes (cf. Spalding and Afgan (1977)). Both second order closures (cf. Zeman and Lumley (1977)) and ASM have been applied to plumes (cf. Chen and Chen (1979) and Ljuboja and Rodi (1981)). In general, the influence of buoyancy on turbulence structure appears to be small.

Fires are further complicated by the effects of low Reynolds number and transitional flow. These features result from the low momentum that typifies fire sources. Transitional flows have been studied in relation to the investigation of boundary layer build-up on walls (cf. Patel et al (1985)). Such low Reynolds number models cannot, however, be expected to model the transitional flow in buoyant fires, since the mechanisms responsible for the onset of turbulence differ greatly. In fires the transition is induced by low frequency instability that is strongly influenced by minor ambient disturbances and burner geometry (cf. Weckman and Sobiesiak (1988)). The development of models for such regimes therefore remains a difficult problem. In view of this, the computational modelling of a fire, which is presented in chapter 5, seeks to avoid such issues by by-passing the transitional region and initiating the calculation at a height where turbulence has been established.

The computational study of fire hazards often involves the investigation of fires in enclosures, where the transport of product gases throughout the domain is of interest (cf. Cox and Kumar (1986) and Pericleous et al (1988)). Such modelling does not ask much detail of fire sources and hence the application of second order turbulence modelling is not justified. Moreover, in the case of fires in large buildings, the source is typically poorly represented by grid nodes and any advantage in turbulence model enhancement is offset by numerical errors. Such studies have therefore not sought to go beyond k-ε modelling.

Modelling of fire sources has also been restricted to k-ε modelling, due to uncertainties related to turbulence transition and the sensitivity of the calculation to initial boundary conditions (cf. Gengembre et al (1984) and Crauford et al (1985)). The evaluation of turbulence models is therefore difficult. Jeng et al (1982), however, investigated flames within which the effect of buoyancy was substantial. They assessed the appropriateness of three turbulence models by numerical simulation and subsequent comparison with experimental data. The first was the standard high Reynolds number k-ε

model (cf. eg. Lockwood and Naguib (1975)) to which laminar exchange coefficients were added to extend to low Reynolds number. The second model was based on the algebraic stress model of Chen and Chen (1979), which includes effects of buoyancy on turbulence properties but does not consider anisotropy. The third incorporated anisotropy by applying the full algebraic stress model of Chen and Chen (1979). They concluded that though the choice of model did influence the fluctuating properties, the mean flame structure was little affected. They also stress the sensitivity of the calculation to the initial boundary conditions. The latter is in concurrence with the present findings in the investigation of a simulated methane fire. In the present computation, k-ε modelling is applied where the effect of buoyancy is considered in both the mean and fluctuating properties (cf. chapter 5).

2.1.3 Chemical source term closure

2.1.3.1 Introduction

Closure of the mean chemical source term represents the biggest challenge in turbulent combustion modelling. The difficulty relates to its highly non-linear form which is introduced through its dependency on several species and, more importantly, temperature. The latter appears in the Arrhenius expression that describes chemical reaction rates (cf. Williams (1985)). This takes the form

$$K = A\, T^{n} \exp(-H_a/R_0T) \qquad \ldots (2.21)$$

where K is the reaction rate, A and n are constants, H_a is the activation energy and T is the temperature.

Moment approaches to describing the mean reaction rate range from those that simply ignore turbulent correlations to those that apply second order closures (cf. Borghi (1975)). Such approaches are,

however, unsatisfactory for practical problems since they become good approximations only in limits far removed from reality; for instance, in the limit of small fluctuation (when higher order correlations become negligible) or small H_a/RT.

Another limiting system is that where the chemistry is infinitely fast. The mean reaction rate then is dependent on the mixing alone, since if the reactants are allowed to mix at the molecular level, reaction occurs instantaneously. This limit is a reasonable approximation in many practical situations; for example, Spalding (1971a) showed that good qualitative agreement could be attained between calculation and experiment, if the mean reaction rate is proportional to a local turbulent dissipation rate. Such a dependency may be derived analytically (cf. Bilger (1976a)). Bilger shows that in the fast chemistry limit, and given equal species diffusivity and unity Lewis number, the mean reaction rate is given by the local scalar dissipation rate, cf.

$$\chi = 2\,D\,\overline{\frac{\partial \xi''}{\partial x_i}\frac{\partial \xi''}{\partial x_i}} \qquad \ldots (2.22)$$

where D is the diffusion coefficient.

More importantly, in the above approximation the concentration of any chemistry dependent scalar can be algebraically related to a conserved scalar. Fast chemistry models are described in the next sub-section.

The fast chemistry assumption has led to the development of tractable and accurate methods for the modelling of practical systems, since the chemistry that relates to the production of the major products and heat release is relatively fast. However, there is an increasing interest in the production of minor species which are governed by relatively slow chemistry. Such species include NO_x and soot which raise environmental issues and hence their limitation becomes a major concern in combustion system design. The production of slow chemistry species also plays a major role in the investigation of accidental

fire; for instance soot poses a major threat to life since it leads to asphyxiation and, owing to its impact on visibility, hinders escape from fires in buildings.

2.1.3.2 Fast chemistry models for turbulent non-premixed combustion

Section 2.1.1 introduced the conserved scalar concept where, under the restriction of fast chemistry and equal diffusivity of species and heat, any chemistry-dependent scalar may be algebraically expressed in terms of mixture fraction. It should also be realised that this is also subject to constant flame stretch and heat loss; more is said about these issues later in this section. The algebraic functions are often called state relationships and, in turbulent flow, describe the instantaneous scalar state.

In this approximation, solution of a turbulent diffusion flame requires the inclusion of a balance equation only for a conserved scalar; the chemical source term closure problem is therefore circumvented. It is a prerequisite, however, that the state relationships, $\phi(\xi)$, are prescribed. Some methods for their derivation are described below.

The simplest method for the derivation of the state relationships is the Burke-Schumann flame sheet approximation (cf. Williams (1985)), where an adiabatic irreversible global reaction of infinite rate is assumed. The reaction zone is then limited to an infinitesimally thin sheet, which is represented as a delta function in ξ space (cf. $\delta(\xi-\xi_{st})$, where ξ_{st} is the stoichiometric mixture fraction).

The above method yields excessive temperatures, since dissociation reactions are not considered, and is a poor representation of the detailed scalar field, since no intermediate species are considered. The chemical equilibrium approach ,adopted by for example Jones and Priddin (1979), is an alternative that does not suffer from these inadequacies. The procedure entails the construction of state

relationships by allowing a mixture of fuel and oxidant, in a concentration ratio defined by the local mixture fraction, to attain equilibrium. The use of a suitable algorithm (cf. Gordon and McBride (1971)) may allow any number of species to be considered. The accuracy of the approach, however, depends on the applicability of chemical equilibrium to practical situations. The approximation is reasonably good at mixture fractions close to stoichiometric, where temperatures and hence reaction rates are high, but becomes less so at richer mixtures. In particular chemical equilibrium greatly overestimates CO levels (cf. Askari-Sardhai (1987)). An additional feature is observed when the fuel is a C_2 or higher hydrocarbon, where most of the fuel is converted into CH_4 even at low temperatures; this is not observed in reality. In view of the poor rich-side representation, Jeng et al (1982) assumed chemical equilibrium upto a certain critical mixture fraction, beyond which inert mixing is prescribed.

A fundamental problem with the chemical equilibrium method is that each mixture state is considered in isolation from its neighbours. In diffusion flames this cannot be so, since gradients in temperature and concentrations will lead to flux across mixture fraction space. An alternative method that is capable of addressing this is the laminar flamelet concept (cf. Liew et al (1981) and Peters (1984)). This views a turbulent flame as comprising microscopic laminar flamelets, which are allowed to be stretched, contorted and spatially fluctuated by the turbulent motion. The maintenance of a laminar structure at the small scale relies on the reaction zone thickness being less than the smallest scale of the turbulence (the Kolmogorov scale) (cf. Bilger (1988)).

The laminar flamelet concept allows the incorporation of chemistry of any degree of detail, since this is confined to the calculation of a representative laminar flame. Moreover, in the absence of sufficient chemical kinetic information, state relationships may be obtained from laminar flame experiment.

In chapter 4 the laminar flamelet approach is used in the modelling of a turbulent C_2H_4-air jet diffusion flame, where the computation of an adiabatic laminar diffusion flame is used to define the state relationships. In chapter 5 the prediction of a Ch_4-air fire is reported, where the state relationships were obtained from the experiment of Mitchell et al (1980).

The importance of flame stretch due to hydrodynamic strain caused by the turbulent motion may play a major role in certain circumstances, leading to local extinction. Liew et al (1984) suggest that this may be addressed by the laminar flamelet approach, by constructing a library of laminar flamelets each for a different strain rate and then applying the appropriate flamelet locally within the turbulent computation. Liew et al (1984) obtained this computationally, but such a library may also be obtained experimentally by resorting to the counter-flow geometry (cf. Tsuji and Yamaoka (1969) and Dixon-Lewis and Missaghi (1988)).

The state relationships $\phi(\xi)$ are non-linear functions and hence the evaluation of the mean mixture fraction is not sufficient to calculate $\tilde{\phi}$ (ie. $\tilde{\phi} \neq \phi(\tilde{\xi})$); the PDF of mixture fraction is required. cf.

$$\tilde{\phi^n} = \int_0^1 \phi^n(\xi)\ \tilde{P}(\xi)\ d\xi \qquad \ldots (2.23)$$

where n is a positive integer and indicates the moment, e.g. when n is unity the first moment (the mean) of ϕ is found.

Typically a presumed form of $P(\xi)$ is prescribed that is defined by a finite number of moments. Given the present state of turbulence modelling this is restricted to the first two moments alone. The variance of mixture fraction required to supplement the mean may be obtained through solution of its modelled balance equation (cf. Launder and Spalding (1972)) which is shown in appendix A.

Two popular forms for $P(\xi)$ are the clipped Gaussian (cf. Lockwood and Naguib (1975)) and the beta function (cf. Liew (1983)). The former is essentially a Gaussian which is truncated to be confined between 0 and 1 which are the physical bounds of mixture fraction. The integrals between $-\infty$ to 0 and 1 to $+\infty$ are then redistributed as delta functions at 0 and 1 respectively. In order to define the mean and variance of the Gaussian, and hence $P(\xi)$, from the computed mean and variance of the clipped Gaussian, an iterative procedure is required. The present study therefore adopts the beta function formulation which is naturally bound between 0 and 1. Both forms were investigated by Jones (1980) who found that either were capable of showing good agreement with experimental data.

The beta function is defined as

$$B = \xi^{\alpha-1}(1 - \xi)^{\beta-1} \qquad \ldots (2.24)$$

(cf. Abramovitz and Stegun (1968)) where the exponents, α and β, are expressed in terms of the mean and variance of the beta function, cf.

$$\alpha = \tilde{\xi}\left(\frac{\tilde{\xi}(1-\tilde{\xi})}{\widetilde{\xi''^2}} - 1\right) \qquad \ldots (2.25)$$

$$\beta = \frac{\alpha\,(1-\tilde{\xi})}{\tilde{\xi}} \qquad \ldots . (2.26)$$

The total area under a PDF is unity since this represents the probability that a variable may take any value. This is not a feature exhibited by the beta function so it is normalised to define the PDF, cf.

$$P(\xi) = \frac{B(\xi)}{\int_1^0 \xi^{\alpha-1}(1-\xi)^{\beta-1}\, d\xi} \qquad \ldots (2.27)$$

Equation 2.27 is used to define the Favre PDF of mixture fraction, $\tilde{P}(\xi)$, since the first and second moments are the Favre mean and variance of mixture fraction computed from their balance equations (cf. appendix A). The mean scalar quantities calculated from equation 2.23 are then Favre averaged quantities. However, if the density may also be expressed as a function of mixture fraction alone then the Reynolds and Favre PDFs are interchangeable (cf. Bilger (1975)). cf.

$$\int_0^{\xi} P(\xi)\, d\xi = \bar{\rho} \int_0^{\xi} \frac{\tilde{P}(\xi)}{\rho(\xi)}\, d\xi \qquad \ldots (2.28)$$

The Reynolds averaged density may then be obtained from

$$1 / \bar{\rho} = \int_0^1 \tilde{P}(\xi)/\rho(\xi)\, d\xi \qquad \ldots (2.29)$$

and any other Reynolds quantity may be found according to

$$\overline{\phi^n} = \bar{\rho} \int_0^1 \frac{\phi^n(\xi)\ \tilde{P}(\xi)}{\rho(\xi)}\, d\xi \qquad \ldots (2.30)$$

The laminar flamelet approach coupled with the presumed two-parameter PDF has proved very successful in the modelling of non-premixed combustion (cf. Liew (1983)). Complications arise when the state relationships become functions of more than one variable, for example when it is also dependent on flame stretch, heat loss and reaction progress variable; the latter is introduced if the chemistry is not fast. The system is then complicated in that a multivariate PDF must be computed which results in a significant increase in complexity. To avoid this issue, statistical independence may be assumed so that a joint PDF is represented as the product of marginal PDFs (cf. Liew et al (1984) and Janicka and Kollmann (1979)). Such a simplification may lead to substantial error in the case of the reaction progress variable since high reaction rate is strongly correlated with

stoichiometric mixture fraction. Therefore for the case of slow chemistry the computation of a multivariate PDF seems unavoidable.

PDF methods and other more simplified approximations for slow chemistry turbulent combustion are reviewed in the next sub-section.

2.1.3.3 Slow chemistry models for turbulent non-premixed combustion

The previous section introduced fast chemistry models, where the thermochemical field may be represented in terms of a conserved scalar whose statistics are obtained by presuming the form of its PDF. The most detailed of these models is the laminar flamelet approach, since the flamelet relationship is capable of incorporating chemistry of any degree of complexity, hydrodynamic strain and differential (molecular) transport of species and heat. Turbulent combustion modelling becomes less tractable if the flamelet regime is not realised and the reaction zone is relatively broad compared to the smallest turbulence scales (cf. Bilger (1988)). Also, the dependence of all scalars on only a conserved scalar becomes a poor approximation if the chemistry is not fast. The flamelet concept does not apply to species such as NO_x and soot. These, however, may be easily appended to a flamelet model if they can be considered to be a perturbation to the thermochemistry. Bilger (1976b) describes such a strategy for NO_x prediction and later (cf. Chapter 4) we extend this to incorporate soot.

Of more fundamental concern is CO. This is controlled by relatively slow processes which is apparent in that typical CO levels in flames are found in concentrations well below those predicted by equilibrium. CO cannot be treated as a perturbation to the thermochemistry since it comprises a notable amount of carbon and oxygen. Liew (1983), however, has shown that the inclusion of CO into a flamelet scheme produces results in good agreement with experiment. Bilger (1988) suggests that this does not necessarily imply the existence of flamelets since lower than equilibrium CO levels may result even for distributed reaction zones. In fires, the scales of turbulence are much larger than in jets

and flamelet theory is less questionable. A flamelet model is used in the present study.

The need to resort to fast chemistry models is to avoid the chemical source term closure problem. In this respect PDF methods (cf. Pope (1985),(1990)) are physically appealing since they incorporate the effect of finite rate chemistry in an exact manner (ie. modelling is not required). These methods involve the solution of an evolution equation for a multidimensional PDF. If the PDF is the joint PDF of all scalars then the reaction rate is closed. If the PDF is the joint vector-scalar PDF then the convective terms appear in closed form and hence there is no need for turbulence modelling. PDF methods therefore resolve the two most important problems in the prediction of turbulent reacting flows. Closure assumptions, however, are still required for the fluctuating pressure, the effect of viscosity and the molecular diffusion. Models for these processes are discussed by Pope (1985) and (1990). The models usually rely on a time or length scale of the turbulence and hence require a modelled balance equation for ε (the turbulence dissipation rate). Recently, Pope (1990) has proposed the solution of the evolution equation for the joint vector-scalar-dissipation PDF which removes the need for a modelled equation for ε.

PDF methods are continually improving (cf. Pope (1990)) in terms of the required closure models, and though Pope (1981) devised a computationally efficient Monte Carlo technique for the solution of a multidimensional PDF, it is unfeasible to consider a large number of independent species. This has led to the development of schemes that simplify the chemistry so as to reduce the number of independent variables. Such methods include the partial-equilibrium model proposed by Dixon-Lewis et al (1975) who suggested, for an H_2-air system, that the fast chain branching reactions that form radicals may be considered in partial-equilibrium and only the relatively slow three-body recombination reactions are allowed to proceed at a finite rate. Janicka and Kollmann (1979) used this method to describe turbulent H_2-air flames where closure required solution of a two-variable (mixture fraction and reaction progress variable) PDF. Janicka (1981) extended

this approach to CH_4 flames where a second reaction progress variable is introduced.

An alternative to the partial-equilibrium scheme, is the more formal reduced reaction schemes (cf. Paczko et al (1986) and Rogg and Williams (1988)). These are derived from detailed reaction mechanisms where the key steps are identified and the redundant steps removed in order to limit both the number of reactions and the number of species. For example Paczko et al (1986) reduced a 46 step reaction mechanism for methane incorporating 23 species to a 4 step mechanism with 7 species. It is important that a reduced reaction scheme should be developed under conditions close to those within which it is to be applied, since under different conditions (eg. temperature, pressure and regime - premixed or diffusion flame) different reactions may become important.

The reduced reaction scheme has a firmer foundation than the partial-equilibrium approach and its extension to higher hydrocarbons can be easily envisaged. It is important to note from a computational point of view, however, that partial-equilibrium models are preferable since the degree of "stiffness" is reduced as equilibrium is assumed for the fast reactions.

2.2 Soot in combustion

2.2.1 Soot formation and oxidation

The study of soot formation and burnout has received a great deal of attention in recent years mainly owing to environmental concerns. Devices that involve non-premixed combustion, for example gas turbines, diesel engines and furnaces, are capable of producing soot in the combustion zone due to the presence of local rich regions, even though the device as a whole may be operating fuel lean. This soot, if not subsequently oxidized, will be emitted through the exhaust as

smoke. For all devices the emission of smoke is undesirable, both from the standpoint of pollution and because smoke represents uncombusted carbon and hydrogen and therefore reduced combustion efficiency. In some devices, such as candles and furnaces, the formation of soot is desirable since hot soot particles are effective radiators; in the case of the candle the visible radiation is utilised whilst in furnaces the enhanced thermal radiation provides efficient heat transfer to the walls. In the gas turbine and diesel engine, however, the formation of soot is undesirable, the major concerns being radiative heating of the combustor walls and soot deposition. In addition to the aforementioned devices where soot emission is unwanted, the carbon black industry is concerned with producing copious amounts of soot which is subsequently utilised in, for example, the manufacture of motor car tyres.

As well as soot formation and emission being of concern in devices designed to combust, it is of major interest in accidental fires. Large scale fires are known to produce large quantities of soot due to poor mixing, long residence times and subsequent heat loss which freezes the soot oxidation chemistry. The understanding of soot formation and burnout in fires is essential, both in terms of the radiating properties of hot soot particles in the burning zone and smoke emitted in the plume. The large radiative flux offered by hot soot particles contributes strongly to fire spread due to heat feedback to the fire source and heating of external bodies. Smoke emission from fire in buildings is of great importance since its asphyxiating properties and impact on visibility make it a major contributor to fatalities.

It is the better understanding of fire hazards, where soot can play a major role, to which the present study is directed. The soot model presented in chapter 3, however, is more widely applicable to non-premixed combustion systems in general and related work (Moss et al (1987), (1988) and Stewart et al (1990)) is aimed towards applying the model to gas turbine combustors.

The purpose of this section is to give an overview of the current understanding of soot and its governing processes, and in view of the present aims, to review models for soot in turbulent combustion. The review is not comprehensive and the reader is therefore referred the following reviews in the literature :- Glassman (1988), Haynes and Wagner (1981), Calcote (1981), Appleton (1973), Mullins et al (1987).

Before describing the processes that govern soot formation and burnout it is useful to give some information on soot itself, for example what it is.

Electron micrographs of soot show basic soot elements to be spherical of diameters that can reach upto 40 nm (cf. Megaridis and Dobbins(1989) and Palmer and Cullis (1965)). These spheroids are formed at first by gas phase reactions that form the condensed phase (soot nuclei). The smallest particles detected are the order of a nanometer; this, however, reflects the sensitivity of the diagnostic technique. The soot nuclei grow to form bigger spheroids through heterogeneous surface growth reactions and physical coagulation. Further coagulation results in the formation of chains (straight and branched) (cf. Haynes and Wagner (1981)) which constitute the smoke emitted by combustion systems.

At the molecular level soot constitutes approximately 90 % (by mole) carbon and 10% hydrogen. The particles are made up of graphite type layers where the inter layer spacing is somewhat greater than for graphite. There is also evidence of many lattice defects. The density of soot is ~1800kg/m^3 (cf. Graham et al (1975) and Mullins et al (1987)).

The major processes involved in soot formation and burnout may be characterised in the following way :- **(i)** formation of the first condensed phase, **(ii)** surface growth, **(iii)** coagulation and **(iv)** oxidation. The entire process involves many reaction steps and one might have identified more processes, for example the formation of the first ringed molecules from which soot is constituted, however, the

four groups include all the major processes :- homogeneous gas phase formation reactions, (i); heterogeneous gas-solid phase formation reactions, (ii); physical interaction between particles, (iii); heterogeneous gas-solid phase burnout, (iv).

Several studies of soot formation in premixed flames, diffusion flames and shock tubes have concluded that the bulk of the soot formed is due to surface growth rather than nucleation (cf. Glassman (1988)). This has generally been based on a comparison between the evolution of soot volume fraction and number density; the former continues to increase when the latter has gone into decline. Where estimates have been made of the coagulation rate (eg. Bockhorn et al (1984)) it has been shown that the decrease in number density due to this process does not upset this conclusion. In the present study, where soot formation in a laminar Wolfhard-Parker methane-air diffusion flame is investigated, the results strongly suggest the dominance of surface growth (chapter 3).

Tesner (1959) showed that surface growth can occur at lower temperatures than nucleation, whilst Palmer and Cullis (1965) showed that surface growth can occur at lower hydrocarbon concentration than nucleation. These observations are, at least in part, due to the high reactivity of young soot particles. This was demonstrated by Dugwell and Foster (1973) who found, during the pyrolysis of methane, that surface deposition was an order of magnitude greater in the presence of soot particles than alumina or graphite. Furthermore, several authors have shown (eg. Bockhorn et al (1984)) that the reactivity, as deduced by the rate of formation of soot mass, of young soot particles is greater than older particles. Frenklach et al (1985) explain this as a reduction in the radical nature of the soot particles.

Frenklach et al (1985) and (1986), through detailed kinetic computation, have demonstrated the feasibility of radical mechanisms in the formation of soot; in particular, they draw attention to the H radical which is effective in promoting the radical nature of soot particles and their precursors. It is a common view that soot

formation is governed by radical mechanisms (cf. Glassman (1988)). It should, however, be pointed out that others (cf. Calcote (1981)) believe that soot formation is controlled by ionic mechanisms and the enhanced soot formation in reaction zones is attributed to the high ion concentration known to exist in flames (cf. Gaydon and Wolfhard (1979)). Calcote (1981) suggests that neutral mechanisms cannot account for the fast rates observed for soot formation. However, more recently, Weissman and Benson (1989) who investigated the pyrolysis of methane in the presence of chlorine, suggest that neutral radical mechanisms are capable of producing soot at the rates observed. They emphasise the importance of H abstraction from polycyclic aromatic hydrocarbons and soot by H atoms.

Weissman and Benson (1989) postulated that in the case of methane pyrolysis, acetylene is a major intermediate. This is substantiated by Smyth et al (1985) in their experimental investigation of a methane - air diffusion flame, where acetylene was discovered to be a major pyrolysis product. Weissman and Benson drew attention to the key role of the methyl radial (CH_3) in the soot formation process. This, however, was thought to be restricted to methane pyrolysis.

It should be noted that detailed mechanisms describing soot formation (eg. Frenklach et al (1985) and Weissman and Benson (1989)) necessarily include many radicals and intermediate species for which accurate thermochemical data is not available; quantitative analysis is therefore not possible. In view of this and that a unified theory of soot formation, though proposed (Glassman (1988)), is not yet proven, practical problems must rely on more empirical global approaches. In addition, when the application is to turbulent combusting environments, as is the case here, one is restricted to the use of global mechanisms to limit closure problems. Global models and their application to turbulent flame prediction are reported in the next sub-section.

The major oxidising species found in flame environments are O_2, O and OH. In co-flowing laminar diffusion flames, oxidation is evident as

soot burnout at the tip of the flame, since lower down soot is confined to rich regions where formation is dominant. Given the structure of diffusion flames, soot first passes through a region of O and OH oxidation, since these species are found in and around stoichiometric, and then into an O_2 oxidising region which is restricted to the lean of stoichiometric. The extent to which a diffusion flame emits smoke then depends on the oxidation rate and residence times spent in these regions. The size of the soot particles is also important since oxidation may be limited by the surface area available for reaction. The effect of flame heat loss is also significant since it can extinguish soot oxidation and lead to smoke emission from flames (cf. Kent and Wagner (1984)).

In addition to the ability of O_2 to oxidise soot, many studies (cf. Haynes and Wagner (1981)) have demonstrated that the presence of small amounts of O_2 may lead to enhanced soot formation. Frenklach et al (1986) investigated the effect of O_2 addition on a detailed reaction mechanism for soot formation, where enhanced pyrolysis was observed. The underlying reason was deduced to be the concentration of H which reached super-equilibrium levels in comparison to H_2. This results in an increased tendency of H abstraction from the surface of soot particles and precursors, therefore enhancing their radical nature and speeding up the formation rate.

It is difficult to know which species is the most dominant oxidising species in diffusion flames. In the present study where soot in turbulent diffusion flames is studied, the global mechanism of Nagle and Strickland-Constable (1962) is used, which considers O_2 oxidation. Though the model was developed in conditions far removed from flame environments - heated O_2 jets were directed onto rods of pyrolytic graphite - Appleton (1973) found that it correlated data obtained from soot oxidation in shock tubes operating over a wide range of conditions. More recently Kent and Wagner (1984) and Megaridis and Dobbins (1989) found that the Nagle and Strickland-Constable expression could describe soot burnout in laminar ethylene-air diffusion flames.

2.2.2 Models for soot formation and oxidation

The previous section described the present understanding of soot formation and burnout which are as yet unsolved problems. Successful design of devices such as gas turbine combustors and diesel engines, however, requires a knowledge of these processes in order to limit soot emission. This has led to the development of empirical approaches where experimental data are correlated using simple global expressions. These have recently been reviewed by Mullins et al(1987). In view of the present interests, the discussion below is restricted to models that have been applied to turbulent flame prediction.

Khan and Greeves (1974) investigated the formation of soot in diesel engines and derived the correlation

$$\frac{dm}{dt} = C_f \, P_{fu} \, \phi^n \, e^{-T_a/T} \qquad \ldots (2.31)$$

where m is the concentration of soot (kg/m^3), C_f is the rate coefficient and is related to the volume ratio of the soot formation zone to that of the cylinder, ϕ is the equivalence ratio and P_{fu} is the partial pressure of unburnt fuel. The parameter n and activation temperature T_a were found to be 3 and 20,000K respectively.

The above model, like many such approaches (cf. Mullins et al (1987)), treats soot formation in a single step. In contrast Tesner et al (1971) described the rate of formation of soot particles in acetylene/hydrogen-air diffusion flames in two steps - the formation of gas phase radical nuclei and thence the formation of soot particles.

The rate of formation of radical nuclei is expressed as

$$\frac{dn}{dt} = n_0 + (f-g)n - g_0 N n \qquad \ldots (2.32)$$

where n is the number of radical nuclei (cm^{-3}), f is the linear branching coefficient, g is the linear termination coefficient, g_0 is the linear termination coefficient on soot particles and N is the soot particle number density (cm^{-3}). n_0 is the spontaneous generation of soot particles ($cm^{-3}s^{-1}$), cf.

$$n_0 = 10^{13} [HC] e^{-87,800/T} \qquad \ldots (2.33)$$

where [HC] is the concentration of acetylene ($mole/cm^3$). The rate of generation of soot particles is then expressed as

$$\frac{dN}{dt} = (a - b N) n \qquad \ldots (2.34)$$

where a and b are empirical coefficients. The rate of generation of soot mass then requires an assumption for the mass of a soot particle.

Tesner et al (1971) found the above model could describe their observations, most notable of which was the apparent maximisation (and subsequent decline) of particle formation rate. This was found not to be a kinetic effect since it was accompanied by little change in acetylene concentration and temperature. The model describes this by the destruction of radical nuclei through collision with soot particles.

Gilyazetdinov (1972) investigated the rate of formation of carbon black where hydrocarbons of various aromatic content were injected into the hot exhaust gases of a fuel-lean premixed methane-air flame. A two-step mechanism was proposed which describes the formation of soot particle nuclei and their subsequent growth through heterogeneous reaction. The processes considered are particle nucleation, surface growth and coagulation. The latter can account for the apparent decline in particle formation rate observed by Tesner et al (1971).

Particle nucleation is assumed to result through collision between hydrocarbon precursors and ambient molecules, and surface growth through the collision between precursors and the surface of soot particles. Coagulation is assumed to result from soot particles that are subject to free molecular collision (cf. Fuchs (1964)) and is therefore dependent on the square of the particle number density and the root of the temperature. This model is used in the present work and is described further in chapter 3.

Abbas and Lockwood (1985) applied the model of Khan and Greeves (1974) to the prediction of turbulent acetylene jet diffusion flames. The values of n and the activation temperature (cf. eqn 3.31) were taken directly from Khan and Greeves (1974) whilst C_f was found to be proportional to the Richardson number ($Ri=gD/u^2$, where g is the gravitational acceleration, D the burner diameter and u the initial jet velocity). Averaging of the formation rate was achieved through expressing it in terms of mixture fraction and then applying equation 2.30.

To account for oxidation, Abbas and Lockwood (1985) used a hybrid formulation, where the mean rate was related to the averaged form of the expression of Lee et al (1962) and the turbulent dissipation rate as adopted by Magnussen et al (1979). Lee et al (1962) investigated soot oxidation in propane flames which they related to the partial pressure of oxygen, P_{O2}, cf.

$$R = 1.085\times10^{4}\ P_{O2}\ T^{-1/2}\ e^{-20,000/T} \qquad (kg\ m^{-2}s^{-1}) \quad \ldots\ (2.35)$$

Abbas and Lockwood (1985) assumed the surface area of the soot to be proportional to its mass concentration.

Magnussen and co-workers (cf. Magnussen and Hjertager (1976) and Magnussen et al (1979)) applied the model of Tesner et al (1971) to the prediction of acetylene jet diffusion flames. The model was grafted onto an eddy break-up description of the gas phase chemistry (cf. Spalding (1971a)). The soot formation was assumed to occur in fuel-rich eddies whilst oxidation was assumed to occur in fine

structures where the gas phase combustion also occurred. The rate of soot oxidation was controlled by the turbulent dissipation.

In the present study the mechanism of Gilyazetdinov (1972) is used to describe soot formation, since it is capable of describing soot build-up in the laminar methane-air diffusion flame in chapter 3. The model of Tesner et al (1971), which lacks a description of surface growth, and the single-step mechanisms, which cannot describe particle surface area, proved inadequate. In the turbulent flame predictions reported in chapters 4 and 5, soot oxidation is addressed using the correlation of Nagle and Strickland-Constable (1962). The latter investigated the oxidation of pyrolytic graphite through the action of heated O_2 jets and derived the following correlation:-

$$R = \frac{W_C K_a P_{O2}}{(1 + K_t/(P_{O2}K_b))(1 + K_z P_{O2})} + \frac{W_C K_b P_{O2}}{1 + P_{O2}K_b/K_t} \quad (kgm^{-2}s^{-1}) \quad .. \quad (2.36a)$$

where W_C is the molecular mass of carbon (kg kg-mole^{-1}), P_{O2} is the partial pressure of O_2 (atm) and

$$K_a = 200 \exp(-125.5/R_0T) \quad \text{kg-mole m}^{-2}\ \text{s}^{-1}\ \text{atm}^{-1} \quad .. \quad (2.36b)$$

$$K_b = 4.46\text{x}10^{-2} \exp(-63.6/R_0T) \quad \text{kg-mole m}^{-2}\ \text{s}^{-1}\ \text{atm}^{-1} \quad .. \quad (2.36c)$$

$$K_z = 21.3 \exp(-17.2/R_0T) \quad \text{atm}^{-1} \quad .. \quad (2.36d)$$

$$K_t = 1.51\text{x}10^{6} \exp(-405.8/R_0T) \quad \text{kg-mole m}^{-2}\ \text{s}^{-1} \quad .. \quad (2.36e)$$

Kent and Wagner (1984) and Megaridis and Dobbins (1989) found that the Nagle and Strickland-Constable (1962) expression could describe soot oxidation in laminar ethylene-air diffusion flames.

2.3 Thermal radiation in combustion

2.3.1 Introduction

Combustion flows are capable of emission and absorption of thermal radiation. The latter contributes to local enthalpy sources, and hence affects temperature and density, and must therefore be modelled to close the set of governing equations (cf. eqn. 2.1 to 2.4). In addition to its coupling with the flowfield, radiative emission from a combustion zone to its surroundings is of great importance. In furnaces, for example, efficient operation requires effective radiative heating of its walls. In other devices, such as gas turbine combustors, radiative emission is also of great concern, though here the desire is for its limitation; heating of the combustor liner has an adverse effect on its durability.

Radiation is also important in the study of fires, where its coupling with the flowfield structure is enhanced given the buoyancy-dominated nature of such flows. Furthermore radiative emission from large fires is strongly related to their hazard potential, as this mode of heat transfer is largely responsible for the heating of external bodies.

The calculation of radiation in combusting environments requires the solution of the radiative transfer equation (cf. Siegel and Howell (1972). This describes the passage of a monochromatic beam through an emitting, absorbing and scattering medium. In the present study scattering is ignored, since this is negligible for molecules and also for soot particles, provided they are small compared to the wavelength of the radiation (cf. Kerker (1969)). Negligible scatter is typically assumed in the study of radiation in combustion systems (cf. Viskanta and Menguc (1987)).

The radiative transfer equation through an absorbing/emitting medium takes the form (cf. Siegel and Howell (1972))

$$\frac{dI_\lambda}{ds} = - k_\lambda(s) \left(\frac{E_\lambda}{\pi}(s) - I_\lambda(s) \right) \qquad \ldots (2.37)$$

where I_λ is the monochromatic energy emitted at wavelength λ in the direction s per unit time per unit solid angle per unit area normal to the beam. k_λ and E_λ are the monochromatic absorption coefficient and blackbody emission as described by Planck's function. cf.

$$E_\lambda = \frac{C_1}{\lambda^5} \left(e^{C_2/\lambda T} - 1 \right)^{-1} \qquad \ldots (2.38)$$

where C_1 and C_2 are Planck's first and second constants (cf. Siegel and Howell (1972)).

The spectral absorption coefficient is dependent on the partial pressures of all species capable of absorbing at wavelength λ, temperature and total pressure. In hydrocarbon-air combustion, the major thermal radiators are CO_2, H_2O, CO and particulate soot. Models for the optical properties of these are described in the following subsections.

Radiation is a non-linear function of partial pressures and temperature, and is therefore influenced by turbulence which causes fluctuations in gaseous properties. This is a particular issue in the present study where radiative emission from buoyant fires is of interest, since such flows exhibit large scale scalar fluctuations. The influence of turbulence interaction is related to the amplitude of the scalar fluctuations (cf. Cox (1977) and Grosshandler (1985)). More is said about turbulence-radiation interaction in chapter 6, where the Monte Carlo method of Faeth et al (1986) is used to assess its impact on radiation from a buoyant fire.

In the following subsections, models for the optical properties of gaseous species and soot are presented and then practicable methods for the solution of the radiative transfer equation. The latter is complex since it involves integration over distance, area and solid

angle. The discussions are brief and draw attention to several references for greater detail. It is useful at this stage to highlight the following review articles: Viskanta and Menguc (1987) and Sarofim (1986) give a detailed discussion of all the major aspects of radiation in combustion systems; De Ris (1979) focuses on radiation in fires; Tien and Lee (1982) discuss models for optical properties of inhomogeneous paths through soot containing combustion gases and Faeth et al (1986) review turbulence-radiation interaction.

2.3.2 Optical properties of gases

Gaseous absorption and emission are confined to narrow spectral regions resulting from transitions in molecular vibrational states. Superimposed on these is a fine structure comprising several lines which result from rotational transitions. The contribution of these lines to the absorption coefficient depends on their strength, shape and width, which are dependent on pressure-path length, temperature and line-broadening effects - natural broadening, collision broadening and Doppler broadening - (cf. Hottel and Sarofim (1967)). Also critical to the optical properties is line overlap, which may result from sufficient broadening of adjacent lines or the superposition of rotational lines of different species.

A rigorous treatment of the radiation requires that the rotational lines are spectrally resolved. For practical calculations, however, this is computationally unacceptable since these lines are very numerous. This has led to the development of band models which consider spectral elements that contain several lines. The most spectrally resolved model is the narrow band model (cf. Ludwig et al (1973) and Tien and Lee (1982)), where the spectrum is divided into elements of width 5 to 25cm^{-1} in wave number (ω). This is large compared to the the distance between individual lines and yet spectrally resolved enough to define much of the structure of vibrational bands - the widths of the 2.7μm CO_2 and H_2O band and the 4.3μm CO_2 bands are 1050cm^{-1} and 260cm^{-1}.

Narrow band models are unsuitable for coupled radiation-flowfield calculation since their computation requirements are excessive. In combusting flows their use has been restricted to post-process diagnostics (cf. chapter 6 and Gore and Faeth (1986)) or the development of more computationally tractable models (cf. Grosshandler (1980)).

The need for computationally tractable models is in conflict with the nature of gaseous radiation which requires spectral resolution. A compromise is the wide band models (cf. Edwards (1975) and Tien and Lee (1982)). These consider each vibrational band as an element, the optical properties of which are specified in terms of band strength and width. The latter are functions of pressure-path length and temperature. The spectral absorption coefficient across the band is described by some pre-specified function. The most widely adopted function is exponential as suggested by Edwards and Menard (1964).

For heat transfer calculation it is the spectrally-integrated radiative fluxes that are of interest. This has led to the development of models that specify optical properties averaged over the whole spectrum. The simplest of these is the grey gas model which has been used in engineering for several decades. The model assumes an emissivity that is invariant over the whole spectrum, and which may be calculated from the spectral emissivity by weighting with the Planck function, cf.

$$\varepsilon = \frac{\int_0^\infty \varepsilon_\lambda \, E_\lambda \, d\lambda}{\int_0^\infty E_\lambda \, d\lambda} = \frac{\int_0^\infty \varepsilon_\lambda \, E_\lambda \, d\lambda}{\sigma \, T^4} \qquad \ldots \quad (2.39)$$

where σ is the Stefan-Boltzmann constant and E_λ is the spectral blackbody radiation given by equation 2.38.

Hottel constructed charts for the total emissivity for CO_2-H_2O systems (cf. Hottel and Sarofim (1967)) based on substantial experimental data. These were later correlated by mathematical expressions by Leckner (1972) suitable for use in computer codes. The emissivity is prescribed as a function of partial pressure path length and temperature. A correction is required for spectral overlap, since CO_2 and H_2O bands coincide at 2.7μm, and total pressure.

Grey gas models are expected to work well for homogeneous systems but not so for paths with variable species concentration and temperature. Two models that may are the equivalent line model (cf. Edwards and Balakrishan (1973)) and the total transmittance non-homogeneous model (cf. Grosshandler (1980)).

2.3.3 Optical properties of soot

Soot is comprised of small particles that, unlike gases, are capable of radiating at all frequencies. The interaction between small spherical particles and electromagnetic radiation is described by Mie theory (cf. Kerker (1969)). This shows that in the limit of small particles (where the particle radius is much smaller than the wavelength of the radiation), scatter is negligible and the spectral absorption coefficient is simply related to the soot volume fraction f_v, cf.

$$k_{s\lambda} = \frac{36\,\pi\,n\,k}{(n^2-k^2+2)^2+4n^2k^2}\,\frac{f_v}{\lambda} \qquad \ldots (2.40)$$

where n and k are the real and imaginary parts of the complex refractive index (cf. (n-ik)) and $k_{s\lambda}$ is the soot absorption coefficient.

In flame zones equation 2.40 is expected to be a reasonable estimate of soot absorption since the particles are both spherical and small

(cf. Haynes and Wagner (1981)). In post flame regions particles grow through collision to form fractal-like aggregates that are substantially non-spherical and can no longer be considered small. The optical properties of non-spherical soot particles have been studied by Felske and Tien (1977).

The evaluation of the parameters n and m has been made by Dalzall and Sarofim (1969), Lee and Tien(1981) and more recently by Mullins and Williams (1987) amongst others. Typically n and m are insensitive to fuel type but do vary with wave length. The data compiled by Tien and Lee (1982) suggest this may lead to a variation of ~20% for $k_{s\lambda}$, over the wavelength range .5 to 10 μm. In the present study n and k are assumed constant and taken to be 1.93 and .39, which were the values measured by Mullins and Williams (1987) at 633nm. These values are used in chapter 3 where equation 2.40 is used to determine soot volume fraction from the extinction of light from a helium-neon laser (which operates at 633nm), and in chapter 6 where soot radiation is predicted.

2.3.4 Solution of the radiative transfer equation

For problems of engineering interest which typically exhibit multi-dimension and complex geometries, an exact solution of the radiative transfer equation is not viable. Approximate methods that have been widely used in engineering applications are Hottel's zone model (cf. Hottel and Sarofim (1967)), Monte Carlo methods and flux models. The latter have been widely used in recent years since they are easily incorporated into finite difference flowfield solvers and are more economical than the zone or Monte Carlo methods. Flux models, however, are restrictive in that radiation is allowed to propagate in only a few directions (6 for 3 dimensional flow). Also when curvilinear grids are used, their formulation becomes more cumbersome. This has led to the development of the discrete transfer method (cf. Lockwood and Shah (1981)) which is essentially a hybrid of the above three methods. These methods and others are reviewed by Viskanta and Menguc (1987).

In the present study, solution of the radiative transfer equation is very much simplified since only line-of-sight calculation is required (cf. chapter 6); integration over area and solid angle is therefore avoided.

CHAPTER 3

Experimental and numerical investigation of a laminar sooting diffusion flame

3.1 Introduction

In recent years there has been an increasing interest in the emission of pollutants from combustion devices, in addition to the more traditional concerns associated with fuel economy and overall performance. The study of the latter has allowed major simplification in the modelling of turbulent combustion since the heat release is usually governed by reaction in the fast chemistry limit. Here reaction time scales are much faster than those associated with mixing and in the limit can be considered infinitely fast, ie. if fuel and oxidant are allowed to mix, they react instantaneously. The mean reaction rate is then controlled by the small scale mixing rate, and a number of conserved scalar-based approaches apply (cf. chapter 2.1).

When attention is turned to the minor species that are a threat to the environment, however, for example soot and NO_x, the fast chemistry limit does not apply and the tractability of the conserved scalar approach cannot be realised. This re-kindles interest in the closure of the chemical source term that appears in the mean balance equation of a chemistry-dependent scalar - a problem circumvented by the conserved scalar approaches. Such source terms are highly non-linear, in particular with respect to temperature upon which they are exponentially dependent. These are not amenable to traditional methods of averaging non-linear terms, where higher order correlations are modelled in terms of calculable lower order terms. Such methods lead

to poor approximations, since in practical situations, higher order correlations dominate.

The present study involves the modelling of soot in turbulent combustion, where it is not so much its pollutant characteristics that are of concern, but rather its radiative properties. Particulate soot is an effective radiator since, unlike gaseous radiation which is confined to discrete bands, it is a continuum radiator, ie. it is capable of radiating at all wavelengths. Here, particular interest is in buoyant, "accidental" fires whose hazard potential is linked to emitted thermal radiation. The prediction of soot levels in such flows is essential since typically it is there produced in large quantities and may be the dominant radiating species.

In addition to re-opening the chemical source term closure issue, the study of soot is further complicated by the limited understanding of its formation processes. This involves both homogeneous and heterogeneous chemical reactions and complex physical processes resulting from particle interaction. In an effort to gain better understanding of these processes, detailed mechanisms of the type proposed by Frenklach et al (1986) have been developed. Such mechanisms are not suitable here, where the eventual concern is the modelling of soot in turbulent flows, since insurmountable closure and computational problems would arise through dealing with a large amount of coupled equations. Though the study of detailed reaction mechanisms may lead to the deduction of reduced reactions schemes (cf. Rogg and Williams (1988)) which reproduce key features of the gas phase in laminar flames, in the case of soot such mechanisms require further development and validation before they can be used for quantitative prediction. In view of this, the present study chooses an empirical approach whereby the rate of soot formation is determined through experiment. Moreover, since the model is for application in non-premixed combustion regimes, the experiment is performed on a laminar diffusion flame. This approach is essential in view of the simplified formation mechanism that must be assumed for later turbulent flow prediction. Such a mechanism cannot be expected to address the effect

of environmental conditions on soot formation. For instance, soot formation in diffusion flames is likely to differ from that in premixed flames (cf. Glassman (1988)).

The experimental study of a sooting laminar diffusion flame is described in section 3.3, for which the fuel used is methane. Given the global formulation of the model, specific numerical values of key parameters are unlikely to be quantitatively applicable over a range of fuels. The strategy to be described, however, can be applied to any fuel, for instance Moss et al (1988) derived the rate of soot formation in ethylene-air diffusion flames and Stewart et al (1990) in kerosene-air diffusion flames. The experimental study comprises extensive measurement of soot volume fraction, temperature and mixture fraction throughout the flame. The last property is of prime importance, since it is the dependency of soot formation on mixture fraction that is exploited to allow significant simplification when subsequently applying the model to turbulent flame prediction.

In order to deduce the soot formation rate from the (laminar flame) soot concentration measurements, a detailed characterisation of the vector and scalar fields is required. The latter is provided by a detailed numerical simulation of the flame which is described in section 3.4.

The experimentally derived formation rate, under the present scheme, is expressed in terms of mixture fraction. However, rather than assuming some arbitrary functional relationship, as prescribed for example by Kennedy and Kollmann (1990) who assume a Gaussian form, a more fundamentally based relationship is used. Intuition suggests that soot formation will be strongly dependent on temperature and the concentration of hydrocarbon precursors - here this is chosen simply to be the parent fuel. If these properties are then solely functions of mixture fraction, the link between soot formation rate and mixture fraction is established. Such an approach, in principle, would allow the extrapolation of the model to regimes beyond those exhibited in

the experiment, in particular to lower or higher combustion temperatures.

In the present study, the formation rate is correlated by a model initially proposed by Gilyazetdinov (1972) which realises a dependency on temperature and parent fuel concentration through the key processes of particle nucleation, coagulation and surface growth. The model is described in the next section.

3.2 The soot formation model

Gilyazetdinov (1972) proposed a model for soot formation which incorporates a description of the major physical and chemical features in a global manner. This incorporates a two-step mechanism for the formation of soot mass concentration, m (kg/m^3), which is the mass of soot per unit volume of space and which is simply related to soot volume fraction according to

$$m = \rho_s f_v \qquad \ldots \quad (3.1)$$

where ρ_s is the density of soot (typically $1800 kg/m^3$ - cf. Mullins et al (1987). The first step in the formation process is nucleation, whereby the first solid phase is produced as a result of homogeneous gas phase reactions, and the second is surface growth, where heterogeneous reactions between the surface of the soot particles and the gas phase results in soot build-up.

The surface growth rate is dependent on the total surface area available for reaction. In order to define this for a cloud of soot particles, however, it is not sufficient to consider the mass concentration alone. The model therefore incorporates a second parameter, the particle number density, n (m^{-3}), which is the number of soot particles per unit volume of space.

If soot particles are assumed to be spherical and monodispersed in size, a representative particle diameter, d, may be deduced, cf.

$$m = n \left(\rho_s \frac{\pi d^3}{6} \right) \quad \ldots \quad (3.2)$$

Given the particle diameter, the total surface area of a cloud of n soot particles, A_s (m^{-1}), which is the soot surface area per unit volume of space, is easily found. This is most usefully defined in terms of the model parameters, m and n, given equation 3.2

$$A_s = 6^{2/3} \pi^{1/3} \rho_s^{-2/3} m^{2/3} n^{1/3} \quad \ldots \quad (3.3)$$

The particle number density is generated by the nucleation process and is consumed by coagulation. Particles collision and coalescence to form bigger spheres has an impact on the mean size and hence surface area. Its inclusion in the model is therefore essential.

The following presents the adopted soot formation model. In keeping with the assumptions of Gilyazetdinov (1972), soot nucleation results from the collision between a hydrocarbon precursor and an ambient molecule, surface growth from collision between the precursor and the surface of the soot particles, and the collision between soot particles is described as free molecular collision.

Also in this section, the formation mechanism will be analysed to reveal the time dependent behaviour of the soot number and volume fraction. This, it will be seen, gives valuable insight into the competing processes of nucleation and surface growth in laminar diffusion flames, when the model is used to interpret the present laminar flame experiment.

The processes of soot nucleation, coagulation and surface growth are described as

$$\left[\frac{dN}{dt}\right]_n = C_\alpha \rho^2 X_{HC} T^{1/2} \exp[-T_\alpha/T] \quad \ldots \quad (3.4)$$

$$\left[\frac{dN}{dt}\right]_c = - C_\beta T^{1/2} N^2 \quad \ldots \quad (3.5)$$

$$\left[\frac{dm}{dt}\right]_g = C_\gamma \rho X_{HC} T^{1/2} n^{1/3} m^{2/3} \exp[-T_\gamma/T] \quad \ldots \quad (3.6)$$

where the subscripts n, c and g refer to nucleation, coagulation and surface growth, and C_α, C_β and C_γ are empirical constants. The activation temperatures, T_α and T_γ, used in the present work are those deduced by Gilyazetdinov (1972), namely 46.1×10^3K and 12.6×10^3K respectively. N is the normalised number density defined by n/N_0 and the soot mass concentration (m) is simply related to the soot volume fraction by equation 3.1.

In equations 3.4. to 3.6, the coagulation term is dependent on n^2 and on the square root of temperature as is the case for collision between particles in the free molecular regime (cf. Hirschfelder et al (1967)) and the surface growth rate is dependent on $n^{1/3}m^{2/3}$. The latter results from the dependency on soot surface area (cf. eqn. 3.3).

It is tempting to evaluate the constants (C_α and C_γ) from the original expressions of Gilyazetdinov (1972), by assuming reasonable values of collision cross-sections, molecular masses etc. This is not done however, since the pre-exponential factors evaluated by Gilyazetdinov, were deduced in a carbon black experiment, which entails injecting the parent fuel into the hot exhaust gases of a premixed flame. Such an environment is free of the radicals that may diffuse from the reaction zone to the soot formation zone in a diffusion flame - soot formation in flames may be controlled by radical mechanisms which are stimulated by radicals, for example H, that are found in and around reaction zones (cf. Glassman (1988)). In flames one may find, therefore, that soot may be promoted by collision with species that do not exist in post flame gases. This also has implications on the activation

energies, but the present study found no conclusive evidence for their change from the values originally suggested.

An estimate of C_β, in the coagulation term, is not considered either, since the expression does not address the possibility that a certain percentage of soot particles may be charged. Also, two particles may collide and not coalesce to form a bigger sphere, but rather simply to "stick" at their surface which eventually results in large chain flocculates (cf. Megaridis and Dobbins (1989)). Since it is the surface area that is of interest here, rather than the number of free particles, two particles that collide and do not coalesce (in the limit that their area of contact is negligible), are better considered as two individual particles.

In the present study, initial "guesses" for the empirical constants (C_α, C_β and C_γ) were obtained from Moss et al (1988), who evaluated them in a laminar ethylene-air diffusion flame. Ethylene yields soot volume fractions that are an order of magnitude greater than those found in the present methane flame; this is reflected in the values of the empirical constants deduced here.

Equations 3.4-3.6 show that soot formation may be expressed in terms of the model parameters themselves (n and m) and the density, temperature and precursor mole fraction (the latter is assumed to be the parent fuel). If the gas phase parameters can be assumed to be dependent solely in terms of mixture fraction, the usual assumption in the conserved scalar approach, then the rate of formation of soot number density and mass concentration may be expressed as:-

$$\frac{dN}{dt} = \underbrace{\alpha(\xi)}_{\text{nucleation}} - \underbrace{\beta(\xi)\, N^2}_{\text{coagulation}} \qquad \ldots \quad (3.7)$$

$$\frac{dm}{dt} = \underbrace{\gamma(\xi)\, n^{1/3}\, m^{2/3}}_{\text{surface growth}} + \underbrace{C_\delta\, \alpha(\xi)}_{\text{nucleation}} \qquad \ldots \quad (3.8)$$

where α, β and γ can be deduced directly from equations 3.4-3.6. $C_\delta\alpha$ represents the rate of formation of soot mass through nucleation. In the present study, following Raine (1977), a nucleus was assumed to be composed of 12 carbon atoms. This yields C_δ=144.

Figure 3.1 shows the mixture fraction dependent parameters in the soot formation mechanism, α, β and γ, plotted against mixture fraction. All three parameters are shown normalised by their maximum value. The flamelet state relationships $\rho(\xi)$, $T(\xi)$ and $X_{HC}(\xi)$ from which the curves are derived will be presented later in section 3.4. In the present study the precursor, X_{HC}, has been chosen to be the parent fuel. The merits of this assumption will be discussed later in this chapter.

Figure 3.1 shows β to continually increase as the mixture fraction decreases towards stoichiometric, since it is dependent simply on $T^{1/2}$. The nucleation and growth curves are both seen to increase as the mixture fraction reduces towards stoichiometric; this is owing to the increasing temperature upon which they are both dependent. Both curves exhibit a maximum slightly to the rich of stoichiometric, since their dependence on X_{HC}, which is zero at $\xi=\xi_{st}$ ($=0.055$ for methane-air flames), eventually overwhelms the temperature effect. The maximum of the α curve occurs closer to ξ_{st} due to it having a greater activation temperature, 46.1×10^3K compared to 12.6×10^3K for the surface growth process. The higher activation temperature naturally requires a higher temperature to be reached before α becomes significant, and the implied increased dependence on temperature allows a lower ξ to be reached before the depletion in X_{HC} dominates. The activation temperatures quoted above were those originally suggested by Gilyazetdinov (1972) and used throughout the present work.

Prior to applying the model to the calculation of soot concentration in a laminar diffusion flame, it is useful to investigate the formation rate itself (cf. eqns. 3.7 and 3.8). Their formulation suggests that approximate solutions can be determined analytically; in

particular, if plug flow can be assumed for a given soot-containing volume (ie. the volume is simply convected and $d/dt = u\, d/dx$ where t is time u velocity and x is the stream-wise direction in the flame) and it experiences a constant mixture fraction, then the soot concentration can be obtained directly from the integration of equations 3.7 and 3.8. The soot number density and volume fraction can then be deduced, for a given residence time and mixture fraction. Unfortunately such a simple approach is unsuitable for a quantitative analysis of sooting laminar flames of the type under investigation, since there, stream lines and mixture fraction contours are not parallel. Increasingly soot, being particulate, tends to follow stream lines and α, β and γ cannot be treated as constant in equations 3.7 and 3.8. The current work, however, has shown that investigation of the plug flow case does yield similar trends, in terms of the time dependent behaviour of the soot number and volume fraction, to the flame situation, and can be used to explore some of the more important interactions.

The ability to divorce the source term and the flowfield, at least for qualitative analysis, is a useful aid to assessing the experimental data in terms of, for example, the relative effect of nucleation and surface growth. The source terms for soot number density and mass concentration are investigated in the next two subsections.

3.2.1 Investigation of the soot number density formation rate

The formation rate of N (eqn. 3.7) can be integrated analytically if α and β are considered constant (ie. for a constant ξ) to give

$$N = \sqrt{\frac{\alpha}{\beta}} \tanh(\sqrt{\alpha\beta}\, t) \qquad \ldots \quad (3.9)$$

The function is shown diagramatically in figure 3.2. The normalised soot number density, N $(=n/N_0)$, can be seen to saturate at $\sqrt{(\alpha/\beta)}$

which therefore indicates its maximum possible value. The saturation is brought about through the coagulation rate increasing and eventually becoming equal to the nucleation rate, which is independent of residence time (see eqn. 3.7) and hence stays constant. The relationship also shows that the coagulation rate cannot become greater than the nucleation rate and cause the number density to fall. This is to be expected in plug flow, since the coagulation rate is simply dependent on particle number and will only increase if the particle number increases; when the coagulation rate equals the nucleation rate, and $dN/dt=0$, the coagulation rate ceases to change. This behaviour does not apply to the flame situation where soot particles may exist beyond the formation zone, in which case coagulation will cause decline in their number.

Further scrutiny of figure 3.2 shows the initial gradient to be $dN/dt=\alpha$. The time at which this linear growth section starts to decline depends on the value of β. Small values of β lead to an earlier departure from a linear relationship and a longer time for N to reach its saturated value. This information together with the maximum N, given by $\sqrt{(\alpha/\beta)}$, allows α and β to be fixed during parameter optimisation, prior to considering the soot volume fraction. The current experimental work did not involve soot number density measurements, these were merely therefore inferred from measurements available in the literature. Haynes and Wagner (1981) report values, in similar laminar flames, of approximately $1x10^{17}m^{-3}$. The values of α and β used in the present analysis were therefore chosen to yield number densities of this order. However, the absolute value of n is not of major significance in the soot formation model since C_γ, by suitable manipulation, may compensate. Of more significance is the time required for n to saturate; as the next subsection shows, this affects the time dependent nature of soot mass concentration.

The absolute value of n and hence the soot particle surface area is important when the additional process of soot oxidation is concerned. The latter is appended to the soot formation terms in the turbulent flame predictions of chapters 4 and 5, where the oxidation and

formation zones cannot be treated independently as they are in the laminar flame investigated here. The present experimental investigation focuses on regions of the flame where newly formed soot particles are drawn into richer regions by the vector field, and hence away from the oxidising zone.

3.2.2 Investigation of the soot mass density formation rate

In this section the formation rate of soot mass (eqn. 3.8) is investigated in certain restrictive regimes. This, as will be shown later, also provides a valuable insight into the nucleation and growth processes, which influence soot mass concentration in the laminar diffusion flames experimentally investigated in this study.

Consider equation 3.8 in the regime where the nucleation term is much larger than the surface growth term. Such a scenario will always exist close to time t=0, since α is independent of time and the growth rate is dependent on n and (through the surface area) m, both of which are zero at t=0. Under such circumstances, there is a linear relationship between m and t, since equation 3.8 can be integrated to show $m=C_{\delta}\alpha t$.

In the situation that the growth term dominates, as must happen when $t\rightarrow\infty$, there are two limiting regimes. The first is where the nucleation term is so small, that at the time when the surface growth becomes much larger than the nucleation term, eqn. 3.9 is still in its linear region, ie. n is far from saturated. In this regime eqn. 3.9 yields:-

$$n = N_0 \alpha t \qquad \ldots (3.10)$$

Substituting this into eqn. 3.8 and integrating (remembering that the nucleation term is negligible) results in

$$m = \frac{\gamma^3}{4^3} N_0 \alpha t^4 \qquad \ldots (3.11)$$

A fourth order dependence of m on t therefore results. The second regime occurs, when the time is large enough for the soot number density to have saturated, ie. n is independent of time. Here, eqn. 3.9 shows

$$n = N_0 \sqrt{\alpha/\beta} \qquad \ldots (3.12)$$

Putting this into eqn. 3.8, ignoring nucleation and integrating gives

$$m = 3\ \gamma^3\ N_0 \sqrt{\alpha/\beta}\ t^3 \qquad \ldots (3.13)$$

A third order dependence on time results.

To summarise, investigation of the source term reveals the dependence of soot volume fraction on residence time is initially always linear. The duration of this phase is dependent on the relative magnitude of the nucleation and growth terms. As t increases, the model shows that surface growth must ultimately dominate, leading to an eventual third order dependence on t. There may, however, be an intermediate region where the dependency may be as high as order four; the appearance of this depends on the soot number being far from saturated when the growth term dominates.

As will be shown in the experimental section (cf. section 3.3), the results of soot volume fraction measurements, made in a laminar methane-air diffusion flame, are plausibly represented by the model and its use therefore justified. Associated work investigating soot formation in ethylene and kerosene flames (Moss et al (1988) and Stewart et al (1990)), however, seem relatively to be poorly represented by this model. This is evident from their data implying a greater than first order dependence on residence time initially, which eventually becomes linear. That the initial dependence is greater than linear is not necessarily incompatible with the model, since the initial linear phase may be negligibly short resulting from early

dominance of surface growth. The model will not, however, allow a greater than order one dependence to become order one, as residence time increases. It may be that the apparent non-linear initial behaviour is brought about by peculiar effects at the burner exit, for example quenching and premixing - close to the burner there is a zone where reactions are quenched by heat loss to the burner which allows a certain degree of premixing. Though this would also happen in the methane flame investigated here, soot inception initiates further away from the burner than for either ethylene or kerosene. The importance of the near-burner region is therefore less. If the near burner region does influence the early development of the soot, then the data of Moss et al and Stewart et al indicate a linear dependence of soot on residence time. This, however, can only occur if the nucleation term is dominant, which is unlikely since surface growth is generally viewed as the major process contributing to the formation of soot mass (cf. Bockhorn et al (1984)). An alternative possibility considers the dependence on precursors that diminish in concentration more quickly than the parent fuel as height is increased. This is investigated by Stewart et al (1990).

Having now obtained an understanding of the adopted soot formation model, the next section describes the experimental investigation of a sooting laminar methane-air diffusion flame. This is an important stage in the proposed approach to the development of a soot formation model for turbulent non-premixed combustion. Following that, analysis of the data is made through a numerical prediction of the flame from which the soot formation rate is deduced.

3.3 Experimental investigation of a sooting laminar diffusion flame

This section briefly describes the experimental rig and procedure for investigating the sooting behaviour of a laminar methane-air diffusion flame, where the objective is to measure the distribution of soot

concentration, temperature and mixture fraction. For more detail the reader is referred to Stewart (1990).

The experiment is performed with a view to deriving, empirically, a soot formation rate, which may be subsequently incorporated into a turbulent calculation. This requires a spatially detailed map of velocity together with soot particle trajectories, so that the history of a soot-containing volume can be specified. The vector field must be supplemented by a detailed map of the scalar field since, in the flame investigated, a soot-containing volume experiences a changing scalar environment throughout its history, as streamlines and scalar contours are not parallel. Such detailed information is necessary to back-out the soot formation rate from the soot volume fraction measurements. Rather than achieving this entirely experimentally, it has been elected to supplement the experimental data with a numerical prediction of the flame. The latter is reported in section 3.4 where, due to difficulties in predicting small scale flames (for example, the specification of boundary conditions is very influential on the calculation), its validity is ensured by comparison between predicted temperatures and mixture fraction with experimental data. Such a validation is essential, especially with regard to temperature, since the rate of soot formation is highly temperature dependent.

The remainder of section 3.3 describes the experimental set-up, the diagnostic techniques and the data reduction. The presentation of the results and their analysis is deferred until section 3.4 where they are discussed in the light of the numerical prediction.

3.3.1 The burner and probes

Wolfhard and Parker (1949) proposed a burner design (referred to as the Wolfhard-Parker burner) which comprises two rectangular slots, one for fuel and the other for oxidant, that are supported within an inert gas surround. This results in a single planar flame sheet supported in the mixing region between the fuel and oxidant streams. The burner was

designed to permit access to line-of-sight optical techniques since they could be aimed parallel to the flame sheet along lines of constant scalar properties. This avoids the necessity to resort to complex reduction algorithms, such as that proposed by Shepp and Logan (1974), which are required to deduce point properties from line-of-sight measurements through inhomogeneous paths. It is the attribute of producing two-dimensional planar flame sheets for which the Wolfhard-Parker burner lends itself for use in the present study, since the method for measuring soot volume fraction relies on line-of-sight laser absorption.

The present study, however, adopts a modification, also adopted by several others (eg. Smyth et al (1985)), which involves a three slot system. This is shown in figure 3.3 which shows a schematic of the burner assembly. Fuel flows from the central slot and air through the two outer slots. The width of the fuel slot is 6mm and that of each air slot 9mm. The slots which are 47mm in length, are mounted inside a rectangular burner, the cross section of which is 90mm x 90mm and has windowed access for the laser system. The area between the slot assembly and the burner casing is occupied by a secondary airflow (the airflow through the slots is referred to as the primary air) which is used to assist flame stability. In order to obtain a near uniform velocity profile for each of the four streams (the fuel stream, two primary air streams and the secondary air stream) they pass through a labyrinth of glass beads before entering the test section. This burner design results in two nominally planar flame sheets which lie between the fuel and each of the primary air streams. Since there is an air surround, two additional flames are formed (referred to as end flames) which result from the mixing of the fuel directly with the secondary air. Such a design suffers from interference of the line-of-sight measurements from the end flames. In this respect the two slot system is more appealing since end flames do not occur. However, the latter yields a more complex mixing process which involves three streams, the fuel, the air and the inert gas surround. The three slot system, in contrast, involves only two streams, the fuel and the air. This permits great simplification in the computational modelling of the

flame as will be demonstrated in section 3.4, where mixture fraction is used to describe the scalar field in the fast chemistry limit. Also, two-stream mixing is more representative of practical situations.

The laser absorption experiment and the numerical prediction assume that the flame sheets are planar, though it is recognised that buoyancy will tend to induce axi-symmetry. In the low Froude number flames investigated, buoyancy is known to be significant. At the heights investigated, however, the flames seemed to be adequately planar. In addition, the flame was arranged to be symmetric about the centre plane of the fuel slot, by ensuring equal air flow through the outer slots. This is an advantage to the numerical simulation since only half the flow need be addressed, with the assumption of a symmetric boundary condition at the centre plane of the fuel slot.

The entire burner assembly is mounted such that it is capable of vertical and horizontal movement, which is sensed by two potentiometers which therefore indicate its position.

The probe system consists of a laser beam and photodiode detector to measure soot volume fraction, a fine wire thermocouple to measure temperature, and a quartz sampling probe to extract gas samples which are analysed by mass spectrometry. All the probes are fixed independently of the burner and therefore remain stationary when the burner is traversed. The thermocouple (Pt/Pt-13%Rh), which has a wire diameter of 50μm and a bead diameter of approximately 80μm, is mounted adjacent to the quartz probe which has an orifice diameter of approximately 200μm. The laser and associated optics are arranged such that the beam is focused half way along the flame and the effective diameter does not exceed ~0.5mm through the flame. The relative positioning of the three probes is arranged as shown in figure 3.3. The distance of each probe, relative to a suitable datum position on the burner, was measured before and after each experimental session. It was ensured that there was no disparity in the positioning system

caused by thermal expansion, which required the flame being left on for approximately one hour prior to measurements being performed.

3.3.2 Data reduction and analysis

A schematic of the data acquisition hardware is shown in figure 3.4. The figure shows two separate systems. The first is associated with soot and temperature measurement and the second with gas analysis. The mass spectrometer has its own dedicated microprocessor and requires a far greater sampling time compared to the other two diagnostics; the time constant of the thermocouple is approximately 0.1s and that of the laser system is negligible, whilst the probe sampling system requires approximately 30 seconds to make one measurement.

The microcomputer controls the data logging of the signals from the thermocouple, photodiode and the two potentiometers. The latter indicate the burner's position and hence the location of the probed point relative to the burner.

The next three subsections describe the data reduction of the thermocouple, photodiode and mass spectrometer output.

3.3.2.1 Data reduction of the thermocouple signal

The voltage generated by the difference in temperature between the hot and cold junction, the latter at room temperature, was digitised and input to the microcomputer. There, the voltages were converted to temperature using a standard calibration (cf. Kaye and Laby (1971)). The microcomputer also performed the task of compensating the thermocouple for thermal inertia. Such inertial effects were introduced through traversing the burner, and hence the flame, past the thermocouple during measurement. This was to minimise the time the thermocouple spent in the sooting and maximum temperature regions.

Prolonged periods in the sooting region resulted in soot build-up on the thermocouple bead and hence erroneous readings. Also the maximum corrected (for radiation and thermal inertia) temperature was found to be approximately 2050K and the melting point of platinum is 2040K. It was found that exposure to this temperature quickly resulted in fracture close to the bead of the thermocouple. By continual traverse the maximum temperature experienced by the thermocouple was reduced by ~40K. In the methane flame investigated here, probe integrity was a far more significant concern than soot build-up.

The remainder of this subsection describes the thermal compensation procedure.

Heat transfer to and from a thermocouple bead may result from convective exchange with the surrounding gases, conduction along the support wires and radiative exchange with the environment. Applying conservation of energy (ie. rate of heat flow to the bead is equal to the rate of heat flow away plus the rate of change of internal energy) we have

$$c\ m \frac{dT}{dt} = h\ A_s\ (T_g - T) + K_c\ A_c \frac{dT}{dx} + A_s\ \sigma\ \varepsilon\ (T_w^4 - T^4) \qquad \ldots (3.14)$$

The term on the left represents the change of internal energy and those on the right represent convection, conduction and radiation respectively. c is the specific heat of the thermocouple bead, m its mass, A_s its surface area, ε its emissivity and T its temperature. T_g and T_w are the temperature of the gas and the temperature of the enclosure walls, h is the convective heat transfer coefficient, Ac the cross sectional area of the support wire and K_c its thermal conductivity.

If the conduction and radiation terms are relatively small the response of the thermocouple may be simplified to

$$\frac{dT}{dt} = \frac{1}{\tau}(T_g - T) \qquad \ldots (3.15)$$

where τ is the time constant given by

$$\tau = \frac{c\ m}{h\ A_s} \qquad \ldots (3.16)$$

This simplification was found to be acceptable since the transient behaviour of the thermocouple could be described by equation 3.15. When using bigger thermocouples a more complex response was observed.

Equation 3.15 shows that if the time constant is known the gas temperature, T_g, may be found since the thermocouple's temperature, T, and its variation with time, T(t), is monitored.

The compensation was applied after performing the experiment, by curve fitting the measured temporal variation of the thermocouple's temperature (T(t)) with a least-squares polynomial. This function was then introduced into equation 3.15 to find the gas temperature. Prior to this, however, the time constant must be found.

To determine the time constant, rather than relying on equation 3.16 (which would introduce uncertainties mainly through the specification of the heat transfer coefficient), an experimental technique was used. This involved positioning the thermocouple in a part of the flame where there were no problems with soot build-up or probe integrity. The temperature of the thermocouple was then raised above ambient by electrical heating (cf. Ballantyne et al (1976)). When the supply was switched off, the cooling of the thermocouple was monitored.

Integration of equation 3.15 with respect to time, whilst keeping T_g and τ constant, shows that the response of the thermocouple to a temperature change is given by

$$T = (T_0 - T_g)\ e^{-t/\tau} + T_g \qquad \ldots (3.17)$$

τ is then found by fitting an appropriate least-square function to the observed thermocouple response. A value τ=0.1 second was deduced for a thermocouple with an 80μm diameter bead.

In addition to inertial compensation, the temperatures were also corrected for radiative loss. Following the procedure described by Fristrom and Westenberg (1965) a maximum correction of ~60K was deduced.

3.3.2.2 Data reduction of the photodiode signal

The photodiode generates a current related to the intensity of light impinging on its active surface. The current is converted to a voltage and fed to the microcomputer via the analogue to digital converter (ADC). The recorded voltage, being linearly related to the intensity of the laser beam transmitted through the soot, is a direct indicator of beam extinction. The soot volume fraction may then be calculated under the assumption that the soot particles are small compared to the wavelength of the light, where the following relationship holds (cf. Kerker (1969)).

$$f_v = \frac{\lambda \ln(I_0/I)}{36 \pi L} \left[\frac{(n^2-m^2+2)^2 + 4 n^2 m^2}{n m} \right] \quad \ldots (3.18)$$

In the above, λ is the wave length of the laser light, which is 633nm for the He-Ne laser used. I_0/I is the relative absorption by the soot, L the path length through the flame and n and m denote the real and imaginary parts of the complex refractive index of the soot particles, cf. n-im. The value of the refractive index was taken to be 1.92-0.45i from the experiments of Mullins and Williams (1987). The small particle limit is assumed valid since the wavelength of the laser beam, emitted by the helium-neon laser, is 633nm compared to soot particle sizes of ~40nm, measured in similar small scale flames (cf. Haynes and Wagner (1981)).

3.3.2.3 Data reduction of the mass spectrometer signal

A mass spectrometer, even after calibration, measures only the relative molar ratios of gases of different molecular masses (cf. Stewart (1990)). Absolute concentrations are therefore particularly difficult to obtain and would require analysis of all gases in the sample, or the determination of the concentration of one species by another method. In the present experiment, however, our interest is not in individual detailed concentrations but in mixture fraction. The latter, which was defined in chapter 2.1, is related to the mass ratio of fuel-originated to oxidant-originated matter in a two stream (fuel and oxidant) mixing system. Unfortunately, this generally implies measuring the absolute mass concentration of all significant species present in the sample (cf. Mitchell et al (1980) and Smyth et al (1985)). To avoid this a simplification was introduced in the present study as described below.

The gas sampled through the probe was mixed with excess oxygen and then passed over a heated platinum catalyst, where it was ensured that all the carbon was fully oxidised to CO_2. Making the assumption that all the carbon atoms had originated from the fuel stream, since the concentration of carbon atoms in air is small, the measured CO_2 can be an indicator for the fuel stream. Using N_2 as a similar indicator for the air stream, allows the relatively simple calculation of mixture fraction. It is assumed that N_2 oxidation is negligible. The procedure is described in appendix B.

3.3.3 Experimental procedure

Prior to igniting the burner, the probe positions were checked against a suitable datum. The positioning was also checked immediately after a run, in order to determine whether thermal expansion had introduced errors. This was avoided by allowing the burner system to reach a steady state, the approach to which was monitored by thermocouples

placed in the fuel and air slots. A period of approximately one hour was required after light-up, before measurements could be taken.

When a steady state had been reached, the burner was positioned, using a hand operated jack, such that the probes were the desired height above the burner. The flame was then continuously traversed past the probes by activating a stepper motor. During the traverse, the microcomputer continually took readings from the thermocouple, photodiode and horizontal potentiometer. Each sample point was recorded at 20ms intervals and the delay between readings from each device was 10μs.

Having performed a traverse for the temperature and soot concentration, a second traverse was performed for the gas analysis. This was necessary since the time required for the mass spectrometer to give a steady reading, after being positioned at a new location, was approximately 30 seconds. The gas analysis therefore required positioning the probe and maintaining at a location until a sensible reading could be taken. The probe was then moved to a new location.

The procedure was repeated for several heights, one of which was as close to the burner as practicable. As described in section 3.4, this was necessary to provide initial boundary conditions for a numerical simulation of the flame.

Presentation and discussion of the results are given in section 3.4, after the numerical prediction of the flame is described. The flow conditions for this case are 9.2×10^{-6}kg/s of methane at a mass averaged velocity of 7.4cm/s, and 6.44×10^{-5}kg/s through each of the air slots leading to a mass averaged velocity of 19.1cm/s.

The numerical prediction relies on all important scalars being dependent only on mixture fraction. Figure 3.5 presents the data of temperature plotted against mixture fraction measured in the present flame, and shows a unique relationship between temperature and mixture fraction may be assumed throughout the flame. In contrast figure 3.6

shows the experimental data of soot volume fraction plotted against mixture fraction, where there is an obvious dependency on height and hence residence time. This reflects the relatively slow processes involved in soot formation.

3.4 Numerical simulation of a sooting laminar diffusion flame

3.4.1 Introduction

Having obtained experimental data of soot volume fraction in a laminar methane-air diffusion flame, a reduction process must ensue whereby the soot formation rate may be deduced. As stated earlier this requires a detailed numerical simulation of the flame, which is presented below.

The simulation of a laminar diffusion flame requires the solution of coupled balance equations for the mass, momentum and scalar properties. The scalar properties include enthalpy and chemical species concentrations, which in turn may yield temperature and hence density through auxiliary relationships (cf. chapter 2.1). The latter, in addition to constitutive relationships for the transport properties, are required to close the equation set. The enthalpy equation requires a radiation term since local adiabatic temperatures are not attained, owing to radiative exchange within the flame and with the burner. Peak measured temperatures differ from adiabatic equilibrium values by as much as 230K. Such discrepancies are unacceptable in the present application, where the simulation provides a property map on which to analyse the soot model. The high activation energies associated with soot formation (cf. Gilyazetdinov (1972)), make it highly temperature dependent, leading to gross errors for modest temperature uncertainties.

A solution procedure of the type suggested, where the flowfield calculation must be coupled with a radiation calculation, is an

awesome task for the degree of accuracy required. In order to calculate the radiative properties, the concentration of gaseous radiators and soot is required. This results in a highly coupled system, since soot is highly dependent on temperature which, in turn, is highly dependent on soot due to its strong radiative properties.

In view of the difficulty, and more so the expense, of a coupled flowfield-radiation calculation, use has been made of the fast chemistry "collapse" of major gaseous species and temperature against mixture fraction, exhibited in laminar diffusion flames (cf. Mitchell et al (1980) and Smyth et al (1985)). It is proposed that mixture fraction be used to describe the scalar field including temperature and, crucially, the temperature-mixture fraction state relationship be derived from the current experimental data (cf. figure 3.5). The use of experimental temperatures allows the radiation to be decoupled from the flowfield since the adopted temperatures incorporate the radiative loss. Moreover, if, in addition, the fraction of the total mass condensed to soot is small, then soot can be treated as a perturbation to the thermochemistry. Its calculation may then be performed as a post process, allowing a considerable saving in computational cost. The present experimental data together with the computed velocities, show that the amount of carbon in the soot does not exceed ~1% of the total available fuel carbon.

The remainder of this section elaborates on the numerical simulation procedure and then seeks to determine the soot formation rate.

3.4.2 The mixture fraction approach

Analytical analysis of a laminar diffusion flame in the restriction of equal species diffusivity, unity Lewis number, zero heat loss and an infinite reaction rate, shows that any chemistry dependent scalar is algebraically related to any conserved quantity (eg. Shvab-Zeldovitch coupling functions and mixture fraction) (cf. Williams (1985)). Such a "collapse" onto single relationships for temperature and major species

against a conserved scalar in laminar diffusion flames, has been demonstrated in more realistic regimes, by for example the experiments of Mitchell et al (1980) and Smyth et al (1985), and the numerical simulation of Liew (1983). The present work, though not measuring individual species concentration, does demonstrate a collapse onto a single relationship for temperature (cf. figure 3.5). These studies therefore imply that mixture fraction may be used to describe the scalar field, and that any other scalar property can be easily determined, provided its functional dependence on mixture fraction is known.

The scalars of interest are the temperature, fuel concentration, density and viscosity. The first two are important in the soot model and the latter two are required to close the balance equations. The functional dependency, or flamelet state relationship, of temperature was deduced from the current experiment. Since species were not measured, the experimental data of Mitchell et al (1980), who measured species and temperature in a co-flowing axi-symmetric laminar methane-air diffusion flame, were used for the composition field.

Figure 3.7 shows the flamelet state relationships for the fuel concentration, density and viscosity. The density was derived using the equation of state, and the viscosity using the appropriate Enskog-Chapman expression (Fristrom and Westenberg (1965)) using the Lennard-Jones parameters as described by Liew (1983).

Figure 3.8 compares the presently measured temperature state relationship with that obtained from Mitchell et al (1980) and that resulting from the adiabatic equilibrium assumption. The latter was derived using the code of Gordon and McBride (1971). The importance of using the experimental temperatures is indicated by the differing trends exhibited by the curves in the sooting zone ($0.055<\xi<0.2$).

3.4.3 The governing equations

Under the present assumptions, where mixture fraction is used to describe the scalar field, balance equations for only the mass, momentum and mixture fraction need be solved. In addition, since it is recognised that soot cannot be described solely in terms of mixture fraction, due to substantially different transport properties and slow chemistry, balance equations for soot are required. These have been formulated on the basis that soot particles behave as a gas with zero diffusivity, ie. there is no slip between the particles and the velocity field. The soot is assumed not to affect the flowfield since, in these small-scale flames, it represents ~1% of the total available carbon. Also any impact it may have on heat loss, through its radiative properties, is incorporated explicitly by adopting a measured temperature state relationship.

In the computation, the flowfield is considered both two-dimensional and of the boundary layer type. In this approximation, the governing steady state balance equation for a general variable ϕ can be written as:-

$$\rho\, u \frac{\partial \phi}{\partial x} + \rho\, v \frac{\partial \phi}{\partial y} = \frac{\partial}{\partial y}\left(\frac{\mu}{\sigma_\phi} \frac{\partial \phi}{\partial y} \right) + S_\phi \qquad \ldots (3.19)$$

where x and y are the stream-wise and cross-stream distance, and u and v their velocity components. ρ is the density, S_ϕ is the volumetric source term, μ the viscosity and σ_ϕ is the Prandtl/Schmidt number. Equation 3.19 may represent momentum conservation, when ϕ is a velocity, or the balance of any scalar quantity. In the present case, the latter group consists of mixture fraction, and the soot parameters ϕ_N and ϕ_m, which are related to soot number density and mass concentration, cf.

$$\phi_N = n \,/\, (N_0\, \rho) \qquad \ldots (3.20)$$

and

$$\phi_m = m \,/\rho \qquad \ldots (3.21)$$

where ρ is the gas phase density.

The balance equation for any parameter can therefore be represented by equation 3.19, which may be tailored by suitable setting of the Prandtl/Schmidt numbers and the source terms. Their settings for the dependent variables considered are shown in table 3.1

The values for σ for the soot are set to very large numbers in order to eliminate the diffusion term; soot being particulate has a negligible diffusion coefficient compared to gases. The source terms for the soot equations can be seen to include, in addition to the modelled formation rate (cf. eqns. 3.7 and 3.8), a term indicated T, this is the thermophoresis term. The latter is a mechanism whereby small particles are transported along temperature gradients, as a result of gas molecules impacting the particle with greater energy on their hotter side. The thermophoresis term, T, can be expressed as

$$T = \frac{\partial}{\partial y}\left(\rho \, v_t \, \phi \right) \qquad \ldots (3.22)$$

v_t is the thermophoretic velocity, and is given by Fuchs (1964), for particles smaller than the molecular mean free path of the ambient gas, to be

$$v_t = \frac{-3}{4(1 + \pi/8)} \frac{\upsilon}{T} \frac{\partial T}{\partial y} \qquad \ldots (3.23)$$

The reason for incorporating the thermophoresis term into the source term is that general CFD codes, and indeed the one adopted here, allow typically for only convective, diffusive and source terms within the general framework. The diffusion term cannot represent thermophoresis since it is driven by the gradient of ϕ, itself, whilst the latter is driven by the temperature gradient.

3.4.4 Solution procedure

The numerical scheme used to solve the balance equations was based on the GENMIX code (Spalding (1977), which is a "time-marching" solver for two-dimensional parabolic flowfields. The code is suitable for both planar and axi-symmetric geometries and is used exhaustively throughout the present study: here to the study of a planar laminar flame; in chapter 4 to an axi-symmetric jet flame and in chapter 5 to the prediction of an axi-symmetric buoyant fire. A brief description of the algorithm is therefore warranted and is given below, though the reader is referred to Spalding (1977) for more detail.

The general two-dimensional boundary layer equation (cf. eqn. 3.19) may be cast into the Von-Mises co-ordinate system where the cross-stream distance is replaced by the stream function, ψ, which is defined by

$$\partial\psi = r\,\rho\,u\,\partial y \qquad \ldots (3.24)$$

where r is the radial location and is introduced since GENMIX may be applied also to axi-symmetric flows; for planar flow r is set to unity. Equation 3.19 then reduces to

$$\frac{\partial\phi}{\partial x} = \frac{\partial}{\partial\psi}\left(r^2\,\rho\,u\,\frac{\mu}{\sigma_\phi}\,\frac{\partial\phi}{\partial\psi}\right) + \frac{S_\phi}{\rho\,u} \qquad \ldots (3.25)$$

This transformation allows the grid to follow stream lines. There is now only one convection term, that in the stream-wise direction, since by definition there is no convection across stream lines. In GENMIX a further transformation is made whereby the grid is cast into the Patankar-Spalding co-ordinate system. Here a normalised stream function is defined, cf.

$$\omega = \frac{\psi - \psi_1}{\psi_2 - \psi_1} \qquad \ldots (3.26)$$

The subscripts 1 and 2 represent the cross-stream boundaries of the domain. This grid is particularly economical since it is restricted to the width of the boundary layer with which it grows. The general equation when cast into the x-ω (or Patankar-Spalding) co-ordinate system, results in

$$\frac{\partial \phi}{\partial x} + (a + b\,\omega)\,\frac{\partial \phi}{\partial \omega} = \frac{\partial}{\partial \omega}\left(c\,\frac{\partial \phi}{\partial \omega} \right) + \frac{1}{\rho\, u}\, S_{\phi} \qquad \ldots (3.27)$$

The terms on the left represent the stream-wise and cross-stream convection and those on the right represent the cross-stream diffusion and source term. Cross-stream convection results since lines of constant ω do not follow stream line, unless there is zero entrainment at both cross-stream domain boundaries. The coefficients a and b are functions of the entrainment at these boundaries and c is the diffusive exchange coefficient.

Equation 3.27 is discretized by the finite volume technique where it is integrated over small control volumes (cf. Patankar (1980)). The implicit scheme is applied in the stream-wise direction which promotes numerical stability for large steps in the x direction. The hybrid differencing scheme is applied in the cross-stream direction to determine values of properties at cell faces from those that prevail at the cell centres. This method results in the central differencing scheme if diffusive processes are overwhelming and in the upwinding scheme if convection overwhelms.

The resulting algebraic equations, the finite domain equations (FDE), may be represented by the following recurrence relationship:

$$D_i\, \phi_i = A_i\, \phi_{i+1} + B_i\, \phi_{i-1} + C_i \qquad \ldots (3.28)$$

where the subscript i refers to the i_{th} cross-stream cell. The coefficients A and B address both convective and diffusive interaction

with neighbouring cells, and the coefficient C incorporates contribution from the source term and the upstream node.

Solution entails marching in the stream-wise direction, where the FDEs are solved simultaneously at each stream-wise step, using the tri-diagonal matrix algorithm (TDMA) (cf. Spalding (1977)). Given the parabolic formulation, solution requires only one pass through the domain.

The code was run in its planar mode, with one cross-stream boundary being a symmetry plane, representing the centre of the fuel stream, and the other a free boundary, representing the undisturbed air stream. At the free boundary the values of the ϕ variables were those associated with the air stream. The only other boundary condition required, given the parabolic formulation, is at the upstream. Its specification was found to be very influential to the solution owing to the small scale of the flame. Also, the experiment indicated some degree of upstream diffusion since the maximum mixture fraction that could be measured 2mm above the fuel slot was 0.6. The applicability of the parabolic assumption is therefore questionable. In order to circumvent the difficult region, the calculation was initiated at a height slightly above the slot (2mm) using experimental data to define the profiles.

The grid consisted of 80 cross-stream nodes and a forward step size of a maximum of 0.005 times the width of the mixing layer. The grid was more than adequate to resolve the flowfield, in that using 40 cross-stream nodes showed no discernible difference. The large number of nodes were required, however, in order to resolve the sooting zone, which occupies a relatively narrow region in physical space.

3.4.5 Numerical predictions

3.4.5.1 Flowfield calculation

The satisfactory simulation of the laminar diffusion flame proved difficult because of problems in specifying the initial conditions. The results of computations initiated with uniform flow, assuming a mixture fraction of unity across the fuel slot, performed poorly. Such simple initial conditions proved particularly inappropriate for flames where the first 3cm are of interest, as inadequacies in their specification affect the computation throughout the domain of interest. The precise burner exit conditions are highly complex, since there is undoubtedly a certain degree of both upstream diffusion and premixing close to the burner face where local quenching restricts combustion.

Recognising that analysis of the fine detail of these processes was unnecessary for present purposes, we elected to initiate the computation at a specific height above the burner, using experimental data to provide the initial profiles. A similar strategy was also adopted by Jones and Lindstedt (1988), who discovered problems in specifying burner exit conditions, whilst modelling the flame of Mitchell et al (1980). In the present work the calculation was initiated at 2mm above the burner.

The data required for the initial conditions are profiles for the mixture fraction and velocity. The latter posed an additional problem since velocity measurements were not made. The initial velocity profile was therefore adjusted such that the predicted field agreed with the available experimental data, subject to an overall constraint on fuel mass flux.

Figure 3.9 shows the velocity profile specified at the 2mm height domain boundary together with profiles computed further downstream. The initial profile was prescribed as a simple function of mixture fraction such that a maximum results at the stochiometric value. In

this figure, and all subsequent ones, the zero on the transverse distance scale is the centre line of the fuel slot.

Figure 3.10, shows the best agreement obtained between the calculated and experimental mixture fraction fields, where profiles are presented at heights of 2, 10, 20 and 30mm above the burner. The 2mm height represents the initial condition. At all subsequent heights a good agreement is achieved. Not surprisingly, since an experimentally derived temperature-mixture fraction state relationship was used in the computation, figure 3.11 shows a good agreement for the temperature field.

The purpose of this section has been the computation of the scalar and vector fields, upon which a soot calculation may be grafted and the soot formation rate determined. If the latter is to be deduced with quantitative accuracy, it is imperative that the computed flowfield is a good representation of the flame. This has been ensured by comparing predicted temperatures and mixture fraction with experimental data. As velocity measurements were not made, the vector field cannot be directly assessed; however, confidence in its computation is given by the well represented scalar field.

Having obtained a reasonable representation of the laminar diffusion flame in terms of mixture fraction, temperature and, it is assumed, velocity, the soot formation mechanism can be investigated.

3.4.5.2 Scaling of the soot formation rate

In this section the soot formation mechanism embedded in the source terms for the soot transport equations is evaluated for methane. This is to be achieved through the adjustable parameters, C_α, C_β, C_γ, T_α and T_γ of equations 3.4-3.6.

The two activation temperatures were maintained at the values suggested by Gilyazetdinov (1972) (namely $T_\alpha=46.1\times10^3$K and

T_γ=12.6x10^{3}K), and the reduced parameter set, the frequency constants (C_α, C_β and C_γ) were adjusted to produce the relative magnitudes of the nucleation, coagulation and surface growth rates consistent with experiment.

The soot source terms deduced in this section will be later applied to the calculation of soot concentration within a turbulent methane fire in chapter 5. As will be shown there, local instantaneous temperatures are lower than those prevalent in the small scale laminar flame investigated here. This leads to the extrapolation of the source term in temperature space, on which it is highly dependent as indicated by the large activation temperatures, T_α and T_γ. The setting of the latter is then of major importance. In the present experimental investigation there was no conclusive evidence undermining the suitability of the activation temperatures specified by Gilyazetdinov (1972), and hence they were left unaltered.

The present predictions indicate the soot to be confined to relatively fuel-lean locations in comparison with the experimental data. This, as will be shown later, results from the nucleation source being confined to mixture close to stoichiometric. This may be due to T_α being too high, which causes a rapid decline in nucleation as the temperature is reduced away from stoichiometric. Equally, however, a spread into richer regions may result through increasing the dependency of the nucleation term on fuel concentration. This mimics a dependency on an intermediate species which is located at somewhat richer mixtures. In view of this, and that the model is able to depict the major experimental features, for example the growth of soot with height, the formulations outlined in equations 3.4-3.6, incorporating the activation temperatures reported by Gilyazetdinov (1972) are used.

The remainder of this section discusses the soot calculation, where the empirical parameters C_α, C_β and C_γ (cf. eqns. 3.4 to 3.6) are manipulated so as to yield soot levels comparable to those experimentally observed.

The purpose of the present exercise is the prediction of soot volume fraction for subsequent radiation predictions (cf. chapter 6). This, however, requires the specification of the soot surface area (in respect to surface growth) which in the adopted formulation requires solution of a further parameter, n. The latter, whose rate of formation is dependent on α and β (and hence C_α and C_β), was not measured here and hence its value was fixed, so as to be in broad agreement with values specified in the literature (cf. Haynes and Wagner (1981)). In the computations, soot number densities are fixed at approximately $1x10^{17}m^{-3}$. This provides some control over the setting of C_α and C_β.

Prior to performing the parameter adjustment, it is useful to explore some of the limiting regimes that may exist, in order to guide this process. Investigation of the soot number density source (cf. eqn. 3.7) identifies two extremes. The first constitutes a regime which is linearly dependent on time. This is followed by one which is independent of time, which accompanies a balance between particle nucleation and coagulation and hence saturated soot number density (cf. figure 3.2). Section 3.2.2 showed the effect of these two regimes on the temporal evolution of soot mass concentration, where they were seen to cause a 3^{rd} (saturated n) or 4^{th} (unsaturated n) order dependence.

The above applies when surface growth dominates in the formation of soot mass concentration. When nucleation dominates, a linear dependence of soot mass concentration on time is observed. The experimental data, when analysed by way of the numerical simulation, indicate a substantially greater than first order dependence of soot mass concentration on time. The empirical parameters were therefore chosen to yield a surface growth dominated regime.

In view of the two extremes in the behaviour of n, two corresponding sets of soot calculation are presented below. Both, it will be shown, are plausible fits to the data. The optimised values of the empirical parameters are shown in table 3.2, where those assumed by both

predictions are presented and are identified as predictions A and B. The former yields unsaturated values of n and the latter saturated. The parameters required to effect this transition are C_α and C_β, where the former is simply increased by a factor of 100 to saturate n (cf. prediction B). In order to keep number densities of the same order in both cases, C_β is increased to accompany that in C_α, thereby balancing the enhanced nucleation with increased coagulation. There is no difference in C_γ between the two cases, since if number density is kept constant then so is the surface growth rate (cf. eqn. 3.8 where nucleation is negligible).

The flamelet state relationships, $\alpha(\xi)$, $\beta(\xi)$ and $\gamma(\xi)$, obtained for prediction A are shown in figure 3.12. Similar relationships are not shown for prediction B, since $\gamma(\xi)$ is the same and $\alpha(\xi)$ and $\beta(\xi)$ are simply increased by factors of 100 and $7.15\text{x}10^4$ (cf. table 3.2).

The peak saturation value of n may be calculated from equation 3.9 by inserting suitable values for α and β. This results in a value of $4.6\text{x}10^{18}\text{m}^{-3}$ for prediction A and $1.6\text{x}10^{17}\text{m}^{-3}$ for prediction B. Though A saturates at much larger values of n, the residence times required to achieve this are relatively long. This is verified in figure 3.13a which shows the variation of peak soot number density plotted against height in the flame. Prediction B is seen to saturate very quickly to its maximum value of $\sim 1.6\text{x}10^{17}$. Prediction A on the other hand is seen to vary more or less linearly with height. A review of the literature does not indicate with any certainty as to which is the more realistic behaviour since no such measurements in methane-air flames are available. Kent et al (1981), however, made measurements in a laminar ethylene-air diffusion flame, and found peak soot number densities to increase from $3\text{x}10^{17}\text{m}^{-3}$ to $6\text{x}10^{17}\text{m}^{-3}$ over the heights 20mm to 30mm above the burner. This suggests a gradual increase of soot number density with height and therefore favours prediction A.

Figure 3.13b shows the variation of peak soot volume fraction with height, where predictions A and B are compared with the experimental data. As observed in the analytical investigation, the dependence of

soot volume fraction on height, and hence residence time, is greater for prediction A than for B. Both curves, however, are seen to show good agreement with the experimental data.

Transverse profiles of soot volume fraction at heights 15, 20, 25 and 30mm above the burner are presented in figure 3.14, where predictions A and B are compared with experimental profiles. Both predictions are seen plausibly to reproduce the lean side behaviour of the experimental data, in addition to achieving approximately the correct rate of growth with height. An obvious discrepancy between the predictions and the experimental data is seen on the rich side, where the model results in soot levels reaching negligible proportions approximately 1mm from the centre line. The experimental data, in contrast indicates the presence of soot at the centre line at all heights. The cause of the predicted trend may be seen in figure 3.15 which shows predicted profiles of α and γ - the magnitude of α is for prediction A but the trend is applicable to both predictions. γ indicates that surface growth is capable of occurring at substantial rates even at the centre line. α, however, is seen to be restricted to regions close to stoichiometric which reflects its higher activation temperature. Preventing the build-up of soot at the centre line is therefore the non-availability of soot nuclei which are required as kernels for the growth process.

To obtain better agreement between the modelled and experimentally observed centre-line soot levels, broadening of the nucleation rate towards richer mixtures is required. This suggests that the activation energy T_α should be lowered or that the dependency on fuel concentration (which is presently of order unity) should be increased. So far as soot prediction in the present flame is concerned either of these actions may be performed to obtain better agreement. This becomes more critical, however, when the model is extrapolated to flames operating under different conditions. For example, if the model is applied to flames exhibiting different temperatures (which may result through a different degree of heat loss or reactant temperature) then the setting of the activation energy becomes more

crucial. This is of particular concern here since in chapter 5, the model is applied to the prediction of soot within a buoyant methane fire which exhibits greater heat loss than in the confined small scale flame investigated here.

At this stage it is felt that the model performs sufficiently well to warrant incorporation into a turbulent flame prediction, since the above uncertainties cannot be resolved here. This is particularly so in view of additional uncertainties; for example, it is feasible that oxidation plays a role in reducing soot levels close to stoichiometric, since this region is rich in oxidising species. Most significant of these is OH which is a highly active soot oxidiser (cf. Neoh et al (1984)) and may diffuse into the soot formation region from the reaction zone. Under these circumstances, the nucleation term would need to be enhanced in order to offset soot consumption at its lean extreme. This enhancement would result in increasing the magnitude of nucleation at richer locations, and hence the spread of soot there.

In terms of the location of the peak soot volume fraction, the experimental data indicate a gradual shift towards the centre-line as height is increased. This is more clearly seen in figure 3.16 which shows the locus of the peak soot volume fraction on a plot of height against transverse distance. This is superimposed on a map showing computed mixture fraction contours and stream lines. Also shown are the loci of peak soot volume fraction resulting from both predictions. Both these are seen to lie close to the experiment and show a movement towards the centre-line as height is increased. This movement, however, is not as severe as indicated by the experimental data. In comparison with the stream lines, the experimental data indicate a movement across the flow to richer locations; the reverse is indicated by the predictions. Given the gradient of temperature that prevails on the rich side of the flame, there is a thermophoretic effect that would encourage particles to move to richer locations. However, this has been incorporated in the model (cf. eqns. 3.22 and 3.23) where its effect, though noticeable, is minimal. Though its magnitude may be

underestimated, substantial enhancement would be required to promote the desired degree of shift. As with the rich side anomaly, the most likely explanation is the confinement of the nucleation term to relatively lean regions.

3.5 Conclusions

This chapter introduced a strategy for the modelling of soot formation in non-premixed combustion. Given the present deficiency in the understanding of the complex processes involved in soot formation (particularly in and near reaction zones), an empirical approach has been adopted. This is necessitated by the desire to obtain a quantitatively accurate model.

The model development entailed the measurement of soot volume fraction within a laminar diffusion flame from which the soot formation rate was determined. The latter required a detailed numerical simulation of the flame, to provide the necessary information about the vector and scalar fields that were not measured; for example, velocities, soot particle trajectories and soot precursor concentration. However, given the importance of quantitative accuracy, it is imperative that the simulation is an accurate representation of the flame. This was ensured by comparison between predicted temperature and mixture fraction with those experimentally measured. Good agreement was obtained but care was required in specifying initial conditions for the computation; this is especially so in the small scale flames investigated here where the first 30mm is of interest.

The rate of soot formation was correlated with a model, proposed by Gilyazetdinov (1972), which addresses the major physical and chemical process of particle nucleation, coagulation and surface growth. Here these expressions are reduced to their dependency on gas phase density, parent fuel mole fraction and temperature. Crucially, in line with the laminar flamelet approach (cf. Peters (1984)), the latter are presumed to be functions of mixture fraction alone. This facilitates

the computationally-tractable extension of the model to turbulent flame prediction.

The model is seen to describe the major features exhibited by the experimental soot volume fraction data, for example the rate of soot growth with height, but also indicates deficiencies, in particular the cross-stream spread of the soot zone is underestimated. The cause of this is identified as the confinement of the soot nucleation zone to a relatively narrow region close to stoichiometric. Precise reasons for this behaviour could not be identified, however, the following are possible: the activation energy associated with the nucleation process is too high; there should be a greater than order one dependency on parent fuel concentration; the soot formation process is not isolated from oxidation due to the diffusion of oxidising species from the reaction zone. The adopted activation energies and the dependency on fuel concentration were as specified by Gilyazetdinov (1972).

Further refinement of the model requires more detailed investigation; however, given that it is able to reproduce major features exhibited by the experimental data, it is appropriate to extend its application to a turbulent flame prediction. This forms the focus of chapter 4. There, however, owing to an absence of detailed soot measurements in turbulent methane flames, the model is applied to the prediction of a turbulent ethylene jet diffusion flame. Given the global nature of the model, it is fuel specific and the model, with its empirical parameters deduced here for methane, is not quantitatively applicable to ethylene. Ethylene flames yield soot levels that are an order of magnitude greater than those observed here for methane (cf. Moss et al (1988). Fortunately, however, Moss et al (1988) applied the same strategy in evaluating the rate of soot formation in a laminar ethylene-air diffusion flame. Their expression is used in the predictions reported in the next chapter.

The formation rate derived here will be applied to the prediction of soot concentrations in a turbulent methane fire in chapter 5. There, however, its performance cannot be easily assessed since there are no

accompanying soot measurements.

ϕ	σ_ϕ	S_ϕ
u	1	$-dP/dx - \rho g$
ξ	0.7	0
ϕ_N	$1x10^{10}$	$\left[\frac{dN}{dt}\right] + T$
ϕ_m	$1x10^{10}$	$\left[\frac{dm}{dt}\right] + T$

Table 3.1

		PREDICTION A	PREDICTION B
C_α	$(m^3kg^{-2}K^{-1/2}s^{-1})$	$6.54x10^4$	$6.54x10^6$
C_β	$(m^3K^{-1/2}s^{-1})$	$1.31x10^7$	$9.36x10^{11}$
C_γ	$(m^3kg^{-2/3}K^{-1/2}s^{-1})$	0.1	0.1
C_δ	(kg)	144.0	144.0
T_α	(K)	$46.1x10^3$	$46.1x10^3$
T_γ	(K)	$12.6x10^3$	$12.6x10^3$

Table 3.2

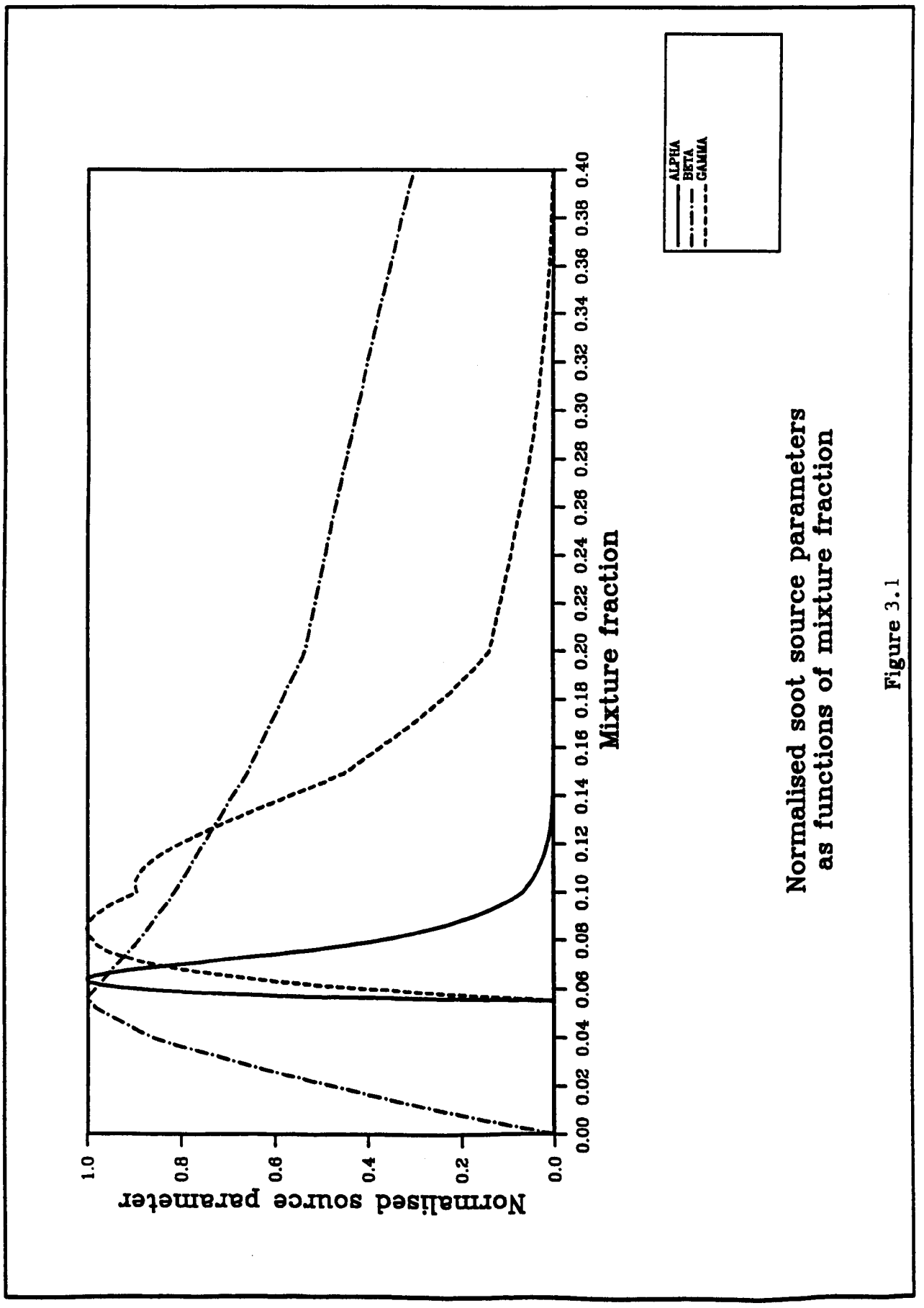
Normalised source parameter
1.0
0.8
0.6
0.4
0.2
0.0
0.00 0.02 0.04 0.06 0.08 0.10 0.12 0.14 0.16 0.18 0.20 0.22 0.24 0.26 0.28 0.30 0.32 0.34 0.36 0.38 0.40
Mixture fraction
ALPHA
BETA
GAMMA
Normalised soot source parameters
as functions of mixture fraction

Figure 3.1

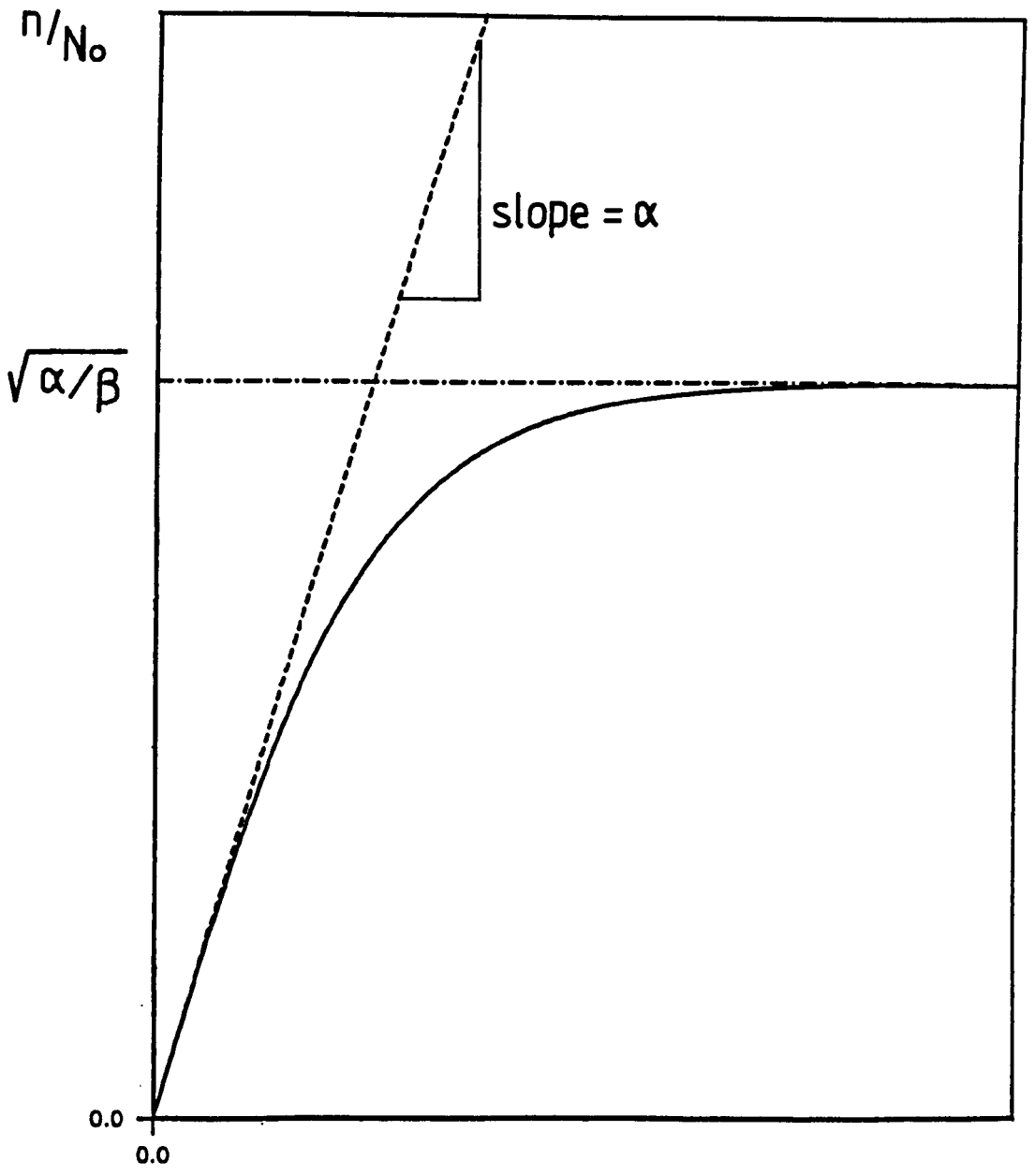

Variation of normalised soot particle number density with plug flow residence time

Figure 3.2

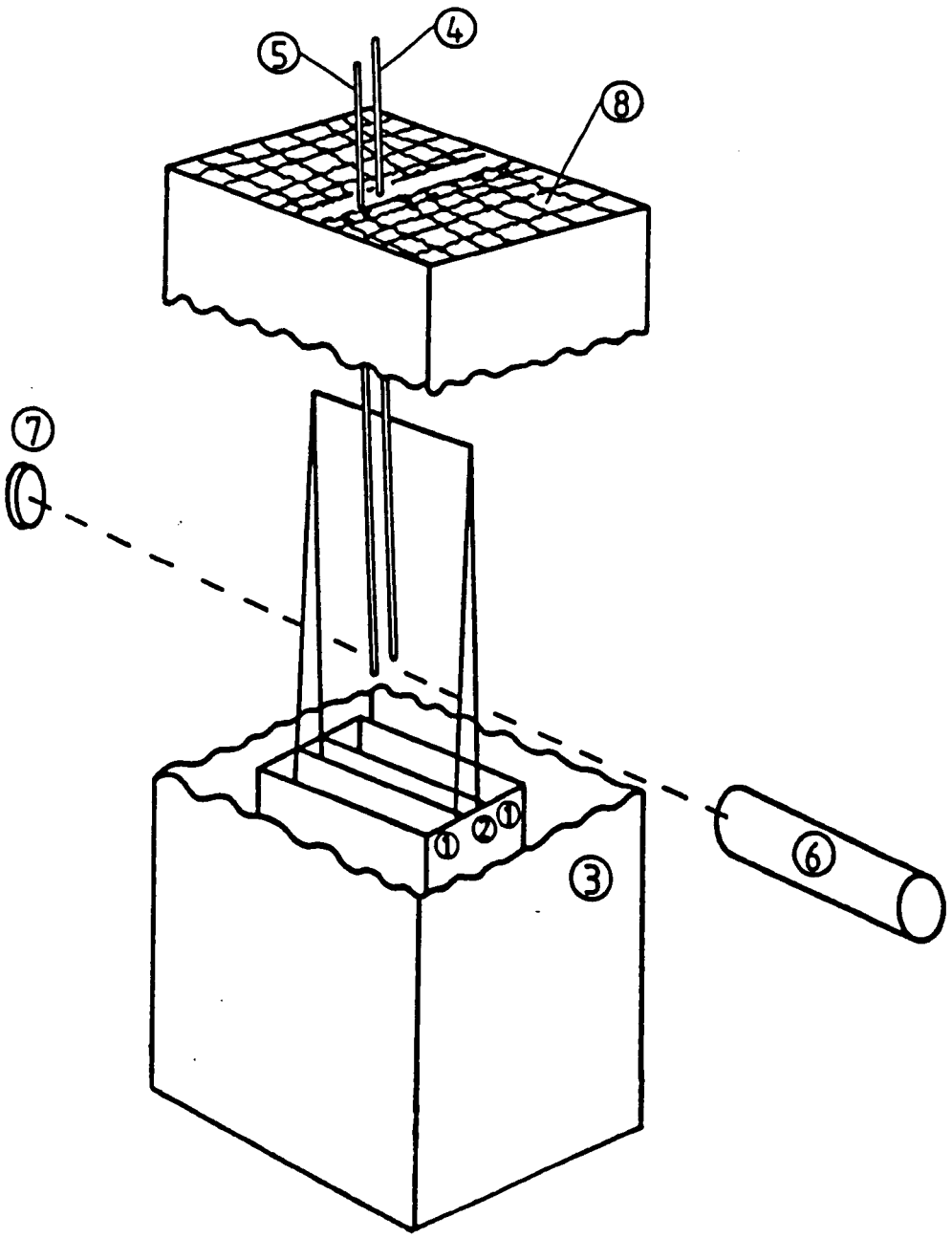

Schematic of Wolfhard-Parker burner and experimental configuration: (1) Air slots 9mm x 47mm; (2) Fuel slot 6mm x 47mm; (3) rectangular duct with windows not shown; (4) quartz microprobe; (5) thermocouple probe; (6) laser; (7) photodiode; (8) gauze

Figure 3.3

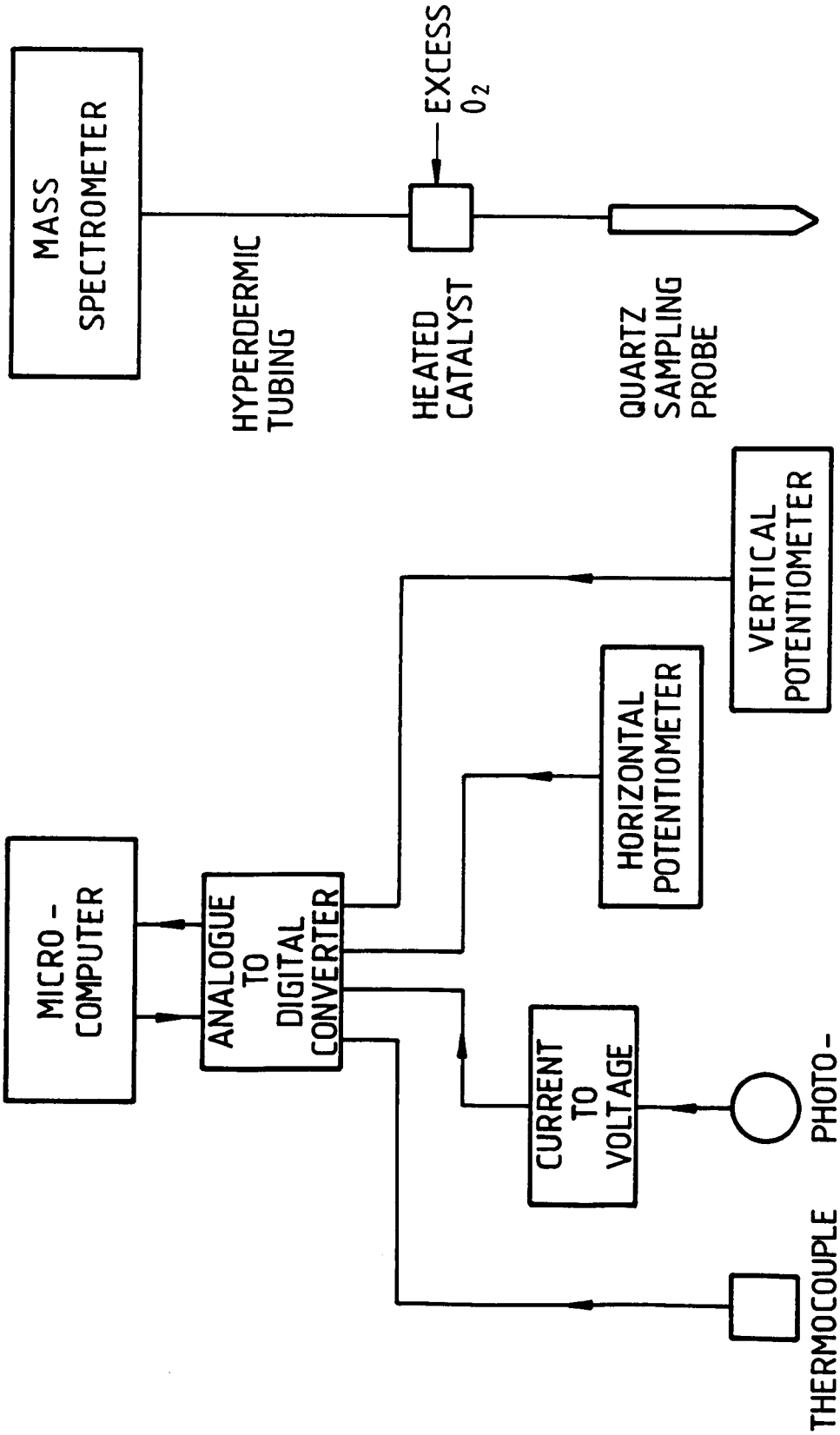

Figure 3.4 - Schematic of data acquisition hardware

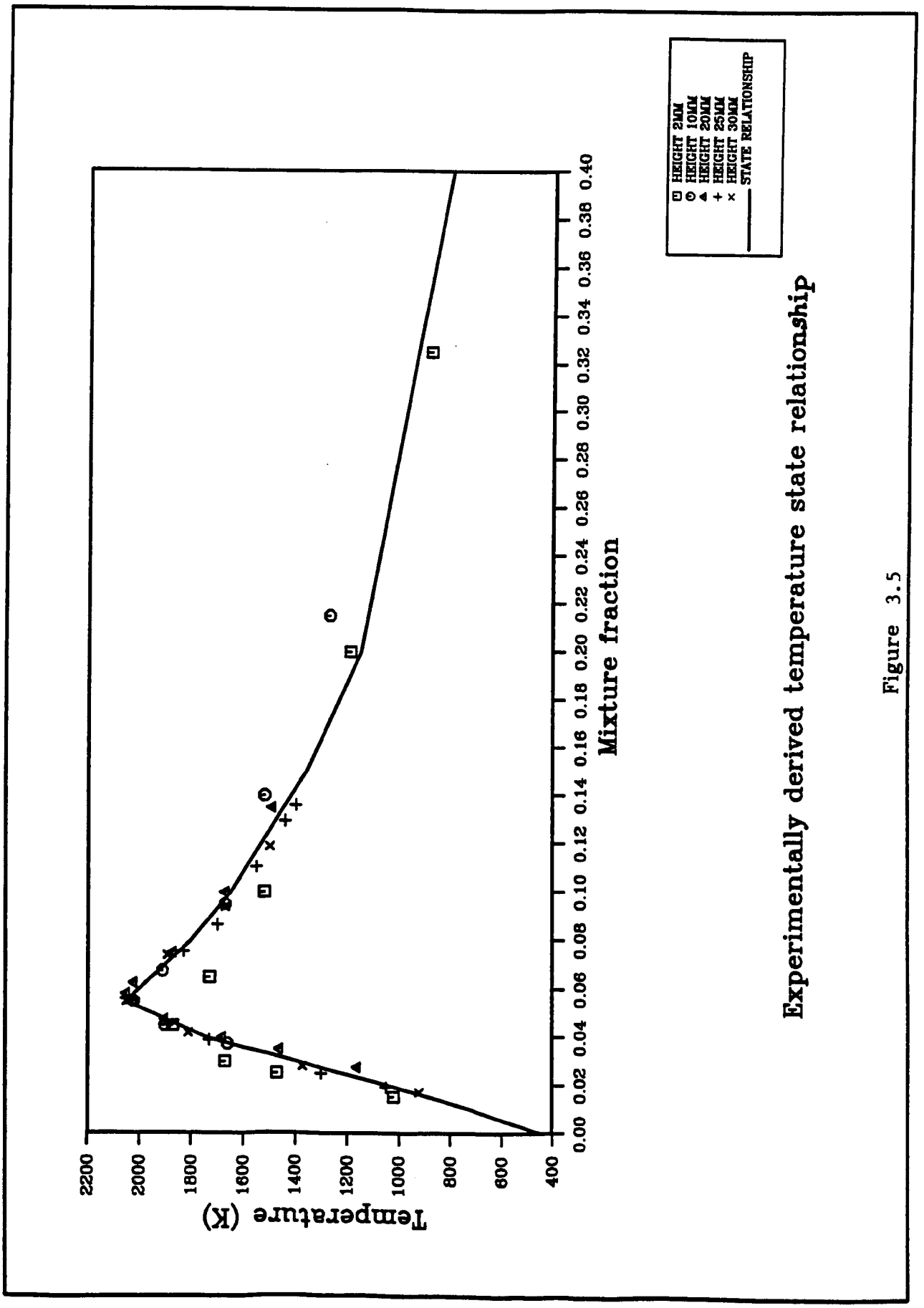
Experimentally derived temperature state relationship
Temperature (K)
2200
2000
1800
1600
1400
1200
1000
800
600
400
0.00 0.02 0.04 0.06 0.08 0.10 0.12 0.14 0.16 0.18 0.20 0.22 0.24 0.26 0.28 0.30 0.32 0.34 0.36 0.38 0.40
Mixture fraction
HEIGHT 2MM
HEIGHT 10MM
HEIGHT 20MM
HEIGHT 25MM
HEIGHT 30MM
STATE RELATIONSHIP

Figure 3.5

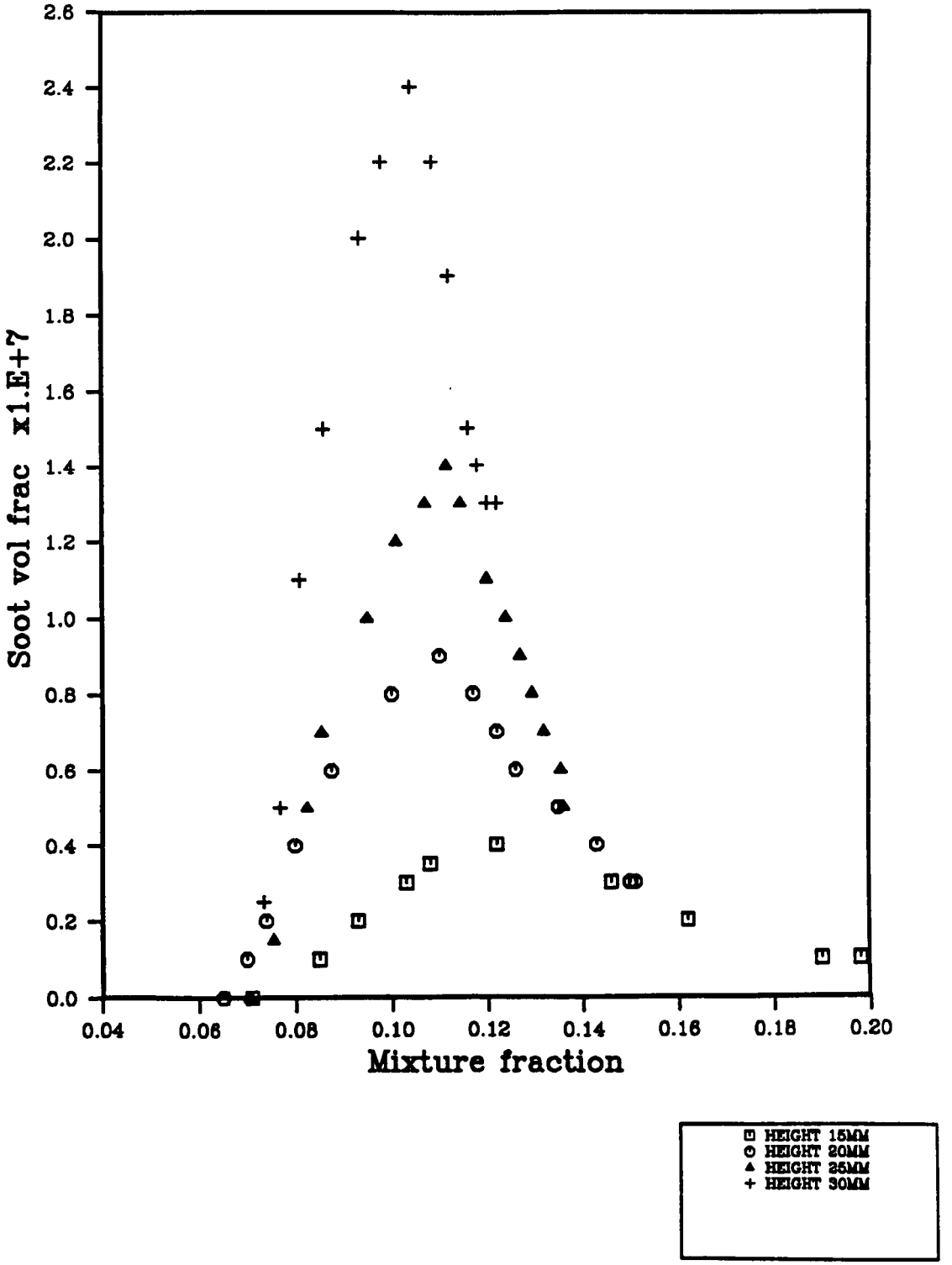

Experimental soot volume fraction – mixture fraction relationship

Figure 3.6

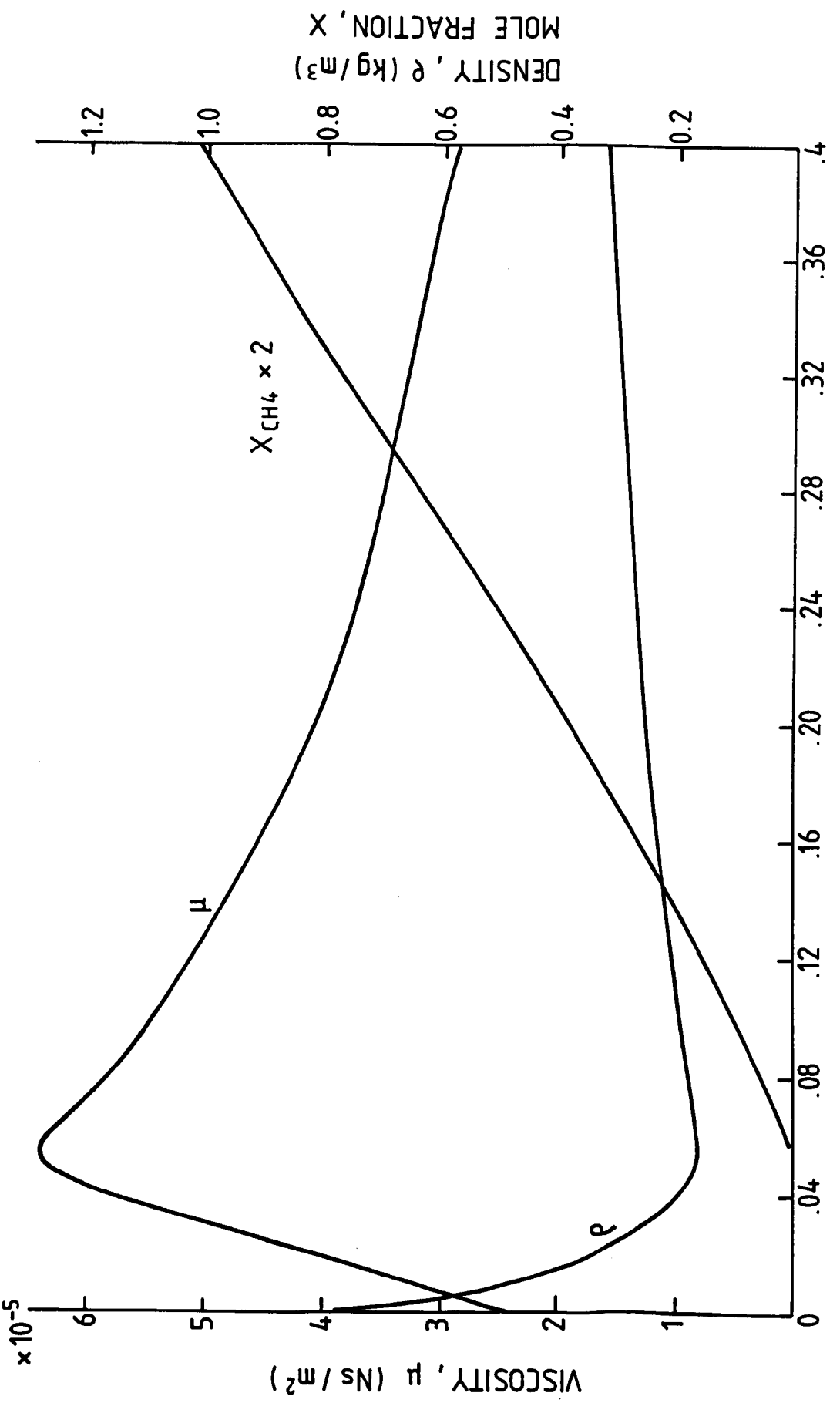

Figure 3.7 - Flamelet state relationships; methane-air

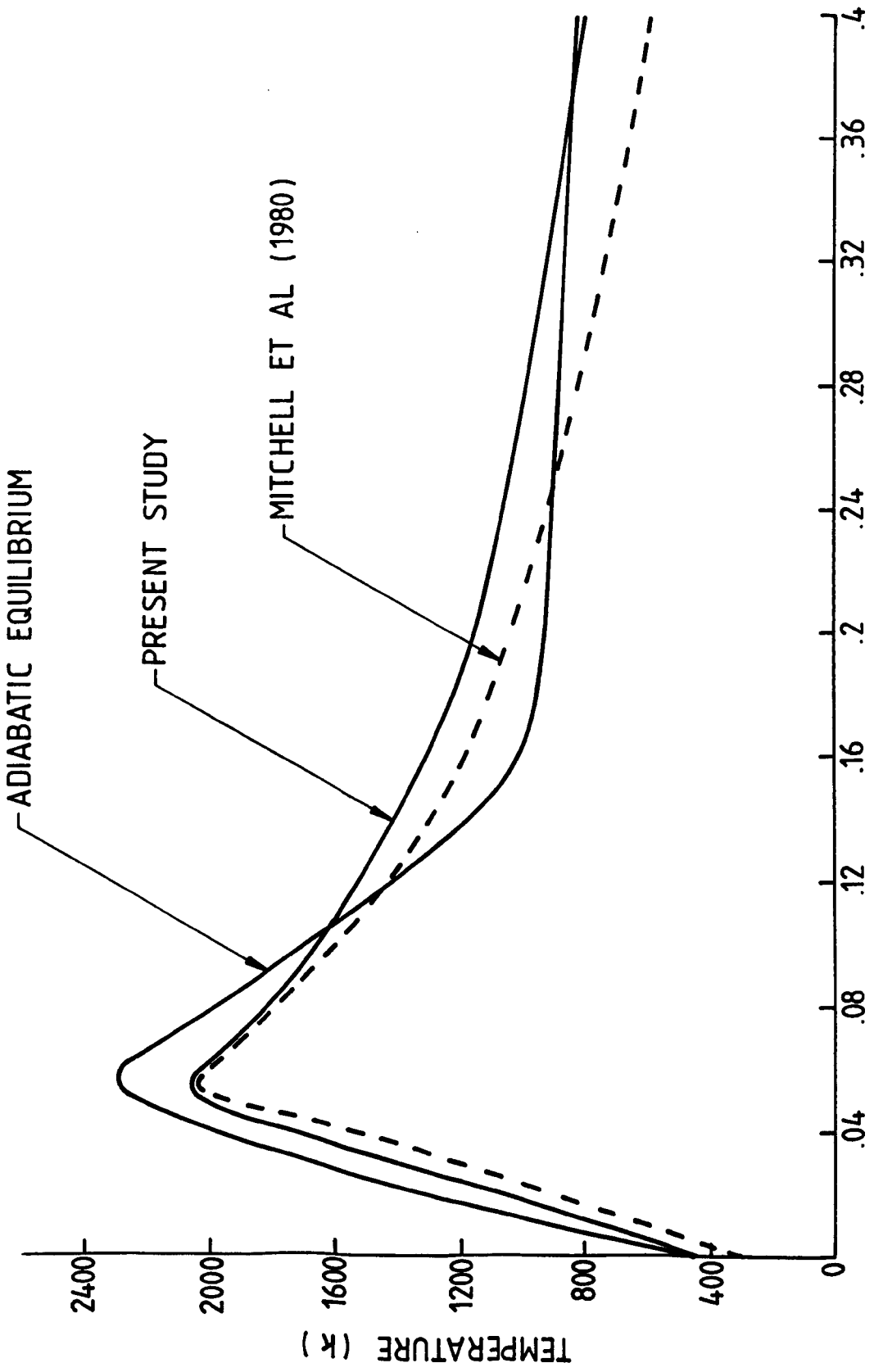

Figure 3.8 - Temperature state relationships

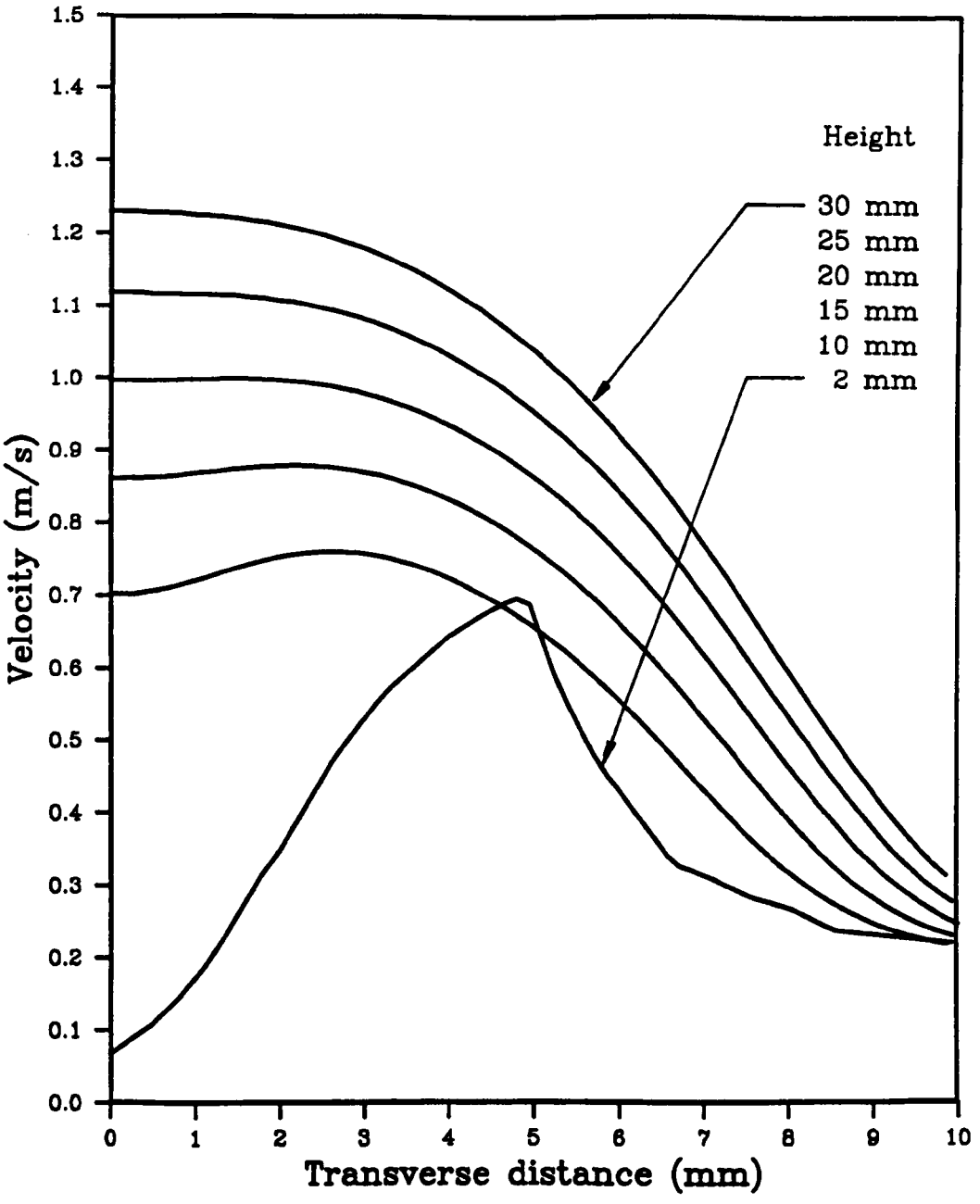

Prediction of vertical velocity component

Figure 3.9

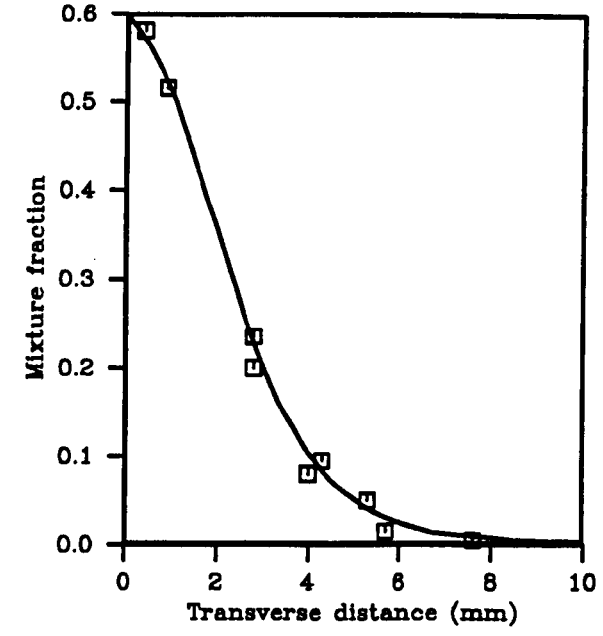

Height : 2mm

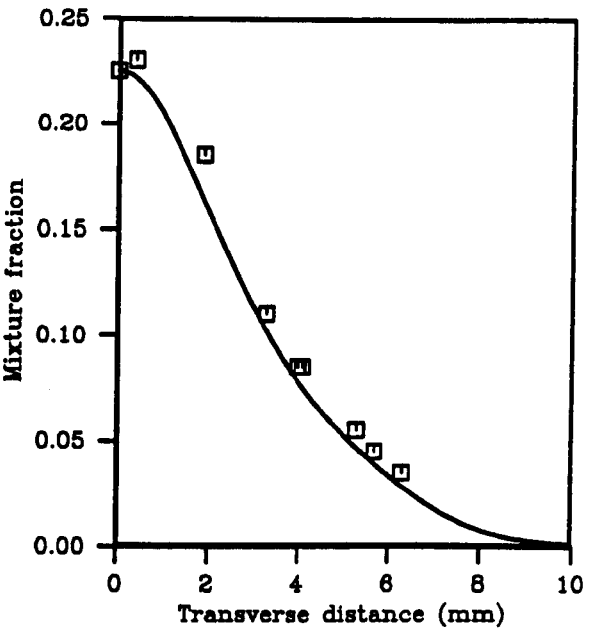

Height : 10mm

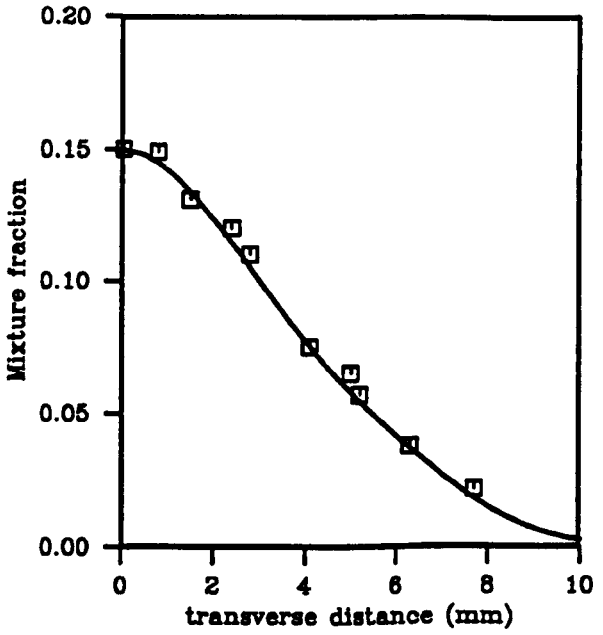

Height : 20mm

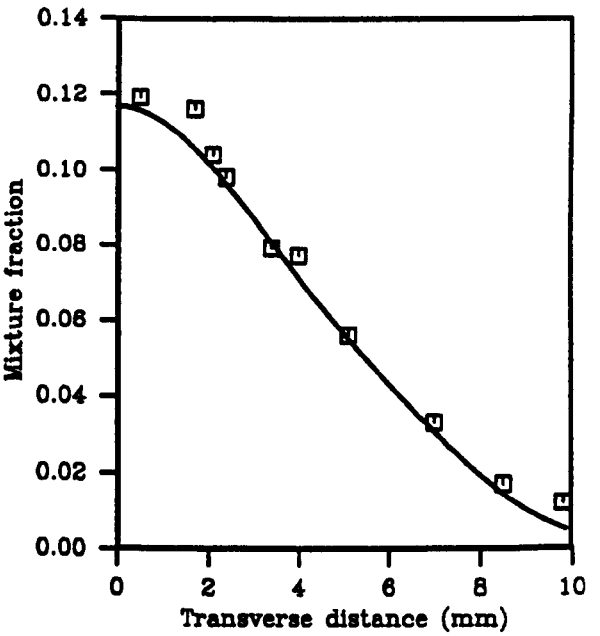

Height : 30mm

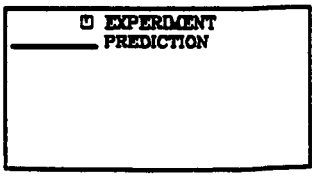

Comparison between predicted and measured mixture fraction

Figure 3.10

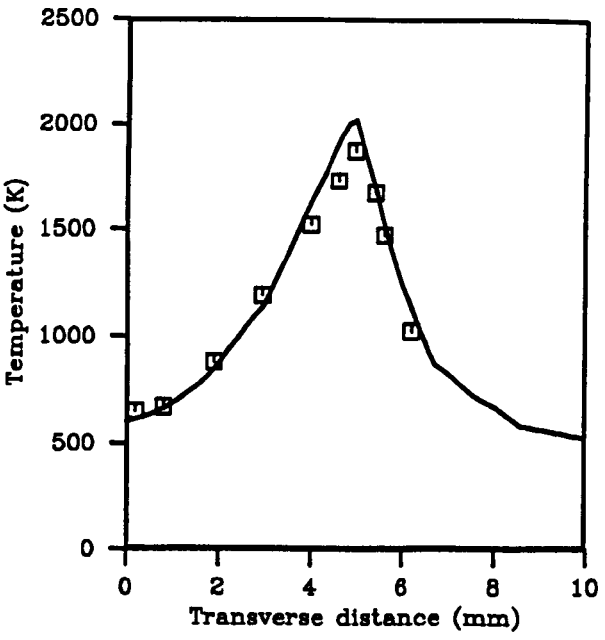

Height : 2mm

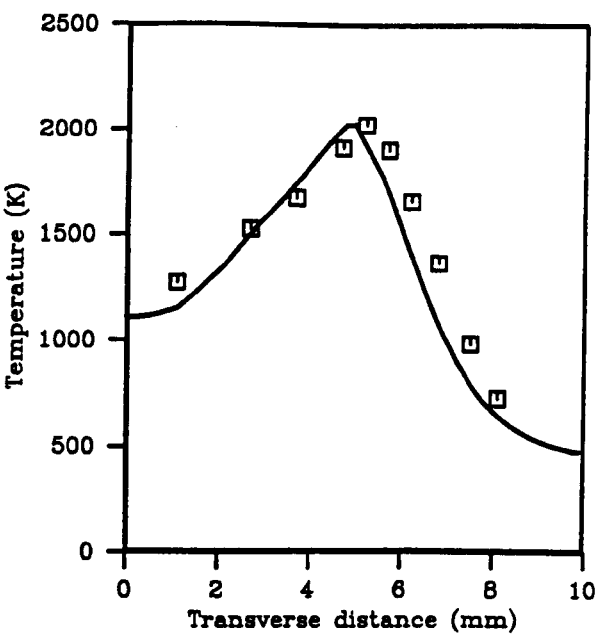

Height : 10mm

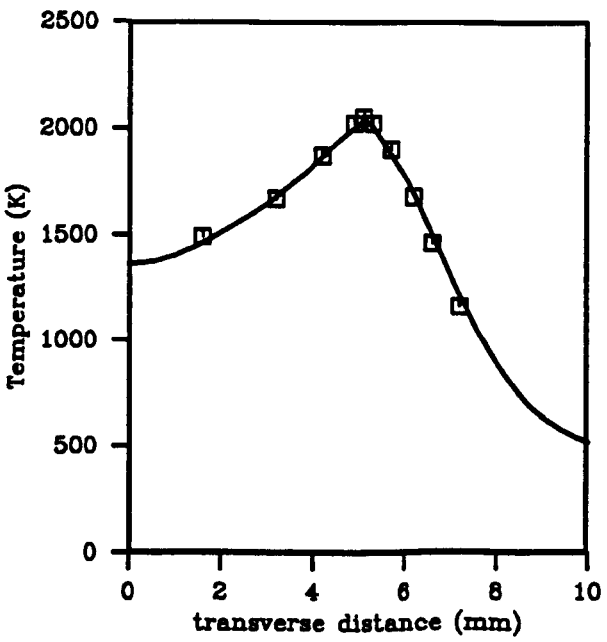

Height : 20mm

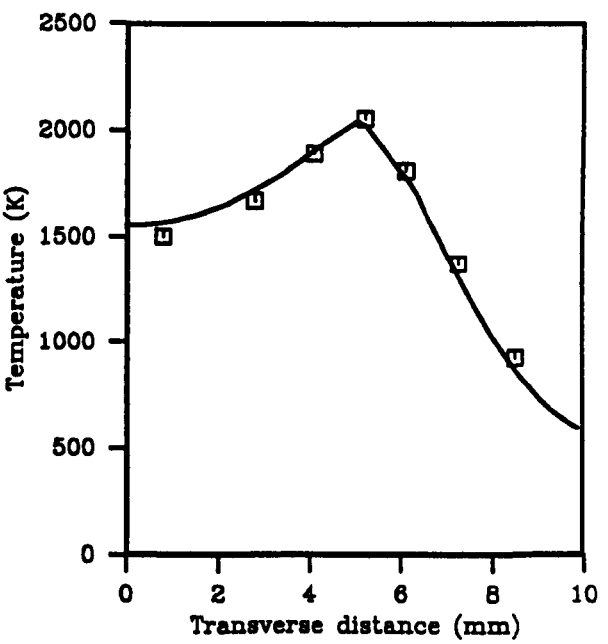

Height : 30mm

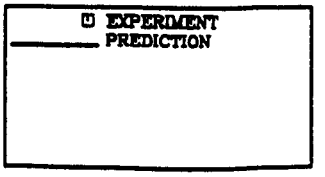

Comparison between predicted and measured temperatures

Figure 3.11

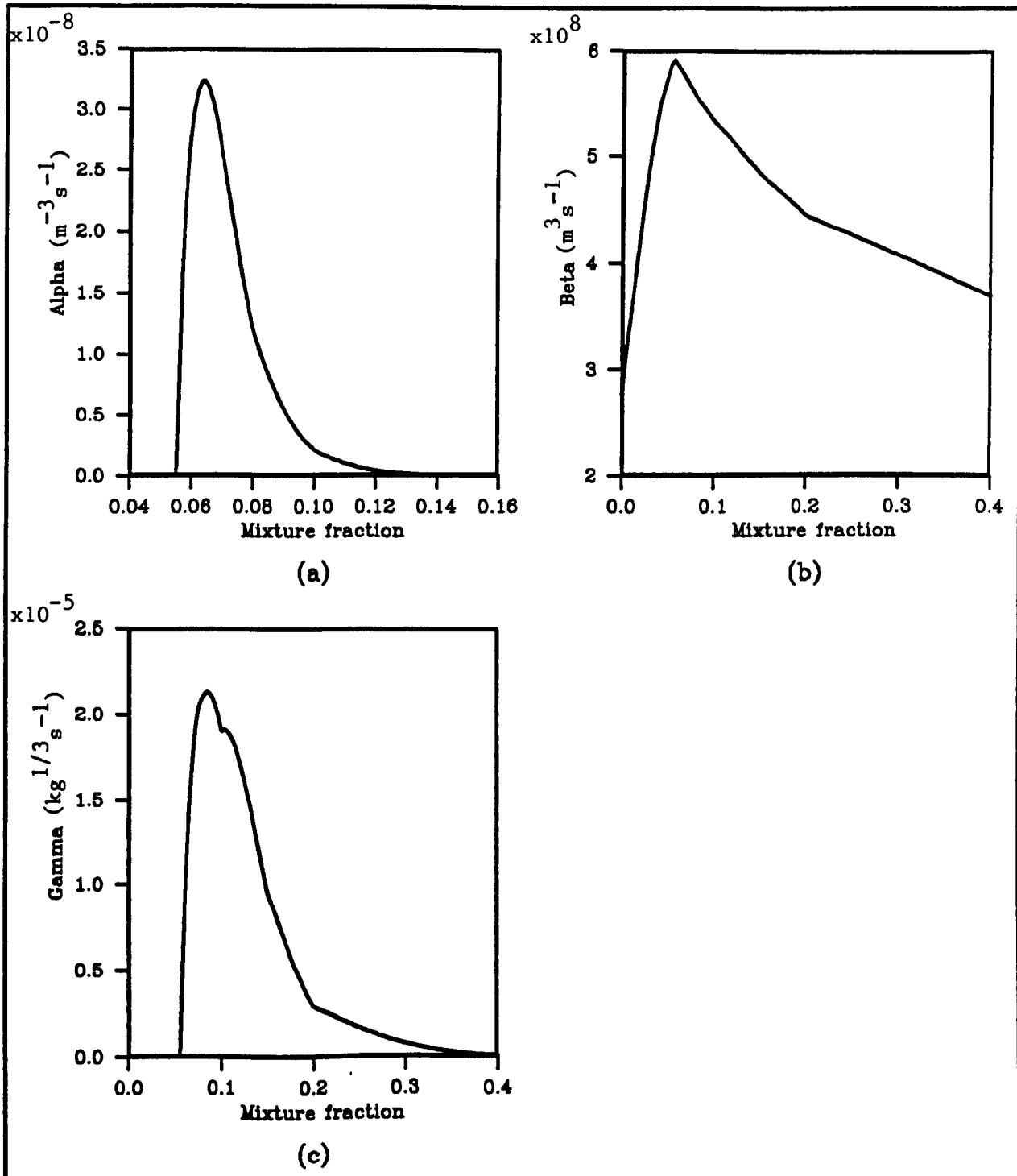

Soot source term parameters, alpha, beta and gamma, for prediction A.

Figure 3.12

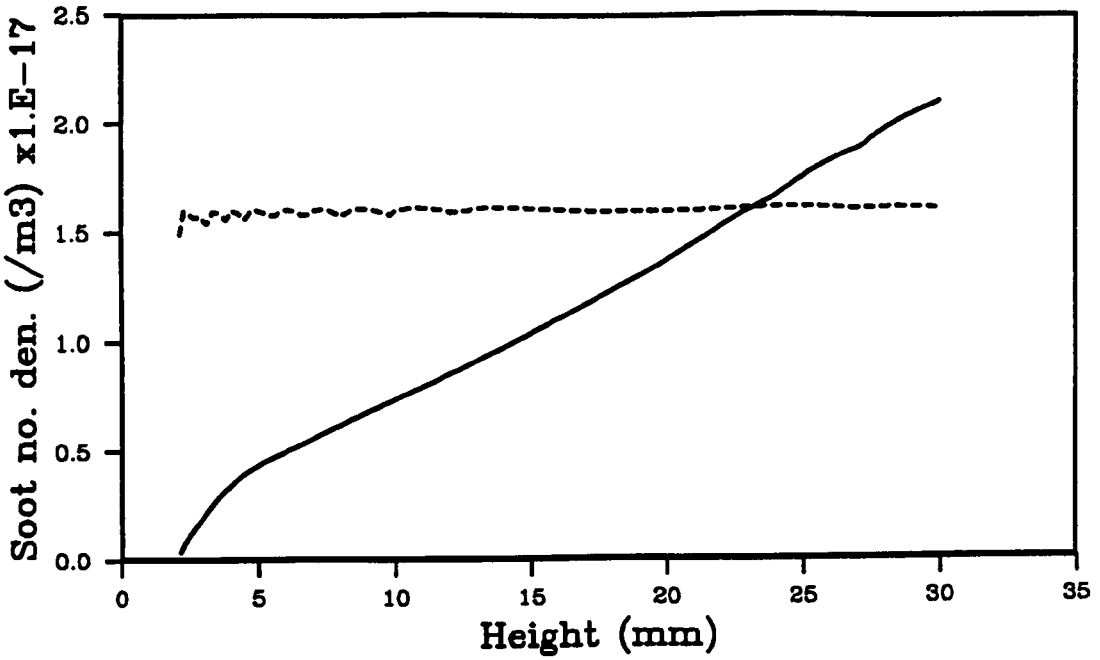

(a)

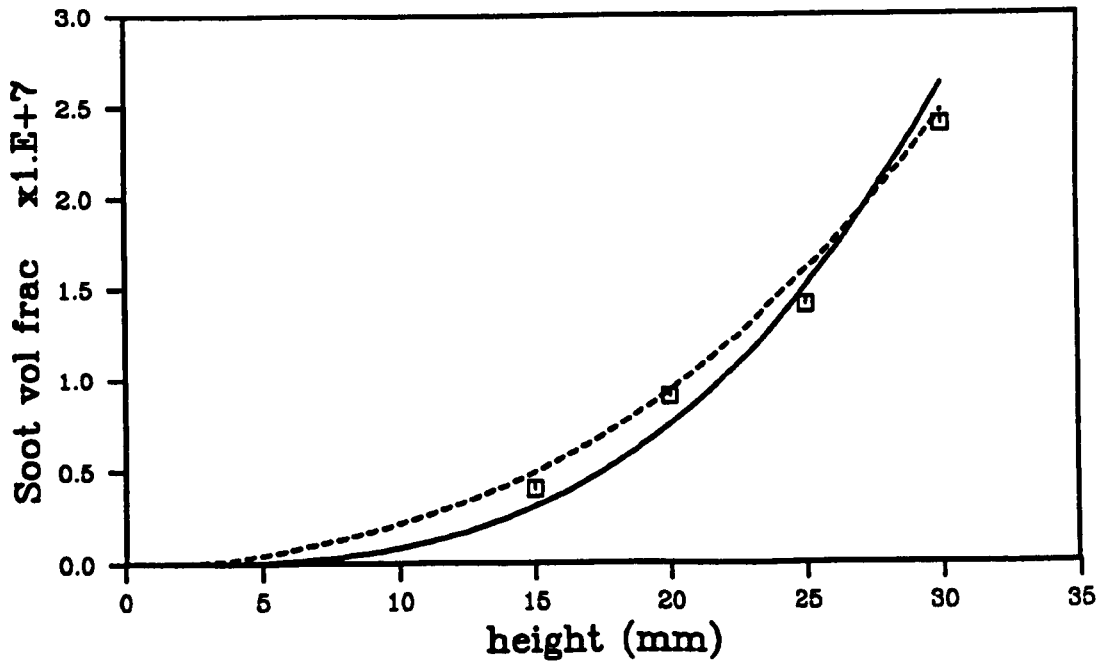

(b)

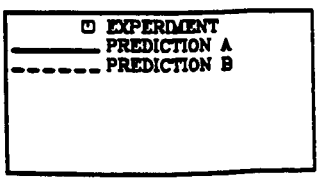

Variation of peak soot volume fraction and number density with height

Figure 3.13

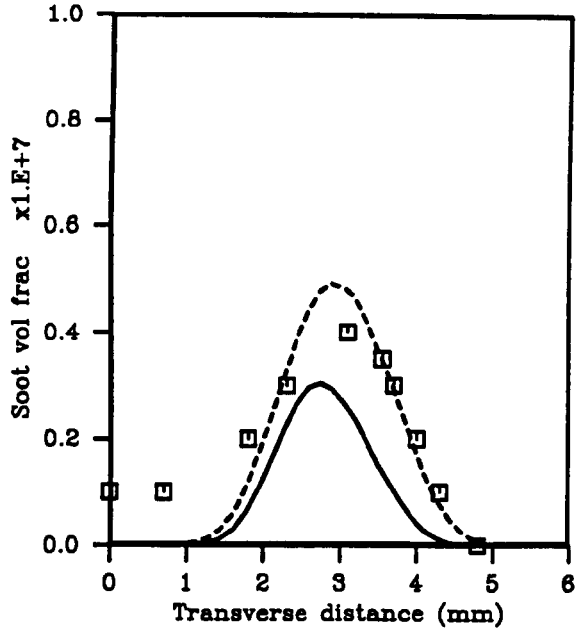

Height : 15 mm

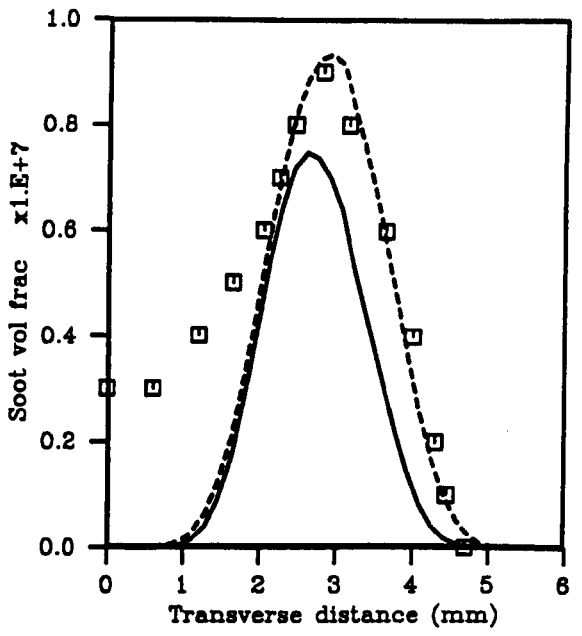

Height : 20 mm

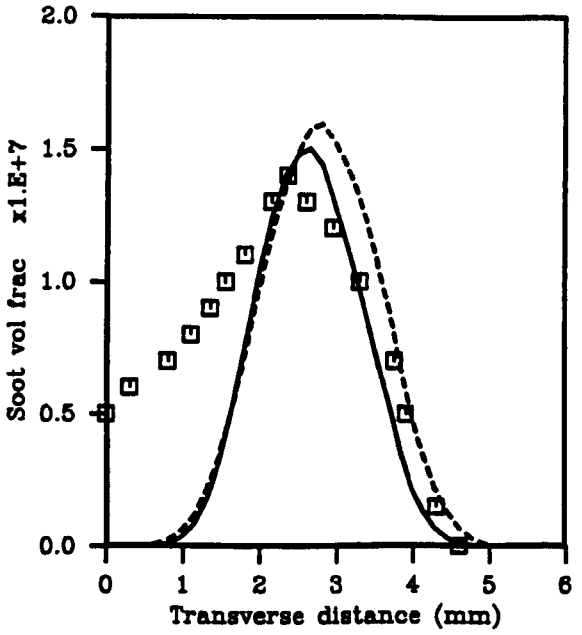

Height : 25 mm

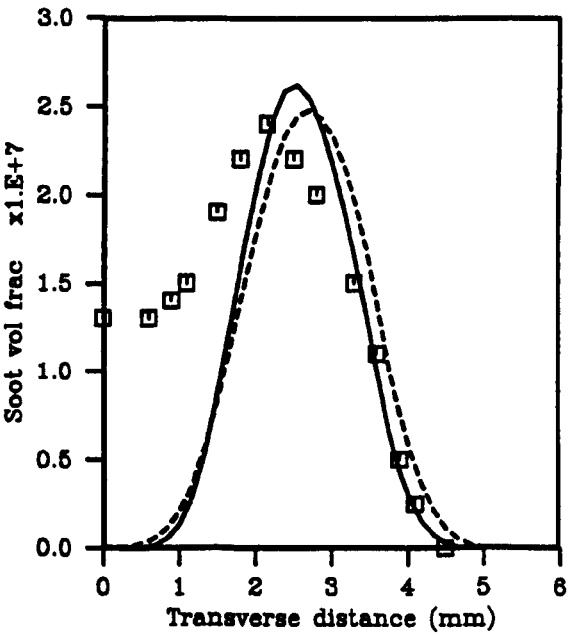

Height : 30 mm

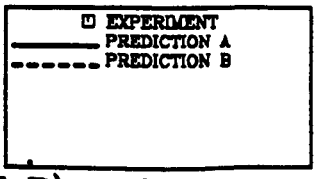

Profiles of soot volume fraction. Comparison between predictions (A and B) and experimental data.

Figure 3.14

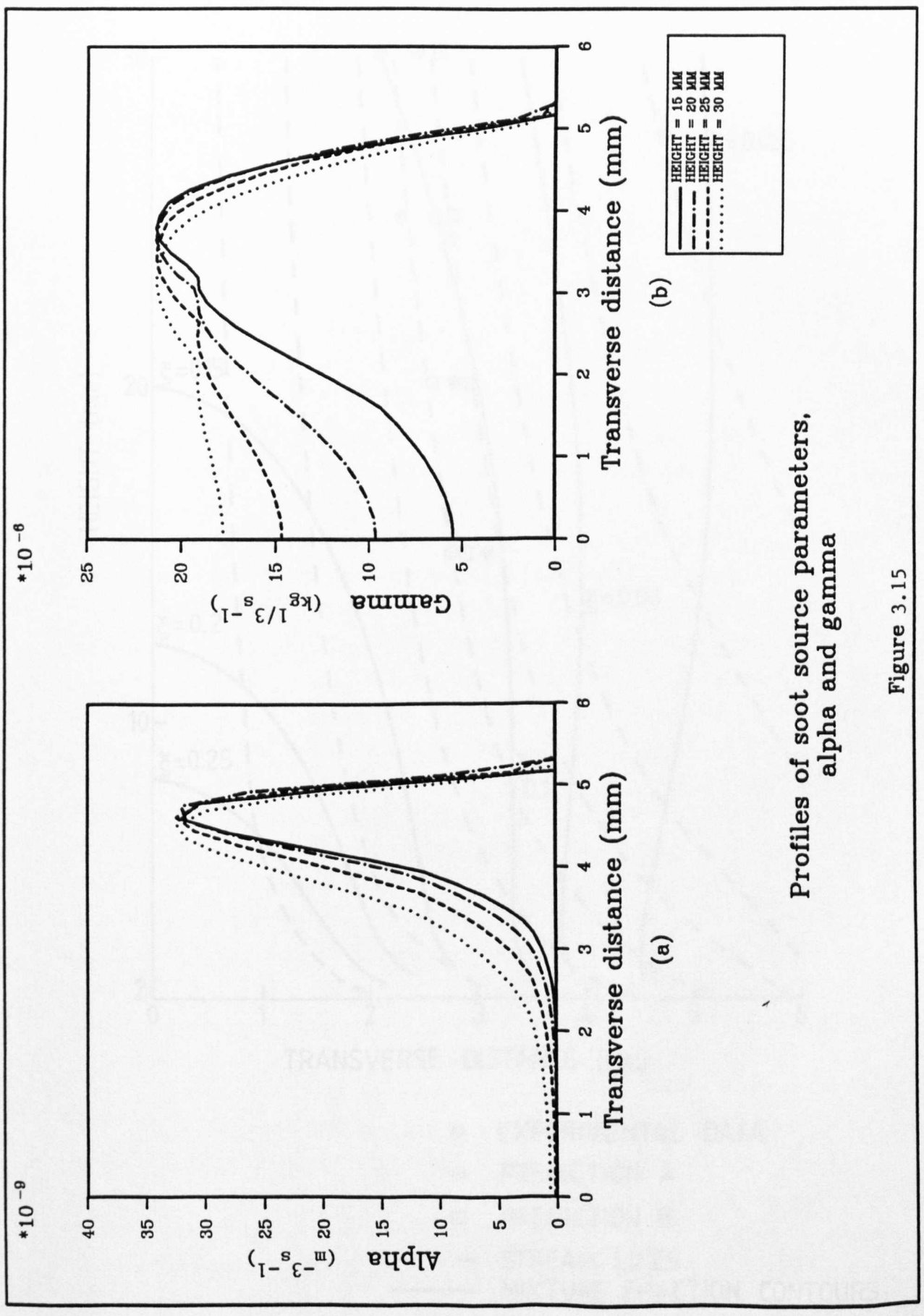

Profiles of soot source parameters, alpha and gamma

Figure 3.15

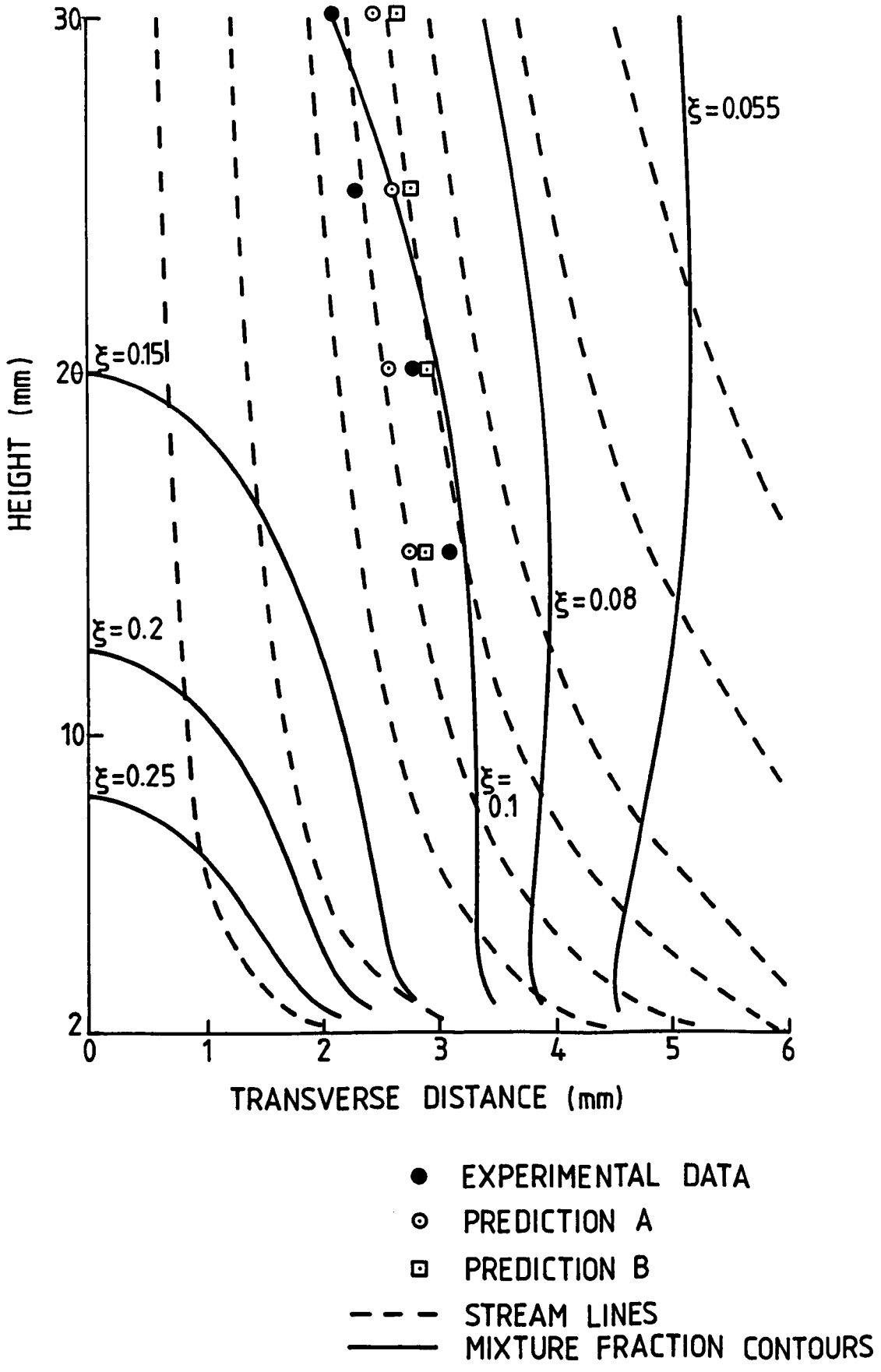

Figure 3.16 - Flowfield map of laminar methane-air flame showing locations of peak soot volume fraction

CHAPTER 4

Soot modelling in turbulent non-premixed combustion

4.1 Introduction

Turbulent flows are characterised by length and time scales that range over several orders of magnitude. These are indicative of the cascade process which describes the energy transfer from the large scale eddies that extract energy from the mean flow, to successively smaller ones, until molecular forces transform the turbulent energy into heat. The former scale is referred to as the integral scale and the latter as the Kolmogorov scale (cf. Tennekes and Lumley (1972)). Direct simulation of such flows by numerical integration of the time-dependent Navier-Stokes equations must encompass the entire physical domain, which is of the order of the largest eddy scale, and resolve down to the smallest. In recent years, given the advances in computer technology, such calculations have been possible (cf. Givi (1989)). These, however, have been restricted to simplified, relatively low Reynolds number (Re) flows, since the ratio between the integral and Kolmogorov scales is proportional to $Re^{3/4}$. This results in the use of $Re^{9/4}$ computational cells for a three dimensional calculation (cf. Schumann et al (1980)). Typical engineering type applications, on the other hand, involve complex geometries and Reynolds numbers of several thousands.

In order to make computation of practical flows feasible, it has become traditional to take a statistical view of the governing processes, where time-dependent properties are averaged over the turbulence scales. Such methods include the moment approach, where balance equations for the first few (usually two) moments of a

property are solved, and the probability density function (PDF) approach, where the entire flowfield may be represented in terms of a multidimensional PDF which is obtained through solution of its evolution equation (cf. Pope (1985)). The latter method may incorporate much of the statistical information that the moment approach lacks and which must therefore be supplied by models. However, the moment approach is well established and is widely used, since it is the more economical and, given suitable closure models, has been successfully applied to a large number of practical scenarios.

In turbulent reacting flows, the addition of chemical source terms pose further and, due to their highly non-linear form (cf. chapter 2), even greater problems. In the averaged balance equation for a chemically active species, the appearance of the mean source term presents closure difficulties. Traditionally, higher order correlations are represented in terms of lower orders; however, the former usually dominate. In this respect the attractions of direct numerical simulation (DNS) and the PDF approach are apparent, as for both the source term is represented in closed form. However, the earlier-mentioned computational limitations of DNS still apply and for a similar reason, the PDF approach has, to date, been applied only to very simple reaction schemes (cf. Chen et al (1989)).

In recent years, however,the problem of mean source term closure has been circumvented owing to the applicability of the fast chemistry assumption. Here reaction time-scales are far shorter than those associated with the mixing process (ie. large Damkohler number); the latter then governs the mean reaction rate (cf. Bilger (1976a)). Under the further assumptions of equal diffusivity of all species and unity Lewis number, it can be shown that all chemistry dependent scalars may be described in terms of any conserved scalar (cf. Williams (1985)), usually the mixture fraction. This approximation has been shown to be valid in laminar flames, where, for example, the experiments of Mitchell et al (1980) demonstrate near-unique relationship of temperature and the major species to equivalence ratio. The approach

is thought to be more appropriate to turbulent flow, where turbulent mixing dominates and the differences in molecular transport of individual species are less important. The thermochemical state in a turbulent reacting flow may then be obtained from mixture fraction, whose mean balance equation is easily solved since it has no source term. This is providing there is a suitable model for the turbulent scalar flux.

The relationship between chemistry-dependent scalars (ϕ) and mixture fraction (ξ) is non-linear and therefore the mean mixture fraction is not sufficient (ie. $\widetilde{\phi} \neq \phi(\widetilde{\xi})$) - a full statistical description is required. This has been overcome by assuming the general form of the PDF of mixture fraction, $P(\xi)$, which is described by its first two moments, $\widetilde{\xi}$ and $\widetilde{\xi''^2}$, both of which may be obtained through mean balance equation, given current turbulence modelling capabilities. The reader is referred to chapter 2 for a more detailed discussion.

Fast chemistry has therefore allowed the successful application of the moment approach to turbulent reacting flows since, through the conserved scalar approach, the chemistry may be decoupled from the turbulent flowfield. Of increasing concern, however, are the relatively minor species which may not have an impact on the overall thermochemistry, but have environmental implications. Such species, in particular NOx and soot, may be governed by slow chemistry and the traditional conserved scalar approach is rendered inapplicable. Bilger (1976b), however, suggested that though NOx concentration cannot be represented as a unique function of mixture fraction, its rate of formation (given by the Zeldovitch mechanism for thermal NOx (cf. Williams (1985)) may. NOx concentration can then be obtained by way of its mean balance equation whose source term is closed through weighting with the PDF of mixture fraction cf.

$$\overline{S} = \int_0^1 S(\xi)\ P(\xi)\ d\xi \qquad \ldots \quad (4.1)$$

(cf. chapter 2). Such an approach, where the relatively narrow reaction zone is of interest, offers a sterner test to the conventional mixture fraction PDF approach which has previously been used directly to obtain scalars, e.g. temperature, which exhibit a greater spread in mixture fraction. The validity of the two parameter PDF over a narrow region of mixture fraction has not yet been demonstrated.

With regard to soot concentration, being important for both its radiative properties and its impact on the environment, predictive capabilities have been hampered both by the turbulent closure issue and the rudimentary knowledge of its formation (and consumption) processes.

Soot modelling in turbulent flows has been attempted by Magnussen et al (1979) who have extended the eddy breakup concept of Spalding (1971a) to incorporate the slow formation of soot - the latter he describes using the formulation of Tesner et al (1971) (cf. chapter 2). Though Magnussen considers the effect of slow chemistry, the description of turbulence interaction is lacking, and hence the generality of the model is questionable. An alternative approach is that adopted by Gore and Faeth (1986,1988) and Kent and Honnery (1987) who apply an empirically determined state relationship for soot concentration, which may then be used to yield mean soot levels from mixture fraction statistics. The turbulent closure issue is therefore addressed more satisfactorily but fast chemistry is assumed. The model is thus restrictive in the range of residence times over which it is applicable.

In order to develop a more widely applicable model, the present study attempts to apply the approach adopted by Bilger (1976b) to the prediction of soot concentration in turbulent non-premixed flames, thereby addressing both slow formation and turbulent interaction. This necessitates the prescription of the soot formation rate as a function of mixture fraction (cf. $S(\xi)$ in eqn. 4.1). Chapter 3 introduced a soot formation model which avoids the uncertainties and complexities

of the detailed mechanisms, by adopting an empirically based approach. There, the rate of soot formation is described in terms of parameters which are functions of mixture fraction dependent scalars, namely temperature, density and fuel concentration (cf. eqns. 3.4 to 3.6). Mean soot concentration may then be determined by solving mean balance equations, where the source term is closed using equation 4.1. However, in addition to being a function of mixture fraction the source term is a function of soot concentration itself, since particle coagulation is dependent on the particle number density (cf. eqn. 3.5) and surface growth is dependent on soot surface area (cf. eqn. 3.6). The mean source term is then given by

$$\overline{S} = \int_0^{\infty} \int_0^{1} S(\Phi,\xi)\ P(\Phi,\xi)\ d\xi\ d\Phi \qquad \ldots \quad (4.2)$$

where Φ is soot concentration and $P(\Phi,\xi)$ is the joint PDF of soot concentration and mixture fraction. Given the present moment-based formulation, this is inaccessible; its derivation requires the solution of its evolution equation and must ideally await time-resolved measurements of soot concentration and mixture fraction. Here, simplifying assumptions have been made in treating the correlations between soot concentration and mixture fraction.

This chapter seeks critically to assess the proposed soot modelling strategy by applying it to the prediction of a turbulent non-premixed flame, with subsequent comparison with experimental data. The adopted simplifications of the two parameter PDF and the above-mentioned simplifications in soot concentration-mixture fraction correlations are investigated. Also of concern is soot oxidation which had not been addressed in the laminar flame of chapter 3 as, given the stream line-mixture fraction map (cf. figure 3.16), soot was unaffected by oxidation in the region of interest. Oxidation is the focus of further study beyond the scope of the present contribution. In turbulent flames, oxidation will certainly be important at the flame tip, where mixing will reduce mixture fraction levels until rich pockets become

scarce; soot will then be forced into leaner regions where it may be oxidized if temperatures are high enough. This does not present a problem in assessing the soot formation model, which may be confined to lower parts of the flame. However, oxidation may interfere with soot formation if soot instantaneously migrates into leaner regions while rich pockets still exist. This is further discussed in section 4.3.7

There is an absence of spatially resolved soot concentration data in turbulent methane diffusion flames, by which the soot model may be assessed. This is also the case for the fire that forms the focus of the present study (cf. chapters 5 and 6), for which the experimental data base consists of temperature, velocity and radiation measurements (cf. Crauford (1984) and Charnley (1986)). The only data from which soot levels may be inferred are line of sight visible radiation measurements (cf. Charnley (1986)) to which soot is the dominant contributor. The derivation of soot levels from such data is, however, subject to uncertainty since point information is required from a single integral measurement and the radiation is subject to a large degree of turbulence interaction (cf. chapter 6).

A wider review of the literature reveals the only suitable soot concentration data to be that of Kent and Honnery (1987) who measured spatially-resolved mean soot volume fraction and temperature. The latter offers an essential guide to the prediction of the scalar field, due to its strong effect on soot formation. Ideally, more information is required since temperatures are affected by radiative loss and successful prediction of mean temperatures alone will not ensure the correct mixture fraction or vector fields.

The Kent and Honnery experiment was performed on a jet diffusion flame of ethylene-air and therefore is incompatible with the soot formation mechanism, derived for a methane system in chapter 3 and to be applied to the fire calculation in chapter 5. However, the objective here is to assess the proposed soot modelling approach which may be achieved using the Kent and Honnery data given a soot formation rate for

ethylene. Fortunately, in a related study, Moss et al (1988), by a method similar to that described in chapter 3, derived a soot formation rate for ethylene flames. This is used to predict soot levels in the Kent and Honnery flame (cf. section 4.3.7).

4.2 Mean balance equations for soot in turbulent non-premixed combustion

The numerical simulation of a sooting laminar diffusion flame was described in chapter 3. There the soot, which is comprised of sub-micron particles, is assumed to be transported as a gas of zero diffusivity and subject to thermophoresis, as is apparent in the case of small particles (cf. Fuchs (1964)). The same assumptions are adopted here for the mean balance equations for soot concentration in turbulent flames whence, for steady state, variable density, high Reynolds number flow we have

$$\bar{\rho}\,\tilde{u}_i \frac{\partial \tilde{\Phi}}{\partial x_i} = - \frac{\partial}{\partial x_i}\left(\bar{\rho}\,\widetilde{u_i'' \Phi''} \right) + \overline{S_\Phi} \qquad \ldots \quad (4.3)$$

The left-hand side represents the mean convection, the first term on the right the turbulent scalar flux and the second term the mean volumetric source. Φ is a soot concentration parameter which, given the adopted two-equation soot formation formulation (cf. chapter 3), may represent ϕ_n or ϕ_m (both of which are defined in the nomenclature). As is generally the case for mean molecular diffusion in gaseous transport, the mean thermophoresis is neglected, on the ground that it is small compared to the turbulent scalar flux. A typical thermophoretic velocity observed in the laminar flame of chapter 3 is 1cm/s and a typical molecular diffusion velocity is 8cm/s.

The dependent variables of the soot concentration balance equations which are Favre averaged quantities (given the variable density flowfield) may be directly translated into the Reynolds averaged soot

number density and mass concentration since, by definition,

$$\tilde{\Phi} = \overline{\rho\ \Phi} \ / \ \bar{\rho} \qquad \ldots \quad (4.4)$$

This leads to

$$\tilde{\phi}_n = \bar{n} \ / \ (N_0\ \bar{\rho}) \qquad \ldots \quad (4.5)$$

and

$$\tilde{\phi}_m = \bar{m} \ / \ \bar{\rho} \qquad \ldots \quad (4.6)$$

The soot volume fraction, the property of interest from an optical point of view, is then easily obtained given the density of soot (ρ_s) cf.

$$\overline{f_v} = \bar{m} \ / \ \rho_s \qquad \ldots \quad (4.7)$$

The two terms on the right hand side of equation 4.3 include turbulent correlations, which must be modelled to provide a closed set of equations. The turbulent flux is similar to that resulting in the mean balance equations of gaseous species and may therefore be closed using a conventional turbulence model. Here, the eddy viscosity concept is used (cf. Launder and Spalding (1972)) where

$$-\ \bar{\rho}\ \widetilde{u_i'' \Phi''} = \frac{\mu_t}{\sigma_\Phi} \frac{\partial \tilde{\Phi}}{\partial x_i} \qquad \ldots \quad (4.8)$$

σ_Φ is the turbulent Schmidt number for soot, taken to be unity, and μ_t is turbulent viscosity, here obtained using the two equation k-ε model of Jones and Launder (1972), where, in Favre averaged form,

$$\mu_t = C_\mu\ \bar{\rho}\ \tilde{k}^2 \ / \ \tilde{\varepsilon} \qquad \ldots \quad (4.9)$$

More specific features of the turbulence model are described in section 4.3.3 where the modelling of the Kent and Honnery flame is described. The next subsection describes the closure of the mean source term.

As will be shown later, in light of the soot predictions of the Kent and Honnery (1987) flame, oxidation plays a significant role in the upper reaches of the flame and, more importantly, a possible role at the extremities of the mixing layer throughout the flame. As the present work considers only a model for soot formation, the oxidation mechanism proposed by Nagle and Strickland-Constable (1962) has been appended to the source terms of the soot concentration balance equations. The mechanism and its incorporation into the modelling scheme is detailed in section 4.2.2.

4.2.1 Source term closure

The overall strategy to source term closure was outlined in section 4.1, which highlighted the dependence of soot formation rate on mixture fraction to be a key feature. Since formation is dependent on both mixture fraction and soot concentration, closure requires their joint statistics (cf. eqn. 4.2). At this stage, however, such information is not accessible and equation 4.2 has been simplified to

$$\overline{S} = \int_0^1 S(\overline{\Phi},\xi)\ P(\xi)\ d\xi \qquad \ldots (4.10)$$

The correlations between soot concentration and mixture fraction are therefore neglected. In addition, correlations resulting from non-linearities involving the soot terms alone (e.g. coagulation is dependent on n^2 cf. eqn. 3.5) are neglected. This leads to the following representations of the source of the soot number density and mass concentration equations

$$\overline{S_{\phi_n}} = \overline{\left[\frac{dN}{dt}\right]} = \overline{\alpha} - \overline{\beta}\,\overline{N}^2 \qquad \ldots (4.11)$$

and

$$\overline{S_{\phi_m}} = \overline{\left[\frac{dm}{dt}\right]} = \bar{\gamma}\ \bar{n}^{1/3}\ \bar{m}^{2/3} + C_\delta\ \bar{\alpha} \qquad \ldots (4.12)$$

the α, β and γ are mixture fraction dependent parameters and defined in chapter 3.2. C_δ is a constant of value 144 which implies a soot nucleus to contain 12 carbon atoms.

Moss et al (1988) represented the surface growth rate by γn rather than $\gamma n^{1/3} m^{2/3}$ which is adopted here. The former is a simplification in that it allows the surface growth rate to increase with particle number, but does not consider the increase in particle surface area as a result of growth. The γ in the two formulations are similarly prescribed but the dimension of C_γ (cf. eqn. 3.6) differs - in the γn formulation, γ is proportional to the rate of growth per particle (kg/s), whilst in the $\gamma n^{1/3} m^{2/3}$ formulation, γ is proportional to the growth per unit surface area (kg/(s m^2)). The simpler approximation was chosen by Moss et al (1988) since it satisfactorily described their laminar flame data whilst posing fewer closure difficulties in turbulent flame application.

The γn formulation was not adopted here since the soot measurements in the laminar methane flame studied in chapter 3, show a cubic dependence of soot volume fraction with height (cf. fig. 3.13b). The numerical predictions in chapter 3 showed that this could be translated into a cubic relationship between soot, inferred directly from the source term, and residence time - this is inherent in the $\gamma n^{1/3} m^{2/3}$ formulation. The experimental data of Moss et al (1988), on the other hand, show a substantially linear relationship between soot volume fraction and height, which is inherent in the γn formulation. The non-linear expression is more physically appealing in respect of surface growth, and Stewart et al (1990) discuss possible explanations for the observed differences. In the predictions of the Kent and Honnery flame reported later, the formulation adopted by Moss et al (1988), coupled with their empirically derived soot formation rate, is

used. Following the earlier simplification, the source of soot mass concentration is then represented by

$$\overline{S_{\phi_m}} = \overline{\left[\frac{dm}{dt}\right]} = \bar{\gamma}\ \bar{n} + C_\delta\ \bar{\alpha} \qquad \ldots (4.13)$$

4.2.2 The mean oxidation rate

Chapter 2.2 provided a discussion of the various possible oxidation mechanisms that may be significant in non-premixed flames. The two most important species are thought to be the hydroxyl radical (OH), which is a highly active oxidizer, and the relatively more sedate O_2. OH is found in and around the reaction zone and may attain a peak level of 0.005 mole fraction according to equilibrium for an ethylene-air system. O_2 is restricted to lean regions as it is fully consumed close to the stoichiometric point. Soot is formed on the rich side of stoichiometric, peaking at a mixture fraction of approximately 0.1 (cf. fig.3.6 and Moss et al (1988)) and must therefore migrate to leaner mixtures if it is to be oxidized. Hence it will firstly encounter OH. The degree to which OH will oxidize the soot will depend the flame geometry. This controls the residence time spent by the soot in the formation region, and hence the particle size and the mass of soot formed, and subsequently the OH oxidizing region. If the soot survives, and continues to migrate to leaner regions, O_2 oxidation will occur until temperatures become too low. Subsequent emission of smoke will depend on whether the soot survives this region.

The present study does not seek to address the finer points of soot oxidation since such is not feasible in turbulent flames given the additional statistical uncertainties. Here oxidation is presumed to result from O_2 oxidation alone, where the rate is obtained from Nagle and Strickland-Constable (1962). Kent and Wagner (1984) and Megaridis and Dobbins (1989) both demonstrated that this mechanism could

correlate their experimental data of oxidation in laminar ethylene-air diffusion flames.

The Nagle and Strickland-Constable (1962) oxidation mechanism is shown in equation 2.36 where the consumption of carbon per unit surface area (ω kg/sm^2) is given in terms of O_2 concentration and temperature. Here, these are treated as mixture fraction dependent parameters and therefore the oxidation rate may be expressed as $\omega(\xi)$. The following casts this oxidation rate into suitable forms to describe the rate of consumption of soot mass concentration and particle number density.

The rate of change of soot mass concentration due to oxidation may be expressed as

$$\left.\frac{dm}{dt}\right|_{ox} = -\omega \times (\text{soot surface area per unit volume})$$

$$= -\omega\, n\, \pi\, d^2 \qquad (\text{kg/ s m}^3) \qquad \ldots (4.14)$$

where d is a mean particle diameter defined as

$$d = \left(\frac{6\, m}{\pi\, \rho_s\, n}\right)^{1/3} \qquad \ldots (4.15)$$

where ρ_s is the soot density. Substituting equation 4.15 in 4.14 leads to

$$\left.\frac{dm}{dt}\right|_{ox} = -\varepsilon\, n^{1/3}\, m^{2/3} \qquad \ldots (4.16)$$

where

$$\varepsilon = \left(\frac{36\, \pi}{\rho_s^{\,2}}\right)^{1/3} \omega \qquad \ldots (4.17)$$

Equations 4.15 and 4.16 may be used to determine the rate of consumption of soot number density cf.

$$\frac{d}{dt}\left[\rho_s\, n\, \frac{\pi\, d^3}{6}\right]\Bigg|_{ox} = -\,\varepsilon\, n^{1/3}\, m^{2/3} \qquad \ldots\ (4.18)$$

this may be approximated to

$$\frac{d(n/N_0)}{dt} = -\,\frac{1}{N_0}\,\frac{6}{\rho_s\, \pi\, d^3}\,\varepsilon\, n^{1/3}\, m^{2/3} \qquad \ldots\ (4.19)$$

Substituting for d yields

$$\left.\frac{dN}{dt}\right|_{ox} = -\,N_0^{1/3}\,\varepsilon\, N^{4/3}\, m^{-1/3} \qquad \ldots\ (4.20)$$

Following the earlier simplifications that lead to equations 4.11-4.13 the mean oxidation rate may be expressed as

$$\left.\overline{\frac{dN}{dt}}\right|_{ox} = -\,N_0^{1/3}\,\overline{\varepsilon}\;\underline{\overline{N}}^{4/3}\;\underline{\overline{m}}^{-1/3} \qquad \ldots\ (4.21)$$

and

$$\left.\overline{\frac{dm}{dt}}\right|_{ox} = -\,\underline{\overline{\varepsilon}}\;\underline{\overline{n}}^{1/3}\;\underline{\overline{m}}^{2/3} \qquad \ldots\ (4.22)$$

These can then be appended to the mean formation rates (eqns. 4.11 and 4.12 (or 4.13)) to consider simultaneous formation and oxidation.

4.3 Validation of the soot model in a turbulent jet diffusion flame

4.3.1 Introduction

This section describes the prediction of the sooting ethylene-air jet diffusion flame experimentally investigated by Kent and Honnery (1987). Given the present diagnostic nature of the soot modelling exercise, the soot calculation is performed as a post process, which

avoids the complex interaction between soot concentration and, particularly, temperature. The implication that soot is simply a perturbation to the gas phase seems reasonable, since the experimental data coupled with the present velocity predictions show the maximum soot mass flux to be 7% of the total fuel stream (or mixture fraction) flux. However, in ethylene diffusion flames soot is a major contributor to thermal radiation (cf. Faeth et al (1986)) which for the present flame is significant. This is indicated by the later reported adiabatic prediction, where temperatures are substantially over-estimated. Here in order to obtain more plausible temperatures, whilst still maintaining a decoupling between the soot and flowfield calculations, radiative loss is introduced explicitly through perturbation of the temperature state relationship. The latter describes the instantaneous temperature state, in the adopted laminar flamelet combustion model, and is assumed to apply to the entire flowfield.

This procedure is somewhat questionable, since radiative loss will more typically vary throughout the flame, as it depends on local soot levels and flamelet thickness (and hence path length). However, given the sensitivity of the soot formation rate to temperature (cf. chapter 3 and Moss et al (1988)), it is imperative to infer the locally applicable temperature flamelet, and hence the instantaneous soot formation rate, from the mean enthalpy that would result from an enthalpy balance equation coupled with a radiation model. It is straightforward to imagine the derivation of such flamelets by, for example, equating the computed mean enthalpy (incorporating radiative loss) with that obtained from a state relationship cf.

$$\tilde{h}_{\text{balance eqn.}} = \int_0^1 h(\xi)\ \tilde{P}(\xi)\ d\xi \qquad \ldots\ (4.23)$$

The function $h(\xi)$ may be adjusted to produce the equality by perturbation of the adiabatic $T(\xi)$ according to some algebraic rule. More accurately, one may compute a library of flamelets with varying

degrees of radiative loss which would remove the necessity for a, somewhat arbitrary, rule for adjusting $T(\xi)$. This, however, violates the overriding aim to decouple the soot calculation, since it is a major contributor to radiation and must be considered in the derivation of a suitable $T(\xi)$.

At this stage, it is felt that further uncertainties introduced through a radiation model, its effect on enthalpy, and thence its inference of a local temperature state relationship, are best avoided.

The next three subsections describe the numerical scheme and the turbulence and combustion models, where the latter alludes to the need for state relationships given the adoption of the laminar flamelet combustion model. These are derived numerically, as described in section 4.3.5, using the SNECKS algorithm (Liew (1983)). Following that, the flowfield predictions are presented, which form a scalar and vector map upon which the soot predictions are then grafted.

4.3.2 Governing equations

The jet diffusion flame in a stagnant environment can be described as a two dimensional, axi-symmetric, parabolic boundary layer since the strong convection in the streamwise direction is very much greater than diffusive processes. Under these circumstances the governing equations take the form

$$\bar{\rho}\,\tilde{u}\,\frac{\partial\tilde{\phi}}{\partial x} + \bar{\rho}\,\tilde{v}\,\frac{\partial\tilde{\phi}}{\partial r} = \frac{1}{r}\frac{\partial}{\partial r}\left(r \left[\frac{\mu_l}{\sigma_l} + \frac{\mu_t}{\sigma_t}\right]\frac{\partial\tilde{\phi}}{\partial r}\right) + \bar{S} \qquad \ldots (4.24)$$

where u and v are the streamwise (x) and radial (r) velocity components, ϕ is a general dependent variable, S is the volumetric source term and the subscripts l and t refer to laminar and turbulent quantities. Equation 4.24 may represent any vector or scalar balance equation with suitable settings of the Prandtl/Schmidt number (σ) and

source term. The Reynolds stresses and turbulent fluxes, as implied are modelled using the eddy viscosity concept, where μ_t may be expressed in terms of k and ε (cf. eqn. 4.9).

A suitable solver for this system of equations is the GENMIX algorithm (Spalding (1977)) described in detail in chapter 3.4.4. This works in the Patankar-Spalding co-ordinate system, where fulfilment of mass continuity is ensured and the cross stream velocity is a grid dependent parameter. The only flowfield variables requiring solution through equation 4.24 are therefore u and the scalar variables necessary for closure. For the adopted two-equation k-ε turbulence model and the laminar flamelet combustion model, closure may be achieved by solving for $\tilde{u}$, k, ε, $\tilde{\xi}$ and $\widetilde{\xi''^2}$. When soot is to be considered, equations for $\tilde{\phi}_n$ and $\tilde{\phi}_m$ are also to be solved. The prescription of the appropriate Schmidt numbers and source terms is given in table 4.1.

4.3.3 Turbulence model

The two-equation k-ε model of Jones and Launder (1972) is used in the present study since it has been widely used in the prediction of jet diffusion flames and has met with success in terms of mean and fluctuating temperatures and velocities. Of the alternatives, the second moment closures (cf. Launder et al (1975) and Dibble et al (1986)), where balance equations are solved for the Reynolds stresses and turbulent scalar fluxes, offer the next degree of complexity and generality. These remove some of the more restrictive turbulence modelling assumptions and in particular that of gradient diffusion. Second order closures, however, still require modelling of higher order terms and length scale information and hence the solution of a modelled equation for ε.

The balance equation for k and ε in a two dimensional axi-symmetric boundary layer may be represented by equation 4.24 where the turbulent

Schmidt numbers are 1.0 and 1.3 respectively. The modelled source terms are

$$\bar{S}_k = \mu_t \left(\frac{\partial \tilde{u}}{\partial r}\right)^2 - \bar{\rho}\,\tilde{\varepsilon} \qquad \ldots (4.25)$$

and

$$\bar{S}_\varepsilon = C_{\varepsilon 1} \frac{\tilde{\varepsilon}}{\tilde{k}} \mu_t \left(\frac{\partial \tilde{u}}{\partial r}\right)^2 - C_{\varepsilon 2} \frac{1}{\tilde{k}} \bar{\rho}\,\tilde{\varepsilon} \qquad \ldots (4.26)$$

The first term on the right hand side of equation 4.25 represents generation of turbulent kinetic energy extracted from the mean flow, and the second represents the energy dissipation. The terms in equation 4.26 rely heavily on modelling and are not easily interpreted, since in their exact forms the source and sink of ε both tend to infinity for high Reynolds number flows, though their difference remains finite. These source terms do not include the effect of buoyancy on turbulence and its effect is introduced only through its influence on the vertical momentum component. The values of the empirical constants $C_{\varepsilon 1}$ and $C_{\varepsilon 2}$ have been evaluated in cold planar jets to be 1.44 and 1.92, respectively. Liew (1983), amongst others, has demonstrated that constants evaluated in cold flows can be applied to high Reynolds number reacting flows without modification.

Several authors (cf. Pope (1978)) noted that the spreading rate of round jets was over-estimated by approximately 40%, when using the k-ε model for which the constants were evaluated in planar jets. The jet spread was found to be most sensitive to $C_{\varepsilon 1}$ and $C_{\varepsilon 2}$; increasing $C_{\varepsilon 1}$ or reducing $C_{\varepsilon 2}$ have the desired effect since both accelerate the decay of turbulence and hence reduce the eddy viscosity that controls the spreading. Setting $C_{\varepsilon 1}$ to 1.6 produces reasonable results for round jets (cf. Pope (1978)). However, simply changing the constants reduces the generality of the model and has led some authors to prefer manipulation of the constants through algebraic expressions incorporating local conditions. For example, Launder et al (1972) chose to manipulate $C_{\varepsilon 2}$ according to an expression incorporating the

centre line velocity gradient. McGuirk and Rodi (1977) chose such an expression to manipulate $C_{\varepsilon 1}$. In the present work, following Liew (1983), the amendment introduced by Morse (1977) cf.

$$C_{\varepsilon 1} = 1.4 - 3.4 \left(\tilde{k}/\tilde{\varepsilon} \; \frac{d\tilde{u}}{dx} \right)_c^3 \qquad \ldots (4.27)$$

is used. The subscript c refers to centre line conditions.

Though offering modifications that show good agreement with data, the above approach, and its analogues (cf. McGuirk and Rodi (1977) and Launder et al (1972)), do not seek to give an explanation of the planar-round jet anomaly. In addressing this, Pope (1978) argued that an increase in dissipation rate may result through the stretching of vortex tubes. The stretching will cause the size (radius) of the vortex to diminish, due to conservation of angular momentum, and therefore accelerate the decay of the energy containing eddies that control the Reynolds stresses. This stretching may occur due to mean velocity gradients in the plane of the vorticity vector ie. perpendicular to the plane of rotation. In two-dimensional flow, no such stretching may occur since the vorticity vector is perpendicular to the plane of the flow and hence the mean velocity vector. However, in axi-symmetric flows, as the jets spread, the circular vortex tubes are stretched, therefore increasing the decay of turbulence and hence the spreading rate.

Pope (1978) offers a general approach to the problem which considers a local vortex stretching parameter. Here, however, given that the geometry is that of a round jet, the algebraic correction of Morse (1977) (eqn. 4.27) is used. Liew (1983) demonstrated that the k-ε turbulence model with this modification may be applied to jet flames with success.

In the light of the earlier argument, such correction has not however been incorporated in the fire calculation (cf. Chapter 5).

4.3.4 Combustion model

The present modelling strategy uses the laminar flamelet approach which assumes that a turbulent flame is comprised of laminar flamelets which may be stretched and transported by the turbulent motion. This is valid if the reaction zone thickness is not greater than the Batchelor length scale (the scalar equivalent of the Kolmogorov length scale). If it is further assumed that the chemistry is fast (ie. the system is mixing controlled) and all scalars have the same transport rate, then, any chemistry dependent scalar may be expressed in terms of a single conserved scalar. The mixture fraction (ξ) is used here. In the fluctuating turbulent field, the PDF of a scalar, and hence its moments, can therefore be determined from the PDF of mixture fraction, $P(\xi)$.

As is common practice, $P(\xi)$ is of an assumed form, here the beta function (previously adopted by Jones and Priddin (1979) and Liew (1983)) which is fully described by its first two moments (ie. the mean and variance of mixture fraction). The latter are readily obtained from their balance equations (cf. appendix A). In equation 4.24, with $\tilde{\xi}$ as subject, there is no source term since it is a conserved scalar. The balance equation of $\widetilde{\xi''^2}$, however, contains a source due to both turbulent generation and dissipation, the modelled form of which, for 2-D boundary layers may be written as

$$\overline{S}_g = C_{g1}\,\mu_t \left(\frac{\partial\tilde{\xi}}{dr}\right)^2 - C_{g2}\,(\tilde{\epsilon}\,/\,\tilde{k})\,\widetilde{\xi''^2} \qquad \ldots\ (4.28)$$

The subscript g refers to $\widetilde{\xi''^2}$ (cf. Launder and Spalding (1972).

Spalding (1971b) suggested the values of C_{g1} and C_{g2} to be 2.8 and 2.0 respectively. The literature, covering both inert and reactive systems, shows C_{g1} to vary little from the above value but C_{g2} to vary from 2.0 (cf. Spalding (1979)) to 1.25 (cf. Gibson and Launder

(1976)). Liew (1983) found the values C_{g1}=2.8 and C_{g2}=2.0 to be reasonable for jet diffusion flames. Following Faeth et al (1986), the values used here are C_{g1}=2.8 and C_{g2}=1.89. These, however, result in negligible difference compared to the values adopted by Liew (1983).

In chapter 5, however, which reports the modelling of a buoyancy driven fire, it seems that a value of C_{g2}=1.25 may be more appropriate. This is discussed more fully there.

Having obtained the mean and variance of mixture fraction through solution of their balance equations the PDF, $P(\xi)$, may be defined, given the beta function form, cf.

$$\tilde{P}(\xi) = \frac{\xi^{\alpha-1}(1-\xi)^{\beta-1}}{\int_0^1 \xi^{\alpha-1}(1-\xi)^{\beta-1}\, d\xi} \qquad \ldots (4.29)$$

where

$$\alpha = \tilde{\xi}\left(\frac{\tilde{\xi}(1-\tilde{\xi})}{\widetilde{\xi''^2}} - 1\right) \qquad \ldots (4.30a)$$

and

$$\beta = \alpha\,(1-\tilde{\xi}) \,/\, \tilde{\xi} \qquad \ldots (4.30b)$$

(cf. Abramovitz and Stegun (1968)). The beta function in equation 4.29 is normalised by its total area to ensure that the integral of $P(\xi)$ is unity, a condition not met by the beta function.

Alternatives to the beta function PDF include the intermittent beta function (Kent and Bilger (1977)) and the clipped Gaussian (Lockwood and Naguib (1975)). The former is used in the present study, in order to gauge the effect of an alternate PDF form on the later reported soot predictions, and is therefore discussed in detail below.

Derivation of $P(\xi)$ given an intermittent beta function form, requires, in addition to $\tilde{\xi}$ and $\widetilde{\xi''^2}$, the intermittency function, I. This is

defined as the fraction of time that turbulent fluid is experienced as opposed to non-turbulent. The latter is representative of the free stream in a turbulent shear layer and, for jet flames, exhibits a zero mixture fraction. I may be deduced through solution of a balance equation (cf. Libby (1975)). Kent and Bilger (1977), however, proposed an empirically derived algebraic expression cf.

$$\tilde{I} = \frac{K + 1}{(\widetilde{\xi''^2} / \tilde{\xi}^2) + 1} \quad , \quad I \leq 1 \qquad \ldots (4.31)$$

where K is a constant which they deduced to be 0.25. This is used in the present study.

It is possible to deduce a mean and variance of mixture fraction, $\tilde{\xi}_t$ and $\widetilde{\xi_t''^2}$, which are appropriate to the turbulent fluid alone, cf.

$$\bar{\xi} = \tilde{I}\,\tilde{\xi}_t \qquad \ldots (4.32)$$

and

$$\widetilde{\xi''^2} = \tilde{I}\,\widetilde{\xi_t''^2} + \tilde{I}\,\tilde{\xi}_t^2 - \tilde{\xi}^2 \qquad \ldots (4.33)$$

The PDF is then defined as

$$\tilde{P}(\xi) = (1-\tilde{I})\,\delta(\xi) + I\,\frac{\xi^{\alpha_t-1}(1-\xi)^{\beta_t-1}}{\int_0^1 \xi^{\alpha_t-1}(1-\xi)^{\beta_t-1}\,d\xi} \qquad \ldots (4.34)$$

where $\delta(\xi)$ is the dirac delta function and is unity at $\xi=0$ and zero elsewhere. α_t and β_t are given by equations 4.30 where $\tilde{\xi}_t$ and $\widetilde{\xi_t''^2}$ are used in place of $\tilde{\xi}$ and $\widetilde{\xi''^2}$.

Given $P(\xi)$, it is straight forward to deduce the mean and variance of any mixture fraction dependent variable $\phi(\xi)$ via equation 2.23. It should be noted that the deduced $P(\xi)$ is a Favre quantity, since it is described by the Favre mean and variance of mixture fraction. However, if $\rho(\xi)$ is a known function then the Reynolds quantity $P(\xi)$ is readily

obtainable (cf. eqn 2.28) and Reynolds averaged quantities are obtained from equation 2.30. $\phi(\xi)$ is stored as a piece-wise linear function and the integration (cf. eg. eqn. 2.30) is performed numerically using a 10 point Gaussian integration. The latter is applied several times to cover the range $0 \leq \xi \leq 1$, dictated by the number of piece-wise linear segments of $\phi(\xi)$.

The function $\phi(\xi)$ describes the instantaneous state relationship between ϕ and ξ in a laminar flamelet and may be deduced within the confines of a representative laminar flame. $\phi(\xi)$ may be valid over the entire turbulent flowfield under the assumption of zero or constant heat loss and zero or constant strain rate.

In the present study, the state relationships were deduced through numerical solution of a time dependent reacting-diffusing system effectively looking at a one dimensional non-premixed flame. The SNECKS algorithm (Liew (1983)) was used for this purpose and is described in more detail in the next subsection. The calculation was performed under the constraints of zero heat loss and zero stretch. In the Kent and Honnery flame, however, radiative loss was found to be significant. Here this is treated explicitly through perturbing the temperature state relationship, as will be described later.

Liew et al (1984), in their simulation of methane-air jet diffusion flames, showed that in such geometries, flame stretch was minimal and confined to the potential core region. The effect of flame stretch on the soot formation process is believed to be twofold. Firstly, the reduced temperatures accompanying increasing stretch will tend to reduce soot formation rates and secondly, the slower reaction rates may allow oxygen to diffuse through the flame and into the soot formation region where soot production may be enhanced (cf. Glassman (1988)). The relative effects of reducing temperature and increasing local oxygen levels are not known but since flame stretch is minimal it has been neglected.

4.3.5 Numerical derivation of an ethylene-air diffusion flamelet

The simulation of a laminar diffusion flame to be described, is for zero heat loss and strain rate. Conceptually, the simulation is spatially one dimensional and considers time dependent chemical reaction, as two streams (fuel and air) diffuse into one another. The code used is SNECKS (solver for non-equilibrium chemical kinetics systems) (cf. Liew (1983)) which is described in detail by Pratt (1977), Liew (1983) and Askari-Sardhai (1987). Here, therefore, only a brief overview is provided.

The governing equation solved by SNECKS is

$$\frac{\partial \phi}{\partial t} = \frac{1}{\rho}\frac{\partial}{\partial y}\left(\rho\, \Gamma_{\phi} \frac{\partial \phi}{\partial y} \right) + \frac{1}{\rho} S_{\phi} \qquad \ldots (4.35)$$

where ϕ is species mole number (σ = mass fraction/molecular mass) or mixture enthalpy. Γ_{ϕ} is the transport coefficient and S_{ϕ} is the volumetric source term.

The source term for the species equations is expressed as

$$S_{\sigma_i} = \sum_{j=1}^{jj} (\alpha'_{ij} - \alpha''_{ij}) \; (R_j - R_{-j}) \qquad \ldots (4.36)$$

where jj is the total number of reactions, i is the species and R_j and R_{-j} are the forward and reverse rates for the j^{th} reaction. α' and α'' are stoichiometric coefficients cf.

$$\alpha'_{1j}\phi_1 + \alpha'_{2j}\phi_2 \underset{K_{-j}}{\overset{K_j}{\rightleftharpoons}} \alpha''_{3j}\phi_3 + \alpha''_{4j}\phi_4 \qquad \ldots (4.37)$$

where K is the rate constant and is later detailed for the adopted reaction scheme.

R_j and R_{-j} are given by

$$R_j = K_j \ (\rho\sigma_m)^{\bar{\alpha}_j} \ \prod_{k=1}^{ns} (\rho\sigma_k)^{\alpha'_{kj}} \qquad \ldots (4.38)$$

and

$$R_{-j} = K_{-j} \ (\rho\sigma_m)^{\bar{\alpha}_j} \ \prod_{k=1}^{ns} (\rho\sigma_k)^{\alpha''_{kj}} \qquad \ldots (4.39)$$

where σ_m is the reciprocal of the mixture molecular mass, ns is the total number of species and $\bar{\alpha}_j$ is zero and unity for two and three body reactions.

The balance equation for enthalpy, when written in the form of equation 4.35, has an apparent source term resulting from the differential diffusion of species and heat cf.

$$S_h = \frac{\partial}{\partial y} \left(\mu \sum_{i=1}^{ns} \left[\frac{1}{Sc} - \frac{1}{Pr} \right] h_i \frac{\partial \sigma_i}{\partial y} \right) \qquad \ldots (4.40)$$

where h_i is the enthalpy of species i and includes both the sensible and formation heats.

The resulting equations are written as a set of Newton-Raphson correction equation and are solved by pivotal Gaussian elimination (cf. Pratt (1977)).

A semi-global chemical kinetic mechanism is used here, where the primary step is an irreversible reaction where fuel and oxygen react to form carbon monoxide and hydrogen. The reaction rate is obtained from Edelman et al (1972) who proposed a mechanism for a general hydrocarbon cf.

$$C_nH_m + O_2 \xrightarrow{K} n\,CO + \frac{m}{2} H_2 \qquad \ldots (4.41)$$

for which the volumetric rate (mole/cm^3s) is given by

$$K = A\ T^n \exp(-T_a/T)\ [C_{fuel}]^a\ [C_{O2}]^b\ p^c \qquad \ldots (4.42)$$

where A is the pre-exponential factor, T_a is the activation temperature, P is the pressure in atmospheres and a, b and c are constants. These are reported as

A	n	Ta	a	b	c
5.52×10^8	1	12200	0.5	1.0	-.825

The above reaction is supplemented by a further twelve which describe the detailed oxidation of CO and H_2 cf. appendix C.

Figure 4.1 shows the numerically derived state relationships for O_2 concentration, C_2H_4 concentration, and density. Though other species were considered in the calculation (cf. appendix C), only those of direct relevance to the flowfield calculation or the soot model are shown for clarity.

As will be shown in section 4.3.6, the adiabatic assumption greatly over-estimates mean temperatures, whilst for the radiatively cooled case substantial agreement is observed with experiment. The latter does, however, underpredict the temperature at the lower height - this is in keeping with the assumption that radiative loss is important, since lower down there are lower levels of soot and smaller flamelet path lengths, resulting in an increase of radiative loss with height.

4.3.6 Flowfield prediction of the Kent and Honnery (1987) flame

This section describes the prediction of the flame referred to as **flame A** by Kent and Honnery (1987), which results from ethylene emitted vertically from a 3mm diameter port, at a mass averaged velocity of 52m/s and temperature of 322K, into a stagnant air environment. The experimental data consist of axial and radial mean temperature profiles, measured by thermocouple and corrected for radiative loss, and radial mean soot volume fraction profiles. The

latter were measured by laser absorption with subsequent deconvolution to obtain point values from the integral line of sight measurements. The axial location for the radial plots are 13.8cm (x/D=46, x/Xm=0.4), 24.2cm (x/D=80.5, x/Xm=0.7), 34.5cm (x/D=115, x/Xm=1.0) and 48.3cm (x/D=161, x/Xm=1.4) above the burner; x is the height above the burner, D is the burner diameter and Xm is the height at which the maximum laser absorption occurred along a diameter.

The adopted parabolic formulation of the governing equations requires the boundary conditions at the burner exit (initial conditions) and at the free stream interface. The remaining boundary is along the axis of the burner and is simply treated as a symmetric boundary ie. zero flux and zero gradient. The values of all dependent variables ($\tilde{u}$, k, ε, $\tilde{\xi}$, $\widetilde{\xi''^2}$, $\tilde{\phi}_n$ and $\tilde{\phi}_m$) are set to zero in the free stream. The initial profile for velocity is given by the 1/7th power law, representative of fully developed pipe flow, which leads to a centre line velocity of 63m/s to achieve the required mass averaged velocity of 52m/s. The initial values of k are obtained from the local velocity assuming a constant turbulence intensity cf.

$$\tilde{k} = 0.003\ \tilde{u}^2 \qquad .. (4.43)$$

The turbulent dissipation is then obtained by relating the integral length scale to the burner radius, R, cf.

$$\tilde{\varepsilon} = \tilde{k}^{3/2} / R \qquad ... (4.44)$$

Altering the initial turbulence parameters by an order of magnitude was seen to have effect on only the near burner region.

A uniform initial $\tilde{\xi}$ profiles was specified, of value one, indicating neat fuel. The initial profiles of $\widetilde{\xi''^2}$, $\tilde{\phi}_n$ and $\tilde{\phi}_m$ were set to zero.

The computational grid consists of 40 cross stream nodes which were sufficient to ensure the solution to be grid independent. The forward step size was limited to a maximum of 1% of the radius of the jet.

The remainder of this section discusses the flowfield predictions, where results are presented for both adiabatic and non-adiabatic conditions. The latter utilises the experimental temperature flamelet of Moss et al (1988). For comparison, predictions assuming an intermittent beta function form for $P(\xi)$ are presented for the non-adiabatic case. This is used to determine the effect of an alternative PDF form on the later reported soot volume fraction predictions.

The radiatively cooled flamelet was obtained from the experiments of Moss et al (1988). Their data extended over the range $0.02<\xi<0.3$ and the experimental conditions were such that the air stream ($\xi=0$) was at a temperature of 700K. The flamelet adopted here was therefore extrapolated to $\xi=1$ on the rich side and was perturbed on the lean side to yield 300K at $\xi=0$ in keeping with the turbulent flame experimental conditions. The rich side extrapolation has little significance, since it is far removed from the reaction zone; that on the lean side, however, is more sensitive.

Figure 4.2 shows the experimental flamelet and its extrapolation to 322K at $\xi=1$, which is shown as a dashed line. Also shown is the computed adiabatic flamelet (cf. fig. 4.1) and for comparison the adiabatic equilibrium obtained using the code of Gordon and McBride (1971). As mixture fraction reduces from stoichiometric towards zero, the experimental and adiabatic flamelets tend to converge, and coalesce at $\xi\approx0.05$. Subsequently at $\xi\approx0.025$, the former flamelet diverts towards 700K at $\xi=0$. The cooled flamelet used in the present analysis deviates from the Moss et al (1988) data at this point and follows the calculated adiabatic flamelet down to 300K at $\xi=0$.

The adiabatic equilibrium in comparison with the adiabatic flamelet, shows the expected higher stoichiometric temperature and the relatively sharp gradient at $0.08<\xi<0.2$. These features indicate the neglect of diffusive effects which tend to reduce the peak temperature and prevent sharp gradient changes. Comparing the experimental and

adiabatic flamelets shows a reduction of ~180K in peak temperature and, more importantly, a 600K difference at ξ=0.1. This facet of the experimental data is accommodated by a steep temperature gradient between the stoichiometric mixture fraction (ξ=0.064) and ξ=0.1, where a sharp change brings the slope more in line with the calculated flamelet. These experimental trends are somewhat questionable especially in the light of their being obtained by thermocouple measurements in high soot loading conditions. The only way in which such results seem plausible is if the radiative loss from the soot is so strong that it results in a local enthalpy drop that is too substantial for diffusive processes to redistribute.

Given the large difference between the adiabatic and experimental flamelets in the sooting region ($0.064<\xi<\sim0.2$), the inferred soot formation rate for an adiabatic case will be far in excess of that in the laminar flame experiment of Moss et al (1988). Furthermore, if the temperature flamelet was simply scaled to bring its maximum value down to that observed in the experiment, there would still be 400K difference at ξ=0.1. This presents a problem in that either the experimental data is erroneous, and hence so is the calculated formation rate of Moss et al (1988), or, a simple perturbation of the adiabatic results, due to high local soot radiation, is not appropriate. In the non-adiabatic predictions reported later, the experimental data was used to prescribe the temperature state relationship in order to avoid this issue.

Figure 4.3 shows the axial variation of Reynolds mean and rms temperatures, predicted using the adiabatic and non-adiabatic flamelets, and figure 4.4 shows the corresponding radial profiles at the earlier mentioned heights. The predictions are compared to experimental mean temperatures, which are thought to be nearer Reynolds quantities than Favre quantities. For the non-adiabatic case two sets of predictions are presented, resulting from a beta function and intermittent beta function form for $P(\xi)$.

The adiabatic predictions show the mean centre line temperatures to be over-estimated from a fairly early height and lead to a maximum discrepancy of 400K, when compared with the experiment. The flame height, given by the maximum centre line mean temperature, however, shows good agreement with the data. The adiabatic predictions are more in line with the experimental data at heights below ~7cm. This is as would be expected if radiative loss was the cause of the overprediction, since at low heights where soot levels are low, losses would also be low. These are expected to increase with height as soot levels increase, and subsequently reduce as the soot is oxidized and mixing reduces temperatures in the upper reaches of the flame. This would imply that the adiabatic predictions should converge with the data as the flame tip is reached, which is not evident in figure 4.3. This is discussed shortly.

Figure 4.4 shows the non-adiabatic predictions to show better agreement with experiment. Maximum temperatures, however, are underpredicted at the lowest height, probably owing to too high an inherent heat loss, and over-predicted at the highest height. This trend is also evident in the axial plot (cf. fig. 4.3) where, at ~40 cm, the predictions start to deviate and show convergence towards the adiabatic results, as must happen given that the two flamelets converge (cf. above).

Figures 4.3 and 4.4 show the influence of assuming an intermittent beta function $P(\xi)$ is limited to the extremities of the jet and, up to 70cm, shows no significant difference at the centre line. This is because the intermittent beta function deviates from the beta function only when a singularity occurs at $\xi=0$. The trend of the intermittent beta function to produce higher temperatures (cf. fig. 4.4), results from the way in which it treats the singularity resulting from intermittency with the air stream. In this formulation, the beta function is forced down to zero as $\xi \rightarrow 0$, resulting in a greater probability of attaining near stoichiometric temperatures. This is illustrated in the later-reported figure 4.13, which shows a comparison between the beta function, the intermittent beta function

and the clipped Gaussian PDF's for various radial locations at the 13.8 cm height in the Kent and Honnery flame.

The over-prediction of temperatures high up in the flame, as mentioned earlier, seems anomalous since one would expect radiative loss to reduce as soot levels reduce, and to expect adiabatic conditions to become more appropriate. This suggests that mixing as predicted by the turbulence model may be a problem. A glance at the literature reveals that of particular concern is the setting of C_{g2} in the source of $\widetilde{\xi''^2}$ (cf. eqn. 4.28), which is seen to vary between 2.0 (cf. Spalding (1971b)) and 1.25 (cf. Gibson and Launder (1976)). Implementing these values in place of the adopted 1.89, shows that setting C_{g2}=2.0 has no noticeable effect whilst setting C_{g2}=1.25, with its implied greater fluctuation levels, leads to lower peak temperatures and even greater deviation at higher heights, where the increased spread of $P(\xi)$ increases the probability of sampling from hotter mixtures. A sensitivity study showed the most significant parameter to influence the mean temperatures to be the lean side temperature flamelet, which was prescribed in a rather ad hoc manner. Reducing the lean temperatures also had the effect of reducing the spread of mean temperature, which is seen to be over-predicted cf. figure 4.4. Also to be noted, is the rapid reduction of temperatures in the experimental flamelet as ξ increases towards 0.1, since it biases high temperatures to lower mixtures compared to the adiabatic flamelet.

Of more fundamental concern is the applicability of the turbulence model to the whole of the jet flame. Flow visualisation of high Reynolds number jet flames (cf. Roquemore et al (1989)) shows the flowfield to consist of small eddies resulting from the shearing of the fuel stream which is surrounded by a flame brush and finally large scale structures. For the most part of the jet the small scale fuel jet structures control the mixing process. Higher up, however, these eddies decay and subsequent entrainment of air is governed by the large scale structures which are capable of entraining large amounts of air. It is the latter that, if important, will reveal deficiencies

in the turbulence model which, by its initial boundary condition, has been set up to describe the small scale structures.

It is difficult to shed further light on the temperature anomaly in the absence of mixture fraction measurements. However, problems have been traced to lean temperatures, while at richer mixtures, where soot formation occurs, temperatures are reasonably predicted. There are, however implications for the soot oxidation rate.

The adiabatic and non-adiabatic predictions yield broadly similar rms temperatures. Figure 4.3 shows there to be two peaks for the adiabatic case. The first (at x≈4cm) results from the intermittency between the fuel stream and leaner, therefore hotter, mixtures. The second (at x≈62cm) is the major peak and results from the intermittency between the air stream and richer, near stoichiometric mixtures. The non-adiabatic predictions show both these peaks, where the former is approximately half the magnitude of its adiabatic counterpart. In addition, an intermediate peak is indicated. This results from the steep gradient between $0.064<\xi<0.1$ in the non-adiabatic temperature flamelet. Unfortunately, there is no experimental rms temperature data for comparison, which might have indicated whether the facets of the experimentally derived non-adiabatic flamelet are representative of sooting flames.

Figures 4.5 to 4.8 complete the flowfield picture, showing axial and radial variations of mean and rms velocity and mixture fraction. The non-adiabatic results include those derived from both PDF forms, and as evident from the centre line temperatures (cf. fig. 4.3), no discrepancy is observed for either the velocities or mixture fraction. Figure 4.5 and 4.6 shows the adiabatic velocities to be higher, which results from the greater volume change signified by the higher temperatures. Though buoyancy is also greater, its influence is negligible given the high velocities. Figures 4.7 and 4.8 show higher mixture fraction values for the adiabatic case for the same reason. The rms velocities (cf. fig. 4.5) show the expected turbulence decay in the potential core, before shear forces work their way to the

centre line and cause turbulence levels to increase. The maximum occurs at a height of ~4cm, above which mean velocity gradients reduce, resulting in a net turbulence decay.

This section presented the flowfield predictions of the Kent and Honnery (1987) flame which were tested against their mean temperature measurements. Temperatures are substantially over-estimated by the adiabatic calculation, but adequate agreement was obtained by adopting a cooled flamelet which was based on the experiments of Moss et al (1988). Though there is cause for concern in lean temperatures which are over-predicted, these uncertainties are restricted to regions remote from the soot formation zone. Soot oxidation, however, will be influenced.

4.3.7 Soot prediction in the Kent and Honnery (1987) flame

The essence of the proposed soot modelling approach is the conserved scalar based closure of the source terms in the soot concentration balance equations. As described in section 4.2, these may be expressed in terms of mixture fraction dependent parameters and soot parameters. The former group is represented by $\alpha(\xi)$, $\beta(\xi)$ and $\gamma(\xi)$, which appear in the nucleation, coagulation and surface growth terms, respectively (cf. eqns 4.11 to 4.13), and are defined in terms of density (ρ), temperature (T) and parent fuel concentration (X_c). Section 4.3.5 described the numerical prediction of an adiabatic ethylene - air diffusion flame from which $\rho(\xi)$, $T(\xi)$ and $X_c(\xi)$, and hence $\alpha(\xi)$, $\beta(\xi)$ and $\gamma(\xi)$, are obtained. As described in the previous section, however, the Kent and Honnery flame is not adiabatic and the experimentally determined temperature flamelet of Moss et al (1988) was used to describe the temperature field. The additional flamelet relationships were then obtained by assuming the heatloss did not affect the species concentrations, therefore allowing the computed concentrations (section 4.3.5) to be used.

Figure 4.9 shows the flamelet relationships $\alpha(\xi)$ and $\gamma(\xi)$. Also shown is $\varepsilon(\xi)$ which appears in the oxidation terms (cf. eqns 4.16 and 4.17) and is a function of O_2 concentration and temperature. For clarity $\beta(\xi)$ is not shown since it varies simply as the square root of temperature. The soot models empirical parameters, C_α, C_β, C_γ, T_α and T_γ, required to complete the formulation of α,β and γ, are obtained from Moss et al (1988) and are shown in table 4.2. Figure 4.9 shows two sets of flamelets for both the adiabatic and non-adiabatic conditions. Confining attention to the non-adiabatic flamelets shows α to be limited to a very narrow region, $0.064(\xi_{st})<\xi<0.1$. On the lean side, as is the case for γ, it is forced to zero at stoichiometric due to the disappearance of X_c, whilst on the rich side, it is rapidly reduced due to the steep temperature gradient and its high activation temperature (T_α=46.1x10^3K) - the higher the activation temperature the stronger the dependence on temperature. γ also begins to fall sharply as mixture fraction increases to 0.1. Above this value γ is observed to increase to a second maximum before it starts to fall. This facet reflects the sharp change in gradient of $T(\xi)$ and the competing effects of temperature and fuel concentration; the former reduces as mixture fraction increases, whilst the latter increases. In comparison with α, γ is broader given its lower activation temperature (T_γ). The adiabatic profiles for α and γ are significantly broader, resulting from the relatively shallow gradient of $T(\xi)$ and illustrates the importance of obtaining realistic temperatures. Of more importance, however, are the maximum values - α and γ are greater by factors of 24 and 10, respectively, for the adiabatic case. The later reported soot predictions show the non-adiabatic parameters to produce good agreement with experimental soot levels, whilst adiabatic soot levels are significant over-predictions. The latter are therefore not presented and all results discussed in the remainder of this section are non-adiabatic predictions.

The oxidation term, ε, is confined to lean mixtures since it is dependent on O_2 concentration. The difference between the adiabatic and non-adiabatic profiles is negligible. This arises from the temperatures being identical below ξ=0.05 (cf. fig 4.2) whilst above

this value, oxygen depletion dominates over temperature effects. The later reported soot predictions show oxidation to be very large. This is also evident from comparing the oxidation rate with the surface growth rate; the latter dominates nucleation in the rate of growth of soot mass. Given the simplified γn formulation of surface growth, which implies γ to be proportional to the surface growth per particle, this comparison is not straightforward. However, this may be translated into growth per unit surface area, analogous to the oxidation term, by assuming an effective particle diameter, d. When d=10nm surface growth is found to be three orders of magnitude smaller than oxidation.

Figure 4.10 shows radial profiles of predicted and experimental soot volume fraction. Three sets of predictions are presented which give an indication of the uncertainty arising from soot source term closure. The solid line, identified as **prediction 1** (cf. fig. 4.10) assumes the closure indicated in equations 4.11 and 4.13, where the mixture fraction and the soot parameters, n and m ,are presumed uncorrelated. However, if mixture fraction and ϕ_n and ϕ_m are assumed uncorrelated and, as before, higher order terms involving fluctuating soot concentration are ignored, the mean source terms are given by

$$\overline{S_n} = \bar{\alpha} - \overline{\rho^2\beta}\ \tilde{\phi}_n \qquad \ldots (4.45)$$

and

$$\overline{S_m} = N_0\ \bar{\rho}\ \tilde{\gamma}\ \tilde{\phi}_n + C_\delta \bar{\alpha} \qquad \ldots (4.46)$$

Soot volume fraction predictions using equations 4.45 and 4.46 to represent the mean source terms are shown as **prediction 2** in figure 4.10.

Prediction 3 (cf. fig. 4.10) results from a simplification which allows full closure of the source of soot mass concentration. If the soot number density formation rate is integrated, assuming plug flow, then the number density may be expressed in terms of α, β and residence time (cf. eqn. 3.9). This rapidly saturates (ie. the rate of

particle nucleation is in balance with coagulation) to its maximum value, where

$$n/N_0 = \sqrt{\alpha / \beta} \qquad \ldots (4.47)$$

The mean rate of soot mass concentration formation may then be expressed solely in terms of mixture fraction dependent parameters, cf.

$$\overline{S_m} = \overline{N_0 \gamma (\alpha/\beta)^{1/2} + C_\delta \alpha} \qquad \ldots (4.48)$$

where the right hand side can be closed exactly using equation 4.1.

Figure 4.10 shows there to be little difference between the above closure assumptions, with all three predictions showing approximately the same rate of growth with height and major features. **Predictions 1** and **2** (cf. fig. 4.10) show little difference. **Prediction 3**, however, differs in that it over-predicts in lean mixtures and under-predicts in rich regions. This stems from the soot number density implied in the source of soot mass concentration. In **predictions 1** and **2**, the source of soot number density becomes negative in lean mixtures, where the nucleation term is very small but the coagulation term remains high. In **prediction 3**, the source term cannot become negative given the plug flow assumption and is zero throughout.

The predictions of soot volume fraction, when compared with the experimental data, show fairly good agreement in centre line and maximum values at the first three heights (cf. fig. 4.10). The rate of growth with height is, however, underestimated, in that peak levels are over-predicted at the lowest height, approximately right at the second height and slightly underpredicted at the third height. This may be due to the evaluation of the source term itself, since Moss et al (1988) also observed this trend in their laminar flame. Despite the relatively good agreement in the rich regions of the flame, the leaner soot volume fractions seem to be substantially overestimated. This is

depicted as an over-prediction in spread, and at the uppermost height soot levels are overestimated at all radial locations.

The over-prediction in the spread of the soot profiles may be due to either soot source term closure approximations, inadequate prediction of the flowfield, incorrect specification of the source term in mixture fraction space (it may be located at too lean a mixture) or soot oxidation. The former does not seem plausible given that the three predicted curves, for which different closure assumptions are made, do not alter significantly in spread (cf. fig. 10). The temperature field (cf. figure 4.4) is indeed over-predicted; however, a comparison between predicted soot profiles (cf. fig 4.10) and predicted temperature profiles show there to be little difference in spread. The experimental data, on the other hand, do show the soot profiles to be narrower than the temperature data.

The source term in mixture fraction space is of concern, because the rapid reduction in temperature on the rich side of stoichiometric (indicated by the data of Moss et al (1988)) confines the source term to leaner values than the computed adiabatic temperature flamelet (cf. fig. 4.9). Adiabatic soot predictions, however, still suggest an exaggeration in spread.

Soot oxidation, if soot transport is highly correlated with that of mixture fraction, will not occur, since soot will always instantaneously appear at the rich mixtures where it is formed. Under these circumstances, oxidation may only take place in the extremities of the flame, where mixing has dissipated rich regions. Elsewhere, soot oxidation must rely on differential transport which allows soot to migrate to leaner regions. Oxidation is the subject of further discussion later in this section.

The remainder of the discussion of the soot predictions focuses on only those resulting from the closure assumptions indicated in equations 4.11, 4.13 4.21 and 4.22.

The $P(\xi)$ necessary to close the mixture fraction dependent parts of the soot source terms is of an assumed form, which is described by its first two moments. Such two parameter PDF's have been widely used to describe mixture fraction statistics, since they are substantially more economical than computing the evolution of $P(\xi)$ and have met with success in predicting mean temperatures and the major gaseous species (cf. Liew (1983)). Their performance over relatively narrow regions of mixture fraction, which is of interest here (cf. fig. 4.9), however, has not been demonstrated. In order to gain some appreciation of the uncertainties in mean soot formation rate, resulting from the prescription of $P(\xi)$, calculations have been performed assuming an intermittent beta function form for $P(\xi)$, in addition to the adopted beta function.

Figures 4.11 and 4.12 show radial profiles of the soot source term parameters, α and γ, obtained through the beta function and intermittent beta function formulations. In general, α is located in leaner regions compared to γ, as is expected, given their state relationships (cf. fig. 4.9). The most significant effect of the alternative PDF is seen at the lowest height at a radial distance of approximately 2cm, where α and, to a lesser extent γ, are increased. This trend can be deduced from figure 4.13 which shows $P(\xi)$, assuming the beta function, the intermittent beta function and, for comparison, the clipped Gaussian forms, at different radial locations at the 13.8cm height. There is seen to be no difference between the beta function and intermittent beta function $P(\xi)$ within a radius of ~2cm. Beyond this, the beta function exhibits a singularity at $\xi=0$, depicting intermittent behaviour with the oxidant stream. The intermittent beta function, on the other hand, is forced down to zero at $\xi=0$ and intermittency is described by a delta function at $\xi=0$. This allows a greater probability of attaining mixtures at which α and γ are prevalent, in the intermittent beta function formulation (cf. fig. 4.13), which results in the larger values of α and γ, evident in figures 4.11 and 4.12. The effect on α is more pronounced since the two PDF forms differ most at lean values and where γ is most significant (cf. fig. 4.9), the PDF's are substantially similar (cf.

fig. 4.13). This suggests that soot oxidation, which is limited to $0.02<\xi<0.064$, will be most sensitive to the PDF form. Figure 4.14 shows radial profiles of ε where this is confirmed. The maximum deviation, which occurs at the 13.8cm height, however, is limited to a factor of 1.3 which is insignificant, as will be shown later.

Figure 4.13 also shows PDF's that assume a clipped Gaussian formulation, which is presented since it is widely used (cf. Lockwood and Naguib (1975)). At rich mixture there is seen to be limited deviation from the beta function forms, whilst at leaner values, since it is not forced down to zero at $\xi=0$ (cf. intermittent beta function) its deviation from the beta function, in the region of interest ($0.02<\xi<.35$), is not as great as the intermittent beta function. The latter form is therefore thought to represent the most extreme deviation from the beta function.

The effect of the PDF form on the soot volume fraction, via the soot source term parameters (cf. figs. 4.11 and 4.12), is shown in figure 4.15. The largest deviation is observed at the lowest height, where the peak value is overestimated by 27%. Thereafter, the two formulations converge until there is no discernible difference at the uppermost height. The reason for the intermittent beta function soot volume fractions reducing, relative to the beta function values, at heights above 13.8cm, results from the rich side behaviour of the two PDF's, where the latter leads to greater probabilities of attaining mixtures beyond the intermittent beta function dominating region. This is evident in figure 4.11, 4.12 and 4.14 where all parameters show the beta function to yield greater values when the mean mixture fraction approaches zero, having passed the intermittent beta function dominating regime.

The discussion to date has centred on predictions where only soot formation is considered; however, this represents an incomplete description of soot and the experimental data indicate the importance of soot burnout. Figure 4.16 shows profiles of mean soot volume fraction where three predictions, of which one neglects oxidation and

two consider it (by including equation 4.21 and 4.22 in the soot source terms) are compared with experimental data. The instantaneous oxidation rate is described by the parameter, ε, which is defined in equation 4.17 and the mean profiles of which are shown in figure 4.14. When this oxidation rate is applied, indicated as **oxidation x 1** (cf. fig. 4.16), soot concentrations are seen to fall at too great a rate. The implied excessive oxidation may result from **(i)** the Nagle and Strickland-Constable (1962) oxidation rate (cf. eqn. 2.36) being too great, **(ii)** the soot surface area available for oxidation being too high, **(iii)** incorrect effective oxidation rate resulting from errors in the temperature flamelet and **(iv)** the significance of oxidation term correlations which have been neglected. The former must, at this stage, remain an unresolved issue, since the adopted oxidation mechanism has not been suitably validated. For example, it has not been demonstrated that O_2 is the most significant oxidizer in most diffusion flames or that the Nagle and Strickland-Constable (1962) rate, which was derived in experiments involving diminution of carbon rods through O_2 attack, is representative of combustion zones. A detailed study of soot oxidation is beyond the scope of the present contribution and is the focus of continuing work at Cranfield.

The second possibility arises since the particle number density which is required to infer the soot surface area, has not been measured and has been treated as a free parameter whose value is broadly fixed according to experimental evidence (cf. Haynes and Wagner (1981)). Any errors in n do not affect soot surface growth given its empirical derivation. An order of magnitude change in soot number density results in a factor of 3 change in soot surface area.

There is some uncertainty in lean temperatures of the adopted flamelet. The experimental conditions of Moss et al (1988) yielded an air stream temperature of 700K, which was therefore perturbed to extrapolate down to 300K at ξ=0 (cf. fig. 4.2). This was the condition in the Kent and Honnery (1987) experiment.

The neglect of soot-mixture fraction correlation in terms of soot burnout is potentially a serious deficiency given that this may be a highly intermittent process. If soot particles are very small they are likely to have similar turbulent transport properties as gaseous mixture fraction, in which case they will tend to remain instantaneously at the rich mixtures where they are formed. In this circumstance soot oxidation, which is confined to leaner mixtures, will not occur. However, oxidation must occur at some stage since eventually, small scale mixing will dissipate any rich pockets, forcing the soot into leaner regions.

It is likely that all of the above four suggestions contribute to the excessive oxidation rate. However, more may be learnt from the qualitative effect of the oxidation rate. Figure 4.16 also shows a prediction legend as **oxidation x 0.015**. This simply results from scaling the effective oxidation rate by a factor (here 0.015) which addresses the scenario that there is a systematic error, which **(i)** **(ii)** and **(iii)** above imply. The value of this factor has been set such that the centre line soot volume fraction at the uppermost height, is close to the experimental value. The radial profile of soot volume fraction at this height shows good agreement with the experimental data. At the lower heights, the spread of soot volume fraction is reduced to levels more in line with the data, however, oxidation is seen to reduce centreline values which is not apparent in the experimental results.

This latter facet of the predictions may be due to the neglect of soot mixture fraction correlations. Such information is not, however, accessible in the present formulation where only the PDF of mixture fraction is available. Here, in order to ascertain how such correlations may effect the eventual mean soot concentrations, a simple model has been devised. It is assumed that soot will, instantaneously, always remain in rich regions, where the particles are formed, unless such regions become scarce. Oxidation may then occur as the particles are forced into leaner regions. This condition has been based on $P(\xi)$ where the local probability of attaining rich

mixtures controls the oxidation. It is assumed that if the probability of attaining a mixture fraction greater than a critical value is below a set limit, oxidation may occur according to equations 4.21 and 4.22. Otherwise zero oxidation is enforced.

Figure 4.17 shows profiles of mean soot volume fraction where a prediction, resulting from such a conditioned oxidation mechanism, is compared with the experimental data and the non-oxidation prediction. The critical mixture fraction has been set to the stoichiometric value, ξ=0.064, and the probability cut-off, somewhat arbitrarily, has been set to 10%. The oxidation rate is quantitatively that given by Nagle and Strickland-Constable (1962) and has not been factored. The qualitative trend of the conditioned oxidation is consistent with the experimental data, in that the spread of the soot is reduced whilst the centreline values remain relatively unaffected. At the 48.3cm height, however, this condition persists, whilst the experimental data indicates that oxidation prevails across the whole width of the flame.

It is useful at this point to look at the axial variation of the mean soot volume fraction. This is shown in figure 4.18 where predictions resulting from the non-oxidation run, the two unconditional oxidation runs (with oxidation rate factors of 1 and 0.015) and the conditioned oxidation run, are compared with the experimental data. The experimental point at 34.5cm is at the location of the maximum centreline laser absorption and is therefore thought to represent the maximum value. In comparison with the unconditioned oxidation, the conditional predictions show a rapid decline in soot volume fraction when oxidation is allowed. This is also apparent in figure 4.17 where the radial profiles are very steep. This reflects the large oxidation rate which, when activated, rapidly reduces soot levels.

It is possible to obtain a better comparison by manipulating the oxidation rate factor and the oxidation conditioning. This, however, is not worthwhile since there are uncertainties in the oxidation mechanism and the proposed conditioning is very crude. Also in this case, given that there are no further experimental data, in particular

that of mixture fraction, it is not known whether the flame length is over-predicted. Figures 4.17 and 4.18, however, do suggest the importance of soot-mixture fraction correlations in soot oxidation though their importance in soot formation is limited.

4.4 Conclusions

The last two chapters have proposed, and sought to validate, a soot model for turbulent non-premixed combustion. It aims to address both the finite rate chemistry and turbulence interaction, by capitalizing on the dependence of key soot formation parameters on mixture fraction. The model therefore represents an extension to the conventional conserved scalar approach, in that balance equations are solved for soot concentration, the source terms of which are closed through the conserved scalar PDF approach.

These source terms, however, offer complications since they are not functions of mixture fraction alone but also of soot concentration. The correlations required to fully close such terms are inaccessible in the present formulation, and necessitate the joint PDF of soot concentration and mixture fraction. Here all source term correlations, other than those fully described by mixture fraction, have been neglected. This has been shown to be an acceptable simplification for soot formation, since little deviation results when adopting different source term closures, one of which is solely mixture fraction dependent and hence may be fully closed. Of greater concern are the mixture fraction dependent parameters and their dependence on, particularly, temperature.

The model, with the above simplifications, has been applied to a turbulent ethylene-air jet diffusion flame, where predictions of mean soot volume fraction show good agreement with experimentally observed magnitudes and rate of growth.

The neglect of soot oxidation, the detailed study of which is beyond the scope of the present work, has been seen to be a deficiency in the strategy. To counter this the oxidation mechanism of Nagle and Strickland-Constable (1962) has been included in the overall scheme. The issue of soot concentration-mixture fraction correlations has been shown to be of great importance here, owing to the typically strong negative correlation between soot particles and the, instantaneously leaner-located, oxidation region. At this stage it is not possible to address this process further since ideally more turbulent flame data are required. This should include information that adequately tests the flowfield prediction, for instance, mean and fluctuating velocities, temperature and mixture fraction in addition to soot concentration. Also required is information about the joint statistics of soot concentration and mixture fraction. The latter may validate the prediction of their joint PDF which is required properly to address soot oxidation.

ϕ	σ_ϕ	S_ϕ
$\tilde{u}$	1	$-d\bar{P}/dx - \bar{\rho}\, g$
k	1	$\mu_t (\partial\tilde{u}/\partial r)^2 - \bar{\rho}\varepsilon$
ε	1.3	$C_{\varepsilon 1}(\varepsilon/k)\mu_t(\partial\tilde{u}/\partial r)^2 - C_{\varepsilon 2}\bar{\rho}\varepsilon^2/k$
$\tilde{\xi}$	0.7	0
ξ''^2	0.7	$C_{g1}\mu_t(\partial\tilde{\xi}/\partial r)^2 - C_{g2}\bar{\rho}(\varepsilon/k)\xi''^2$
$\tilde{\phi}_N$	1	$\bar{\alpha} - \bar{\beta}\,\bar{\rho}\,\tilde{\phi}_N^2$
$\tilde{\phi}_m$	1	$N_0\,\bar{\gamma}\,\bar{\rho}\,\tilde{\phi}_N + \bar{\delta}$

$$C_{\varepsilon 1} = 1.4 - 3.4\left(\frac{k}{\varepsilon}\frac{d\tilde{u}}{dx}\right)_c^3 \qquad C_{\varepsilon 2} = 1.92 \qquad C_{g1} = 2.8 \qquad C_{g2} = 1.89$$

Table 4.1

C_α	$(m^3 kg^{-2} K^{-1/2} s^{-1})$	1.7×10^8
C_β	$(m^3 K^{-1/2} s^{-1})$	1.0×10^9
C_γ	$(m^3 K^{-1/2} s^{-1})$	4.2×10^{-17}
C_δ	(kg)	144.0
T_α	(K)	46.1×10^3
T_γ	(K)	12.6×10^3

Table 4.2

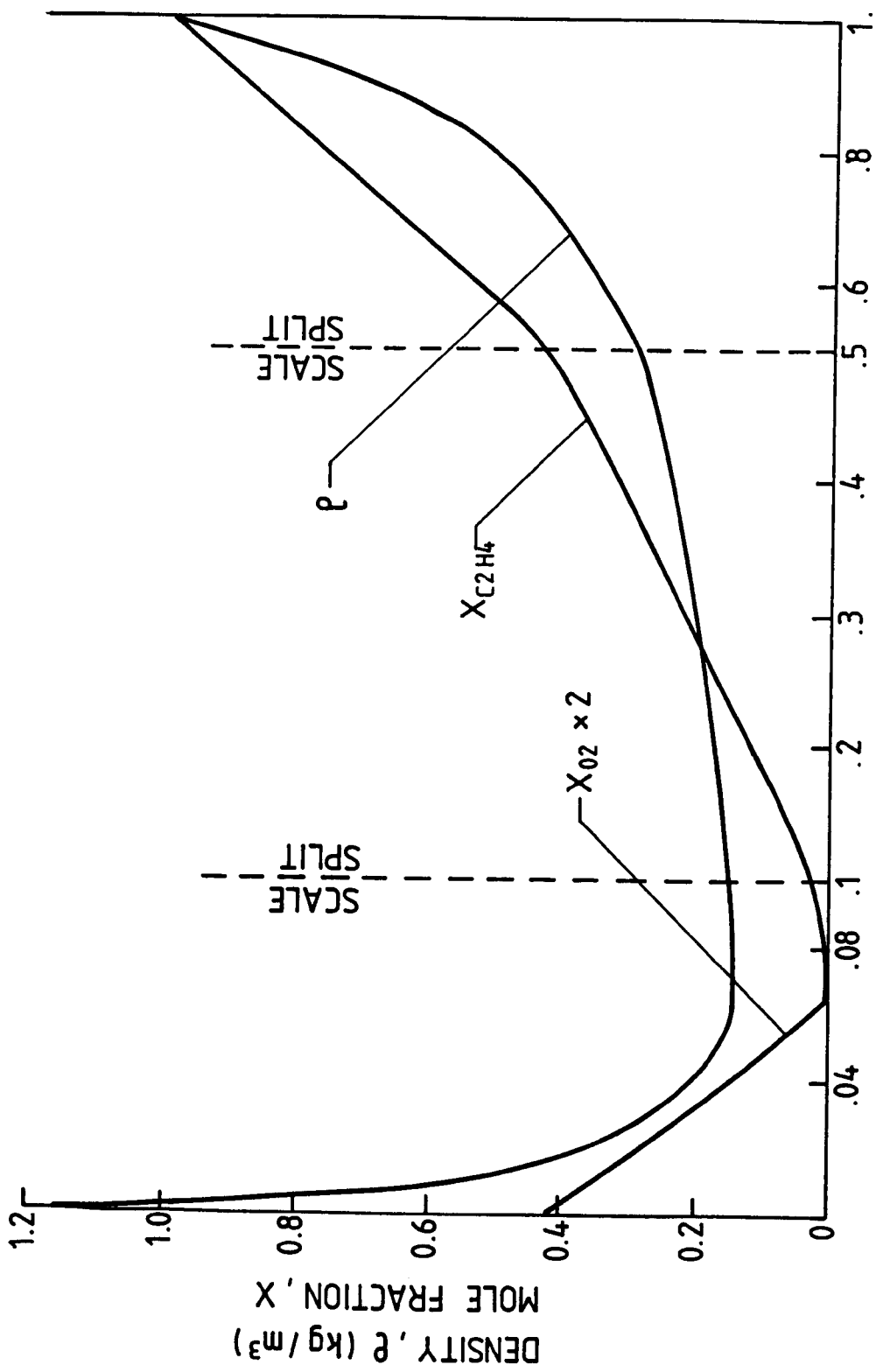

Figure 4.1 - Flamelet state relationships for ethylene-air (adiabatic computation)

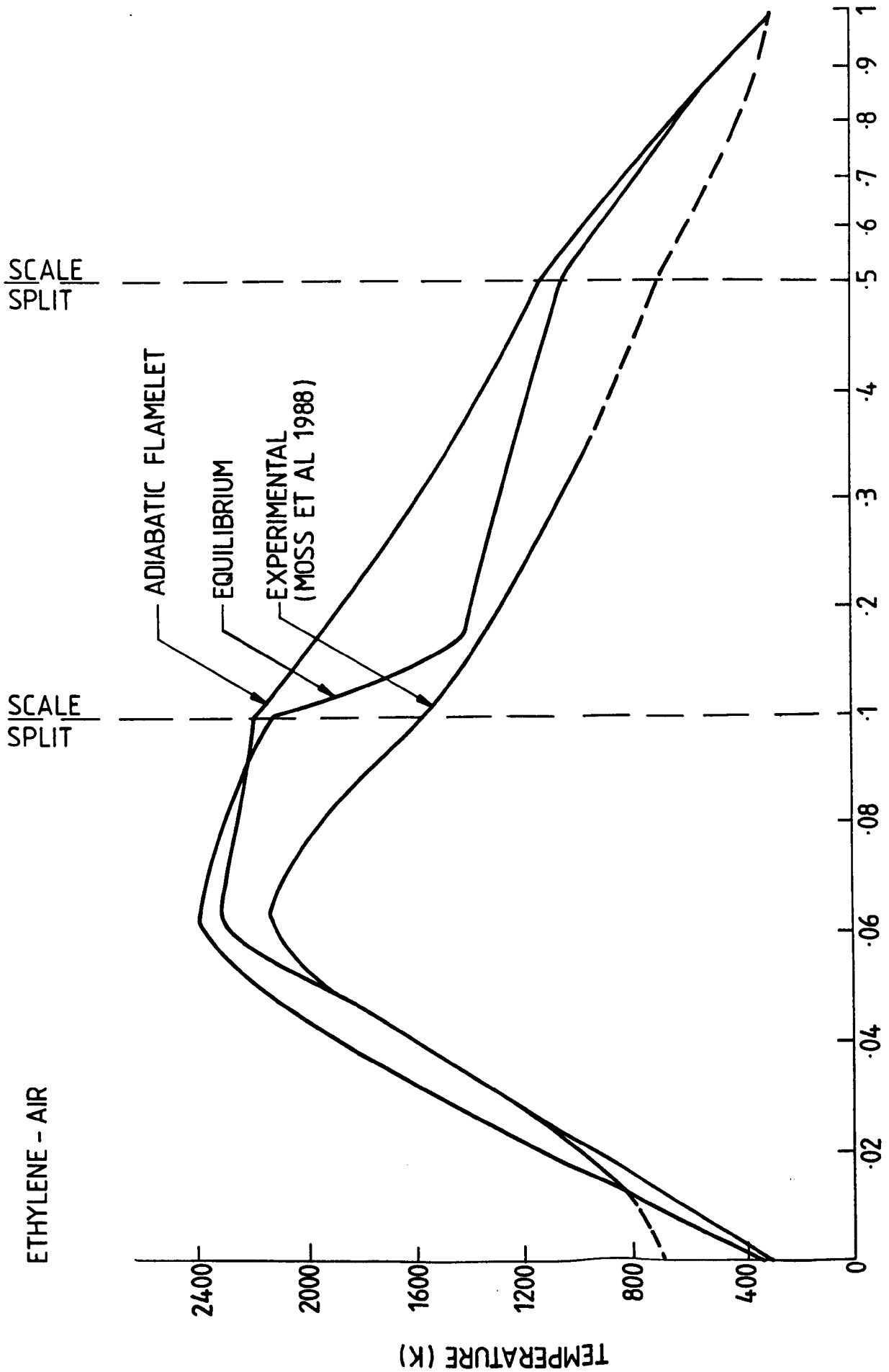
ETHYLENE - AIR
TEMPERATURE (K)
2400
2000
1600
1200
800
400
0
·02
·04
·06
·08
·1
·2
·3
·4
·5
·6
·7
·8
·9
1
MIXTURE FRACTION
SCALE SPLIT
SCALE SPLIT
ADIABATIC FLAMELET
EQUILIBRIUM
EXPERIMENTAL (MOSS ET AL 1988)

Figure 4.2

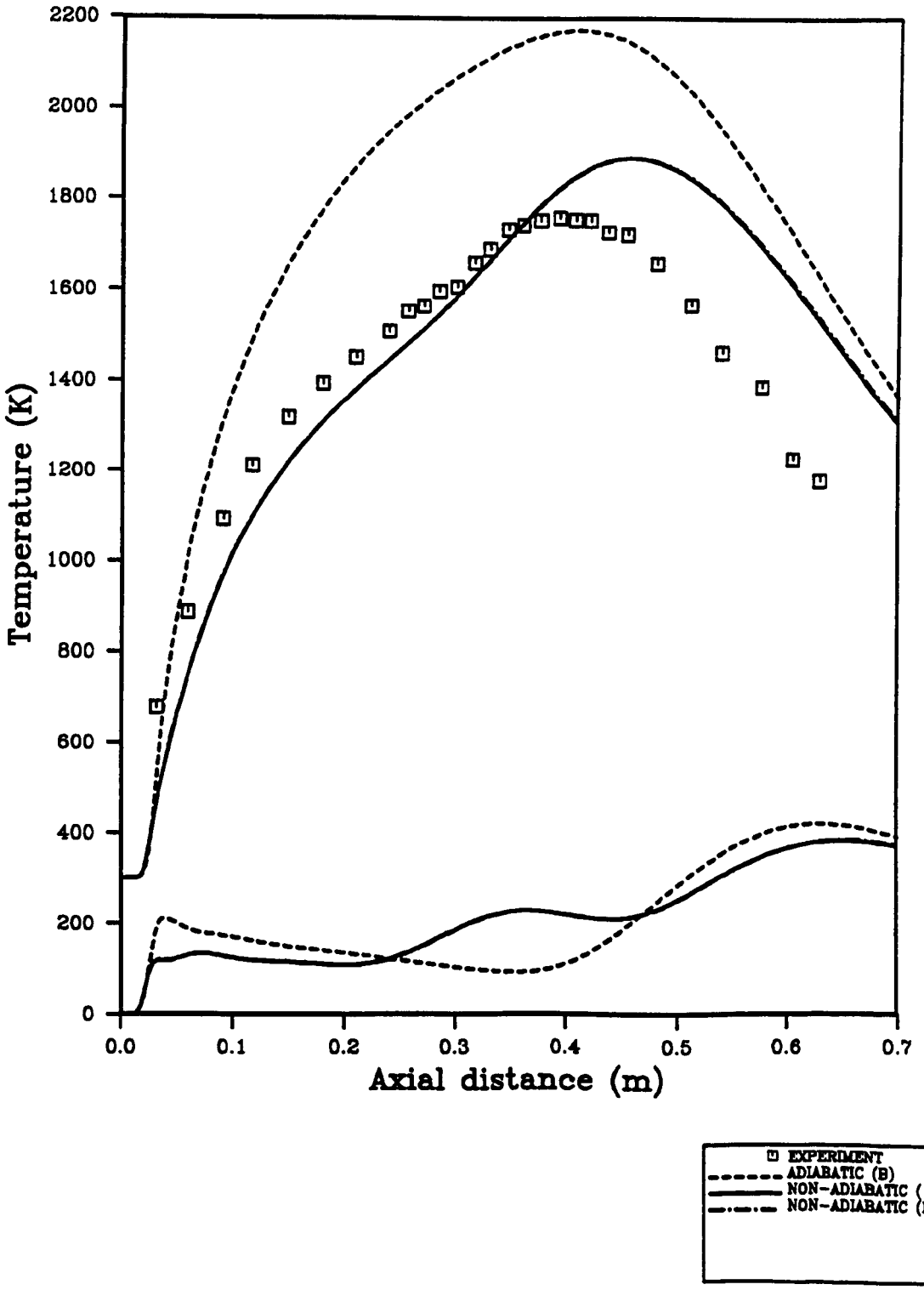

Axial variation of temperature
Predictions : (B) indicates beta function P(ξ) and (IB) indicates intermittent beta function P(ξ). Comparison with experimental data of Kent and Honnery (1987).

Figure 4.3

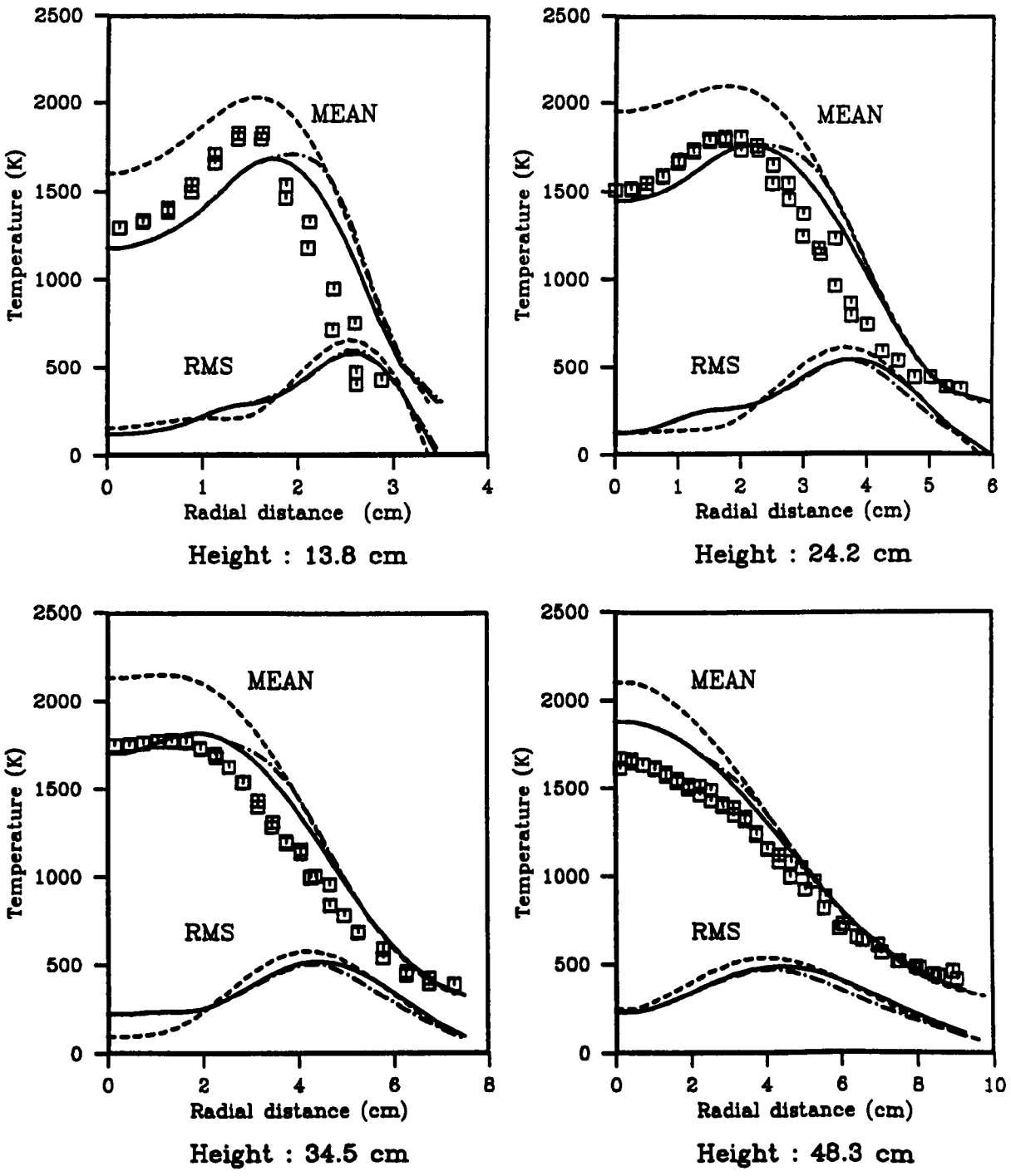

Radial profiles of Reynolds mean and rms temperature. Predictions : (B) and (IB) indicate beta and intermittent beta function form for $P(\xi)$ respectively. Comparison with data of Kent and Honnery (1987).

Figure 4.4

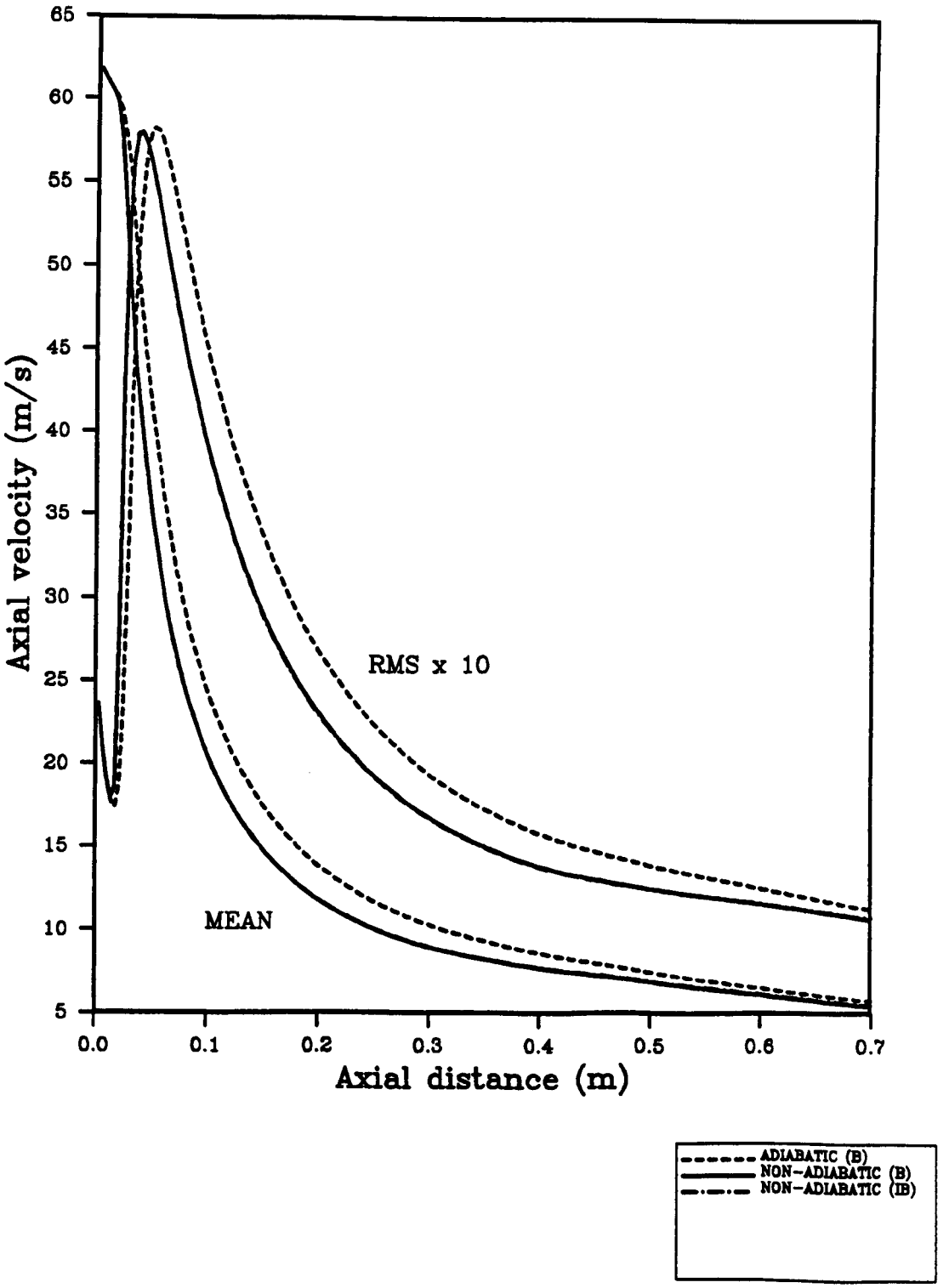

Axial variation of Favre mean and rms axial velocity. Prediction of Kent and Honnery (1987) flame. (B) indicates beta function P(ξ) and (IB) indicates intermittent beta function P(ξ).

Figure 4.5

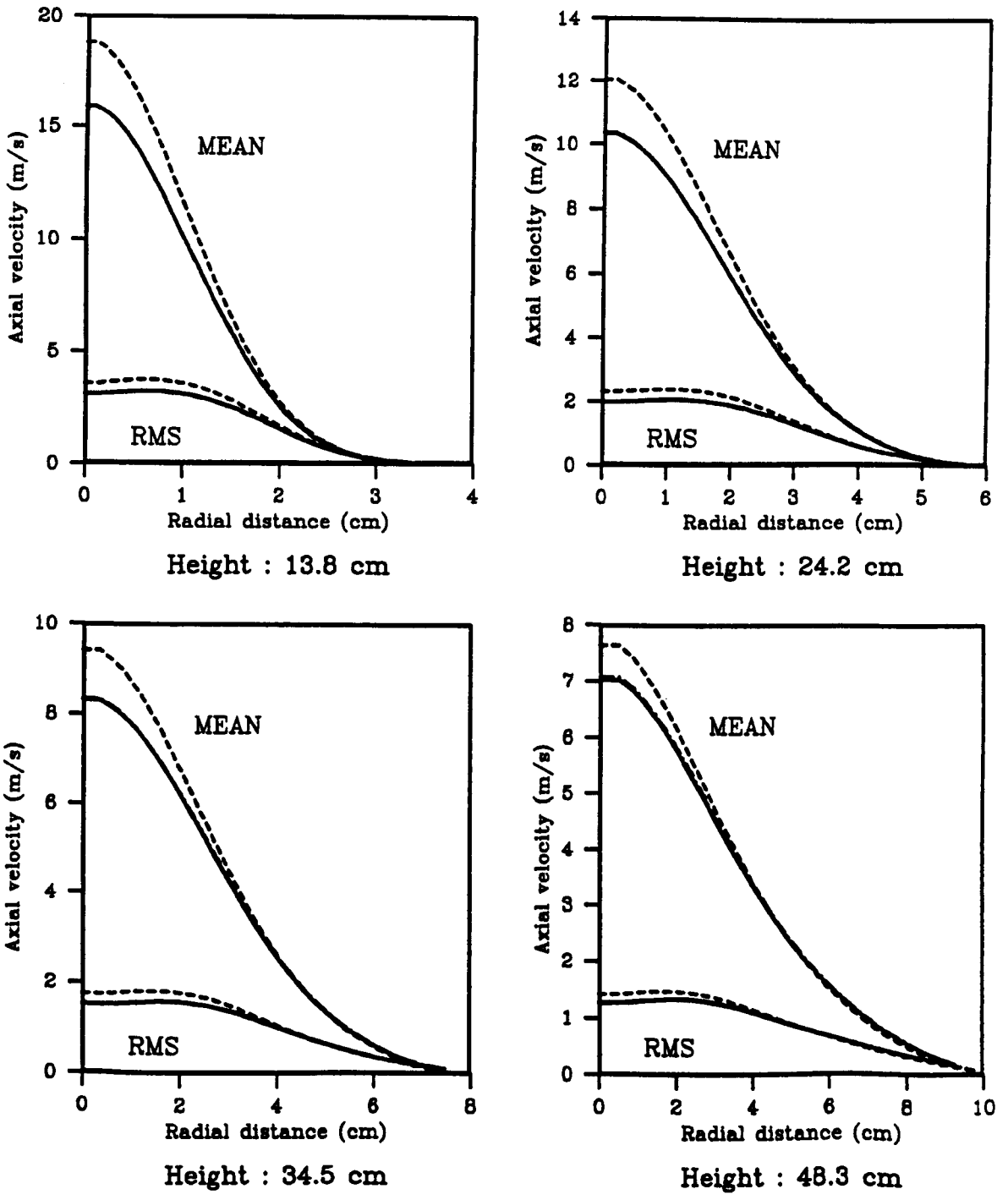

Radial profiles of Favre mean and rms axial velocity. Prediction of Kent and Honnery (1987) flame. (B) indicates beta function P(ξ) and (IB) indicates intermittent beta function P(ξ).

Figure 4.6

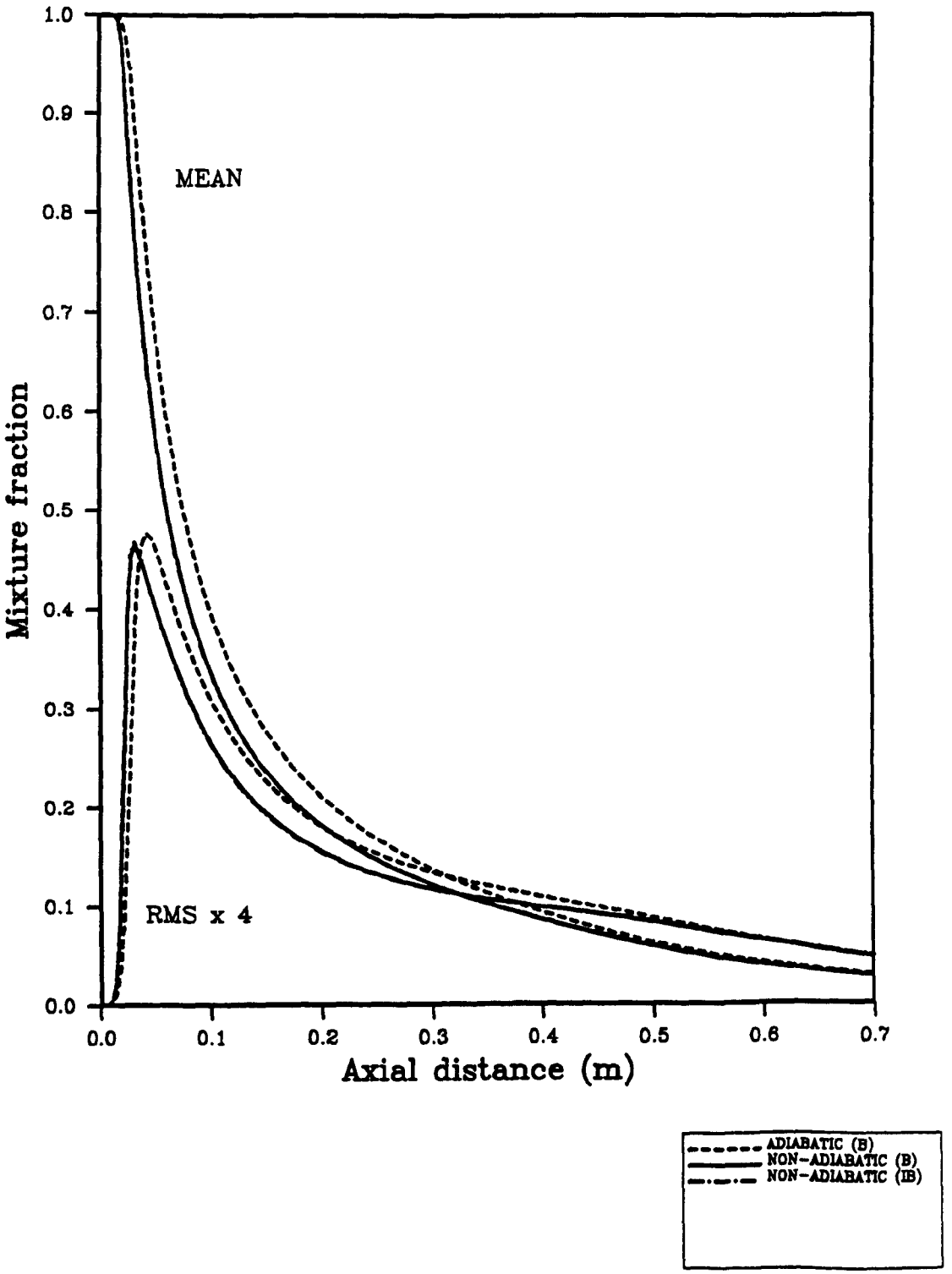

Axial variation of Favre mean and rms mixture fraction. Prediction of Kent and Honnery (1987) flame. (B) indicates beta function P(ξ) and (IB) indicates intermittent beta function P(ξ).

Figure 4.7

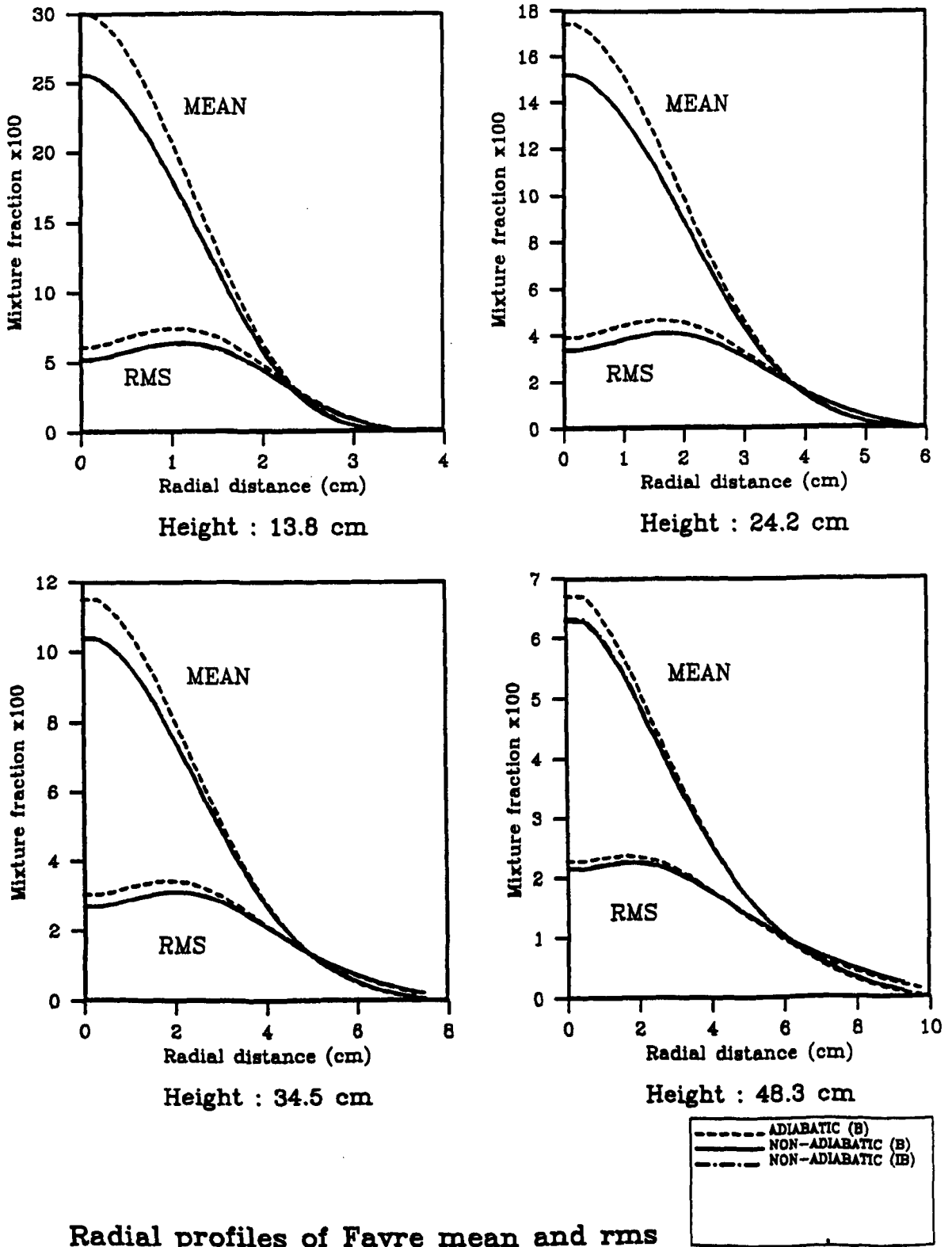

Radial profiles of Favre mean and rms mixture fraction. Prediction of Kent and Honnery (1987) flame. (B) indicates beta function P(ξ) and (IB) indicates intermittent beta function P(ξ).

Figure 4.8

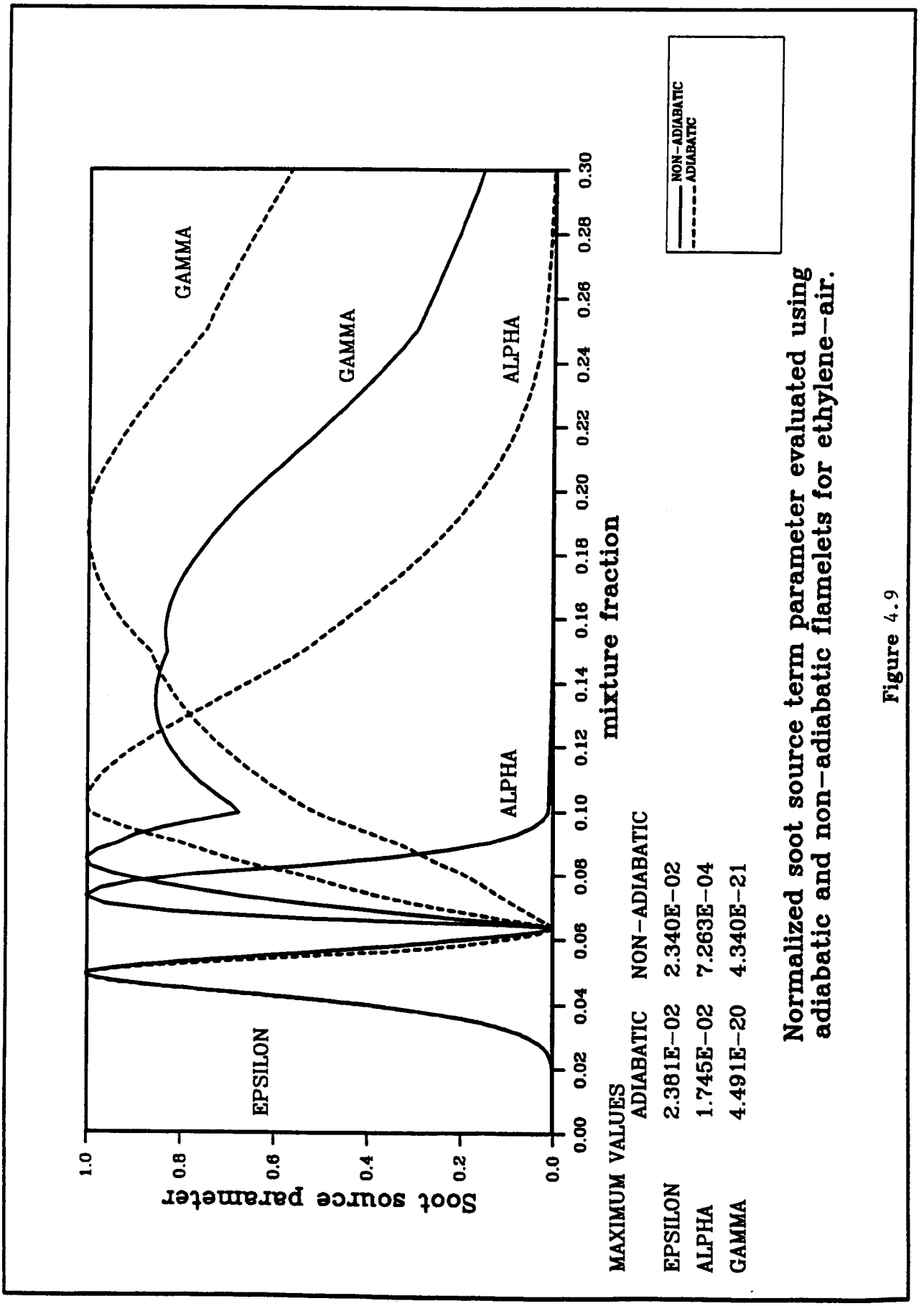

Normalized soot source term parameter evaluated using adiabatic and non-adiabatic flamelets for ethylene-air.

Figure 4.9

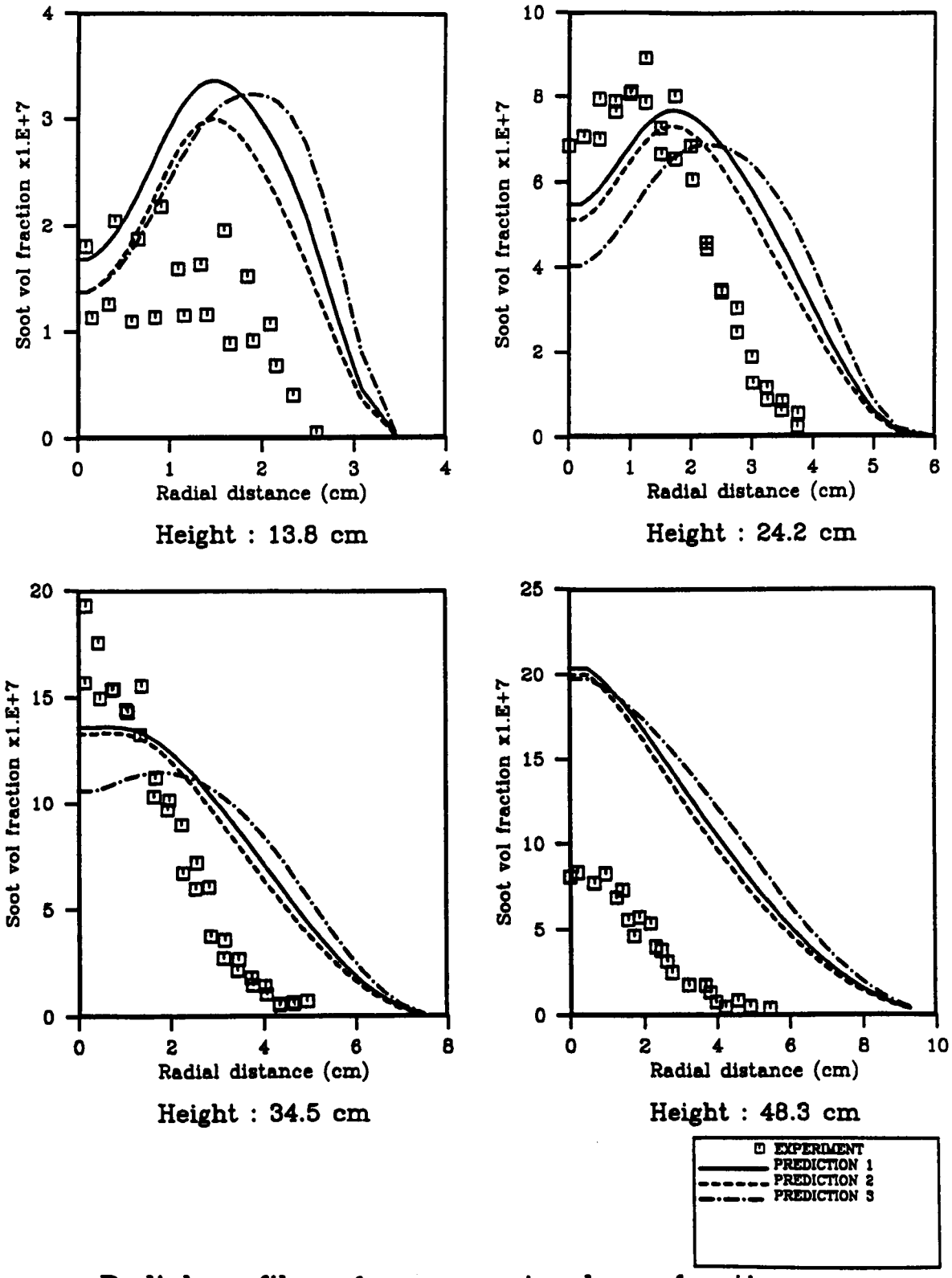

Radial profiles of mean soot volume fraction. Predictions for different soot source term closure assumptions compared with data of Kent and Honnery (1987)

Figure 4.10

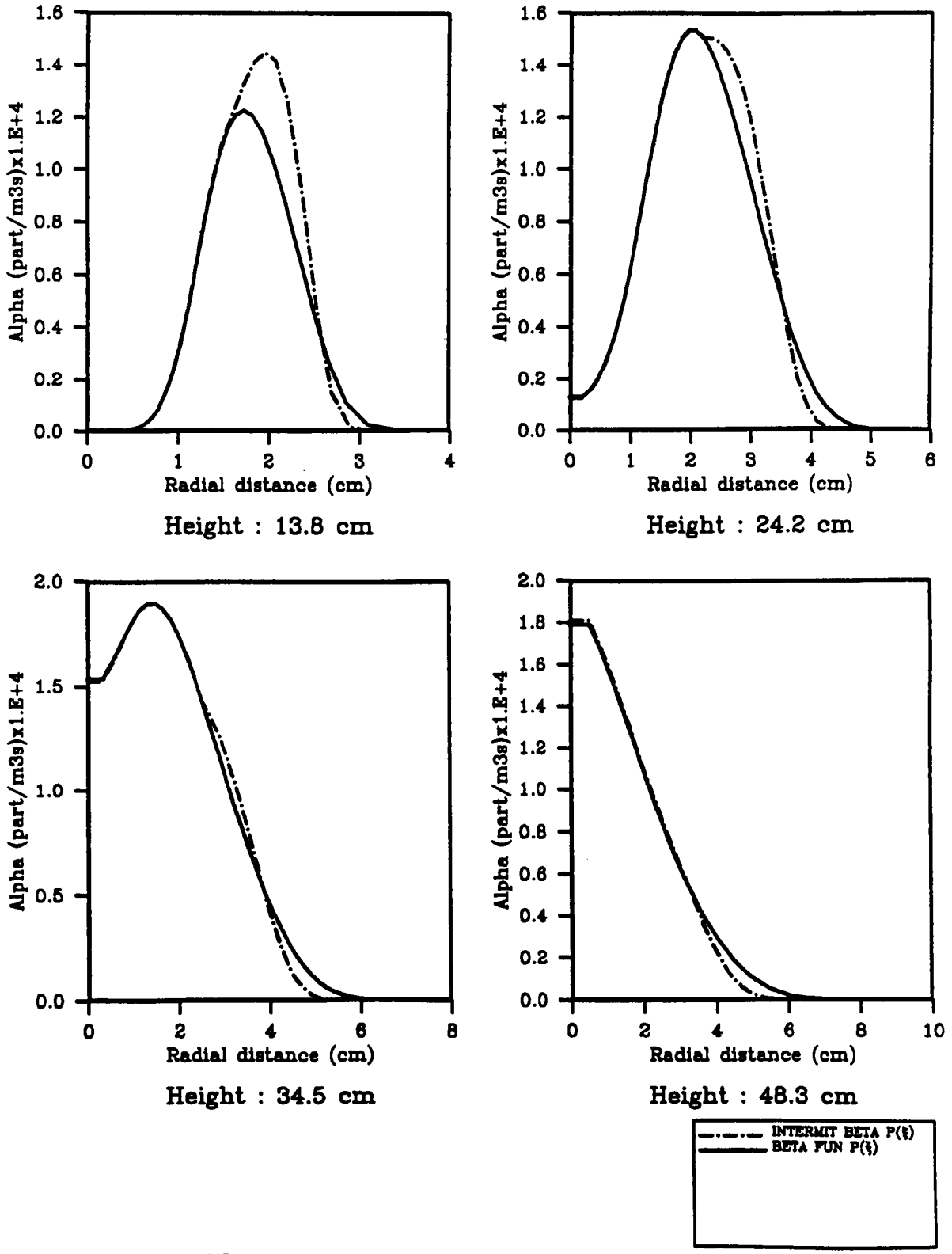

Radial profiles of mean soot source parameter ALPHA in Kent and Honnery (1987) flame. Predictions assuming intermittent and standard beta function forms of P(ξ).

Figure 4.11

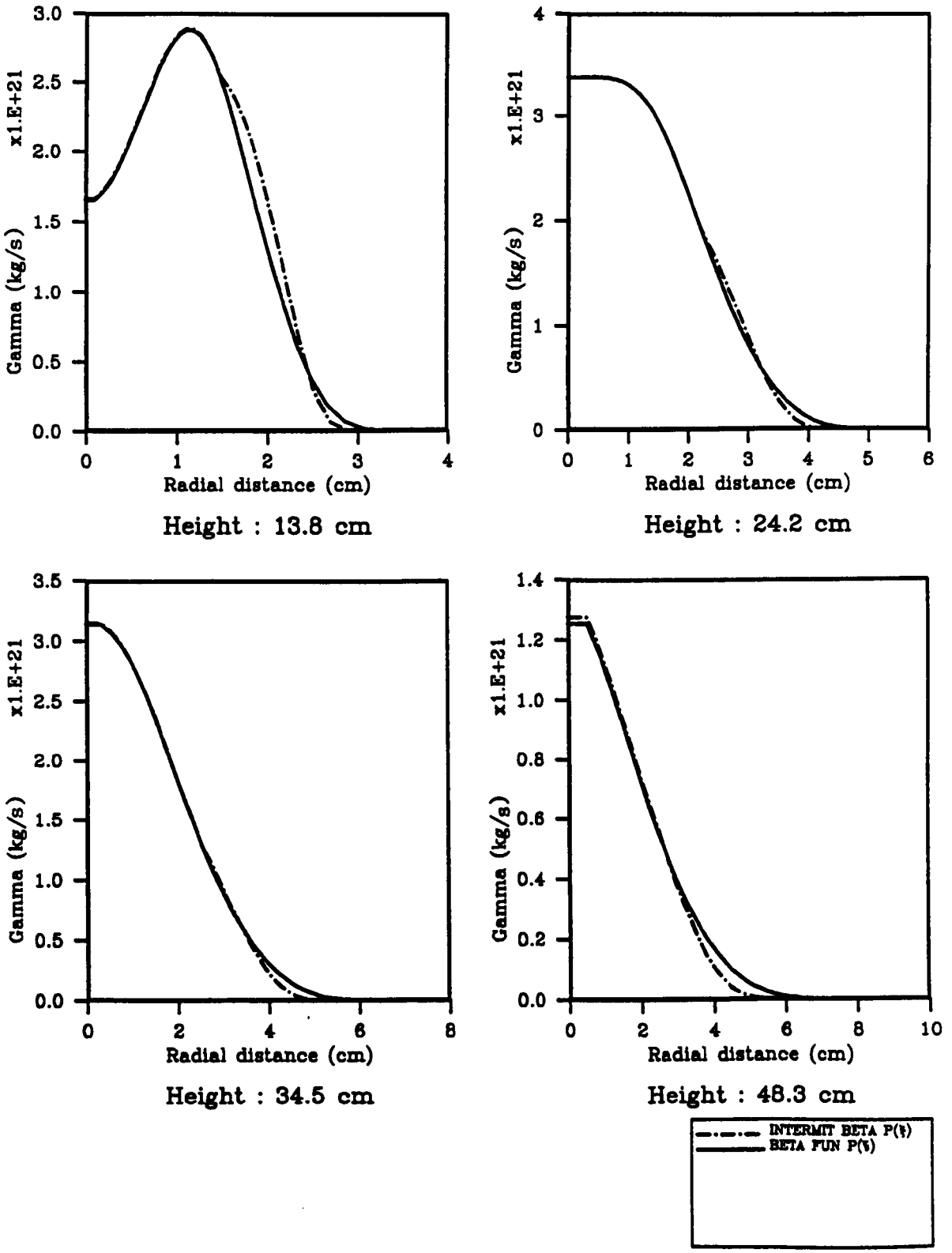

Radial profiles of mean soot source parameter GAMMA in Kent and Honnery (1987) flame. Predictions assuming intermittent and standard beta function forms of P(ξ).

Figure 4.12

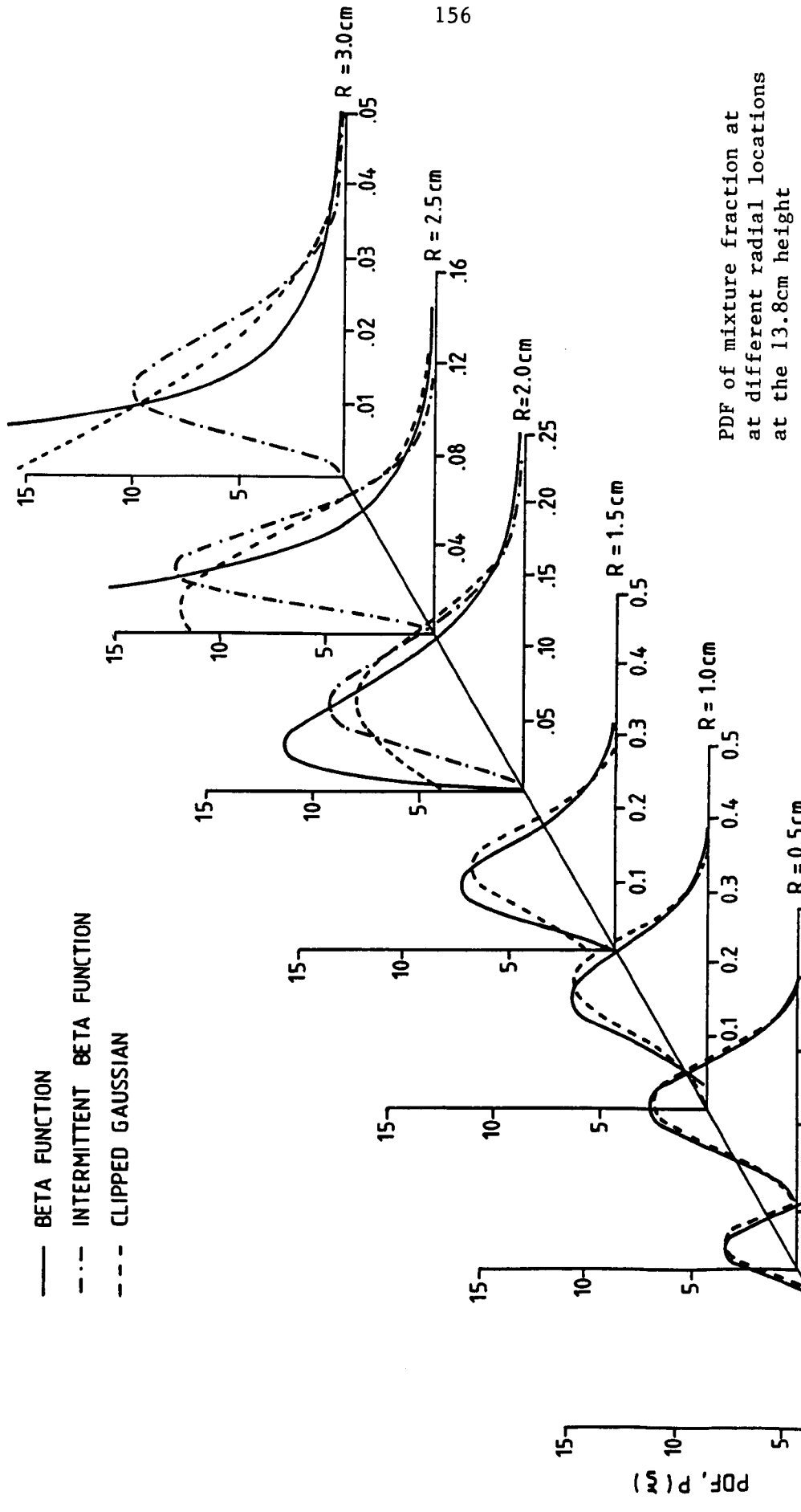
BETA FUNCTION
INTERMITTENT BETA FUNCTION
CLIPPED GAUSSIAN
PDF of mixture fraction at
at different radial locations
at the 13.8cm height
R = 3.0cm
R = 2.5cm
R=2.0cm
R = 1.5cm
R = 1.0cm
R = 0.5cm
R=0cm
PDF, P(ξ)
MIXTURE FRACTION (ξ)

Figure 4.13

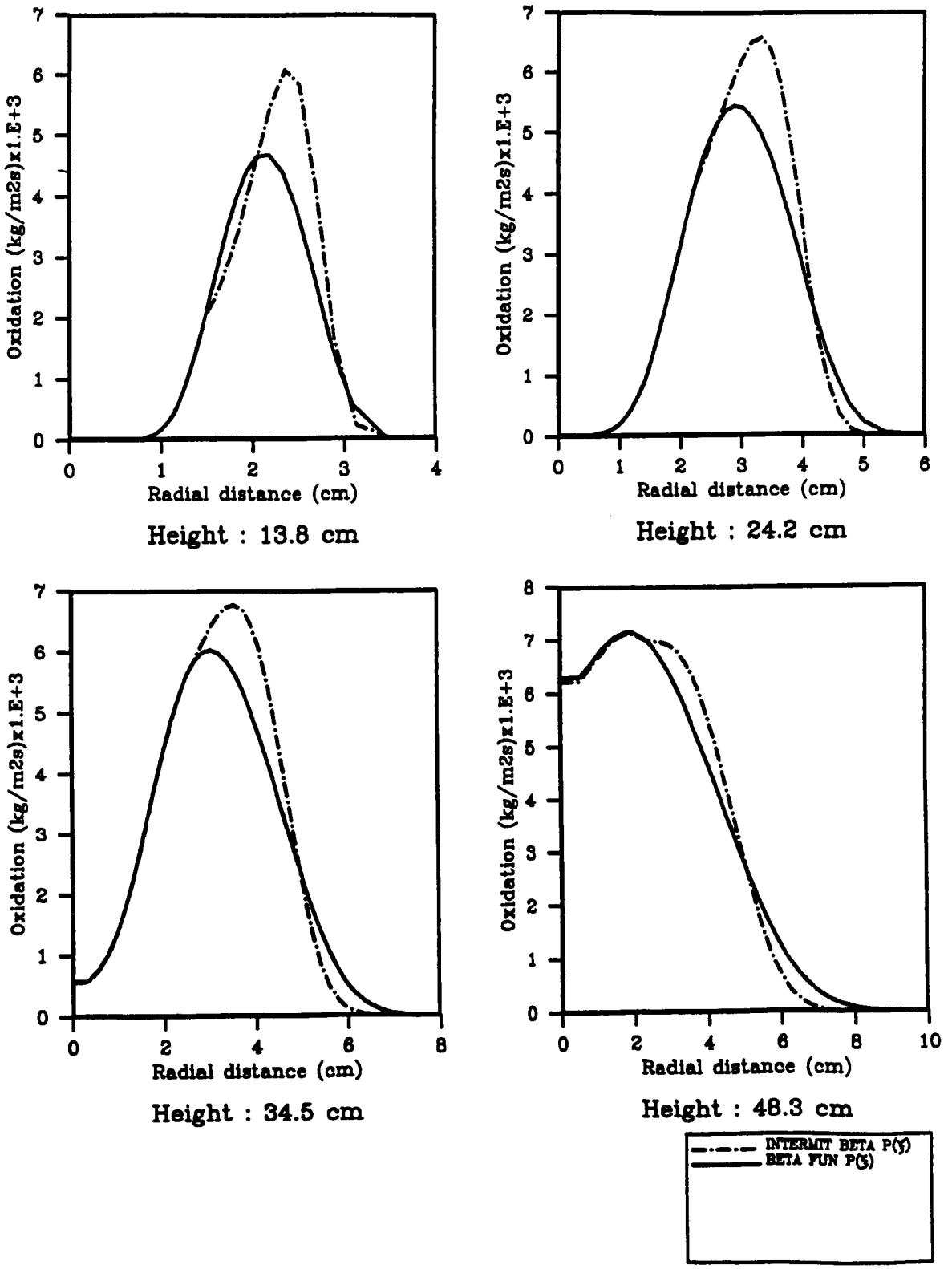

Radial profiles of mean soot oxidation rate in Kent and Honnery (1987) flame. Predictions assuming intermittent and standard beta function forms of P(ξ).

Figure 4.14

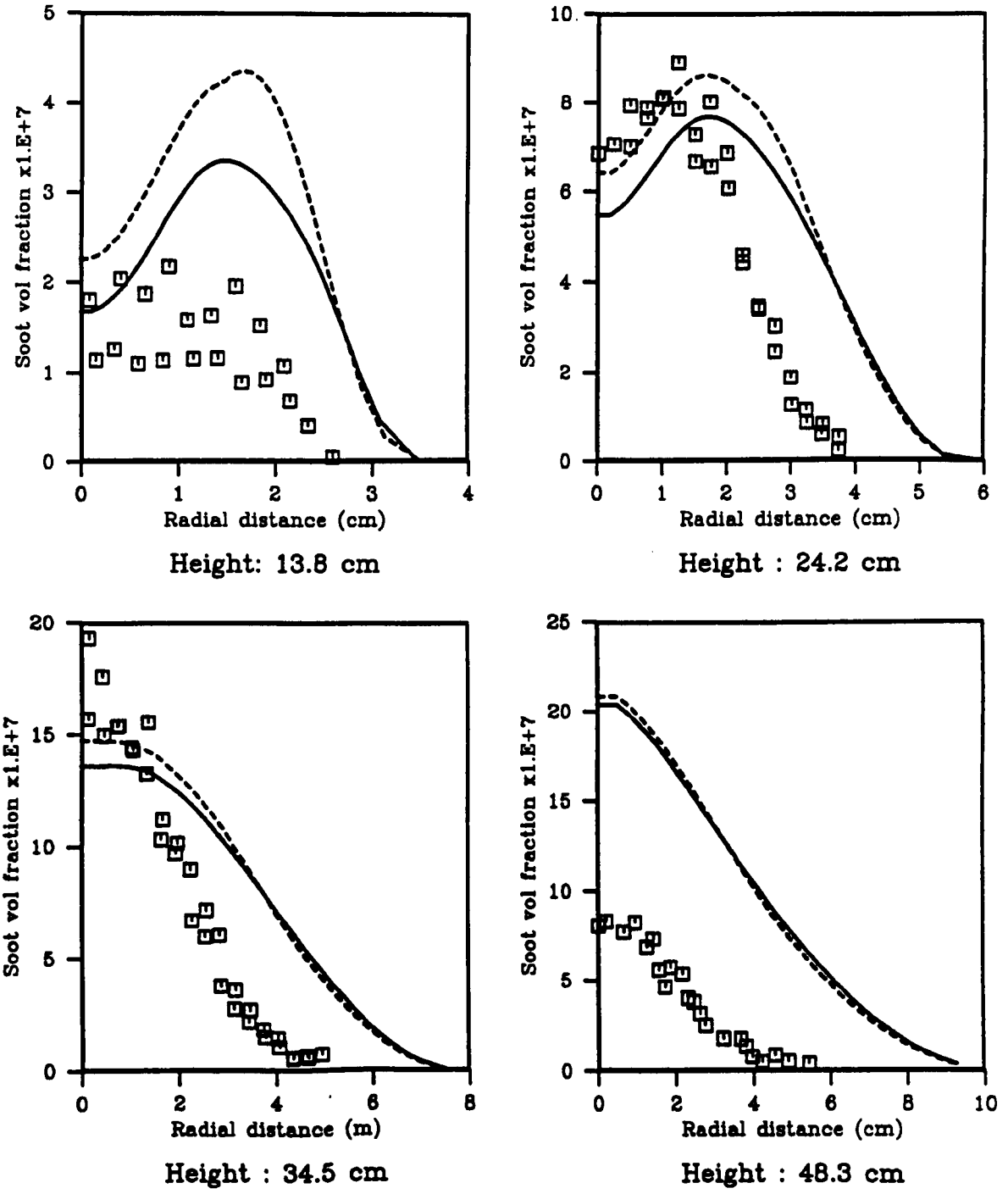

Radial profiles of mean soot volume fraction. Predictions assuming intermittent and standard beta function forms of $P(\xi)$. Comparison with data of Kent and Honnery (1987).

Figure 4.15

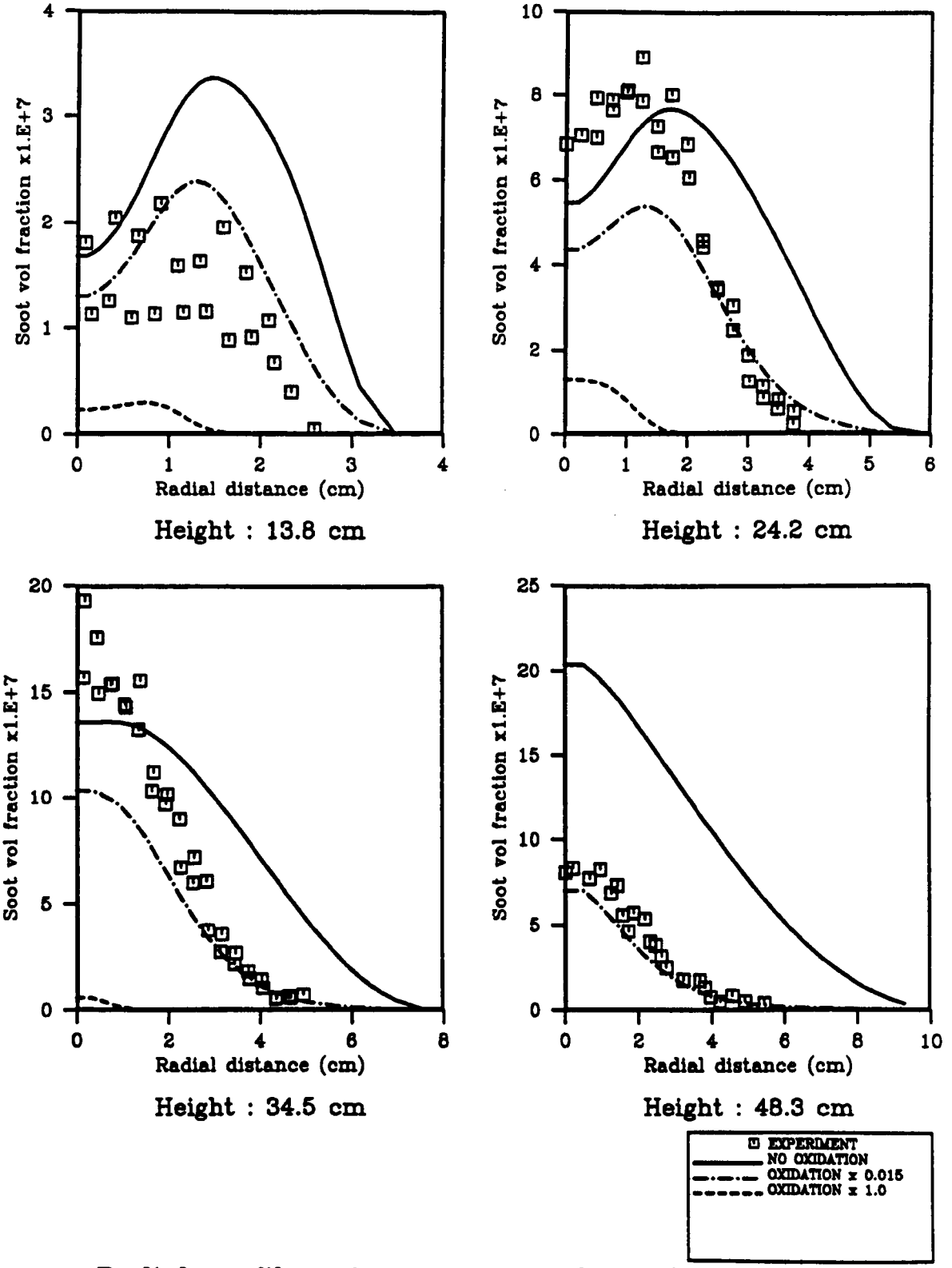

Radial profiles of mean soot volume fraction. Predictions show the effect of oxidation. Comparison with data of Kent and Honnery (1987).

Figure 4.16

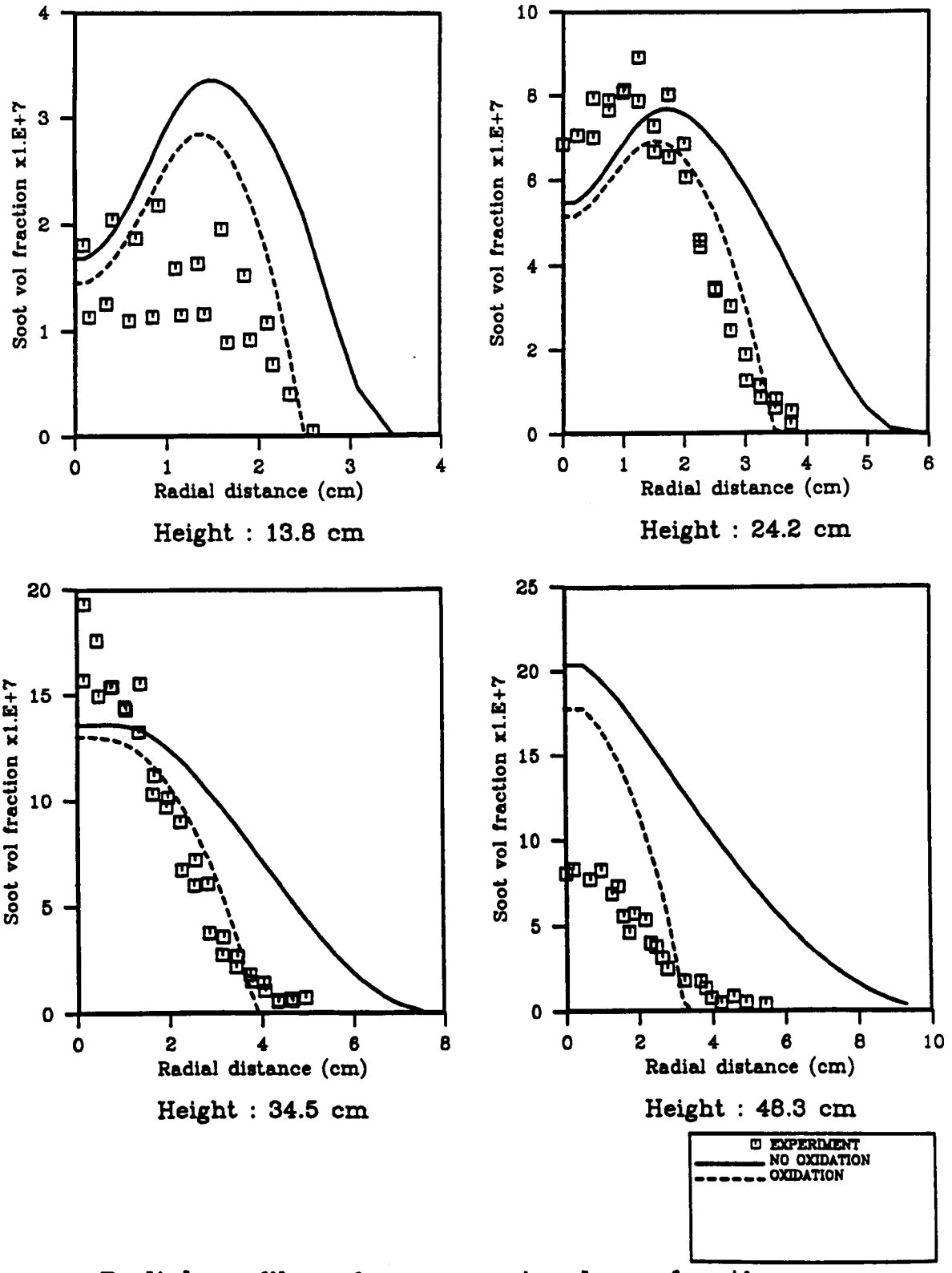

Radial profiles of mean soot volume fraction. Predictions show the effect of conditioned oxidation. Comparison with data of Kent and Honnery (1987)

Figure 4.17

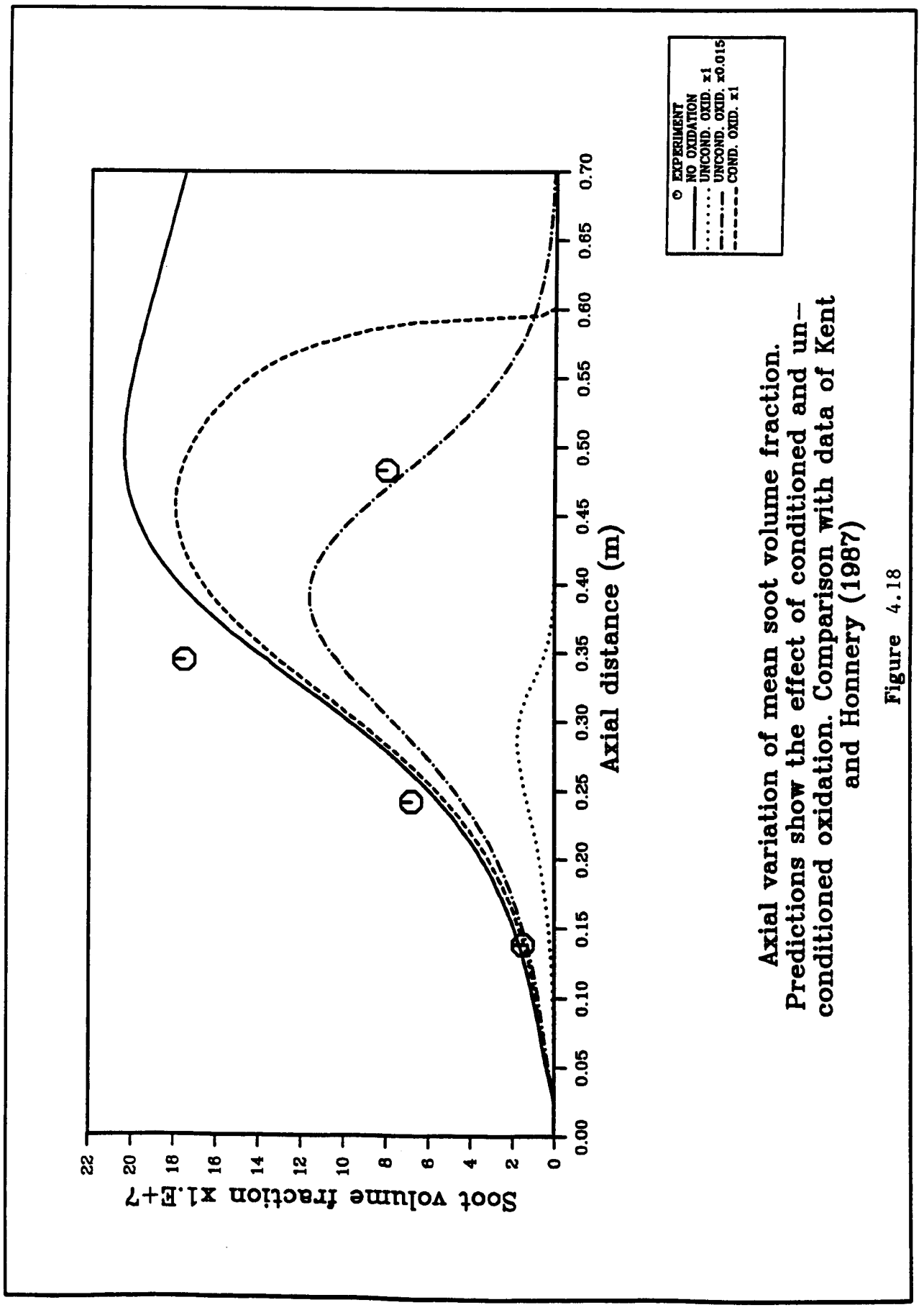

Axial variation of mean soot volume fraction. Predictions show the effect of conditioned and unconditioned oxidation. Comparison with data of Kent and Honnery (1987)

Figure 4.18

CHAPTER 5

Buoyant fire prediction

5.1 Introduction

The detailed computational modelling of fires has to date received relatively little attention compared with their high momentum counterpart, the jet diffusion flame. The study of the latter has been inspired by the desire to understand better the mechanisms underlying turbulent non-premixed combustion, and thereby the development of detailed models (cf. Bilger (1976a)). Such flows moreover are a natural extension of inert jets, the study of which has led to advances in the understanding of turbulence and its modelling. In contrast, the study of fires has been motivated by the more practical need to predict hazard potential; the lack of detailed knowledge of the controlling physical processes necessitates the heavy reliance on empirical approaches. For example, Thomas (1963) offered scaling laws by which the flame size of fires may be deduced from small scale experiment.

At a more detailed predictive level, zone models have been widely used. These offer greater flexibility in terms of range of application, and better spatial detail in that the domain is constructed of a number of zones. Emmons (1979) describes a general computer code for the prediction of fire in buildings. Zone models, however, must still rely on empiricism to obtain, for example, air entrainment into the fire, wall heat transfer and zone emissivity for radiation purposes.

The application of detailed computational modelling techniques to fires has so far been used to extend the applicability of predictive techniques to complex geometries (cf. Pericleous et al (1988) and Cox and Kumar (1987)). These studies, however, have been used to reveal global features, for example the evolution of combustion products through the domain, and the fire source has been treated in a rather simplistic manner. Therefore, an empirical input is essential when, for example, heat loss has an impact on the flowfield pattern. Radiation is dependent on local temperature and species concentration, including soot, and therefore requires a detailed view of the chemistry.

The present work is aimed at furthering the modelling capability of buoyant fires with a view to making a more accurate assessment of their potential hazard, by the use of computational fluid dynamic (CFD) techniques. This entails the detailed modelling of the turbulent flowfield, chemistry, radiative heat transfer and their interaction. The particular area of concern here is radiative emission, since it has a key role in the sustaining and spread of combustion. Radiative heat feedback to the fire source (which is usually solid or liquid) allows the release of vapours which continually fuel the fire. Also radiative heating of external bodies may cause them to ignite.

A critical component that determines the radiative emission is particulate soot, since it is produced in substantial quantity in large fires given the typically long residence times and poor mixing. Also the emitted radiation is significantly influenced by turbulence interaction. The latter has been shown to be very important in fires which are characterised by large scale fluctuations in scalar properties (cf. Grosshandler (1985) and Cox (1977)).

The two previous chapters introduced a soot model suitable for non-premixed combustion, which is representative of the regime in fires. This chapter and the following focus on the prediction of a fire where the turbulent combusting flowfield and emitted radiation are predicted and subsequently compared with experimental data.

Strictly speaking the radiation is coupled to the flowfield via the mean density and their calculation must therefore be coupled. Here however, where greater importance is given to the soot modelling and turbulence-radiation interaction, these calculations have been decoupled for computational simplicity. The influence of radiative heat loss on local temperatures, which has been found to be important, has therefore been included explicitly by perturbing local instantaneous temperatures as described later. The present chapter is concerned with the flowfield and thermochemistry modelling, and the subsequent radiation prediction is described in chapter 6.

The fire considered to be most suitable for investigation is that previously experimentally investigated by Crauford (1984) and Charnley (1986). This is owing to the wealth of available data which may be used to assess the predictions. Crauford measured spatially and temporally resolved velocity, using laser Doppler anemometry (LDA), and temperature, using a fine wire thermocouple. Charnley measured spectrally resolved (in the visible and infrared) line-of-sight time-averaged radiation and temporally resolved integrated line-of-sight radiation.

The experimental configuration is comprised of a methane fire supported on a 25cm diameter porous refractory burner, which allows the gaseous fuel to flow evenly over the entire surface. The mass flow rate of fuel was 5.42×10^{-4}Kg/s leading to a theoretical heat release of 28kW. The burner was mounted within a wire mesh enclosure which protected it from extraneous disturbances and allowed a steady inflow of air. Exhaust gases were directed into a duct positioned above the fire. The burner was mounted on a mechanism capable of vertical and horizontal translation, that allowed movement relative to a fixed probing point (or line). The movement was restricted in such a way that the burner face was never allowed to be less than 25cm above the floor in order to isolate the flame against floor effects. Such a controlled environment, though being well defined and allowing experimental repeatability, leads to turbulence modelling difficulties which will be described later.

In a wider context, the modelling of fires is difficult, since they are buoyancy-controlled rather than momentum-driven and hence the applicability of turbulence models developed in high momentum jets is questionable. Also, the frequencies of the fluctuations differ markedly from those prevalent in high momentum jets (combusting or otherwise). Fires are characterised by low frequency buoyancy-induced instability which is exhibited as a continual pulsation of large scale structures. Crauford (1984) found this characteristic frequency, in the presently studied fire, to be 3Hz, whilst maximum frequencies are of the order of 200Hz (cf. Weckman and Sobiesiak (1988)). Jet flames, on the other hand, exhibit frequencies of up to 5kHz (cf. Lockwood and Moneib (1981)).

A further difficulty is that the eddy viscosity turbulence models are strictly applicable to flows which exhibit local isotropy. This may not be so for fires where turbulent Reynolds numbers are relatively low. Buoyancy may enhance (or suppress) certain Reynolds stress components which suggests the necessity of resorting to second order closures (cf. Launder et al (1975)). These, however, introduce more modelling assumptions and have not been validated in fires. Many authors (cf. Vachon and Champion (1986) and Gengembre et al (1984)) have therefore elected to use the two-equation k-ε model and some (cf. Jeng et al (1982)) have offered modifications to address the effects of relatively low Reynolds number and buoyancy.

In the present study, the k-ε model is used and is modified only to include the effect of buoyancy on the source of k and ε. Non-isotropy is considered only at an elementary level by defining $k=\overline{u'^2}$ where u is the vertical velocity component. This model is utilised here since, despite the earlier reservations, it performs reasonably well when compared with the available experimental data.

The following sections describe the modelling of the fire in more detail, focusing on the turbulence and combustion modelling. The former includes a brief review of turbulence modelling applied to

fires, a more substantial one having been provided in chapter 2. Following the model description, the predictions are reported and the problem of modelling the laminar-turbulence transition in the initial region of the fire is introduced.

5.2 Turbulence models for buoyant flows

Buoyancy is introduced into the equations that govern fluid flow via the momentum equations. The averaged streamwise momentum equation for a two-dimensional, axi-symmetric turbulent boundary layer, where gravity acts in the negative x direction, is

$$\bar{\rho}\,\tilde{u}\,\frac{\partial \tilde{u}}{\partial x} + \bar{\rho}\,\tilde{v}\,\frac{\partial \tilde{u}}{\partial r} = \frac{1}{r}\left(r\,(\mu_l+\mu_t)\,\frac{\partial \tilde{u}}{\partial r}\right) - \frac{d\bar{P}}{dx} - \bar{\rho}\,g \qquad \ldots \quad (5.1)$$

where x and r are the streamwise and radial directions, u and v their velocity components, g is the acceleration due to gravity ($9.81 m/s^2$), and the subscripts l and t refer to laminar and turbulent quantities.

The effect of buoyancy also features in the balance equation for turbulent kinetic energy, since it is derived from the momentum equations as described by Launder and Spalding (1972). In summary, the derivation entails subtracting each of the mean momentum equations (three for 3-D flow) from their instantaneous counterparts, multiplying the resulting equation for u_i by u_j'', averaging and then multiplying by the Kronecker delta, δ_{ij}, ($\delta_{ij}=1$ for i=j and 0 for $i\neq j$). Considering only the buoyancy term we have

$$G_{bk} = - g\,\overline{\rho' u''} \qquad \ldots \quad (5.2a)$$

Only one term results if only one velocity component is influenced by gravity. The fluctuating velocity is u'' rather than u', since it is the equation for the Favre averaged turbulent kinetic energy that is appropriate here.

Mathematical manipulation of equation 5.2a shows that the effect of buoyancy in the k equation may also be expressed in the following ways

$$G_{bk} = g \, \bar{\rho} \, \overline{u''} \qquad \ldots (5.2b)$$

$$G_{bk} = g \, (\bar{\rho} \, \bar{u} - \overline{\rho \, u}) \qquad \ldots (5.2c)$$

$$G_{bk} = - g \, \overline{\rho' u'} \qquad \ldots (5.2d)$$

$$G_{bk} = g \, \bar{\rho} \, (\bar{u} - \tilde{u}) \qquad \ldots (5.2e)$$

Following the arguments which led to the modelling of the production term in the equation for turbulence dissipation as $C_{\varepsilon 1} \, \varepsilon/k \, K_p$, where K_p is the production of turbulence kinetic energy due to the mean velocity gradient, the effect of buoyancy in the ε equation may be modelled as

$$G_{b\varepsilon} = C_{\varepsilon 1} \, (\tilde{\varepsilon} \, / \, \tilde{k}) \, G_{bk} \qquad \ldots (5.3)$$

G_{bk} in the form of equation 5.2d shows that the gradient viscosity hypothesis may be used for closure in the absence of any joint vector-scalar statistical information cf.

$$G_{bk} = - g \, \overline{\rho' u'} = g \, (1 \, / \, \bar{\rho}) \, \frac{\mu_t}{\sigma_\rho} \, \frac{\partial \bar{\rho}}{\partial x} \qquad \ldots (5.4)$$

In the region of the flame investigated (above 14cm) $\partial\rho/\partial x$ is mostly positive leading to a positive value for G_{bk}. This seems reasonable since in the buoyancy dominated flow, $\overline{\rho' u'}$ will tend to be negative.

It should be noted that μ_t, given the present density weighted formulation for the governing balance equations, is deduced from Favre averaged k and ε, yet the averaged quantities in equation 5.4 demand

that it be calculated from Reynolds averaged k and ε. However, gradients, such as $\partial\bar{\rho}/\partial x$, in the streamwise direction of boundary layer type flows are relatively small, hence making the contribution of G_{bk}, in the source of k, small. The impact of the anomaly in μ_t is therefore limited.

The formulation, equations 5.4 and 5.3, has also been adopted by, for example, Markatos et al (1982), though they express G_{bk} as

$$G_{bk} = - \beta\, g \quad \frac{\mu_t}{\sigma_T} \frac{\partial \bar{T}}{\partial x} \qquad \ldots \quad (5.5)$$

where β is the thermal expansion coefficient ($= 1/\bar{T}$). Equation 5.5 results from equation 5.4 under the assumption $\partial\bar{\rho}/\bar{\rho} = -\partial\bar{T}/\bar{T}$.

In the present case G_{bk} and $G_{b\varepsilon}$ (eqns. 5.4 and 5.3) are appended to the sources of k and ε.

Others proposed additional modifications, for example, Chen and Chen (1979) suggested modifications to c_μ and $C_{\varepsilon 2}$. This approach, as well as others, was evaluated by Jeng et al (1982) in the modelling of buoyant flames. Their findings suggest the choice of model to have little influence on the mean flame structure, and more important was the specification of the fuel source boundary conditions. Therefore in order to minimise the uncertainties due to further modelling assumptions, they are not adopted here, since the standard formulations were seen to perform adequately.

The previous chapter introduced a modification to $C_{\varepsilon 1}$ in the source of ε (cf. table 4.1), proposed by Morse (1977) to account for the reduced spreading rate of axisymmetric jets compared to their planar counterparts. Pope (1978) suggested that the fundamental reason underlying this disparity was due to the circumferential stretching of vortex rings as the round jet spreads, leading to a smaller eddy size due to angular momentum conservation (cf. chapter 4.3.3). The decay of

turbulence, which is rate limited by the decay of large eddies, is thereby accelerated. Though the fire is axi-symmetric, the spreading does not alter significantly, remaining as it does more or less the same width as the burner diameter. In the fire calculations reported here, therefore, no such modification is made to $C_{\varepsilon 1}$ as was made in the earlier reported jet flame prediction. When such a modification is made, the spreading rate is indeed found to be significantly underpredicted.

The region where a change in width is evident is near the burner where the flow initially necks in and then quickly spreads due to buoyant instability. This region, however, raises more important concerns, since there the flow is not fully developed. Also the parabolic formulation, used in the present modelling, may not be applicable very close to the burner where the neglected streamwise diffusion can be significant.

5.3 Combustion model

The laminar flamelet approach described in chapter 2.1 and implemented in the jet flame prediction of chapter 4 is used here. This requires suitable state relationships linking chemistry dependent scalars to the conserved mixture fraction. As described in chapter 2, the state relationships may be deduced by detailed kinetic computation (as adopted in chapter 4) or by experiment. Here, the experiments of Mitchell et al (1980) are used to provide these relationships. Mitchell et al experimentally investigated a confined, co-flowing laminar methane-air diffusion flame, where they measured the major species and temperature at various heights in the flame. They then presented their data against local equivalence ratio. Figure 5.1 shows the data plotted against mixture fraction, where density has been deduced from the measurements and the equation of state.

As mentioned earlier, state relationships may be perturbed due to hydrodynamic strain; however, the co-flowing geometry of Mitchell et

al and the buoyant fire to be modelled here are thought to exhibit limited strain and therefore its influence has been neglected.

In addition to flame stretch, the local flamelet structure may be significantly modified due to radiative heat loss. Careful analysis of the available experimental data in the buoyant fire reveals that the local flamelets exhibit a greater heat loss than that inherent in the experimental configuration of Mitchell et al. Figure 5.2 shows the temperature state relationship of Mitchell et al compared with an adiabatic numerically derived flamelet using the SNECKS algorithm (Askari-Sardhai (1987)). The peak temperatures from both curves are comparable, indicating the minimal heat loss in the experiment of Mitchell et al. Also shown in figure 5.2 is a radiatively cooled state relationship found to be more representative of the instantaneous structure in the fire - its derivation is discussed in more detail in section 5.4.2.

5.4 Initial conditions

Current modelling of fluid flows is restricted to either **(i)** laminar flows, where the system may be described exactly, given accurate information about the fundamental processes (eg. molecular transport, chemistry and radiation) or **(ii)** fully developed turbulent flow, where the additional statistical uncertainties may be addressed by turbulence models. Predictions spanning the transition between laminar and turbulent flow still remain difficult, though it has been the focus of several studies related to wall boundary layers (cf. Patel et al (1985)), and low Reynolds number effects have been investigated in the study of thermal plumes (cf. chapter 2). The modelling of fires, therefore, is problematic since initial Reynolds numbers are low, owing to the low source momentum which is typically governed by the evaporation of fuel fragments. To reflect this the simulated fire studied here exhibits a fuel source velocity of 1.7cm/s which leads to a burner Reynolds number of ~ 140. Turbulence develops slowly in

fires from the more ordered low frequency buoyant instability described earlier.

In practical fire situations, factors like floor effects, irregular fuel source geometry and ambient disturbances rapidly induce instability (cf. Weckman and Sobieskiak (1988). In the present case, however, the experimental conditions were strictly controlled which, coupled with the circular burner geometry, leads to a significant transitional region before more representative turbulent flow develops.

Previous works investigating the computational modelling of the fire source (eg. Gengembre et al (1984)) have chosen to initiate their calculations at the burner exit. Here, artificially high turbulence levels must be assigned in order that realistic spreading rates be observed higher up. This is somewhat unsatisfactory since the calculation is sensitive to the initial profiles, the generality of which is not justified. For example Vachon and Champion (1986) chose to use the expressions

$$k_0 = a_k U_0^2 \qquad \ldots (5.6a)$$

$$\varepsilon_0 = a_\varepsilon k_0^{3/2} / R \qquad \ldots (5..6b)$$

where R is the radius of the burner, U_0 the mass averaged source velocity and both a_k and a_ε were taken to be unity. Jeng et al (1982) used $a_k = 4 \times 10^{-4}$ and $a_\varepsilon = 1.2 \times 10^{-4} U_0^3 / R$.

Crauford et al (1985), modelling the same fire studied here, chose to initiate a laminar calculation at the burner face and effected numerical transition to turbulence at a prespecified height - 2cm. The initial turbulence levels were based on computed local velocities and their gradient. This had the effect of mimicking the severe necking in due to large buoyant acceleration. This is not evident in the former approach where the high initial turbulence levels lead to high mixing

and relatively low mean densities (due to the more intermittent appearance of flame fronts) and therefore lower acceleration.

Both of the above approaches may, by suitable manipulation of the initial turbulence conditions, produce respectable agreement with the experimental data down-stream, where the flow is fully turbulent. However, given the unsatisfactory nature of the above approaches, in that they cannot be expected to yield initial profiles suitable for fires in general, an alternative method, also investigated by Crauford et al (1985), is adopted here.

Rather than prescribe unrealistic turbulence levels, we have elected to bypass the region of difficulty and initiate the calculation where full turbulence has been established. Also, in order to further limit uncertainty, experimental profiles were used to provide initial conditions.

The current modelling approach, which adopts the two equation k-ε turbulence model and the laminar flamelet combustion model, requires solution of Favre averaged balance equations (of the form eqn.4.24), and hence initial conditions for the scalars k, ε, $\tilde{\xi}$ and ξ''^2. In addition the two components of momentum (cf. two-dimensional treatment) and the continuity equation are to be solved. As for the previously described simulations (chapters 3 and 4), the boundary layer approximation is applied and the simplified parabolic equations are solved using a modified version of GENMIX (Spalding (1977)) (cf. Chapter 3.4.4).

The following subsection describes the prescription of the initial profiles for each variable.

5.4.1 Initial profiles for $\tilde{u}$, k and ε

The initial profile of streamwise velocity is assumed to be that of the axial component of mean velocity, measured by Crauford (1984) using laser Doppler anemometry (LDA). The LDA results which rely on the transport of seed particles in the flow are not influenced by density fluctuations; the deduced velocities are consequently Reynolds averaged. The parameter required, however, is the Favre averaged $\tilde{u}$. Given that there is no available unconditional correlation linking the vector and scalar fields, the Favre averaged velocity cannot be determined unambiguously from the Reynolds averaged data. The initial Favre averaged profiles have therefore been set equal to the Reynolds averaged data. This is likely to be an overestimate since, by definition,

$$\tilde{u} = \bar{u} + \overline{\rho' u'}/\bar{\rho} \qquad \ldots \quad (5.7)$$

The correlation $\overline{\rho' u'}$ is likely to be negative since, for the buoyancy driven flow, a negative density migration will induce a positive velocity.

An additional problem with the experimental results is that the seeding relied on naturally occurring aerosols, including soot. This resulted in two sets of data, that due to large soot particles (the upper bound velocities) and that due to small particles (lower bound velocities). Given the nature of sooting diffusion flames, the small particles will be highly correlated with the flame front, whilst the larger particles would represent regions away from the flame front. A further criticism of the use of soot as seeding particles is that there is a velocity bias in regions where no soot particles exist. Such regions will be near the air boundary lower down in the flame where entrainment rates are high. At these heights the spread of the flow is likely to be underestimated.

Later the predicted velocity profiles will be compared with both the upper and lower bound experimental data, where the predictions look plausible in that they fall between the upper and lower bounds. For the initial $\tilde{u}$ profile the upper bound $\bar{u}$ data is used, essentially because that is the only data available at the 14cm height. Slight variations in $\tilde{u}$ were found not to alter the results significantly if it was always ensured that the flux of fuel originated material remained constant - mixture fraction was altered to accommodate this.

The turbulent kinetic energy is defined as the energy of the fluctuating motion per unit mass cf.

$$\bar{k} = \frac{1}{2}\left(\overline{u'^2} + \overline{v'^2} + \overline{w'^2} \right) \qquad \ldots \quad (5.8)$$

For isotropic flow, the velocity variance in all three directions is equal, leading to $\bar{k}=3(\overline{u'^2})/2$. Fires, however, exhibit non-isotropic behaviour, for example, Crauford (1984) found that the radial velocity fluctuation was approximately half the axial. Though the eddy viscosity concept is used to close the turbulent correlations, which implies isotropic turbulence, here non-isotropy is reflected in a rather rudimentary manner by defining

$$\bar{k} = \overline{u'^2} \qquad \ldots \quad (5.9)$$

This implies $\overline{u'^2}=\overline{v'^2}+\overline{w'^2}$.

As with velocity, the initial $\tilde{k}$ profile is set equal to the initial $\bar{k}$ profile.

A suitable initial profile for ε is not straightforward. The local values, following Crauford et al (1985), were determined from the algebraic relationship

$$\tilde{\varepsilon} = 16\ \tilde{k}^2 / (R^2\ |\partial\tilde{u}/\partial r|) \qquad \ldots \quad (5.10)$$

where R is the radius of the mixing layer. This expression is dimensionally consistent and expresses ε in terms of parameters thought to influence it.

5.4.2 Initial profiles of $\tilde{\xi}$ and $\widetilde{\xi''^2}$

The only available experimental scalar data are the mean and rms temperatures measured by a compensated fine wire thermocouple. For infinitesimally small thermocouples, Reynolds averaged quantities are measured, whilst for a finite sized thermocouple there is some degree of density weighting, but values may still lie close to Reynolds quantities (cf. Jones and Whitelaw (1981)).

If temperature is assumed to be a unique function of mixture fraction then the following relationships hold

$$\overline{T} = \int_0^1 T(\xi)\ P(\xi)\ d\xi \qquad \ldots(5.11a)$$

$$\overline{T'^2} = \int_0^1 (T(\xi)-\overline{T})^2\ P(\xi)\ d\xi \qquad \ldots(5.11b)$$

where, given the Reynolds temperatures, $P(\xi)$ is a Reynolds PDF. $\overline{\xi}$ and $\overline{\xi'^2}$ may then be deduced by inverting these expressions, provided that $T(\xi)$ is a known function and $P(\xi)$ is dependent on only two parameters. The former is obtained from the data of Mitchell et al (1980) and, given its beta function form (cf. eqns. 4.29-4.30), $P(\xi)$ is defined by only its first two moments. A suitable algorithm to perform the inversion, and the one used here, is that developed by Powell (1970) for solving systems of non-linear equations. This algorithm is available through the NAG library (NAG FLIB:1946/0:mk9:24th February 1982).

There is, however, some ambiguity since $T(\xi)$ is a double valued function and, therefore, there are two possible sets of $\bar{\xi}$ and $\overline{\xi'^2}$ capable of producing a given $\bar{T}$ and $\overline{T'^2}$, reflecting lean and rich conditions. Therefore, some discretion is required when deriving mixture fraction profiles from temperature profiles. There are, however, some useful constraints in that **(i)** the mean mixture fraction profile must be monotonic and have a zero gradient at the centre line (its maximum) and a zero gradient at the outer air interface, **(ii)** the profiles should be continuous and **(iii)** the flux of fuel stream originated material should be consistent with that emitted at the burner ie.

$$m_{fu} = 2\pi \int_0^R r \bar{\rho} \tilde{u} \tilde{\xi} \, dr \qquad \ldots (5.12)$$

where m_{fu} is the mass flow rate of fuel through the burner and R is the radius of the mixing layer. The integral (consistent with the GENMIX formulation) considers one radian and hence the 2π multiplier. No problems with turbulent correlations arise since in the parabolic boundary layer approximation, the effect of turbulence is to redistribute radially.

The above procedure yields $\bar{\xi}$ and $\overline{\xi'^2}$; however, it is $\tilde{\xi}$ and $\widetilde{\xi''^2}$ that are required. A further step will allow the calculation of the latter if a suitable $\rho(\xi)$ is defined, which it may be, given the data of Mitchell et al (1980) (cf. figure 5.1).

Having obtained the Reynolds PDF, the Reynolds mean density may be obtained through an equation similar to eqn. 5.11a. It is then simple enough to obtain the Favre PDF and hence its first and second moments ($\tilde{\xi}$ and $\widetilde{\xi''^2}$) by inversion of

$$\bar{\xi} = \bar{\rho} \int_0^1 \frac{1}{\rho(\xi)} \xi \, \bar{P}(\xi) \, d\xi \qquad \ldots (5.13a)$$

$$\overline{\xi'^2} = \bar{\rho} \int_0^1 \frac{1}{\rho(\xi)} (\xi - \bar{\xi})^2 \, \tilde{P}(\xi) \, d\xi \qquad \ldots(5.13b)$$

Figure 5.3 shows the results of the above reduction process to obtain $\bar{\xi}$ and $\sqrt{(\overline{\xi'^2})}$ profiles at the initial (14cm) height. Two sets of curves are presented, those corresponding to fuel rich and fuel lean conditions. Overall estimates of fuel stream flux, using plausible velocities, indicate that the centre line mixture fraction must be greater than stoichiometric. This is also indicated by figure 5.3, where the upper $\bar{\xi}$ curve has a minimum and the lower curve a maximum; a transition from one curve to the other is therefore necessary to achieve a monotonic profile. The nature of the two curves, however, shows that such a transition will yield a physically implausible discontinuity. A discontinuity is also apparent between the rich and lean $\sqrt{(\overline{\xi'^2})}$ curves.

The reason for the apparent discontinuity is revealed in figure 5.4 which presents $\bar{T}$ plotted against $\sqrt{(\overline{T'^2})}$. The experimental data are shown together with contours (derived using equations 5.11) generated for a constant mean mixture fraction of 0.055 (which is stoichiometric for methane) and varying $\widetilde{\xi''^2}$. Curve 1 is derived using Mitchell et al's data and the other curves represent a perturbation to their data to simulate heat loss. The previously observed discontinuity is immediately apparent in that, if at some point $\tilde{\xi}=\tilde{\xi}_{st}$, then the experimental data in figure 5.4 should be tangential to curve 1. Further analysis of figure 5.4 shows there to be two possible causes for this anomaly. The first is that the function $T(\xi)$ obtained from Mitchell et al's experiment exhibits temperatures that are too high to describe the instantaneous temperature field in the fire. The second casts doubt on the temperature fluctuation measurements themselves. Both arguments are plausible - the former since the fire is in a large enclosure, unlike the small confined flame that Mitchell et al investigated. Also, the fire exhibits greater residence times allowing flamelets to broaden and hence their optical path lengths to increase. Both the above imply a greater degree of radiative loss for the fire.

The reduction of fluctuating temperatures using thermocouple is at best difficult due to the necessity to compensate for thermal inertia (cf. Ballantyne et al (1976)) where the time constant itself is a fluctuating quantity, based as it is on local fluid properties. Traditionally a local average time constant is assigned, a method for the derivation of which can be found in Ballantyne et al (1976). Such compensation has been successfully applied in jet flame environments. Fires, however, provide a far sterner test in that they are highly intermittent with large scalar and vector fluctuations and the temporal variation of the time constant is likely to be large. Also Crauford (1984) found that, due to the low frequency large scale fluctuations, the time constant could not easily be determined. Crauford, therefore, deduced a time constant which resulted in plausible maximum and minimum instantaneous temperatures. Again, however, the time constant was assumed not to fluctuate.

Curves 2 to 4 (fig. 5.4) show further contours of constant mean mixture fraction ($\tilde{\xi}=\tilde{\xi}_{st}$). The curves show the effect of heat loss where the heat loss factor, r, is given by the expression

$$T_r(\xi) = (1 - r)(T(\xi) - T_0) + T_0 \qquad \ldots (5.14)$$

where T_0 is the ambient temperature (300K). The value of r used in the predictions reported in the next section is taken to be 0.1 which gives a maximum flamelet temperature of 1875K. This flamelet is shown in figure 5.2.

5.5 Flowfield simulation

The chapter to date has established the framework for the fire simulation which is to be described in this section. It is useful at this point to summarise.

The governing equations are expressed in two-dimensional parabolic

form and therefore, apart from the free stream boundary, only the initial profile needs to be prescribed. This is taken from the experimental data at 14cm above the burner which therefore circumvents the problematic laminar-turbulent transitional region. The equations are solved using a modified version of GENMIX (Spalding (1977)) which was introduced in chapter 3. Here, the domain is expressed in the Patankar-Spalding co-ordinate system and therefore the only flowfield variable to be solved is the streamwise velocity. Mass continuity is automatically obeyed by the choice of co-ordinate system and the ω (normalised stream function) velocity component is grid dependent.

The k-ε turbulence model is used in conjunction with the laminar flamelet combustion model, which entails the solution of four further equations cf. k, ε, $\tilde{\xi}$ and $\widetilde{\xi''^2}$. Radiative loss is treated explicitly by perturbing the temperature flamelet and hence there is no need to solve a balance equation for enthalpy.

The parameters used in the balance equations for each of the variables are listed in table 5.1. There the source terms are seen to be similar to those used in the jet flame predictions of chapter 4 (cf. table 4.1) except that the sources of k and ε include the influence of buoyancy and the $C_{\varepsilon 1}$ term is unmodified from that derived in planar jets. In addition, the predictions to be presented shortly compare the effects of varying C_{g2} in the source of mixture fraction variance, since a review of the literature suggests a suitable value for this parameter may be as low as 1.25 for buoyant flows (cf. Gibson and Launder (1976)). This compares with 2.0 (cf. Liew (1983)) and 1.87 (cf. Faeth et al (1986)) applied to jet flames and weakly-buoyant flames respectively.

Figures 5.5 and 5.6 show the development of the mixture fraction field, where the former presents the axial variation and the latter radial profiles at heights 14, 30, 45 and 77cm above the burner. These heights coincide with the radial data of Crauford (1984) and the line-of-sight radiation measurements of Charnley (1986).

Mean mixture fraction values are affected to only a small degree by the setting of C_{g2} whose influence is exerted by way of the mean density. The C_{g2} setting does, however, have a large effect on the rms mixture fraction where it has a direct influence through the source term. Here, the lower decay rate indicated by the lower C_{g2} value allows high fluctuation levels to persist further downstream.

Figure 5.5 shows the rms mixture fraction to fall, above the initiation height, reaching a minimum at approximately 20cm before subsequently increasing. This feature is also apparent in the temperature and velocity fluctuations presented later and is probably due to the initial levels of turbulence dissipation rate being too high. The extent of this region is, however, insubstantial.

It is useful at this point to focus attention on the temperature and velocity since these can be compared with experimental data.

Figures 5.7 - 5.10 present the predictions of mean and rms temperature and velocity where comparison is made with the experimental data of Crauford (1984). Both axial and radial profiles are shown where the latter are presented at heights 14, 30, 45 and 77cm above the burner.

Figure 5.7 and 5.8 show the radial and axial variation of mean and rms temperature. As stated above, two sets of predictions are presented, where C_{g2} is set to 1.89 and 1.25. The radial profile at 14cm (cf. fig.5.7) represents the initial condition, where the mean temperatures were used to obtain the profiles of the mean and variance of mixture fraction. As stated earlier limited reliance was put on the experimental rms temperatures which explains the deviation in the computed and experimental values. The profiles are somewhat discontinuous; however, any smoothing was seen to be purely cosmetic, since mixing rapidly brings about this effect as the calculation proceeds. The downstream profiles were seen to be most dependent on the initial turbulence levels and the overall fuel flux.

At the upper heights (30, 45 and 77cm above the burner cf.fig.5.7) the predicted mean temperatures show good agreement with the experimental data for both C_{g2}=1.89 and 1.25. The former tends to overpredict both the experimental data and the C_{g2}=1.25 calculation in fuel rich regions, as indicated at the central regions of the 30 and 45cm heights. In leaner regions the C_{g2}=1.25 calculation yields the greater mean temperatures of the two predictions (cf. outer region at 45cm and entire width at 77cm). Both these facets reflect the influence of the greater spread in $P(\xi)$ offered by the lower C_{g2} values. When the mean mixture fraction is around stoichiometric, a greater spread in $P(\xi)$ results in lower mean temperatures as the probability of sampling lower temperatures is increased. However, for leaner mean mixture fractions the greater spread allows the sampling of richer, near stoichiometric, mixtures. This is illustrated in figure 5.11 where the centre-line $P(\xi)$, at the 77cm height, is shown for both predictions. The lower C_{g2} value is seen to allow greater sampling from rich mixtures.

The physical interpretation of the effect of reducing C_{g2} is to increase the durability of fuel-rich structures before molecular effects dissipate them. Referring to figure 5.11, the lower C_{g2} value is seen to result in the persistence of fuel-rich pockets and hence reaction zones.

Both sets of rms temperature predictions exceed the experimental data. The validity of the latter, however, is questionable as suggested in section 5.4.2. The biggest discrepancy between the two predicted rms temperatures is at the 77 cm height where the maximum deviation is approximately 100K. The higher rms values result from the greater spread of $P(\xi)$ offered by the lower C_{g2} setting. These trends are also apparent in figure 5.8 where the axial temperatures are presented.

Both predictions show reasonable agreement with the experimental data for the location of the peak mean temperature (cf. fig.5.8). The lower C_{g2} value results in better comparison with data until approximately 60cm, and then deviates as it takes on a shallower slope than the

temperature decay observed in the data. The higher C_{g2} value, on the other hand, performs less well at lower heights where temperatures are too high, but manages the correct slope higher up.

To assess which of the two predictions is the more appropriate to the fire is not straightforward since temperatures are also affected by heat loss. This has been treated at a rather simplistic level by the use of a single temperature flamelet, which was evaluated using the data at 14cm and then applied throughout the fire. However, it is expected that flamelets will more typically lose greater heat through radiative emission as height increases. This would occur since, as residence time increases, the flamelets broaden (due to molecular mixing) which results in a greater optical depth. Also soot levels increase, and so therefore does soot radiation, until burnout becomes significant. In the present fire, however, soot levels are low and gaseous emission dominates (cf. chapter 6). Eventually as the height increases still further and reaction zones no longer occur, the system will be controlled by the mixing of products and ambient air. Here, the lower temperatures will reduce radiative emission and an adiabatic flamelet becomes more appropriate.

It may be suggested that the reason for the C_{g2}=1.89 calculation to overpredict at heights below 60cm, is due to the adopted flamelet exhibiting insufficient heat loss for reasons suggested above. The subsequent agreement between the prediction and experimental data may then be due to the decreasing influence of heat loss as product-air mixing dominates.

The earlier arguments, however, could also be used to favour the C_{g2}=1.25 prediction. Here, the flamelet radiative loss is presumed to increase less rapidly with height and the divergence from the experimental data to occur further downstream. Figure 5.8 shows this to occur at approximately 55cm. The argument about the subsequent convergence between the data and adiabatic conditions implies that the prediction must eventually converge with the data. In this case it is presumed that this occurs further downstream (ie. above 77cm). As

figure 5.11 indicates, reaction zones are still apparent at 77cm for this prediction.

Neither of the two predictions violates the trends of Charnley's (1986) radiation measurements, where radiative emission is seen to fall drastically by 77cm. In the C_{g2}=1.89 case, lower emission results from the lower temperatures of the mixing dominated regime, whilst in the case of C_{g2}=1.25, the infrequent appearance of reaction zones leads to lower mean temperatures. At this stage, the problem cannot be resolved and the subsequent soot calculation (cf. section 5.6) and radiation predictions (cf. chapter 6) use the C_{g2}=1.25 results, since this produces better agreement with experimental temperatures at mid-heights, where radiative emission is highest.

Turning attention to the velocity field, figures 5.9 and 5.10 show the radial and axial plots. The predicted mean velocities seem plausible since they lie between the upper and lower bound data. Both the experimental data and the predictions indicate that high acceleration occurs within the first 20cm, above which the velocities start to level off. The experimental rms velocities indicate a near constant value over the heights 14 to 77cm. This is also apparent in the calculation though they are slight underpredictions.

To complete the flowfield picture, figure 5.12 and 5.13 show the axial and radial variation of the Favre mean species mole fractions. There are, however, no experimental data with which to verify these predictions. These profiles are used to determine local absorption coefficients in the radiation modelling of chapter 6.

This section has led to the prediction of the vector and scalar fields in the fire to be studied for radiation purposes in the next chapter. However, soot has so far been excluded and its calculation forms the focus of the next section.

5.6 Soot modelling

The model to be used to calculate soot concentrations in the present fire was introduced in chapter 3. There the semi-empirical derivation of the soot formation rate, as a function of mixture fraction, was derived from the experimental investigation of a laminar methane-air diffusion flame. Chapter 4 then described the incorporation of such a model in a turbulent computation. This entails setting up two additional balance equations (given the two-equation formulation (cf. chapter 3)), one for the soot number concentration and the other for the soot mass fraction.

Here, as in chapter 4, the soot balance equations are represented by eqn 4.24 for which the dependent variables are $\tilde{\phi}_n$ and $\tilde{\phi}_m$. Closure of the turbulence flux, as for the other balance equations, is achieved using the k-ε turbulence model. This leaves the source terms which take the following forms

$$\overline{S_n} = \overline{\alpha - \beta \ (n/N_0)^2} \qquad \ldots (5.15)$$

and

$$\overline{S_m} = \overline{\gamma \ n^{1/3} m^{2/3} + C_\delta \alpha} \qquad \ldots (5.16)$$

The α, β and γ are mixture fraction dependent parameters and were quantitatively derived in chapter 3 where the parameter set **prediction A** (cf. table 3.2) is used. Here their values differ from those in chapter 3 owing to the difference in flamelet temperature. Figure 5.14 shows the functions where the peak values of α, β and γ are 10%, 95% and 50% of the values obtained in the laminar flame.

The source terms (cf. eqns. 5.15-5.16) remain unclosed, given the present modelling strategy where soot-mixture fraction correlations are not available. However, chapter 4 showed that such correlations are relatively unimportant in comparison to those inherent in the mixture fraction dependent parameters. It was shown that adequate

closure could be achieved by neglecting terms involving fluctuation in soot properties. This leads to the following simplifications

$$\overline{S_n} = \bar{\alpha} - \bar{\beta}\ (\overline{n/N_0})^2 \qquad \ldots (5.17)$$

and

$$\overline{S_m} = \bar{\gamma}\ \bar{n}^{1/3}\ \bar{m}^{2/3} + C_\delta\ \bar{\alpha} \qquad \ldots (5.18)$$

These are more usefully expressed in terms of $\tilde{\phi}_n$ and $\tilde{\phi}_m$ which are the dependent variables of the balance equations cf.

$$\overline{S_n} = \bar{\alpha} - \bar{\beta}\ \bar{\rho}^2\ \tilde{\phi}_n^2 \qquad \ldots (5.19)$$

and

$$\overline{S_m} = \bar{\gamma}\ \bar{\rho}\ \tilde{\phi}_n^{1/3}\ \tilde{\phi}_m^{2/3}\ N_0^{1/3} + C_\delta\ \bar{\alpha} \qquad \ldots (5.20)$$

These sources now appear in closed form since $\tilde{\phi}_n$ and $\tilde{\phi}_m$ are the dependent variables of balance equations and the mixture fraction dependent parameters are straightforwardly averaged given $P(\xi)$ (cf. eqns 2.30).

Having set up the soot balance equations, boundary conditions are needed for their solution. The free stream is simply defined as having zero soot levels and the axis of symmetry is prescribed as a zero flux and zero gradient boundary. The initial boundary, however, is more problematic since the present calculation is initiated above the burner, where there is a non-zero soot profile. Furthermore there are no experimental soot measurements from which an initial profile can be defined. The following subsection describes how the available experimental information has been used to infer such boundary conditions.

5.6.1 Initial profiles

Though there are no soot measurements from which initial boundary conditions may be assigned, the spectral radiation measurements of Charnley (1986) may be used. These include line-of-sight mean spectral radiation over the range 0.5-0.9μm, where soot is the only significant radiator since the major gaseous peaks lie in the infrared. To infer local soot levels from such data, however, is not straightforward since, **(i)** point information is required from a single integral measurement, and **(ii)** the perceived mean radiation is subject to a substantial degree of turbulence interaction. This results from, for example, the link between soot concentration and temperature. For instance, Charnley (1986) estimated the minimum soot temperatures to be ~1600K, by fitting the Planck curve to the experimental data. This compares with a maximum mean temperature of about 1200K, indicating that even if the soot was radiating as a black body at the maximum mean temperature, the emitted radiation would be substantially underestimated. Turbulence-radiation interaction is addressed in the next chapter, where its modelling is described in detail. Below, therefore, only a brief description is provided for the purposes of giving sufficient information to allow the reader to follow the strategy to obtain an initial soot profile. It should be appreciated, however, that turbulence-radiation interaction must be considered and that more uncertainties are introduced since radiation is a path integral phenomenon and therefore includes multi-point statistics. The latter are not available from the simple moment approach used in the present modelling scheme, and as described in chapter 6, such correlations have been necessarily neglected.

The method used to address turbulence-radiation interaction used in chapter 6 is based on the Monte-Carlo approach of Faeth et al (1986). This requires the joint statistics of all radiatively-important scalars, which can then be randomly sampled to give instantaneous local properties along a path length, from which an instantaneous realisation of radiation may be obtained. Several such realisations may then be ensembled to yield mean radiation levels.

In the conserved scalar approach where all scalars are related to mixture fraction, its PDF, $P(\xi)$, holds all the relevant local statistical information. Random sampling of $P(\xi)$ will then yield instantaneous mixture fraction values from which instantaneous values of any scalar, ϕ, may be obtained from the state relationship $\phi(\xi)$. The instantaneous values sampled in this way will yield the appropriate ensembled statistics.

The incorporation of soot introduces complications since it is governed by relatively slow formation processes and cannot therefore be described in terms of mixture fraction alone; it is also a function of residence time ie. $f_v=f_v(\xi,t)$. Its statistics are therefore described by the joint PDF, $P(\xi,t)$. Such a two-parameter PDF is, however, not forthcoming, given the present modelling scheme and its evaluation should ideally await temporally resolved measurements of soot concentration and mixture fraction. A simplification has therefore been introduced whereby the appropriate residence time, at any location, has been assumed to be invariant. Here one may write $f_v=f_v(\xi;t)$ ie. for a particular characteristic residence time soot is purely a function of mixture fraction. If it is further assumed that soot always remains at the same mixture fraction (ie. plug flow), then the soot formation rate given by equation 3.8 becomes an ordinary differential equation, for any given constant mixture fraction, and may be integrated to yield f_v at any residence time. If such a calculation is repeated for all mixture fractions at which the source term is active, relationships $f_v(\xi;t_p)$, where t_p is plug flow residence time, may be constructed for a range of residence times. Figure 5.15 shows these relationships for soot formation residence times ranging between 0.03 and 0.08 seconds.

Under the above assumptions therefore, a unique function $f_v(\xi)$ may be prescribed, allowing soot to be treated as any other mixture fraction dependent scalar in the radiation model. The precise function, however, requires a suitable plug flow residence time. To define the initial profile, the appropriate residence time was found in an

iterative manner by matching calculated soot radiation with the experimental data. The procedure can be described as follows:-

(i) Guess t_p (assume it to be constant for all points at the 14cm height)

(ii) calculate $f_v(\xi;t_p)$ through plug flow integration of formation rate

(iii) calculate mean visible radiation

(iv) compare with experiment and go to **(i)** if unsatisfactory.

Figure 5.16 shows the mean line-of-sight radiation intensity at 0.9μm plotted against plug flow residence time. Also shown is the experimentally observed intensity which indicates a suitable plug flow residence time to be ~0.06 s. This compares with an estimated bulk convection time of 0.2s, which was deduced from the experimental centreline velocities. The convective time, however, is expected to be longer since the plug flow time represents a limit where the soot always exists at a favourable mixture fraction. However, low down in the fire, where the flow is quasi-laminar, soot and mixture fraction transport will differ and such a limiting condition will not be realised. It should also be noted, as will be pointed out in chapter 6, that the radiation model tends to overpredict emitted fluxes. This would result in too modest a calculated plug flow residence time.

Figure 5.17 shows the mean spectral radiation over 0.5-0.9μm, where the instantaneous soot profile is evaluated at a residence time of 0.058s. This is compared to the data of Charnley (1986).

Having defined an appropriate plug flow residence time for the 14cm height, the soot number density and soot volume fraction may be expressed solely in terms of mixture fraction cf. $n=n(\xi;t_p)$ and $f_v=f_v(\xi;t_p)$. Local mean values, $\bar{n}$ and $\bar{m}$, can then be derived from local $P(\xi)$. It is, however, profiles of $\tilde{\phi}_n$ and $\tilde{\phi}_m$ that are required since they are the dependent variables of the soot balance equations. These are readily found from

$$\tilde{\phi}_n = \bar{n} \; / \; (N_0 \, \bar{\rho}) \qquad \ldots (5.21)$$

and

$$\tilde{\phi}_m = \rho_s \, \bar{f}_v \; / \; \bar{\rho} \qquad \ldots (5.22)$$

Having obtained initial boundary conditions and having earlier prescribed the source terms of the soot balance equations, the latter can be solved. The soot predictions are reported in the next subsection.

5.6.2 Soot predictions

Figure 5.18a shows radial profiles of f_v at heights 14, 30, 45 and 77cm where the former represents the initial profile which was specified as described above. Figure 5.19 shows the corresponding axial prediction. The soot source terms were closed as shown in equations 5.17 and 5.18 where the empirically determined constants in the mixture fraction dependent parameters are taken from chapter 3 (cf. **prediction A** table 3.2). The parameters themselves are shown in figure 5.14. Also shown in figure 5.19 and in figure 5.18b are the results of a prediction where some measure of oxidation is included. Discussion of the latter is deferred until later.

The figures show soot volume fraction to increase with height at a rate somewhat greater than linear (~1.45 maximum) upto a height of approximately 50cm. Subsequently the slope decreases; this results from the decay of the soot source terms as the availability of hydrocarbon soot precursors diminish. Unfortunately there is no experimental data with which the predicted trends may be verified. However, the soot radiation data of Charnley (1986), when coupled with the later reported radiation calculations (cf. chapter 6), indicates soot volume fraction levels to be more or less comparable at the 14, 30 and 45cm heights. At the 77cm height lower levels are indicated.

It seems, therefore that either the soot formation rate is overestimated or soot oxidation, which has not been incorporated in the soot source terms, plays a role at heights as low as 30cm. As discussed in chapter 4, soot oxidation is possible if soot instantaneously migrates from the rich formation zones to leaner regions, where OH and O_2 oxidation may occur.

It should also be stressed that errors may result from the simplifications made in closing the soot source terms ie. in simplifying equations 5.15 and 5.16 to 5.17 and 5.18. Chapter 4, however, estimated these to be of relatively minor significance in comparison to the specification of the instantaneous source term itself; in particular, its dependence on mixture fraction.

It is interesting to look at the soot volume fraction results in terms of time scales. Figure 5.20 shows the plug flow residence time of the soot volume fraction derived by equating

$$\bar{f}_{v_{b.e.}} = \bar{\rho} \int_0^1 \frac{f_v(\xi;t_p)}{\rho(\xi)} \tilde{P}(\xi)\, d\xi \qquad \ldots (5.23)$$

where the suffix **b.e.** indicates the mean soot volume fraction as obtained through solution of its balance equation. The 14cm profile of t_p is set to a constant value as specified. At subsequent heights, it is interesting to note that, for the most part, the profiles are reasonably flat. At the extremities of the jet at height 77cm, however, the residence time increases. This indicates that much of the soot in these locations is due to transport rather than formation. If the latter was more dominant, then the residence time, obtained in the manner specified, should fall as the free stream boundary is approached, since the continual entrainment of air into the fire would ensure that lower residence times pertain. Such is observed at the lower heights cf. 14, 30 and 45cm. The soot levels in the outer regions at 77cm would therefore be affected by oxidation. This

analysis, however, does not rule-out the possibility of oxidation at the lesser heights.

The soot model constants specified as **prediction B** (cf. table 3.2) yield lower soot levels than the one adopted above, since the growth rate is lower (cf. chapter 3). Though both sets of constants produce plausible fits to the laminar flame data (cf. fig. 3.13b), there is a substantial extrapolation in residence time between the flame studied in chapter 3 and the present fire. However, though the situation may be improved by adopting the alternative model constants, the importance of oxidation is still apparent.

Oxidation terms, as represented by equations 4.21 and 4.22, were therefore appended to the source terms of the soot number density and mass concentration equations. These were derived from the correlation of Nagle and Strickland-Constable (1962) which considers soot oxidation by molecular oxygen (cf. equation 2.36). The simplifications made in averaging the oxidation terms are similar to those adopted for the mean formation rate discussed earlier.

As observed in chapter 4, when the Nagle and Strickland-Constable expression is applied without modification, excessive oxidation is observed. This leads to negligible soot levels at the 30cm height. Possible causes of this feature were discussed in chapter 4, where the most likely was identified as being the typically strong negative correlations occurring in the mean oxidation rate, which have been neglected. These result from the necessary instantaneous coexistence of soot particles and an oxidizing environment in order for oxidation to occur. If soot particles always remain in rich formation regions, oxidation cannot take place.

There are also other uncertainties over, for example, the specification of the instantaneous oxidation rate itself, such as how applicable is the Nagle and Strickland-Constable expression to flame zones? Also, OH and O oxidation will undoubtedly occur in addition to O_2 oxidation.

The satisfactory incorporation of soot oxidation cannot be achieved in view of the above uncertainties and further progress would ideally require laminar flame soot oxidation measurements and, perhaps more importantly, a better representation of the intermittency between the sooting sheets and oxidizing mixtures. Here, in order to specify a reasonable oxidation rate, use has been made of the experimental luminous radiation data at the 30cm height. The instantaneous oxidation rate was multiplied by a factor which was fixed in such a way that the calculated radiation at 30cm was consistent with the data. The factor was deduced to be 0.056.

Figure 5.18b shows the profiles of soot volume fraction incorporating the scaled oxidation rate, and figure 5.19 shows the axial variation where it is compared with the non-oxidation prediction. As arranged, the levels of soot at the 30cm height are similar to those at 14cm, dictated by the radiation data of Charnley (1986) and its subsequent interpretation by the radiation model, described in chapter 6. It is interesting to note that the level at 45cm is similar to that at 14cm and 30cm and that levels are reduced at 77cm. Both these features are indicated by the radiation measurements of Charnley (1986).

Further discussion of the soot predictions is left until chapter 6, where the radiation predictions are reported. It should be mentioned, however, that though the predictions are unsatisfactory in respect of the soot oxidation, the study of which is to be highlighted as future work, radiation in the present fire is dominated by gaseous emission. Uncertainties in soot levels are therefore of only minor importance in the investigation of the radiative emission and do not influence the conclusions drawn in aspects of turbulence-radiation interaction. The latter is a major concern in chapter 6.

5.7 Conclusions

This chapter has described the modelling of a laboratory-scale simulated methane fire, which included the calculation of temperature, gaseous species concentration and soot. This fire was also experimentally investigated by Crauford (1984), whose study provided detailed velocity and temperature data with which to compare the predictions. Good agreement is evident between prediction and experiment.

Closure of the Reynolds stresses and scalar fluxes was achieved through use of the two-equation k-ε model, where the effect of buoyancy on turbulence was included only through its influence in the source terms of k and ε.

The scalar field is addressed using the laminar flamelet model, where the PDF of mixture fraction is specified as a beta function. The flamelet relationships that describe the instantaneous scalar state are obtained from the experimental data of Mitchell et al (1980). Their temperature flamelet, however, was perturbed in order to incorporate the effect of increased radiative heat loss.

The modelling of soot introduces difficulties, since it is governed by relatively slow formation processes and the conserved scalar approach does not apply. It is treated here using the model described in chapter 3, where both the slow chemistry and turbulence interaction may be considered by defining the formation rate in terms of mixture fraction. In the present application there are additional difficulties related to initial conditions and the soot predictions must therefore be considered tentative. No soot data is available for direct comparison.

The flamelet view of the scalar state, where statistical scalar information is available in the computed mixture fraction PDF, offers the detail necessary to evaluate the influence of turbulence-radiation interaction. The latter is studied in chapter 6.

ϕ	σ_ϕ	$\sigma_{\phi t}$	S_ϕ
$\tilde{u}$	1	1	$-d\bar{P}/dx - \bar{\rho}\, g$
k	1	1	$\mu_t (\partial\tilde{u}/\partial r)^2 + G_{bk} - \bar{\rho}\varepsilon$
ε	1	1.3	$C_{\varepsilon 1}(\varepsilon/k)[\mu_t (\partial\tilde{u}/\partial r)^2 + G_{bk}] - C_{\varepsilon 2}\bar{\rho}\varepsilon^2/k$
$\tilde{\xi}$	0.7	0.7	0
ξ''^2	0.7	0.7	$C_{g1}\mu_t (\partial\tilde{\xi}/\partial r)^2 - C_{g2}\bar{\rho}(\varepsilon/k)\xi''^2$
$\tilde{\phi}_N$	$1x10^{10}$	1	$\bar{\alpha} - \bar{\beta}\,\bar{\rho}\,\tilde{\phi}_N^2$
$\tilde{\phi}_m$	$1x10^{10}$	1	$N_0^{1/3}\,\bar{\gamma}\,\bar{\rho}\,\tilde{\phi}_N^{1/3}\,\tilde{\phi}_m^{2/3} + \bar{\delta}$

$C_{\varepsilon 1} = 1.44 \qquad C_{\varepsilon 2} = 1.92 \qquad C_{g1} = 2.8 \qquad C_{g2} = 1.89$

$$G_{bk} = g\,(1/\bar{\rho})\,\frac{\mu_t}{\sigma_\rho}\,\frac{\partial\bar{\rho}}{\partial x}$$

Table 5.1

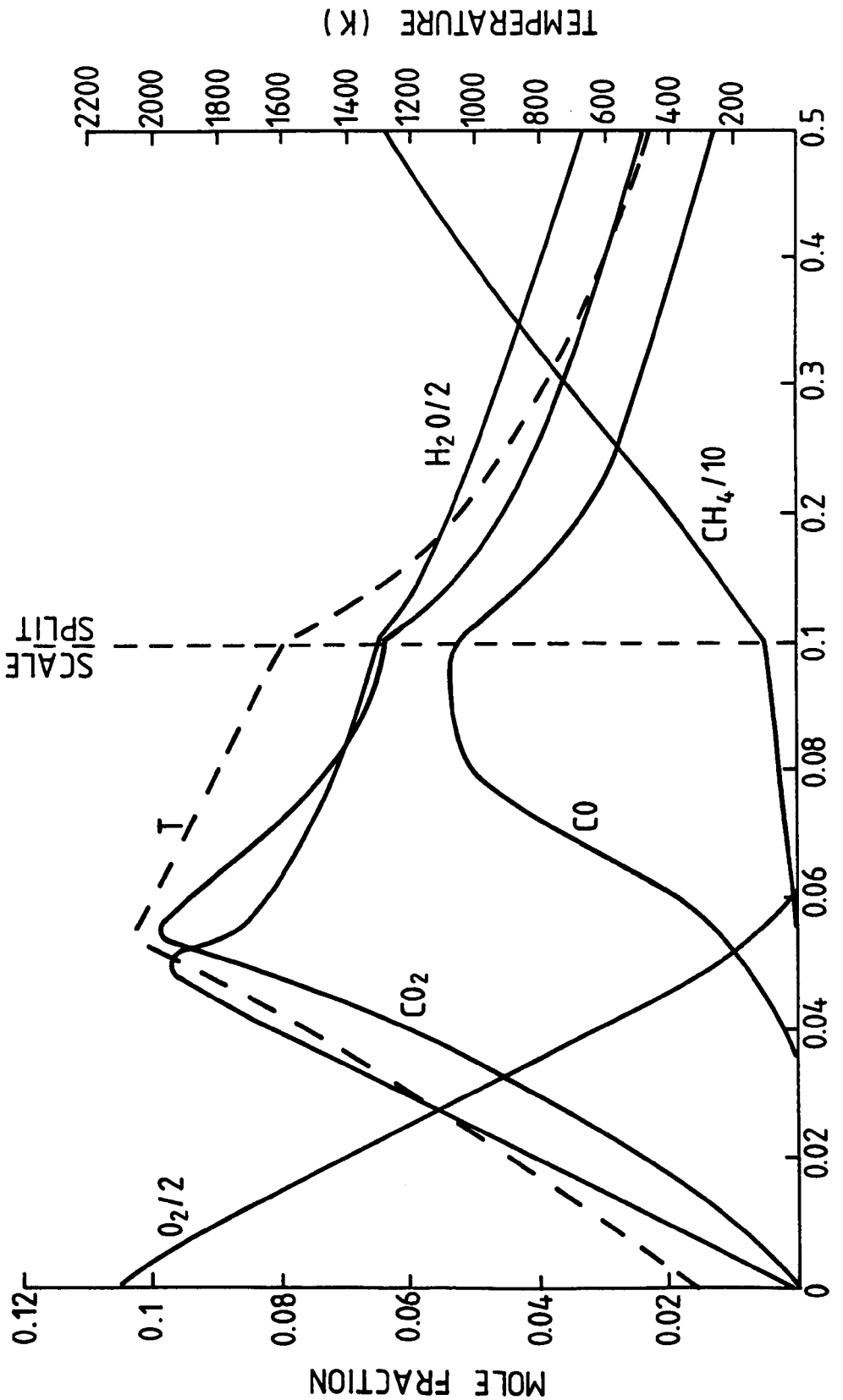

Figure 5.1 - Data of Mitchell et al (1980)

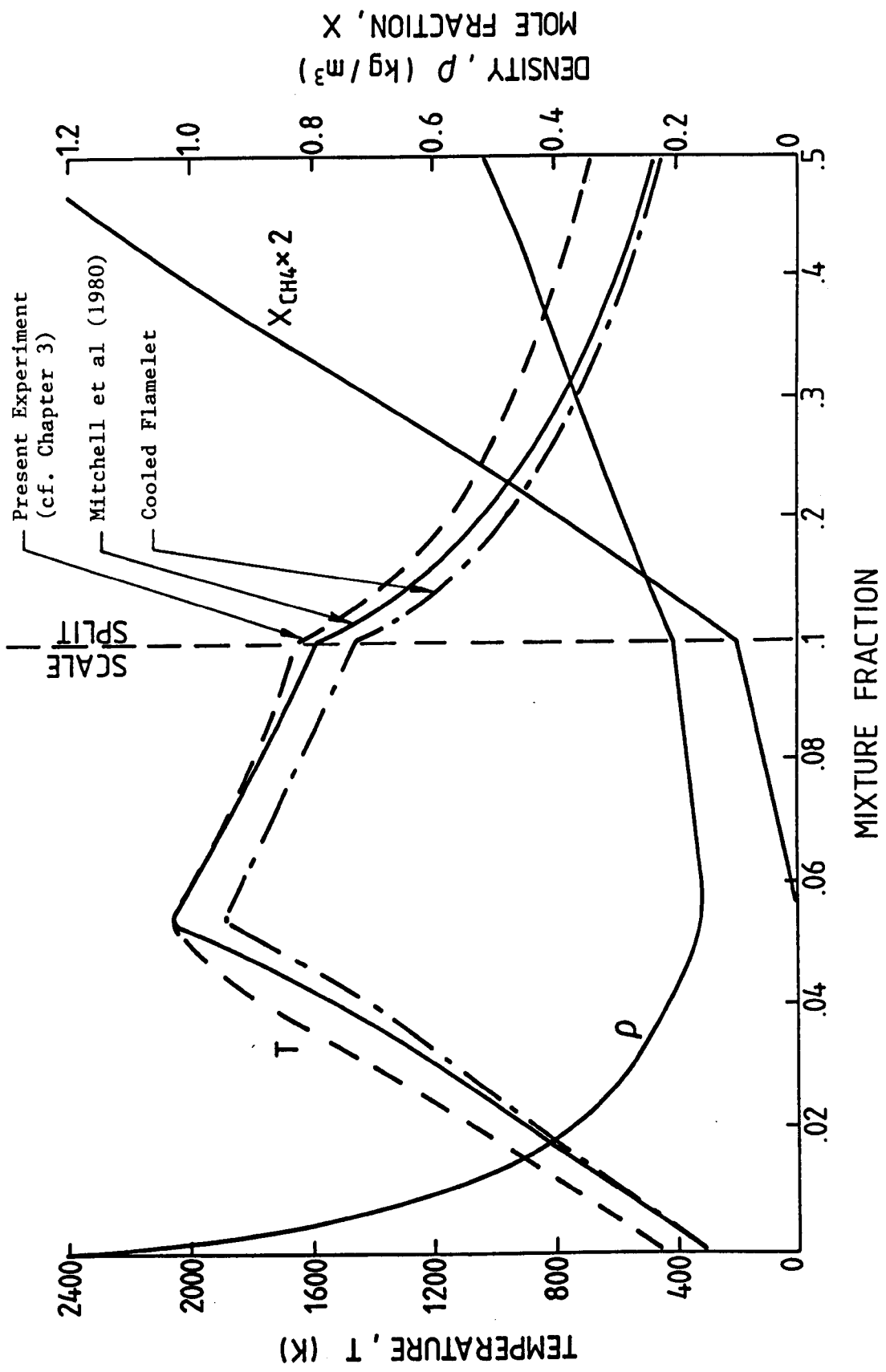
TEMPERATURE , T (K)
DENSITY , ρ (kg/m³)
MOLE FRACTION, X
MIXTURE FRACTION
T
ρ
X_{CH4}×2
SCALE SPLIT
Present Experiment (cf. Chapter 3)
Mitchell et al (1980)
Cooled Flamelet
2400
2000
1600
1200
800
400
1.2
1.0
0.8
0.6
0.4
0.2
0
.02
.04
.06
.08
.1
.2
.3
.4
.5

Figure 5.2

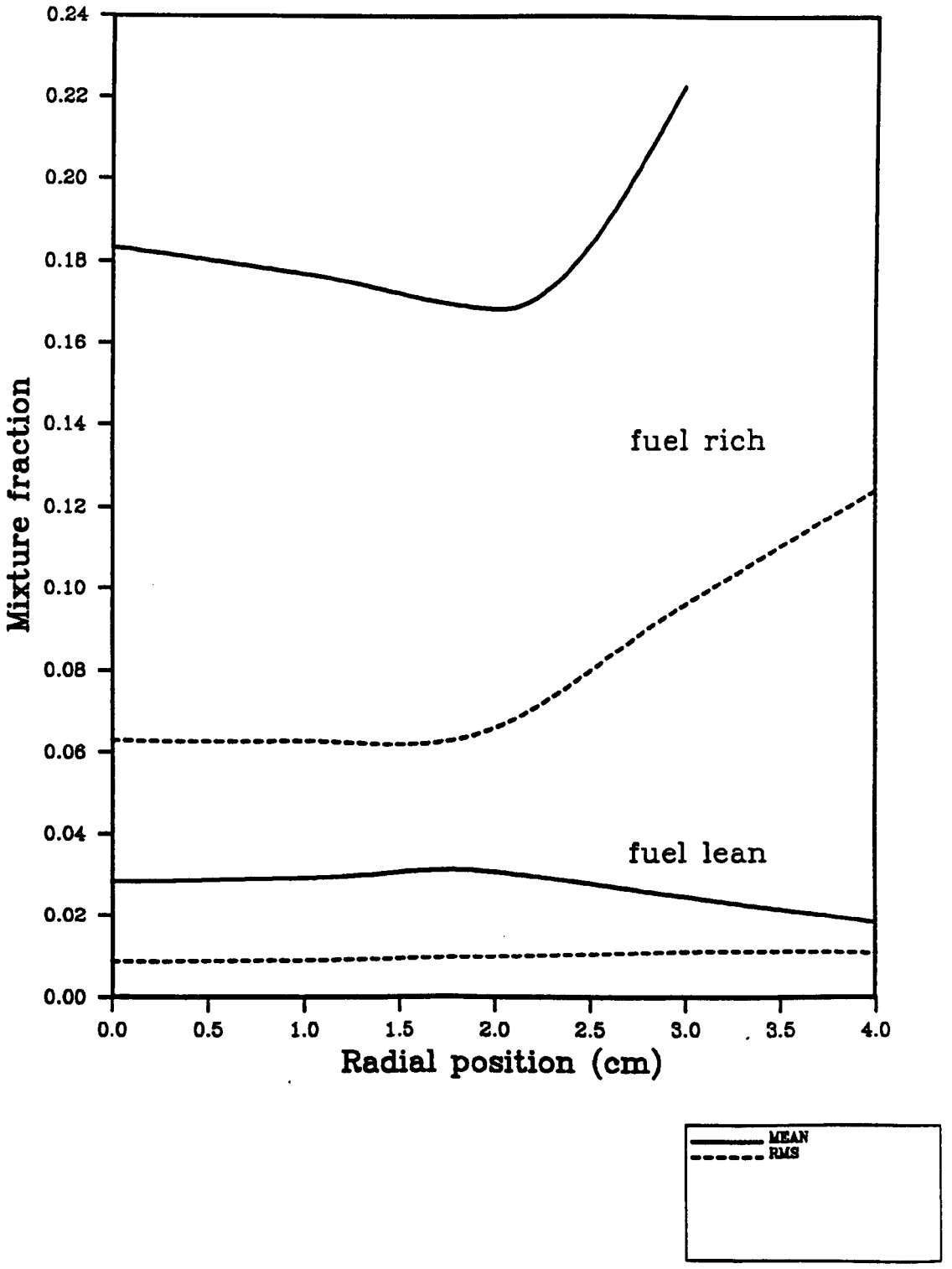

Profiles of Reynolds mean and rms mixture fraction deduced from 14cm height temperature data of Crauford (1984) using temperature state relationship of Mitchell et al (1980)

Figure 5.3

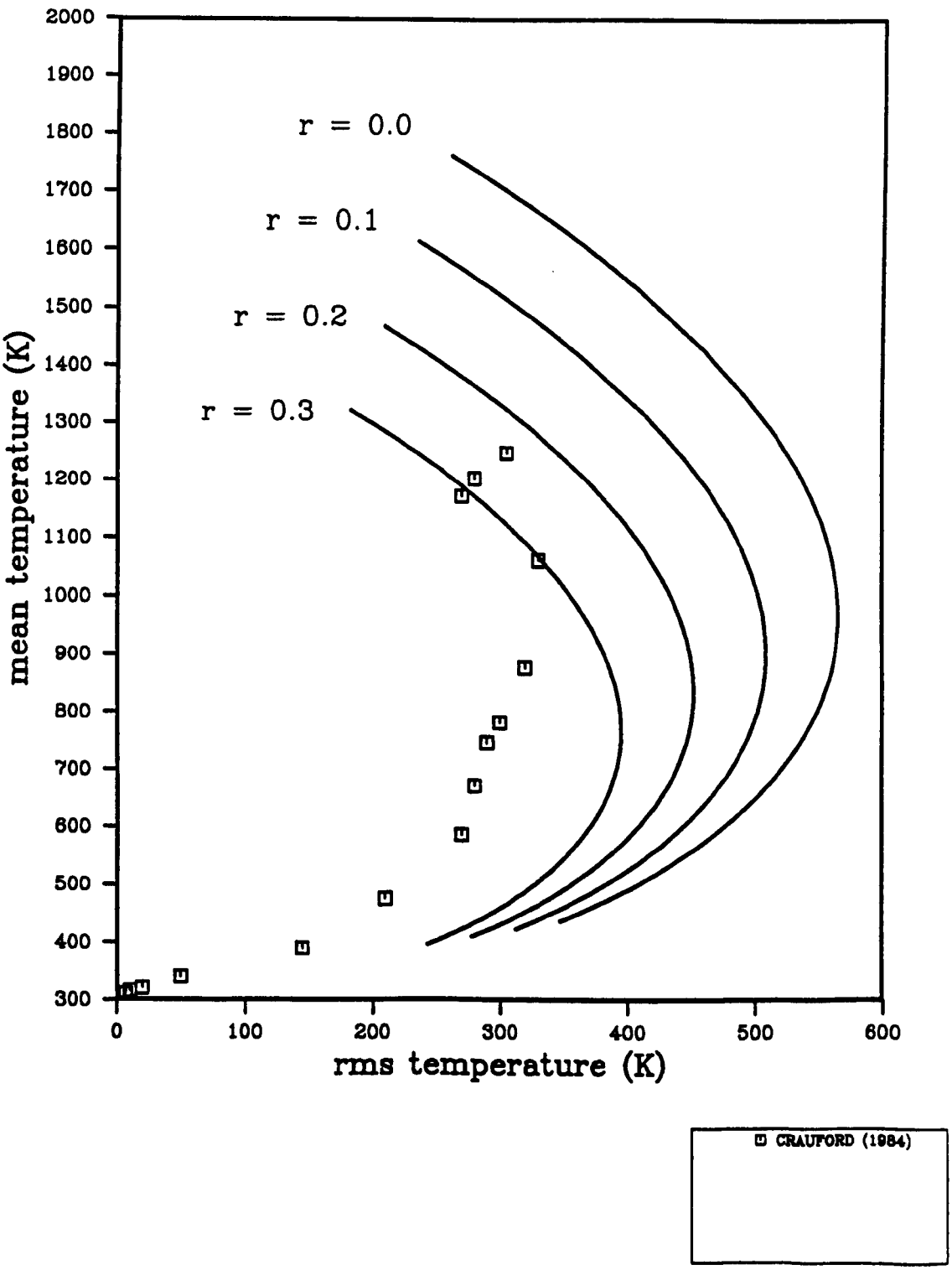

Experimental data of Crauford (1984) (height=14cm) shown against stoichiometric boundaries derived for varying flamelet heatloss.
The parameter r is defined in equation 5.14.

Figure 5.4

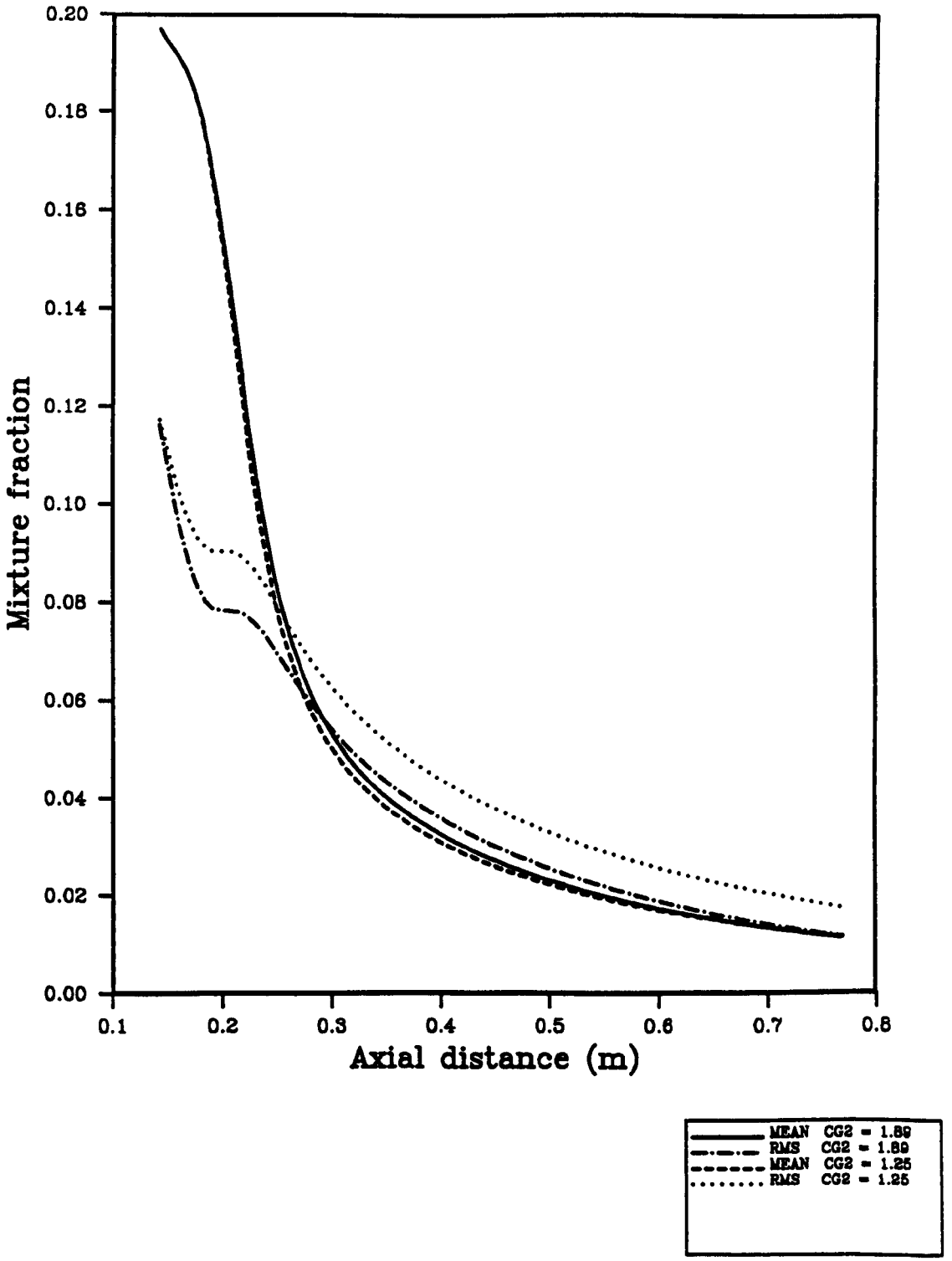

Prediction of axial variation of Favre mean and variance of mixture fraction in fire of Crauford (1984). Predictions show the effect of Cg2.

Figure 5.5

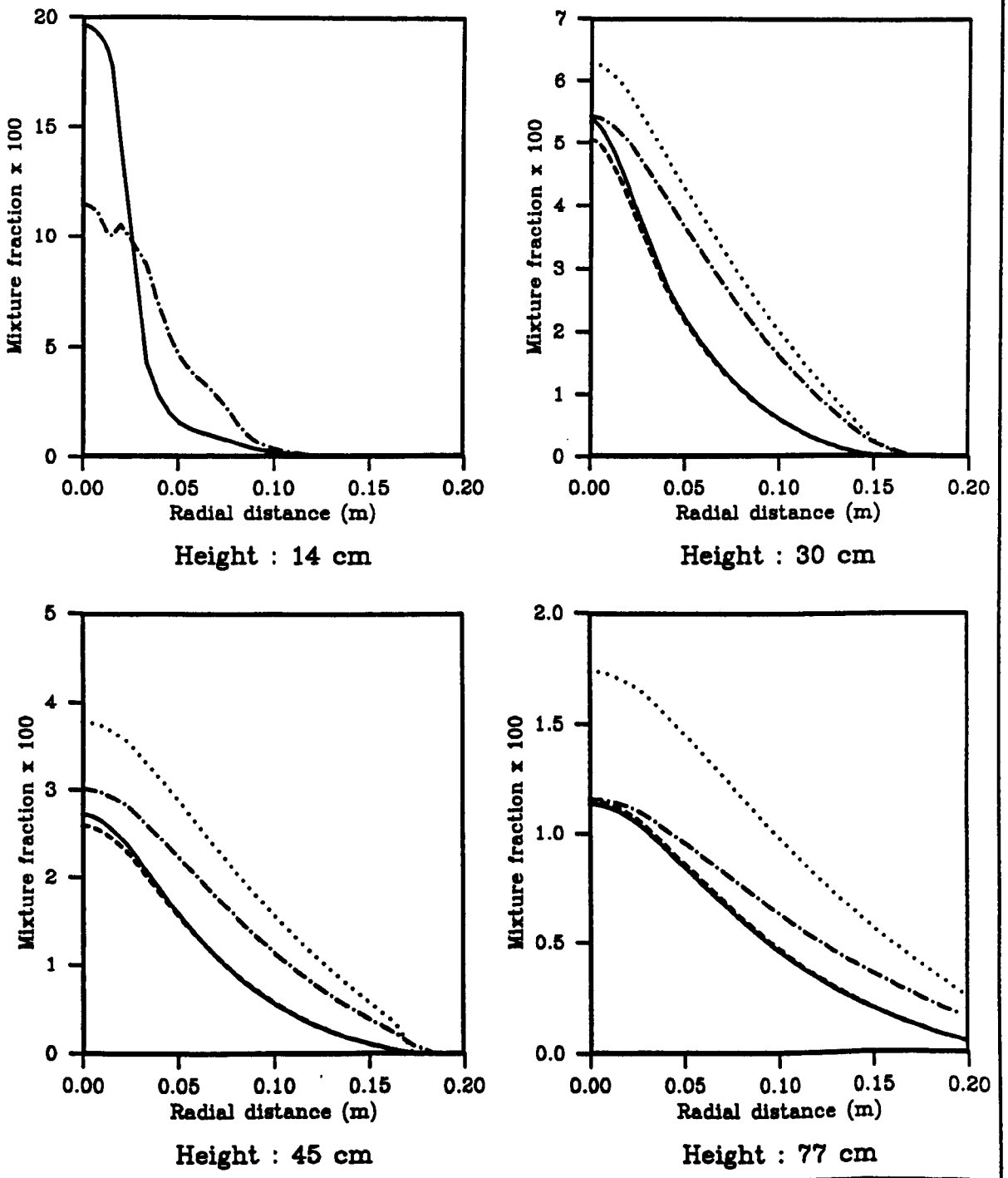

Predictions of radial profiles of Favre mean and rms mixture fraction in fire of Crauford (1984). Predictions show the effect of Cg2.

Figure 5.6

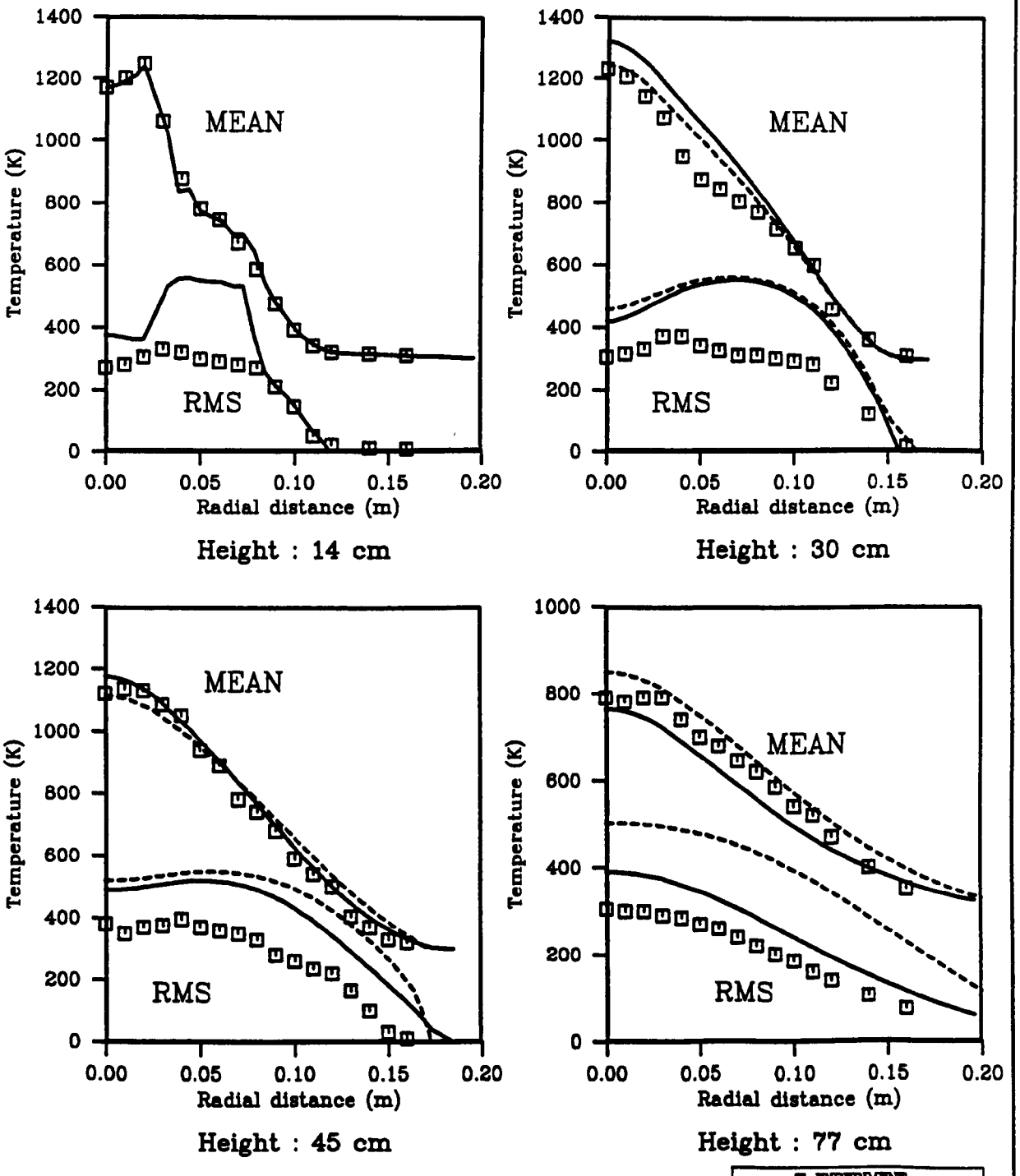

Radial profiles of temperature
Predictions of Reynolds mean and rms temperature compared with data of Crauford (1984)

Figure 5.7

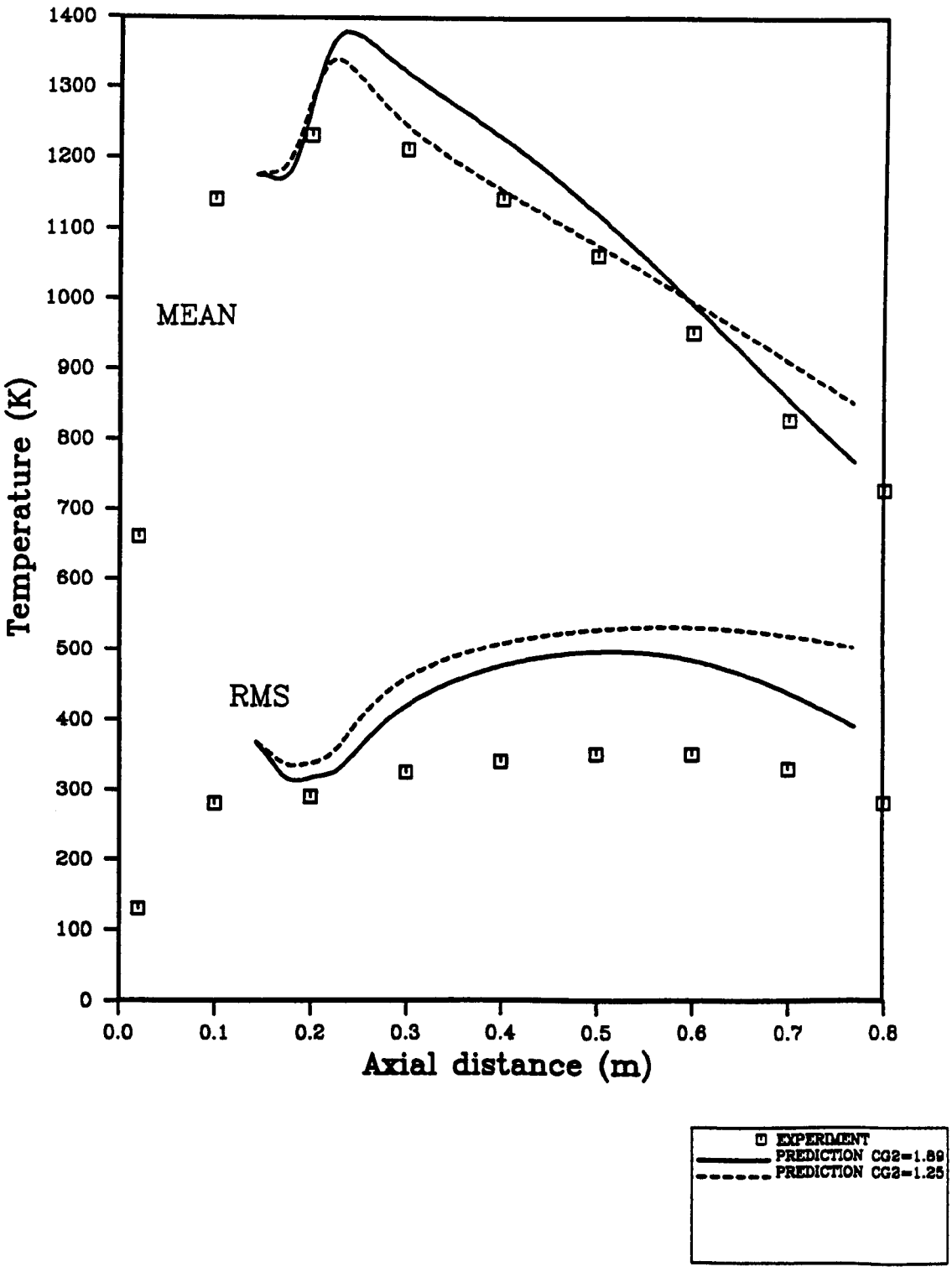

Axial variation of temperature
Predictions of Reynolds mean and rms temperatures
compared with data of Crauford (1984)

Figure 5.8

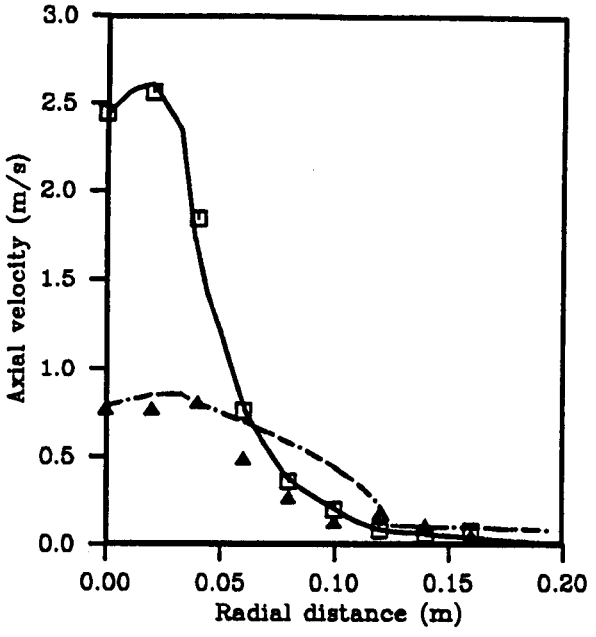

Height : 14 cm

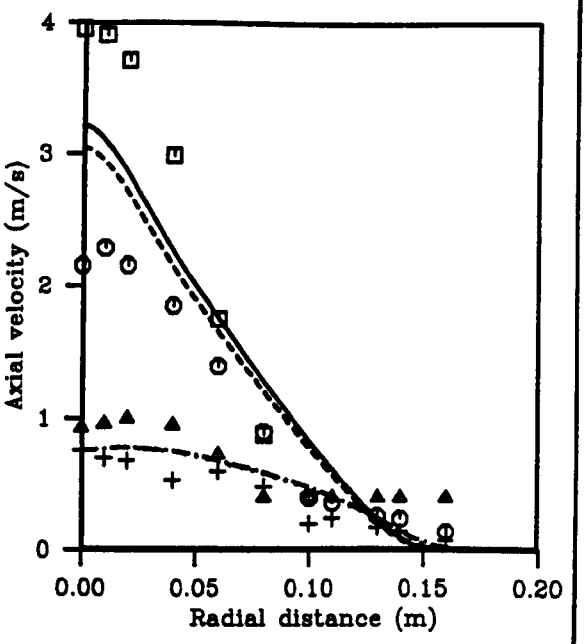

Height : 30 cm

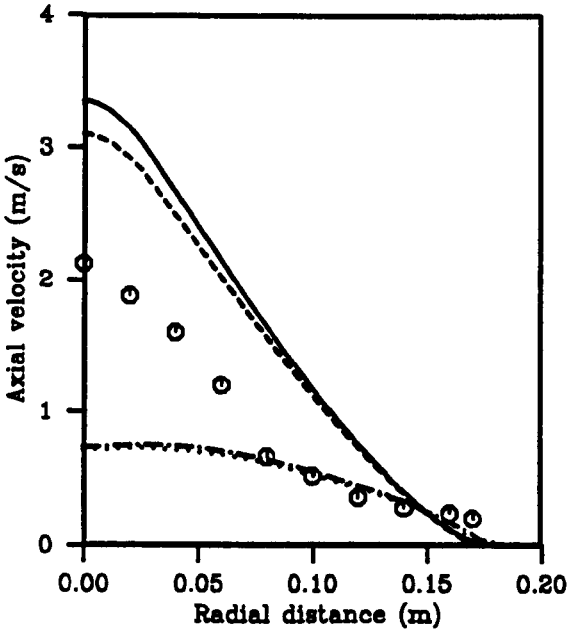

Height : 45 cm

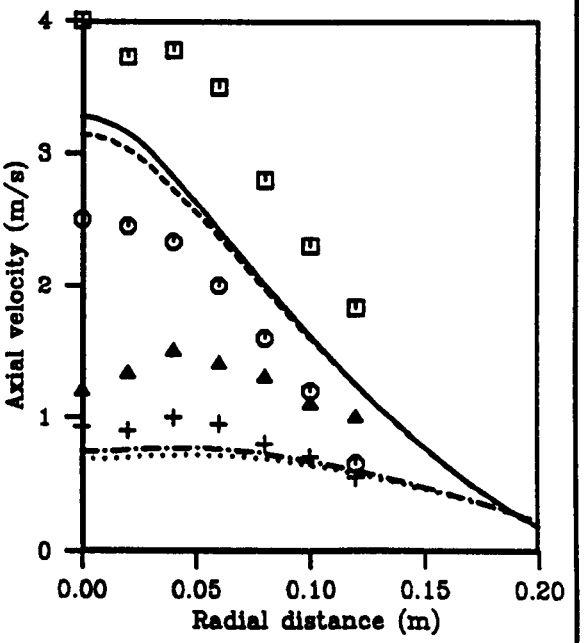

Height : 77 cm

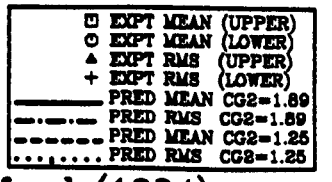

Radial profiles of mean and rms axial velocity compared with data of Crauford (1984).

Figure 5.9

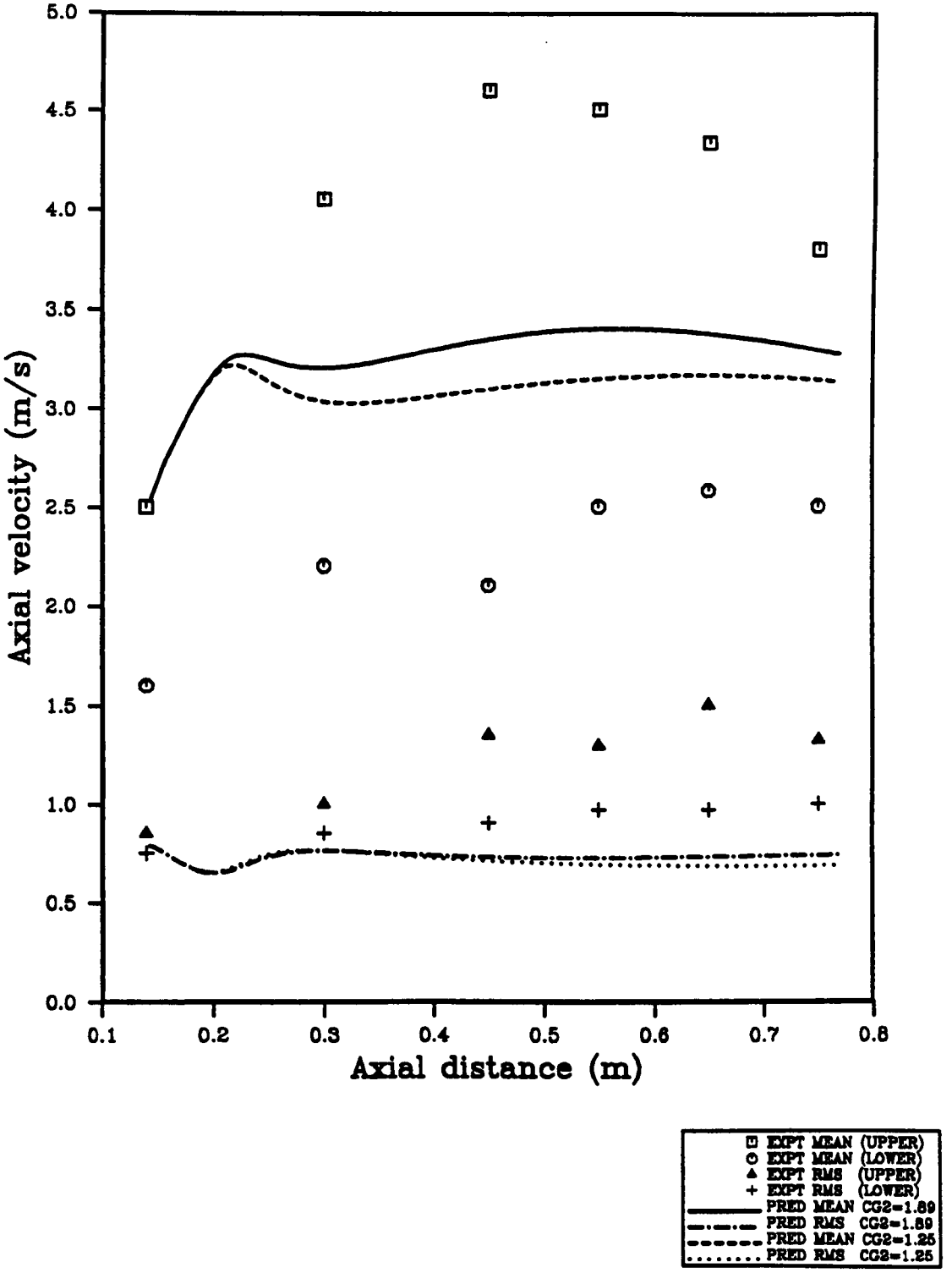

Axial variation of mean and rms velocity. Prediction of Favre mean quantities compared with Reynolds mean data of Crauford (1984). Predictions show the effect of Cg2.

Figure 5.10

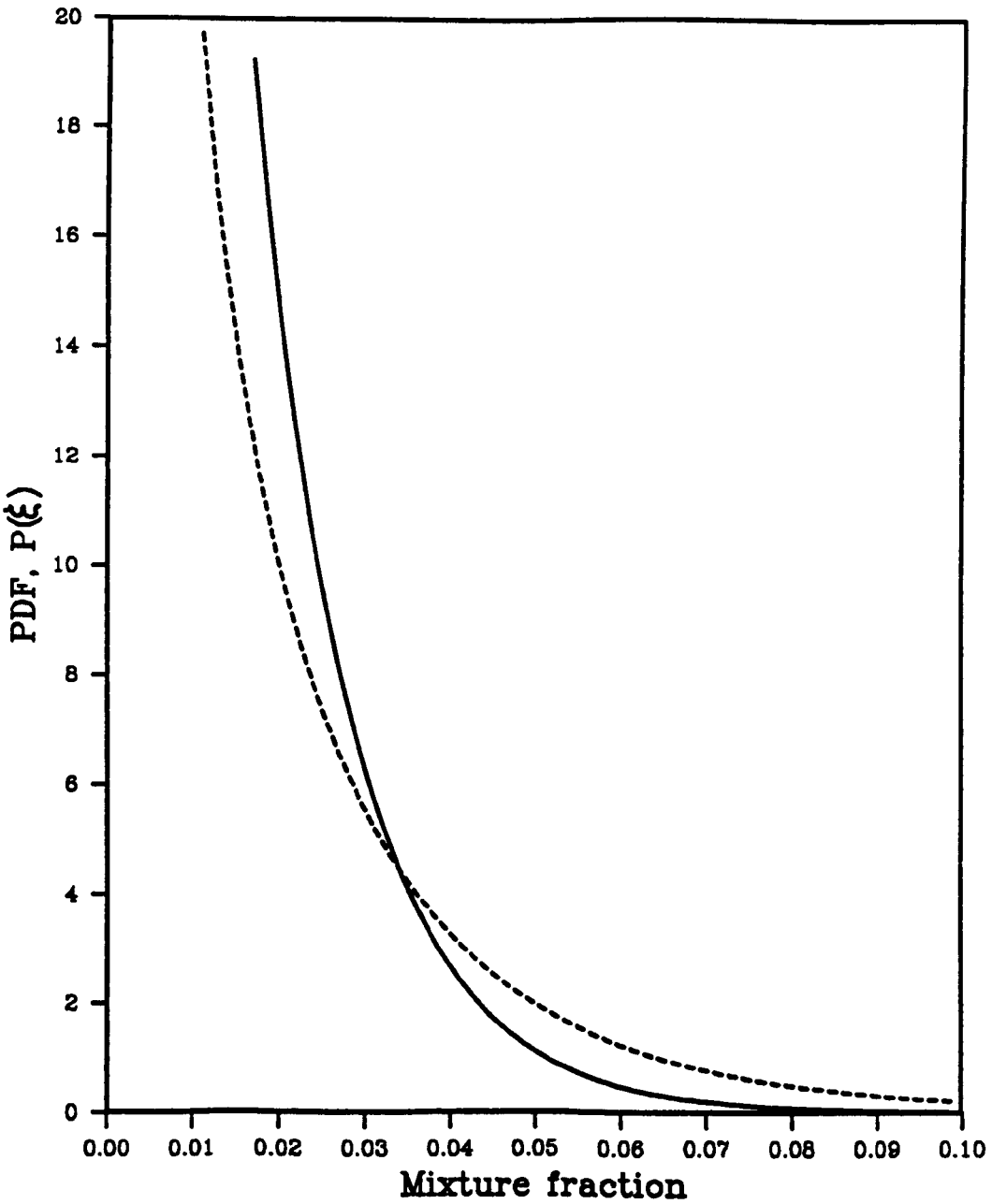

Centre-line PDF of mixture fraction at 77cm above burner in fire of Crauford (1984).
Predictions show the effect of Cg2.

Figure 5.11

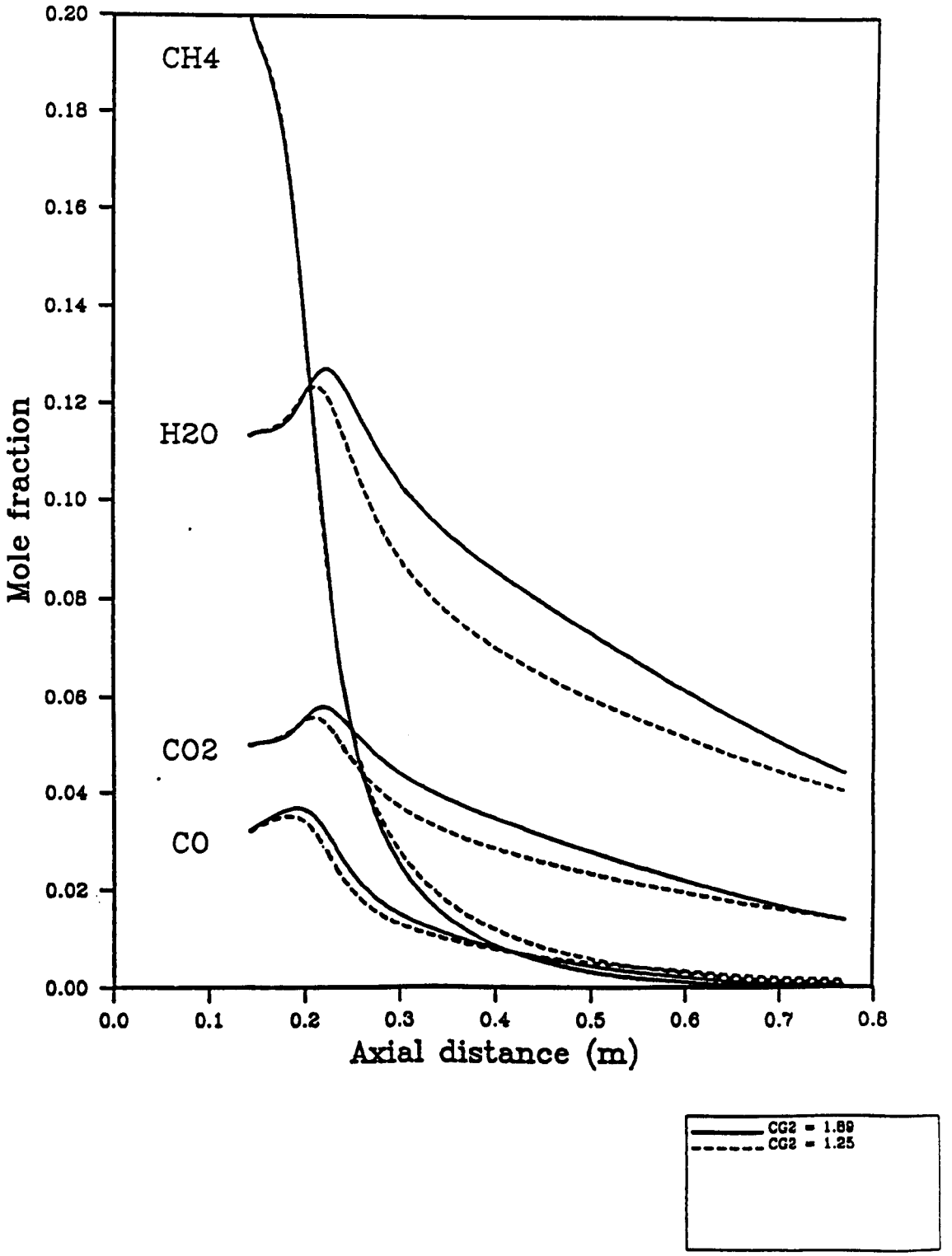

Prediction of axial variation of Favre mean species concentration in fire of Crauford (1984). Predictions show the effect of Cg2.

Figure 5.12

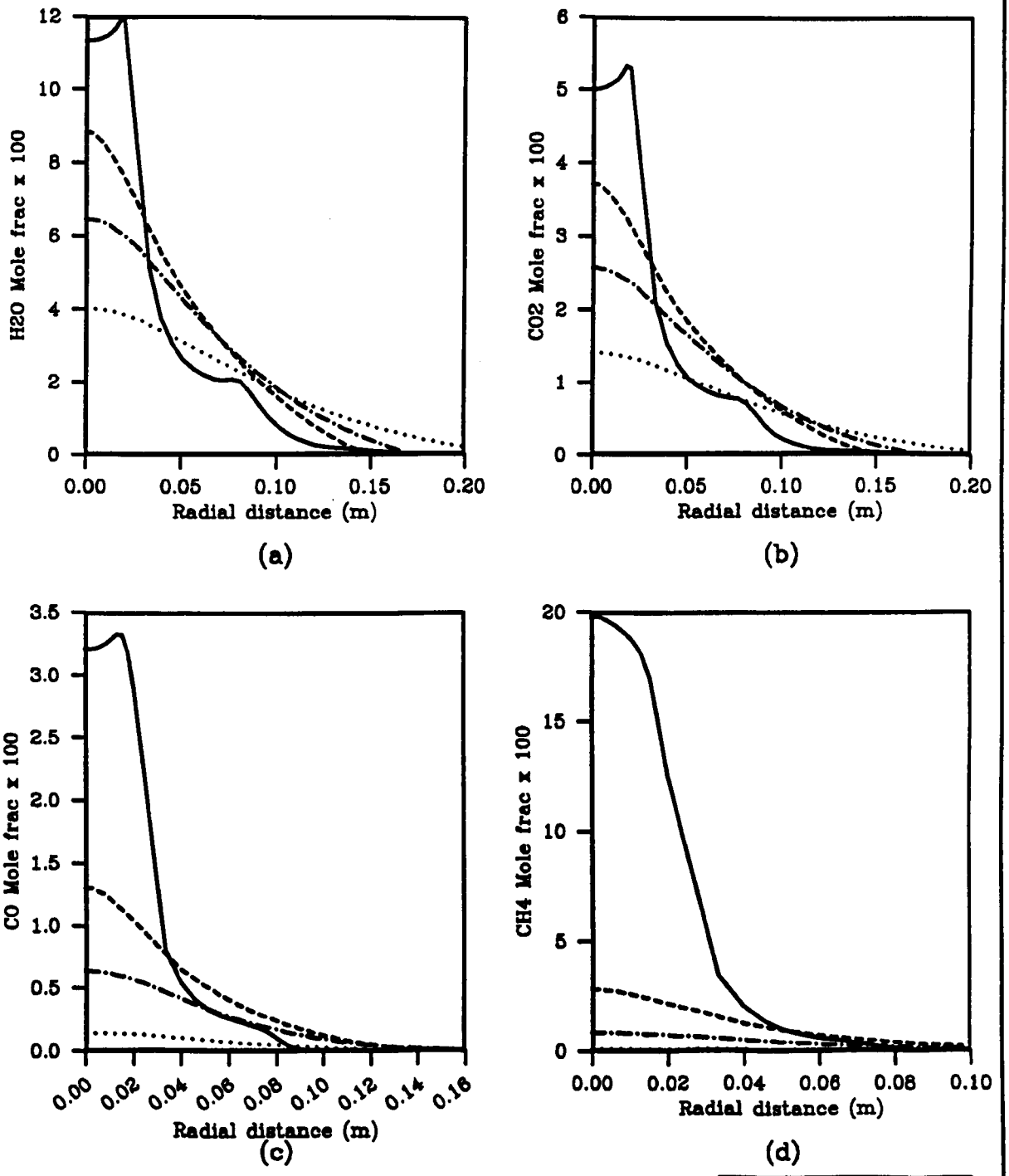

Predicted radial profiles of Favre mean species concentrations in fire of Crauford (1984)

Figure 5.13

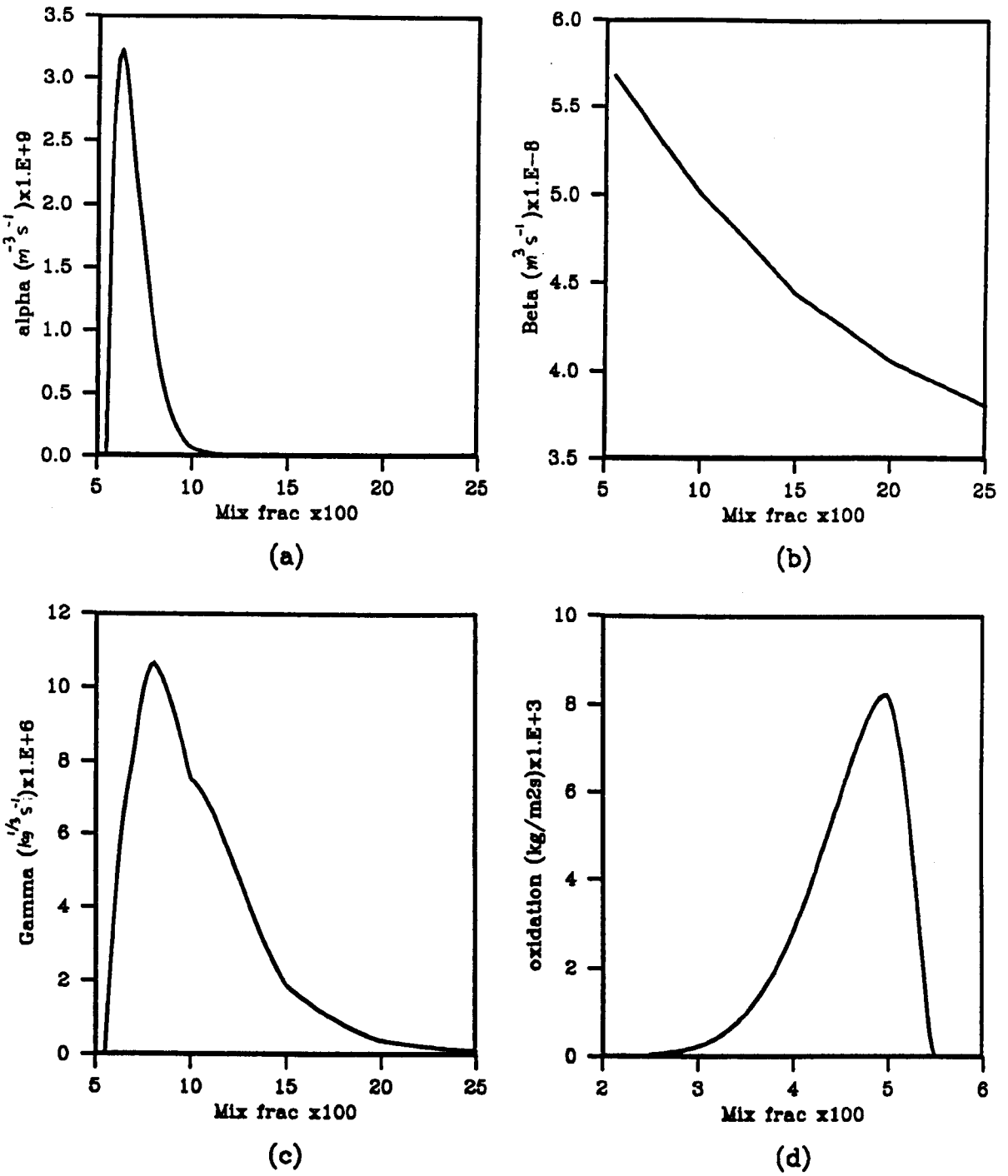

Soot source parameters used in prediction of Crauford (1984)'s fire.

Figure 5.14

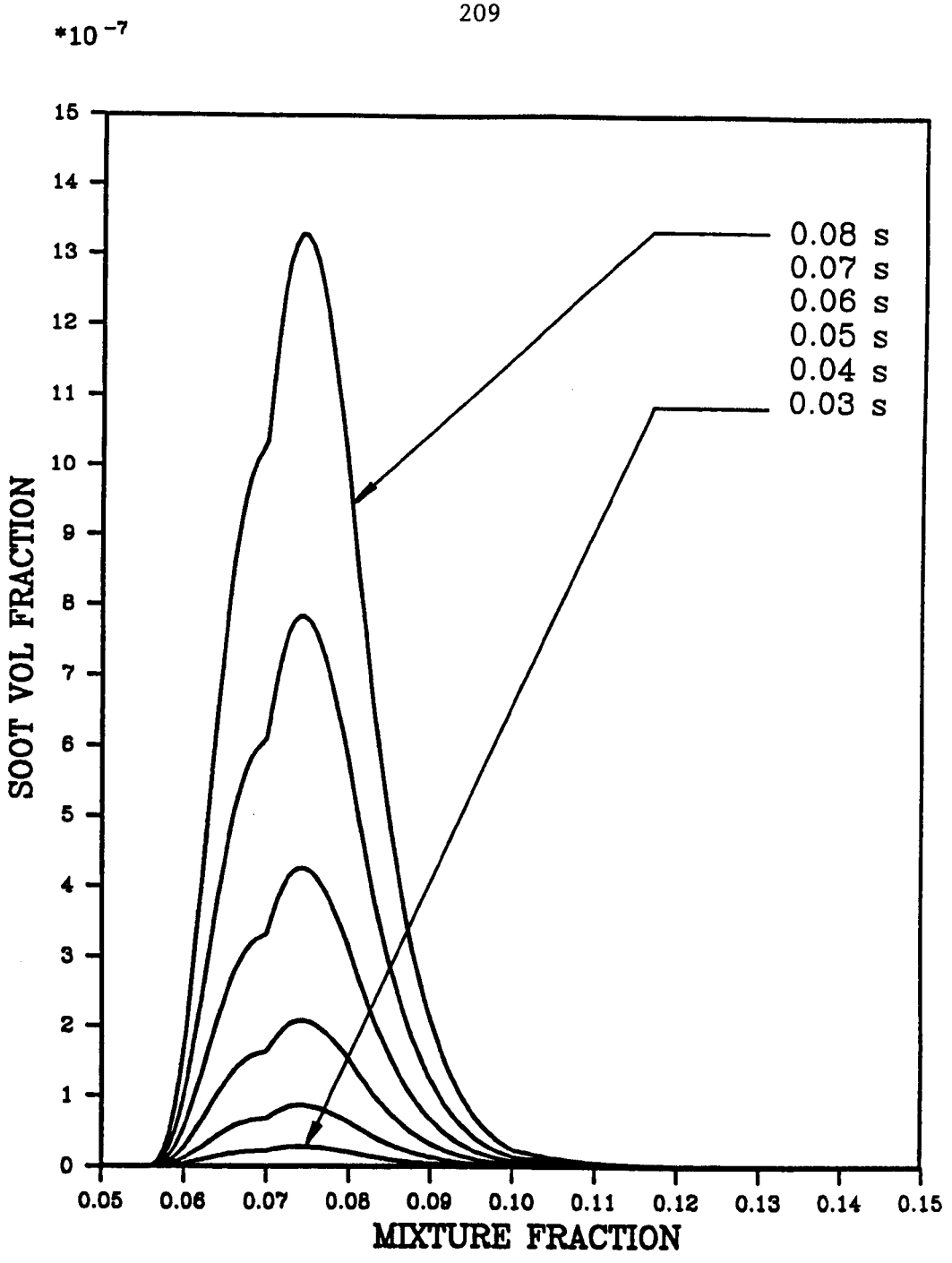

Soot volume fraction state relationships

Figure 5.15

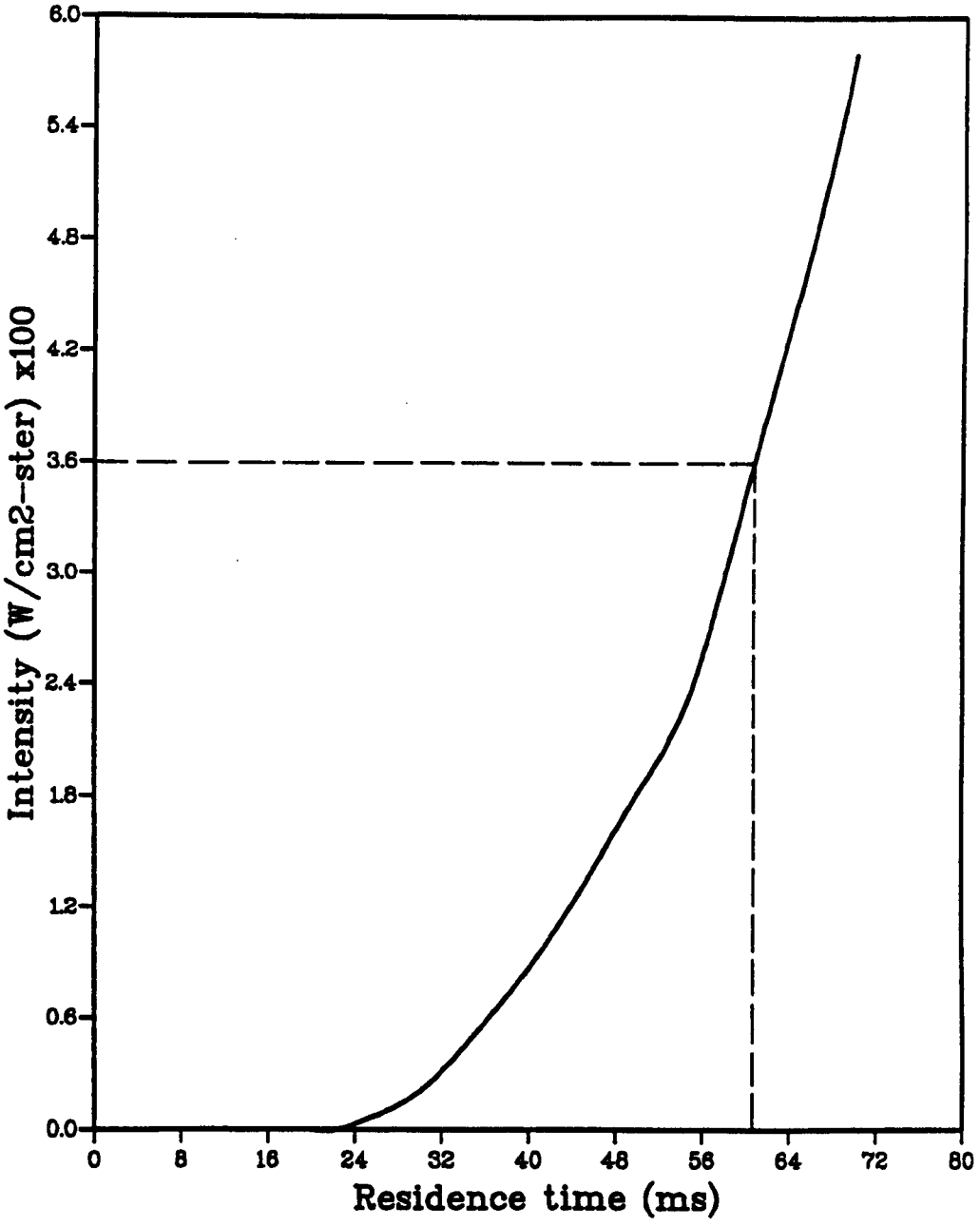

Spectral intensity at 0.9micron as a function of soot plug flow residence time

Figure 5.16

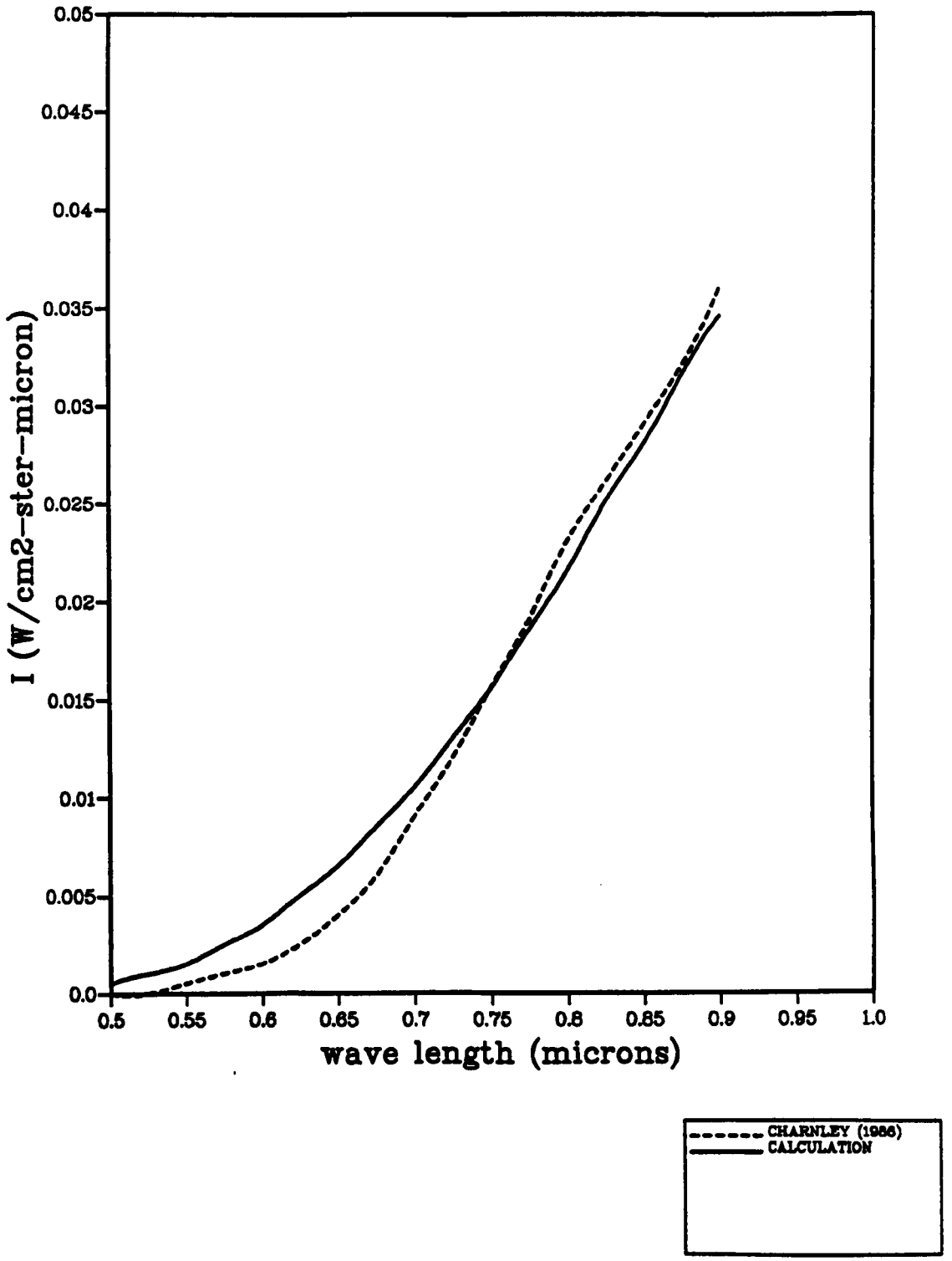

Spectral intensity of soot radiation
The calculation is deduced for a plug flow residence time time of 0.058 seconds

Figure 5.17

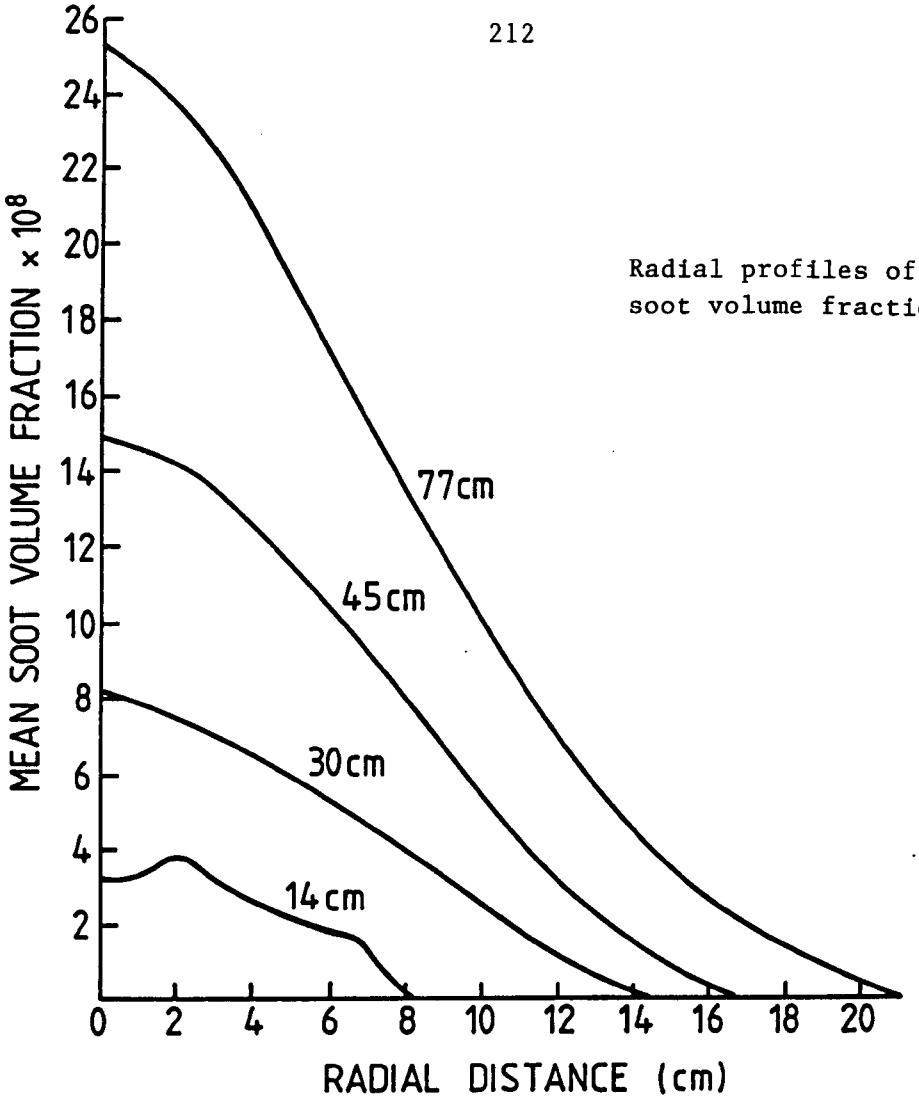

(a)

Radial profiles of mean soot volume fraction

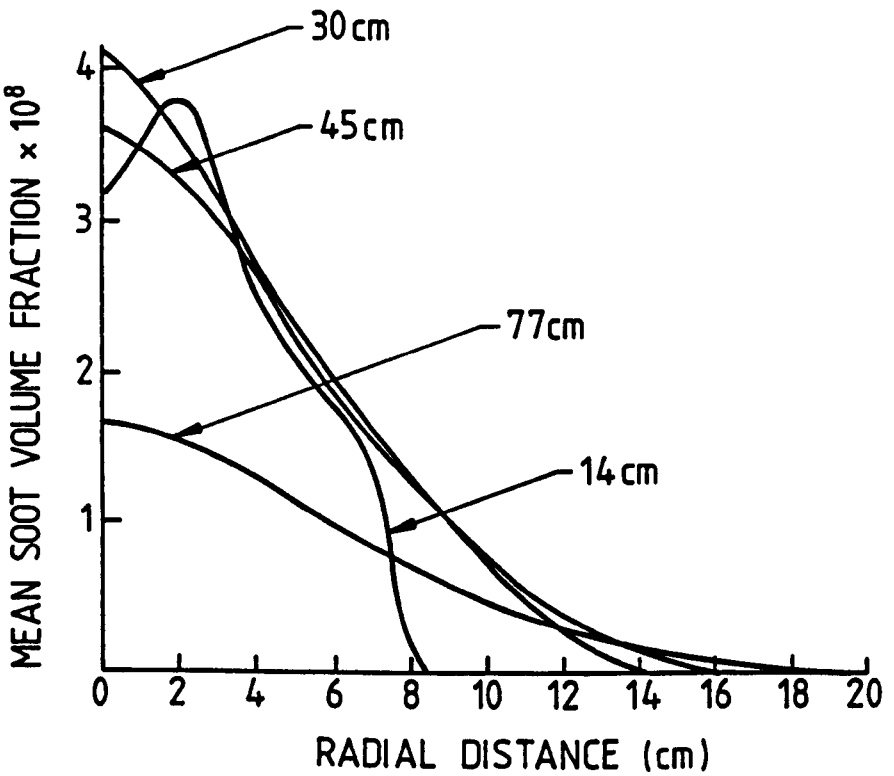

(b)

Figure 5.18

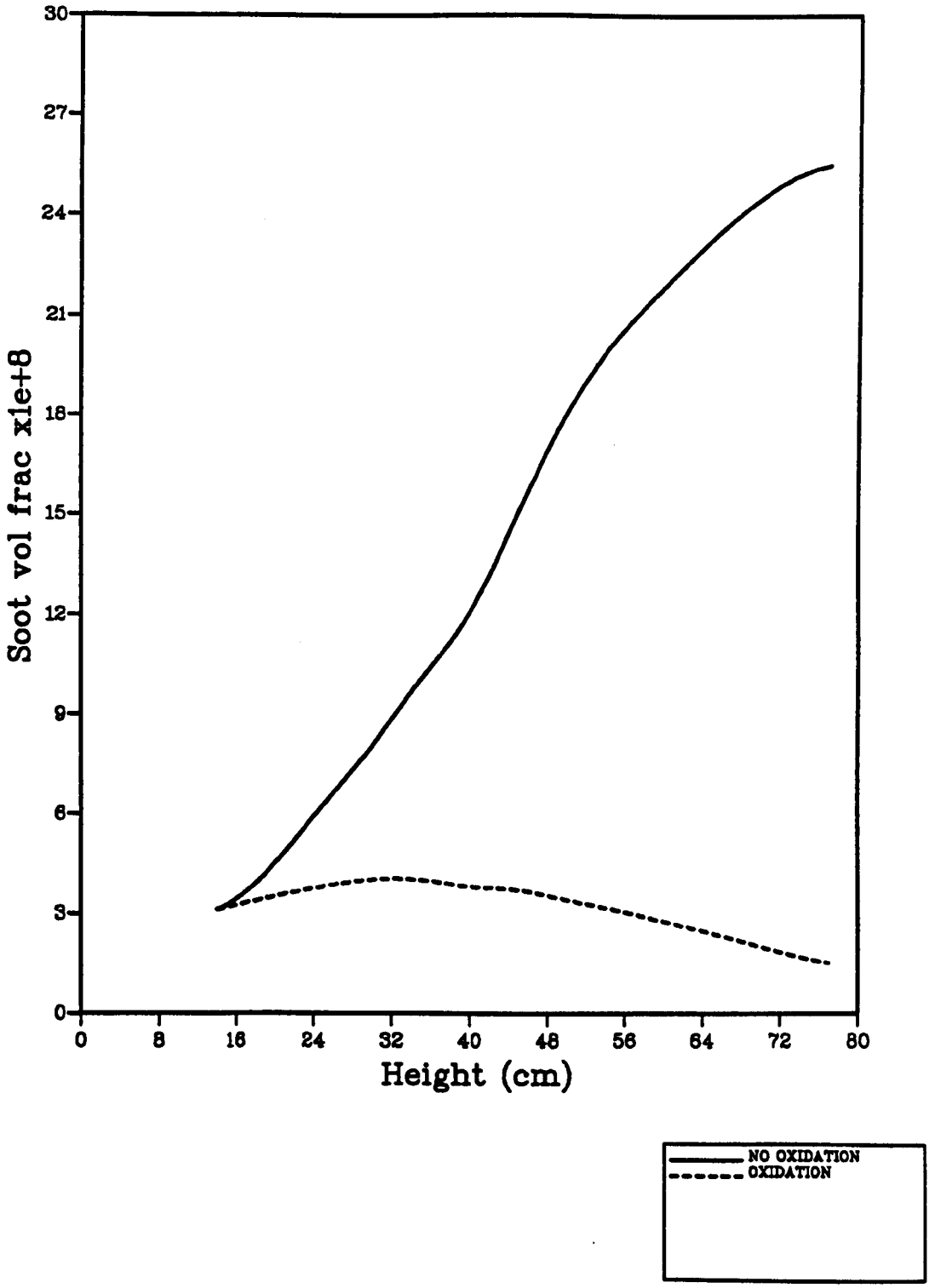

Axial variation of mean soot volume fraction

Figure 5.19

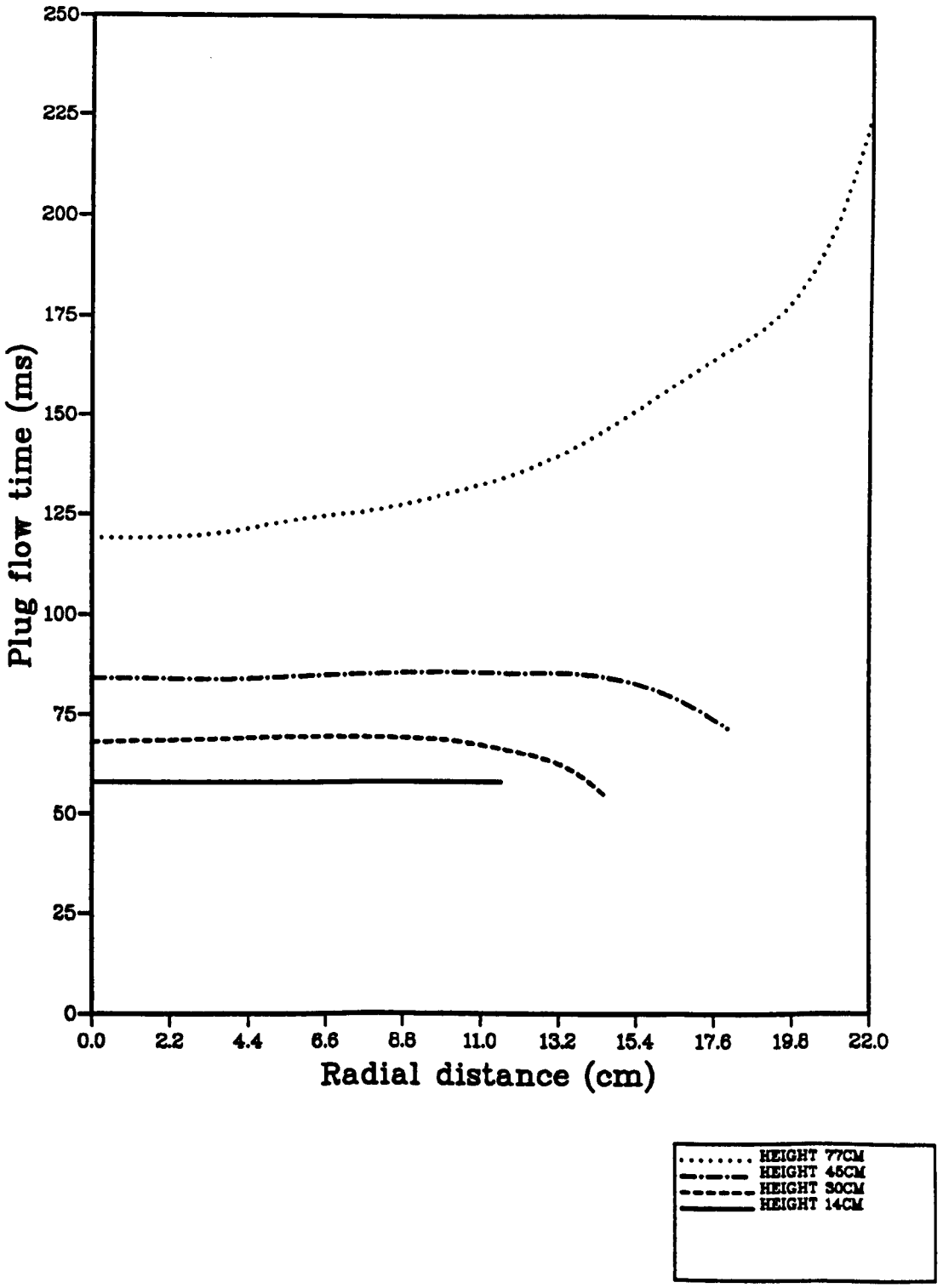

Radial profiles of soot formation plug flow residence time

Figure 5.20

CHAPTER 6

Radiation from a buoyant fire

6.1 Introduction

Radiation plays a principal role in the development of fire hazards since such flows may emit ~30% of their theoretical heat release as thermal radiation (cf. De Ris (1979)). This results from their typically large size which leads to large optical depths. Also, fires exhibit poor mixing and long residence times which, for hydrocarbon fuels, produce substantial quantities of soot; the latter is an efficient radiative emitter. Radiative heat feedback from the combustion zone to the fire source is largely responsible for sustaining combustion, by releasing combustible vapours which subsequently fuel the fire. Radiative emission may also heat external bodies causing them to ignite, if temperatures are high enough, or release further combustible vapours. These vapours, if not ignited at their source, are drawn into the ambient atmosphere and may result in an explosion or flash-over, if the ambient mixture approaches flammability. A model which attempts to predict the development of even an isolated fire, must therefore address radiative heat transfer since it affects the fuel flow rate and reduces local flame zone temperatures. The former controls the heat release rate and the latter feeds-back to radiative emission. The details of the flowfield structure are also affected through the effect of local temperature on density.

The modelling of radiation requires a knowledge of local scalar properties, namely the concentration of thermally radiating/absorbing species and temperature. This allows the calculation of local

absorption coefficients and blackbody emission. Within a predictive tool, such information may be fed into a radiation model, which solves a representative radiative transport equation. Solution of the latter results in local enthalpy loss (or gain) which may be incorporated into the source of an enthalpy balance equation. Auxiliary thermodynamic relationships may then result in the derivation of local temperatures (cf. chapter 2.1). Such procedures are fairly well established (cf. Viskanta and Menguc (1987)).

In turbulent media, where fluctuations in properties arise, additional complications result from the appearance of turbulent correlations. For example consider the radiative emission from a grey body, the emissivity and temperature of which fluctuate. The mean emission is given by

$$\overline{E} = \sigma \overline{\varepsilon \, T^4} \qquad \ldots \quad (6.1)$$

where σ is the Stefan-Boltzmann constant, and ε and T the emissivity and temperature of the body. Equation 6.1 indicates that non-zero correlations may result from joint fluctuations in the emissivity and temperature. Correlations also arise from the non-linear dependence of blackbody radiation on temperature. In a more detailed analysis which considers radiation resulting from an inhomogeneous turbulent medium, additional multi-point correlations result (cf. section 6.3). These arise because radiation is a path integral phenomenon.

In many practical combustion systems, for example furnaces and other confined combustion chambers in which there is strong radiative exchange throughout the enclosure, turbulence/radiation interaction may be ignored resulting in little error. In fires, however, such simplifications may lead to substantial error due to the typically large amplitude scalar fluctuations that characterise fires. Grosshandler (1985) and Cox (1977), amongst others, demonstrated the increasing importance of turbulence interaction with increasing amplitude of fluctuation. The present work both confirms the

importance of turbulence/radiation interaction through the study of the simulated methane fire which forms the focus of this chapter, and describes a strategy to accommodate the effects. Not surprisingly, the non-linear dependence of blackbody radiation on temperature is found to be of major importance. The most notable influence of large scale fluctuations was consequently the reduction in mean flame zone temperatures.

In order to model radiation from fires therefore, it is essential to be able to predict all radiatively important scalars and address turbulence/radiation interaction. Chapter 5 described the numerical derivation of a scalar map of a fire which was predicted using the laminar flamelet approach to model turbulence/chemistry interaction. Since soot plays a major role in most practical fire scenarios, a conserved scalar based model for its formation in turbulent non-premixed combustion was proposed in chapter 3. The model considers, in an approximate manner, the influence of turbulence on the formation (and burnout processes - cf. chapter 4) and addresses the relatively slow formation mechanisms which preclude soot from direct incorporation into the conserved scalar scheme. In chapter 5, this model was used to derive soot concentrations (to supplement those of the major gaseous species) in the simulated methane fire, which will later be investigated for its radiative properties. This entails the comparison of predicted radiative intensities with the data of Charnley (1986), who measured line-of-sight radiative emission through the fire.

As reported in chapter 5, the flowfield calculation explicitly accounted for radiative heat loss by perturbation of the temperature flamelet state relationship. The radiation calculations reported in this chapter are therefore performed as a post-process. This allows the use of a computationally-expensive, but diagnostically instructive, narrow band radiation model. The code used for this purpose is RADCAL (cf. Grosshandler (1979)).

Turbulence/radiation interaction is addressed using the stochastic approach, proposed by Faeth et al (1986), which utilises the link between any scalar and mixture fraction to provide their joint statistics. This is detailed in section 6.4 where the incorporation of soot radiation into the scheme is also described.

Having introduced the models to be used, the predictions of spectrally-resolved line-of-sight radiation are discussed in the light of similarly spectrally-resolved measurements. The latter were obtained by Charnley (1986) (cf. section 6.5.1).

6.2 Program RADCAL

RADCAL (cf. Grosshandler(1979)) is a code for determining the evolution of thermal radiation intensity along a path through an inhomogeneous absorbing/emitting medium. In order to treat the typically banded nature of gaseous absorption, the frequency resolution offered by RADCAL is $5cm^{-1}$ in wave number (ω), where the latter is related to wavelength according to

$$\omega\ (cm^{-1}) = \frac{1}{\lambda\ (\mu m)} \times 10^4 \qquad \ldots \quad (6.2)$$

In the near-infrared, where the major gaseous bands are located, a $25cm^{-1}$ resolution is used. This may be compared with $1050cm^{-1}$ and $260cm^{-1}$ which are the widths of the 2.7μm (combined H_2O and CO_2) band and 4.3μm (CO_2) band, respectively.

The code is based on the single line group (SLG) model suggested by Ludwig et al (1973). Here, the many lines within a narrow band, which result from rotational transitions, are represented by global parameters. This, however, does not reflect the ability of very high temperature lines to resist absorption by low temperature lines - a scenario that may result from radiation along a non-isothermal path. To address this matter better, Ludwig et al (1973) also suggested a

multi line group (MLG) model. However, Grosshandler (1979) demonstrated the acceptability of the SLG model applied to non-isothermal paths exhibiting typical flame temperatures.

The SLG model incorporates the Goody statistical model (cf. Goody (1964)), to describe the distribution and strength of rotational lines within a narrow band, and the Curtis-Godson approximation (cf. Hottel and Sarofim (1967)), to address inhomogeneous paths. The model is described in the next sub-section, but the reader is also referred to Ludwig et al (1973) and Grosshandler (1979) for greater detail.

6.2.1 Theoretical basis

The monochromatic radiative intensity along a line-of-sight through an inhomogeneous absorbing/emitting medium in local thermal equilibrium may be obtained by integration of equation 2.37, cf.

$$I_\omega(\omega,s) = \int_{-\infty}^{s} B_\omega(\omega,s')\ K(\omega,s')\ \exp\left\{-\int_{s'}^{s} K(\omega,s'')\ ds''\right\} ds' \quad \ldots \quad (6.3)$$

In equation 6.3, I_ω and B_ω are the spectral intensity and blackbody intensity ($W/[m^2 cm^{-1} ster]$), ω is the wave number (cm^{-1}) and s is the distance (m).

Now the spectral transmissivity between s′ and s is given by

$$\tau_\omega(\omega;s',s) = \exp\left\{-\int_{s'}^{s} K(\omega,s'')\ ds''\right\} \quad \ldots \quad (6.4)$$

Differentiating equation 6.4 with respect to s and substituting into equation 6.3 results in

$$I_{\omega}(\omega, s) = \int_{-\infty}^{s} B_{\omega}(\omega, s') \frac{\partial}{\partial s'} \left[\tau(\omega; s', s) \right] ds' \qquad \ldots \quad (6.5)$$

It is equation 6.5 that is solved by RADCAL, where the integro-differential equation is represented in the approximate form

$$I_{\omega} = \sum_{m=1}^{m=M} B_{\omega}(T_m) (\tau_{\omega,m} - \tau_{\omega,m-1}) \qquad \ldots \quad (6.6)$$

The summation is over M cells, each assumed to be homogeneous. $\tau_{\omega,m}$ is the spectral, or rather the narrow band average, transmissivity over the cell m and T_m its temperature.

The cell transmissivity for a mixture is found from

$$\tau_{\omega} = \exp\left(\sum_{i} X_{\omega,i} \right) \qquad \ldots \quad (6.7)$$

Where $X_{\omega,i}$ is the band average optical depth for species i.

Solution of equation 6.6 may result in the total spectrally-integrated radiative intensity by summing the contribution from all narrow bands. However, prior to this, the optical depth, $X_{\omega,i}$, is required; its derivation is described next.

To determine the sum effect of the numerous rotational lines that may occupy a narrow band, it is important to consider their interaction. For instance, if the strengths of all the individual lines were known, their net contribution to the band absorptivity would only equal their sum if they did not overlap. However, such overlaps invariably occur. To address this, RADCAL adopts the Goody statistical model (cf. Goody (1964)), where the band is assumed to comprise a number of randomly located lines of exponentially varying strengths and equal width.

Alternative models are described by Viskanta and Menguc (1987) and Sarofim (1986).

Broadening of the absorption lines must also be considered since their individual strength is given by the integral under the absorption coefficient-wave number curve cf.

$$S = \int K(\omega)\ d\omega \qquad \ldots \quad (6.8)$$

where S is the line strength and K the absorption coefficient. Ideally, since transition between energy levels is quantised, the individual lines should exhibit a unique frequency. However, line broadening may result due to **(i)** natural broadening because of uncertainty in molecular energy levels (Heisenberg's uncertainty principle), **(ii)** collision broadening due to energy exchange between colliding molecules and **(iii)** Doppler broadening resulting from the relative velocity between a molecule and an observer. Of these, the first is usually ignored since the others lead to far greater line broadening. At atmospheric pressure and at normal flame temperatures (~2000K), collision broadening is the more dominant. Doppler broadening becomes the greater at low pressures and very high temperatures such as may exist in plasmas.

For an array of collision broadened lines, having a Lorentz profile (cf. chapter 2) and arranged as in the Goody statistical model, an algebraic relationship results for transmissivity, τ, in terms of the mean line strength, S_e, and the mean line spacing, d_e, cf.

$$X = \frac{S_e\ d_e}{1 + \left(\frac{S_e\ u}{4\ \gamma_c}\right)} \quad (= - \mathrm{Ln}(\tau)) \qquad \ldots \quad (6.9)$$

X is the optical depth, γ_c is the collision half-width and u is the a standardised distance parameter which is used in RADCAL since the

necessary optical data are supplied at stp conditions, ie. at a temperature of 273K and a pressure of 1 atmosphere. u is thus defined as

$$u = s \left(\frac{273}{T}\right)\left(\frac{P}{1}\right) \qquad \ldots \quad (6.10)$$

where the temperature, T, is in Kelvin and pressure, P, in atmospheres.

RADCAL addresses combined collision and Doppler broadening by adopting the approximation suggested by Ludwig et al (1973), cf.

$$X = \sqrt{1 - Y^{-1/2}}\; X^* \qquad \ldots \quad (6.11)$$

Y is the combined collision and Doppler broadening optical depth, cf.

$$Y = \left[1 - \left(\frac{X_c}{X^*}\right)^2\right]^{-2} + \left[1 - \left(\frac{X_d}{X^*}\right)^2\right]^{-2} \qquad \ldots \quad (6.12)$$

X^* is the optical depth in the weak line limit, defined by

$$X^* = K_e\, u \quad ; \quad K_e = S_e/d_e \qquad \ldots \quad (6.13)$$

X_c and X_d are the optical depths in the pure collision and Doppler broadening regimes and are defined

$$X_c = X^* \left(1 - \frac{X^*}{4\, a_c}\right)^{-1/2} \qquad \ldots \quad (6.14)$$

and

$$X_d = 1.7\, a_d \sqrt{Ln\left[1 + \left(\frac{X^*}{1.7 a_d}\right)^2\right]} \qquad \ldots \quad (6.15)$$

a_c and a_d are termed the collision and Doppler fine structure parameters and are defined as

$$a_c = \frac{\gamma_c}{d_e} \frac{K_e\ u}{X^*} \qquad \ldots (6.16)$$

and

$$a_d = \frac{\gamma_d}{d_e} \frac{K_e\ u}{X^*} \qquad \ldots (6.17)$$

γ_c and γ_d are the collision and Doppler half-widths.

Equations 6.9 to 6.17 refer to a homogeneous path. To consider inhomogeneous paths, that are more characteristic of flames, the Curtis-Godson approximation is adopted (cf. Hottel and Sarofim (1967)), where the following re-definitions are made to account for variable path properties:

$$X^* = \int_0^u K_e\ du \qquad \ldots (6.18)$$

$$a_c = \frac{1}{X^*} \int_0^u \frac{\gamma_c}{d_e} K_e\ du \qquad \ldots (6.19)$$

$$a_d = \frac{1}{X^*} \int_0^u \frac{\gamma_d}{d_e} K_e\ du \qquad \ldots (6.20)$$

Equations 6.6 to 6.20 require, for their solution, γ_c, γ_d, S_e and d_e. The prescription of the half-widths is described below, and that for

the mean line strength and spacing forms the focus of the following subsections for each of the gaseous species considered.

Following Ludwig et al (1973), the collision half-width for species i, within a mixture, is given by

$$\gamma_{c,i} = \sum_j \left((\gamma_{i,j})_{stp} \, p_j \, (273/T)^{\eta_{i,j}} \right) + (\gamma_{i,i})_{stp} \, p_i \, (273/T)^{\eta_{i,i}} \qquad \ldots (6.21)$$

The summation is over all species including i. The second term arises to account for the possibility of resonant collision which may occur when two molecules of the same species collide, whilst being in neighbouring energy states. The collision half-widths at stp conditions and the indices (η) are tabulated in appendix D.

The Doppler half-width may be determined from equilibrium statistical mechanics (cf. Ludwig et al (1973)) resulting in

$$\gamma_{d,i} = 5.94 \times 10^{-6} \frac{\omega}{m_i^{1/2}} \qquad \ldots (6.22)$$

where m_i is the molecular mass of species i.

The gaseous species considered in the radiation calculation are CO, CO_2, H_2O and CH_4. Some of these, in particular H_2O, have many vibrational-rotational (and pure rotational) bands located in the thermal part of the electromagnetic spectrum. Those particular bands addressed in the present study are shown in table 6.1, and the method for obtaining their mean line strength and spacing (which for a particular species are dependent on temperature and wave number) is described in the following subsections. In addition to gaseous emission, particulate soot is also considered. The latter is described in section 6.2.7.

6.2.2 S_e and d_e for carbon monoxide

For the relatively simple CO molecule, it is possible to describe the vibrational and rotational nature from fundamental theory. For the 5μm band, S_e and d_e were taken from the study of Malkmus and Thomson (1961) who calculated these values based on modelling the molecule as a diatomic anharmonic non-rigid rotator.

6.2.3 S_e and d_e for carbon dioxide

The 2.7μm and 4.3μm bands of CO_2 are treated in a similar manner to the 5μm CO band. Though CO_2 is not a diatomic molecule, Malkmus (1963a) and Malkmus (1963b) extended the approximation of Malkmus and Thomson (1961) to describe the 2.7 and 4.3μm bands of CO_2.

The 2 and 10μm bands of CO_2 are represented by a wide band model, for which the parameters were obtained from Leckner (1972).

The 15μm band of CO_2 utilises the tabulated data compiled by Ludwig et al (1973) from several studies. Here S_e/d_e is supplied as a function of wave number and temperature.

6.2.4 S_e and d_e for water

The triatomic H_2O molecule, unlike the CO_2 molecule, is non-linear and is consequently capable of vibrating and rotating in a more complex manner. This makes a theoretical treatment very difficult and hence the data tabulated by Ludwig et al (1973), which is compiled from several experimental studies, is used. Though both S_e/d_e and d_e are tabulated, the following suggested correlation (cf. Ludwig et al (1973)) is used to obtain d_e:

$$1/d_e = \exp[\ 0.7941\ \sin(3.6\times10^{-3}\omega - 8.043)\ ] - 2.294 + 0.3004\times10^{-2}T - 0.366\times10^{-6}T^2 \quad \ldots (6.23)$$

The data considers all H_2O bands between 1.075 and 200μm (cf. table 6.1).

6.2.5 S_e and d_e for methane

The two strongest bands of CH_4 lie at 3.3μm and 7.7μm. Here these are prescribed using wide band parameters calculated by Edwards and Menard (1964).

The 2.4μm band utilises the expressions developed by Gray and Penner (1965).

6.2.6 Soot radiation

Unlike the gaseous species, soot absorbs/emits at all wavelengths. The optical characteristics of a cloud of particles may be obtained from Mie theory (cf. Kerker (1969)). For soot particles in the Rayleigh limit (where the particles are significantly smaller than the wave length of the radiation) the following expression for the absorption coefficient is obtained:

$$K_\lambda = \frac{36\ \pi\ n\ m}{(n^2 - m^2 + 2)^2 + 4n^2m^2}\ \frac{f_v}{\lambda} \quad \ldots (6.24)$$

f_v is the soot volume fraction, λ is the wavelength in μm and n and m are the real and imaginary parts of the complex refractive index (which is defined as n-im). n and m are set to the constant values of 1.92 and 0.45 which were taken from Mullins and Williams (1987).

6.3 Turbulence-radiation interaction

Radiation emitted from turbulent media may be significantly influenced by turbulence interaction. This results from the non-linear dependence of radiation on its controlling properties; for instance, blackbody radiation is dependent on T^4. To illustrate this, consider the radiative transfer equation through a number of homogeneous boxes, as given by the recurrence relationship deduced by Lockwood and Shah (1981)

$$I_i = \tau_{i-1} I_{i-1} + (1-\tau_i) B_i \qquad \ldots (6.25)$$

where I is the radiative intensity, τ the transmissivity, B the blackbody intensity and the subscript i refers to the i^{th} homogeneous cell of a group of n such cells that make up an inhomogeneous path. For the n cells equation 6.25 may be expanded to yield

$$I_n = (1-\tau_n) B_n + \tau_n (1-\tau_{n-1}) B_{n-1} \cdots + \tau_n \tau_{n-1} \cdots \tau_2 (1-\tau_1) B_1 + \tau_n \tau_{n-1} \cdots \tau_1 I_0 \qquad \ldots (6.26)$$

The mean radiative intensity emergent from a turbulent inhomogeneous path may then be determined through time averaging equation 6.26, cf.

$$\overline{I_n} = \overline{(1-\tau_n) B_n} + \overline{\tau_n (1-\tau_{n-1}) B_{n-1}} \cdots + \overline{\tau_n \tau_{n-1} \cdots \tau_2 (1-\tau_1) B_1} + \overline{\tau_n \tau_{n-1} \cdots \tau_1 I_0} \qquad \ldots (6.27)$$

It then becomes obvious that turbulence interaction is apparent through single point correlations cf.

$$\overline{(1-\tau_i)\ B_i}$$

and multi-point correlations cf.

$$\overline{\tau_n\ \tau_{n-1}\ \cdots\cdots\ \tau_{i+1}\ (1-\tau_i)\ B_i}$$

The former results from the joint statistics of temperature (which

figures in the blackbody radiation, B, and the transmissivity, τ, (cf. sections 6.2)) and all radiatively important species. The appearance of multi-point statistics results from radiation being a path integral phenomenon. The consequent additional correlations involve the transmissivities at all points along the path.

Given the simple moment approach used in the present flowfield modelling, the multi-point correlations are inaccessible. Their evaluation requires solution of a multi-point PDF evolution equation (cf. Pope (1985)), the solution of which is impractical given both current modelling and computational limitations. Such correlations are therefore necessarily ignored, resulting in

$$\overline{I_n} = \overline{(1-\tau_n)B_n} + \bar{\tau}_n\overline{(1-\tau_{n-1})B_{n-1}}\cdots + \bar{\tau}_n\bar{\tau}_{n-1}\cdots\bar{\tau}_2\overline{(1-\tau_1)B_1} + \bar{\tau}_n\bar{\tau}_{n-1}\cdots\bar{\tau}_1\bar{I}_0 \qquad \ldots (6.28)$$

It is difficult to assess the quantitative effect of this simplification. It is, however, expected that the neglected terms will reduce in importance with reducing optical depth, since in the limit of an optically thin path, the transmissivity, of the medium between the observer and the radiating element, may be neglected (cf. Hottel and Sarofim (1967)). In the presently studied fire, as will become apparent in the discussion of the results, most of the spectrum reveals relatively thin optical depths. This is not the case, however, for the 4.3μm CO_2 band where the spectral transmissivity falls below 0.05. Radiative emission at these frequencies will therefore be subject to reabsorption by the medium between the emitting element and the observer.

In the optically thin limit, therefore, it is possible to consider radiation through a turbulent medium, by considering the fluctuating nature of each individual eddy in total isolation from all others. However, it is then apparent that the prescription of the path length through each eddy is critical since this affects its emissivity. The

latter, it is felt, is not sufficiently well described by the adopted stochastic model (cf. section 6.4), where total path lengths through high temperature reaction zones are probably overestimated. This results in the overpredicting nature of this approach, observed in the present study (cf. section 6.5) and that of Faeth et al (1986).

In so far as the single-point statistics are concerned, the conserved scalar based laminar flamelet approach offers the necessary joint statistics, since all scalars can be related to mixture fraction. The PDF of the latter is readily obtainable, given current modelling practices (cf. chapters 4 and 5). The method adopted in the present study to address single-point correlations is that proposed by Faeth et al (1986) which utilises this link between radiatively important scalars and mixture fraction to define their joint statistics. This approach, referred to as the stochastic approach, is described in the next section.

Soot is controlled by relatively slow formation processes and consequently cannot be expressed solely in terms of mixture fraction. It cannot therefore be readily linked statistically to other scalars. Such links, however, most significantly that with temperature, are very important since recently formed soot is strongly correlated with high temperature zones. This is evident from the luminosity resulting from soot particles in flames. The extension of the stochastic approach to include soot radiation forms the subject of section 6.4.1.

6.4 The stochastic approach

Faeth et al (1986) proposed a Monte Carlo approach for determining radiative emission from a turbulent inhomogeneous medium. The approach entails specifying instantaneous properties along a line-of-sight followed by a radiation calculation, to obtain an instantaneous realisation of radiative intensity. When a sufficient number of realisations are made, statistical analysis may yield a PDF and its moments. It is, however, important that the instantaneous path

properties, when ensembled, yield the correct mean values. This may be achieved through randomly sampling the PDF of mixture fraction, as will be described shortly.

Faeth et al (1986) divided the path length into a number of statistically-independent homogeneous elements, called characteristic eddies, the length of which (L_e), following Gosman and Ioannides (1981), was specified as the local turbulent dissipation length cf.

$$L_e = c_\mu^{3/4} K^{3/2} / \varepsilon \qquad \ldots (6.29)$$

The use of such a length scale is somewhat arbitrary in a sooting diffusion flame; however, Jeng et al (1984) showed that L_e, though having a significant impact on the rms intensity, has little effect on the mean. In later publications (cf. Kounalakis et al (1988)), Faeth and co-workers chose to represent the elemental length by

$$L_e = C_e c_\mu^{3/4} K^{3/2} / \varepsilon \qquad \ldots (6.30)$$

where the value of C_e is an empirically derived parameter. Kounalakis et al (1988) found, in weakly-buoyant flames, a suitable value of Ce to be 6.6 by matching predicted and experimental fluctuating intensities. This results in a characteristic length close to the integral length scale of the turbulence.

Figure 6.1 shows the mean and rms spectral intensity, at 4.3μm, plotted against C_e, for a horizontal path through the axis of the presently studied fire at a height of 30cm above the burner. The trends confirm the findings of Faeth et al in that the mean remains more or less invariant and the rms rises as C_e increases. The increasing rms intensity results from the fewer path eddies causing greater coherence and deviation of the instantaneous intensity from the mean. For large values of C_e (>6), the mean starts to deviate and the rms levels off; this, however, results from the poor representation of the inhomogeneous path by relatively large

homogeneous elements. With Ce set to 6, there are only four eddies representing the whole path through the fire.

The following focuses on the details of the specification of the instantaneous properties for the path elements. The procedure views all thermally important scalars to be solely functions of mixture fraction; then random sampling of the mixture fraction PDF, to obtain instantaneous properties, ensures multi-scalar correlations are addressed. This lies at the heart of the procedure to be described.

The random sampling of each homogeneous element firstly involves constructing $P(\xi)$. This is straightforward, given the local mean and variance of mixture fraction that result from the flowfield simulation (cf. chapter 5), and the assumption of a two-parameter PDF. Such a PDF is shown in figure 6.2a, for which the first and second moments are $\tilde{\xi}=0.1$ and $\widetilde{\xi''^2}=0.001$. In keeping with the flowfield calculation of chapter 5, a beta function form is assumed.

The PDF, $P(\xi)$, may be integrated to yield the cumulative distribution function, $F(\xi)$, cf.

$$F(\xi) = \int_0^{\xi} P(\xi)\, d\xi \qquad \ldots (6.31)$$

The cumulative distribution function, corresponding to the $P(\xi)$ of figure 6.2a, is shown in figure 6.2b.

Random sampling of $F(\xi)$ may then yield instantaneous values of mixture fraction which, when ensembled, result in the appropriate first and second moments, since the instantaneous values are weighted by the $P(\xi)$. In the present study instantaneous values of $F(\xi)$ were obtained using NAG library routines G05CAF (NAGFLIB:2027/1809:MK11:JAN84) and G05CCF (NAGFLIB:144/0:MK6:DEC78). Their use results in (pseudo)random numbers between 0 and 1, for which there is an equal probability of attaining any value.

A random number is generated for each element along the path, resulting in an array of instantaneous values of ξ. Instantaneous values of any scalar, ϕ, may then be obtained from the state relationship $\phi(\xi)$, cf.

$$\phi_i = \phi(\xi_i) \qquad \ldots (6.32)$$

where the subscript i refers to instantaneous value.

The instantaneous properties along the line-of-sight are thus specified and a radiation calculation may then be performed to obtain a single realisation. The entire procedure is repeated several times to obtain a statistically meaningful sample set. In the present case 200 realisations were made. It was found that soot radiation required more realisations than gaseous emission. This is illustrated in figure 6.3 where the mean spectral radiation at 0.9μm and 4.3μm is plotted against number of realisations - the path is for the 14cm height. Soot is the only contributor at 0.9μm whilst CO_2 is the only contributor at 4.3μm. The reason for the relative trend is that soot occupies relatively narrow sheets compared to the gaseous species, as may be seen by comparing the soot flamelets of figure 5.15 with the gaseous species flamelets of figure 5.1. This results in a more intermittent appearance of soot along the path length and hence a greater influence of turbulence interaction. Figure 6.3 also shows that after 200 realisations, the mean CO_2 radiation is within 5% of that resulting from 800 realisations. Though greater than 200 realisations are required to get the same degree of accuracy for soot radiation, its contribution to overall emission is small in the methane fire studied. When using the stochastic radiation model to define the initial profile for the soot balance equations, however, (cf. chapter 5), 800 realisations were used.

The procedure described so far requires that all relevant scalars are linked to mixture fraction and therefore to each other to account for

multi-scalar statistics. Soot, however, was highlighted earlier as a species which cannot be treated in such a simple way since it is not solely a function of mixture fraction. The next sub-section describes how this problem was tackled in the present study.

6.4.1 Extension to incorporate soot radiation

Earlier, the importance of linking all radiatively-important species to mixture fraction was emphasised, since the single-point multi-scalar statistics are then fully closed. Soot, however, does not readily fall into this scheme since its formation mechanisms are not fast and hence its concentration is not controlled solely by mixing. Moreover, the soot model, described in chapters 3 and 4, yields only mean values of soot volume fraction and hence there is no indication of its fluctuating properties. Though it may be feasible to envisage a balance equation for the second moment of soot concentration, which may be used to construct a PDF (by assuming, say, a Gaussian profile), the link between soot and mixture fraction will not be revealed. Therefore the strong link between soot and high temperature, which is apparent in much of the flame (as indicated by the observed soot luminosity), will not be attained. In view of this, it is essential to specify instantaneous soot concentration in terms of mixture fraction. However, since a unique relationship between soot and mixture fraction for the whole of the domain is inappropriate, locally applicable ones are specified as described below.

If soot volume fraction may be expressed as a function of mixture fraction and a characteristic residence time cf. $f_v=f_v(\xi,t)$, its statistics would be described by the two-dimensional PDF $P(\xi,t)$. Such a PDF is not available given the present modelling scheme and hence it is replaced by the conditional PDF, $P(\xi;t)$. Local mean soot volume fractions may then be found from

$$\overline{f}_v = \overline{\rho} \int_0^1 \frac{f_v(\xi;t)}{\rho(\xi)} \tilde{P}(\xi)\, d\xi \qquad \ldots (6.33)$$

The mean soot volume fraction, (cf. left-hand-side of equation 6.33) is obtained through the solution of its mean balance equation, the results of which are shown in figure 5.18b for the present fire. In order to define a suitable state relationship, $f_v(\xi;t)$, it has been assumed that, in the turbulent environment, a soot containing volume always remains, instantaneously, at the same mixture fraction. In this plug flow-like assumption, the soot source term, equations 3.7 and 3.8 may be integrated with respect to residence time . This results in flamelet relationships that may be constructed for a range of residence times as shown in figure 5.15. A locally applicable $f_v(\xi)$ may then be identified from this flamelet library by equating equation 6.33, where the left-hand-side is the local mean soot volume fraction as found through solution of its balance equation and the $P(\xi)$ is determined from the local mixture fraction parameters.

This procedure is likely to be a good enough approximation in fires that do not emit smoke, since otherwise soot breaks through to lean cooler regions where it becomes more significant as an absorber of radiation rather than an emitter. This, however, is not observed in the fire studied where, though soot must move towards leaner regions, as the maximum instantaneous mixture fractions are reduced by small scale mixing, it tends to be oxidised.

Section 6.4 has described the presently adopted stochastic radiation approach to address, to some extent, turbulence-radiation interaction which can be significant in buoyant fires. The procedure capitalises on key features of the laminar flamelet approach where all scalars may be expressed in terms of mixture fraction, the statistics of which are readily obtained. The incorporation of soot into this scheme has also been described. The next section applies the model to the

prediction of radiative emission along paths through a buoyant fire and comparison is made with experimental data.

6.5 Prediction of line-of-sight radiation through a buoyant fire

Chapter 5 presented the prediction of the scalars, necessary to calculate thermal properties and hence radiative transfer, within a buoyant fire. The accuracy of the numerically-derived map was demonstrated through comparison with the experimental velocity and temperature data of Crauford (1984). The previous sections in this chapter described a method for determining spectrally-resolved radiative emission which addresses turbulence/radiation interaction. The strategy, given its Monte Carlo nature and narrow-band resolution, is only practicable for post-processing due to its excessive computational demands. Such a method, however, is in keeping with the overall aims, which are to propose and validate a soot model and to assess the effect of turbulence interaction on radiative emission from fires, utilising a bank of detailed experimental data for comparison. A predictive technique for determining radiative emission from fires is therefore not our principal objective but rather a diagnostic study.

Of the scalar properties derived in chapter 5, soot was identified as a problem due to uncertainties in assigning boundary conditions to its balance equations and soot oxidation. In the presently studied fire, however, soot is produced in small quantities and does not influence the major infrared gaseous bands at 2.7μm and 4.3μm. Uncertainties in soot levels do not therefore hamper analysis of the radiation model and turbulence-radiation interaction. This is illustrated in figure 6.4 which shows predicted spectra of radiation along a horizontal line-of-sight through the axis of the fire, 30cm above the burner. Two predictions are shown which illustrate the effect of including soot radiation. The influence of soot is seen to be restricted to low wavelengths since it is present in low concentration. Also, there is an inverse relationship between soot absorption and wave length (cf.

equation 6.24). In terms of spectrally integrated radiation there is a reduction of 9%, over the range 2.4-4.9μm, through neglecting soot.

The radiation predictions are presented and discussed in section 6.5.4. There the importance of considering turbulence-radiation interaction is emphasised by adopting two approaches: the first, termed the base line approach ignores turbulence interaction and the second is the stochastic approach which has already been described. The implementation of these methods is detailed in section 6.5.2 and 6.5.3.

Prior to presenting the predictions, it is useful to introduce the experimental data which will be used later for comparison. This is particularly necessary in view of assumptions made in their interpretation.

6.5.1 The experimental data of Charnley (1986)

Charnley (1986) made line-of-sight radiation measurements along horizontal diameters through the fire (described in chapter 5) at heights 14, 30, 45 and 77cm above the burner. These measurements supplement the velocity and temperature measurements made by Crauford (1984).

The radiation measurements were made utilising three instruments: a relatively slow-response spectral device operating over the range 2.5 to 4.9μm (near infrared), a similarly slow spectral device operating between 0.5 and 0.9μm (visible) and a quick-response total radiation device. The former two yielded time averaged spectral intensities obtained from several scans, whilst the latter was capable of sufficient temporal resolution to allow the construction of PDFs of spectrally-integrated radiation.

A problem, however, lies in the interpretation of the infrared spectral data, since the data reduction involved noise rectification

which resulted in the introduction of an unknown offset. Figure 6.5 shows the experimental data taken at 30cm above the burner (cf. uncorrected data in fig 6.5) - the trend, however, is representative of all heights. These data indicate the presence of continuum radiation between the major gaseous peaks at 2.7 and 4.3μm. This is most obvious at ~3.8μm where there are no important gaseous bands. The apparent continuum may result from soot radiation or the earlier-mentioned offset. The influence of soot radiation, however, has been shown to be negligible above ~3μm, cf. figure 6.4. Though there are uncertainties in the soot levels, the calculated soot radiation between 0.5 and 0.9μm does coincide with the measurements of the visible radiometer. It was therefore decided to offset the data such that their minimum indicated spectral intensity was zero. This results in the corrected curve shown in figure 6.5. A similar offset is applied to the infrared data at all the heights prior to comparison with the predicted spectra.

6.5.2 Base line radiation calculation

The base method ignores any turbulence interaction, by performing the radiation calculation using only mean properties along the path. The mean path-properties are generated directly from the flowfield results cf. figure 5.7 and 5.13. The flowfield calculation considered only half the flame since it was run in axi-symmetric mode. The data was therefore mirror-imaged prior to conducting the radiation calculation. The latter entailed applying the radiation method for inhomogeneous paths described in section 6.2, for which the homogeneous elements were taken to be the finite difference cells used in the flowfield calculation. These numbered 76 for the whole path, since 40 cross-stream nodes were used in the flowfield computation which leads to 38 cells (cf. Spalding (1977)).

6.5.3 Stochastic radiation calculation

The theoretical basis of the approach was described in section 6.4. Here the application of the approach is detailed.

As mentioned earlier, the approach entails splitting the line-of-sight into homogeneous eddies, the lengths of which are given by equation 6.29 using local turbulence parameters. This procedure was implemented by starting at the flame axis and determining the length of the first eddy from the centre-line k and ε. The length of each subsequent eddy was then based on the values of k and ε pertaining at the first finite difference cell appearing within the element. The elements are shown in figure 6.6 for the 14, 30, 45 and 77cm heights, where typical realisations of instantaneous path temperatures are shown against the predictions of mean temperature. This procedure specifies half the flame. Its mirror image about the axis yields the full path.

Having defined the elements, a representative $P(\xi)$ must be assigned to each. The values of $\tilde{\xi}$ and $\widetilde{\xi''^2}$ used (to define the two parameters beta function PDF), as with k and ε, were taken from the first finite difference cell appearing within an element.

Instantaneous values for mixture fraction are then obtained for each element, by randomly sampling the appropriate $P(\xi)$ as described in section 6.4. This is done for only half the width. The instantaneous mixture fraction values for the other side of the flame were prescribed assuming symmetry at the axis of the flame. This implies axi-symmetry for the instantaneous field as well as the mean field. Fast luminosity photographs of the fire (cf. Crauford (1984)) suggest this to be reasonable. Uncertainties associated with this, however, are limited, as shown in figure 6.7 which compares the mean spectral intensity obtained by the above method, with those obtained through treating both sides of the flame as statistically independent. The rms intensity is reduced in the latter case owing to lesser coherence along the path.

It should be noted that the PDF of mixture fraction, supplied by the flowfield calculation, is the Favre PDF since it is deduced from the Favre mean and variance of mixture fraction. Random sampling of this PDF will therefore yield values of mixture fraction dependent scalars which on average yield Favre statistics. In order to obtain instantaneous values which ensemble to yield Reynolds statistics, it is necessary to sample the Reynolds $P(\xi)$. The latter is attainable given the availability of a state relationship for density, $\rho(\xi)$, since the Reynolds and Favre PDFs are simply related (cf. Bilger (1976a)) according to

$$\int P(\xi)\ d\xi = \overline{\rho} \int \frac{1}{\rho(\xi)} \tilde{P}(\xi)\ d\xi \qquad \ldots (6.34)$$

In fires, due to large scalar fluctuations, there is a significant difference between the Reynolds and Favre PDFs. This is illustrated in figure 6.8 which shows both PDFs at the axial location 14, 30, 45 and 77cm above the burner. This translates into a difference of upto ~300K as shown in figure 6.9 which shows radial profiles of Reynolds and Favre mean temperatures. The Favre mean values of temperature are always less than their Reynolds averaged counterpart. The reason for this becomes apparent when the definition of a Favre averaged variable is considered cf.

$$\tilde{T} = \overline{T} + (\overline{\rho' T'})/\overline{\rho} \qquad \ldots (6.35)$$

The state relationships, $\rho(\xi)$ and $T(\xi)$ (cf. figure 5.2) indicate the correlation $\overline{\rho' T'}$ to be always negative.

The impact of sampling from a Favre PDF can be seen in figure 6.10, which compares the results of the stochastic radiation model adopting both a Reynolds and Favre PDF. The experimental data of Charnley (1986) is also presented for comparison. The figure shows the use of Favre averaged statistics to result in lower intensities, owing to the

implied lower mean temperature and CO_2 and H_2O concentration. This prediction shows better comparison with experimental data. However, this is thought to be a facet of the overpredicting nature of the stochastic approach, rather than the suitability of Favre statistics.

In the predictions reported later, instantaneous values were obtained using Reynolds statistics. For the blackbody emission this is reasonable as there is no inherent density weighting since B_λ is dependent only on temperature. The emissivity, however, involves pressure-path lengths which are linked to density. In the present fire though, radiative intensities were found to be most sensitive to the blackbody radiation.

6.5.4 The predictions and discussion

The predictions of spectral radiation (between 0.5 and 4.9μm) along diameters through the fire at the heights of 14, 30, 45 and 77cm are presented in figure 6.11-6.14. Two sets of predictions are shown, resulting from the base and stochastic radiation calculations. These are compared with the visible (0.5 to 0.9μm) and infrared (2.4 to 4.9μm) experimental data. The latter are shown in their corrected form (cf. section 6.5.1). The integrated radiation is shown in table 6.2.

Examination of the base model predictions show that ignoring turbulence-radiation interaction can lead to severe underestimates of radiative emission. The worst case is at 77cm where high intermittency is exhibited. This leads to relatively low mean temperatures whilst still allowing the instantaneous appearance of high temperature zones. Here the integrated emission between 2.5 and 4.9μm is underpredicted by 82%.

The base prediction at all heights indicates a greater degree of underprediction at low wavelengths; the reasons for this are twofold. Firstly the Planck function is more temperature dependent at lower wavelengths as illustrated in figure 6.15, which shows its variation

with temperature. Turbulence interaction, introduced through the non-linear dependence of blackbody radiation on temperature, is therefore more substantial there. The second reason relates to soot radiation, which is more significant at the lower wavelengths. Soot, whose diffusion is small, lies in narrow sheets mostly located in high temperature regions. This cannot be addressed by the base model.

Of the above two concerns, the effect of temperature dominates. This is illustrated in figure 6.16 which shows radiation predictions at the 30cm height. Here non-luminous radiation alone is considered since only trends are of interest. Four predictions are shown: **a** using the stochastic approach, **b** where the stochastic approach is applied to temperature but the mean species are used, **c** where mean temperatures are used but the stochastic approach is applied to the species and **d** resulting from the base model. The experimental data are also presented. The integrated spectra are shown in table 6.3. The full stochastic approach, **a**, yields the highest levels since all single-point non-linearities are addressed. In particular the dependence of blackbody radiation on temperature. Also, the high temperature zones are linked to high concentrations of CO_2, H_2O and soot. Prediction **b** results in the next highest intensities, where blackbody radiation non-linearities are incorporated but high temperature zones are no longer associated with high concentrations of radiatively important species - this reduces local emissivities. Prediction **c** exhibits lower intensities than **b**, implying a greater importance of fluctuations in temperature than those in the species concentrations, and hence emissivity. It is worth noting that in the 4.3μm CO_2 peak, prediction **d**, which completely neglects turbulence interaction, indicates larger intensities than **c**. This results from the possibility that instantaneously, cool CO_2 may appear and absorb the radiation emitted by hotter regions. This does not occur at other wavelengths, since there the optically thin limit applies and reabsorption is negligible.

Prediction **b** is seen to lie closest to the experimental data. This does not justify the assumptions made in deriving it but rather

reflects the overpredicting nature of the stochastic approach; this is described in more detail later.

It should be noted when examining the soot radiation, that it was the stochastic approach that led to the prescription of the soot balance equation boundary conditions. It is therefore unwise to draw any conclusion by comparing the soot predictions with the experimental data. Analysis of the soot radiation should be restricted to comparison between the predictions.

Turning attention to the stochastic approach reveals that radiation levels are consistently overpredicted (cf. figs. 6.11 to 6.14 and table 6.2). Such a tendency was also observed by Faeth et al (1986). This overpredicting nature may result from the prescription of the length scale assigned to characteristic eddies and the neglected multi-point correlations - the elements are assumed to be statistically independent. The latter, as has already been shown, is only important in the 4.3μm CO_2 band, where the optically thick limit is approached. However, overprediction is also apparent at the 2.7μm band where the path is optically thin. Perhaps more important therefore, is the overestimate of path lengths through instantaneous burning zones. The burning zone within a laminar flamelet, characterised by mixture fractions close to stoichiometric, will typically be only millimetres wide. The computed dissipation length scale associated with the turbulence, however, is approximately 1.5cm in the present case. Too great a path length would therefore be assigned to burning zones. This would not be adequately counteracted by realisations where the mixture fraction is far from stoichiometric, since if eddies are viewed as fuel rich (or oxidant rich) pockets surrounded by narrow burning zones, the assigned path length is more realistic.

The effect of length scale over-prescription may be more marked for soot radiation, since it is known to occur in narrow sheets due to negligible particle diffusion. This would have implications for the soot concentration predictions since the initial conditions were based

on the stochastic radiation results. If the stochastic radiation predictions are too high, then the soot levels would also be higher than those suggested.

Figures 6.11 to 6.14, as well as showing the spectral intensities, show the line-of-sight transmissivity. Though there is significant difference between the intensities predicted by the stochastic and base models, the transmissivities show relatively little difference. This suggests that for the fire investigated here, the major impact of turbulence interaction is introduced through the non-linear dependence of blackbody radiation on temperature. Furthermore since it is the transmissivity through which multi-point correlations are introduced, the current predictions suggest these may be negligible.

6.6 Conclusions

This chapter described the prediction of radiation levels emitted along lines-of-sight through a buoyancy-driven simulated methane fire. These supplement the flowfield predictions already made in chapter 5 where comparison with the temperature and velocity data of Crauford (1984) showed reasonable agreement. This allows a degree of confidence in the predicted scalar field, and hence permits evaluation of the radiation predictions free from any associated uncertainties. Analysis of the radiation predictions has been made possible through comparison with the spectrally-resolved measurements of Charnley (1986).

The importance of turbulence/radiation interaction has been emphasised, particularly with regard to the non-linear dependence of blackbody radiation on temperature. Also of importance is the link between species and temperature. The major gaseous radiators (H_2O and CO_2), given a flamelet description of the turbulent combustion, are instantaneously evaluated at the maximum temperature. If this link is not realised, emitted radiation will be underestimated due to both lower emission and absorption by relatively high concentration of cooled gases. The method used to address the multi-scalar statistics

is that proposed by Faeth et al (1986), where the statistical information is provided by the laminar flamelet approach.

Turbulence interaction is most apparent at lower wave lengths. This results from a greater dependence of blackbody radiation on temperature (cf. fig 6.15). Also, the lower wave lengths are where soot radiation dominates, for which turbulence interaction is of great importance since soot is largely confined in narrow sheets. Moreover, soot is typically limited to zones that are instantaneously located close to peak temperature regions. The link between soot and temperature then becomes paramount. Such a link, however, is not readily forthcoming, since soot formation is relatively slow and it cannot therefore be described as a function of mixture fraction alone. In order to overcome this, a method has been proposed whereby locally applicable soot flamelets are obtained. Soot can then be readily incorporated into the stochastic radiation model and hence all single-point correlations closed.

Radiation is a path integral phenomenon and hence multi-point correlations arise. These, however, are indeterminate given the usual moment based approaches to flowfield modelling; solution of a multi-point PDF is required. This at present is unfeasible given both modelling and computational limitations. However, such multi-point correlations result from path transmissivity which is relatively unimportant in optically thin media. In the present fire, most of the spectrum is optically thin, except the 4.3μm CO_2 band where multi-point correlations are expected to be most significant. The stochastic approach, adopted in the present study to address turbulence interaction, tends to overpredict at all wavelengths, even in optically thin regions. This is thought to result from the overestimate of path lengths through high temperature burning zones, resulting in an overestimate of their emission.

Species	Spectral range μm	Spectral range cm-1	Band centre μm
CO_2	1.75-2.20	5725-4550	2
	2.63-3.28	3800-3050	2.7
	4.05-5.06	2474-1975	4.3
	9.09-11.36	1100- 880	10
	11.36-20.00	880- 500	15
CO	4.17-6.25	2400-1600	5
H_2O	All bands between1.075 and 200μm, the prominant ones are centred at: 1.38, 1.87, 2.7, 6.3 and 71 μm		
CH_4	2.00-2.86	5000-3500	2.4
	2.86-4.00	3500-2500	3.3
	6.25-10.31	1600- 300	
Soot	All wavelengths		

Table 6.1

Height	total		non-luminous		experimental
	base line	stochast	base line	stochast.	
cm	W/cm^2 ster				
14	.1342	.1361	.1289	.3090	.201
30	.1220	.4866	.1171	.4740	.239
45	.0798	.4364	.0764	.4205	.221
77	.0194	.2525	.0189	.2576	.104

Table 6.2a - Integrated intensity 2.5-4.9μm

Height	total		non-luminous		experimental
	base line	stochast	base line	stochast.	
cm	W/cm^2ster				
14	.0106	.0990	.0067	.0205	-
30	.0106	.1307	.0052	.0373	-
45	.0054	.1242	.0026	.0340	-
77	.0004	.0691	.0002	.0189	-

Table 6.2b - Integrated intensity 0.9-2.5μm

Height	total		non-luminous		experimental
	base line	stochast	base line	stochast.	
cm	W/cm^2ster				
14	.00002	.0052	0	0	.005
30	.00003	.0057	0	0	.005
45	.00001	.0064	0	0	.006
77	.00000	.0040	0	0	.001

Table 6.2c - Integrated intensity 0.5-0.9μm

	$\bar{I}$ (W/cm^2-ster)	$\overline{(I'^2)}^{1/2}$
Curve A	0.4638	0.1546
Curve B	0.2017	0.0810
Curve C	0.1323	0.0332
Curve D	.1171	-
Experiment	.201	

Table 6.3

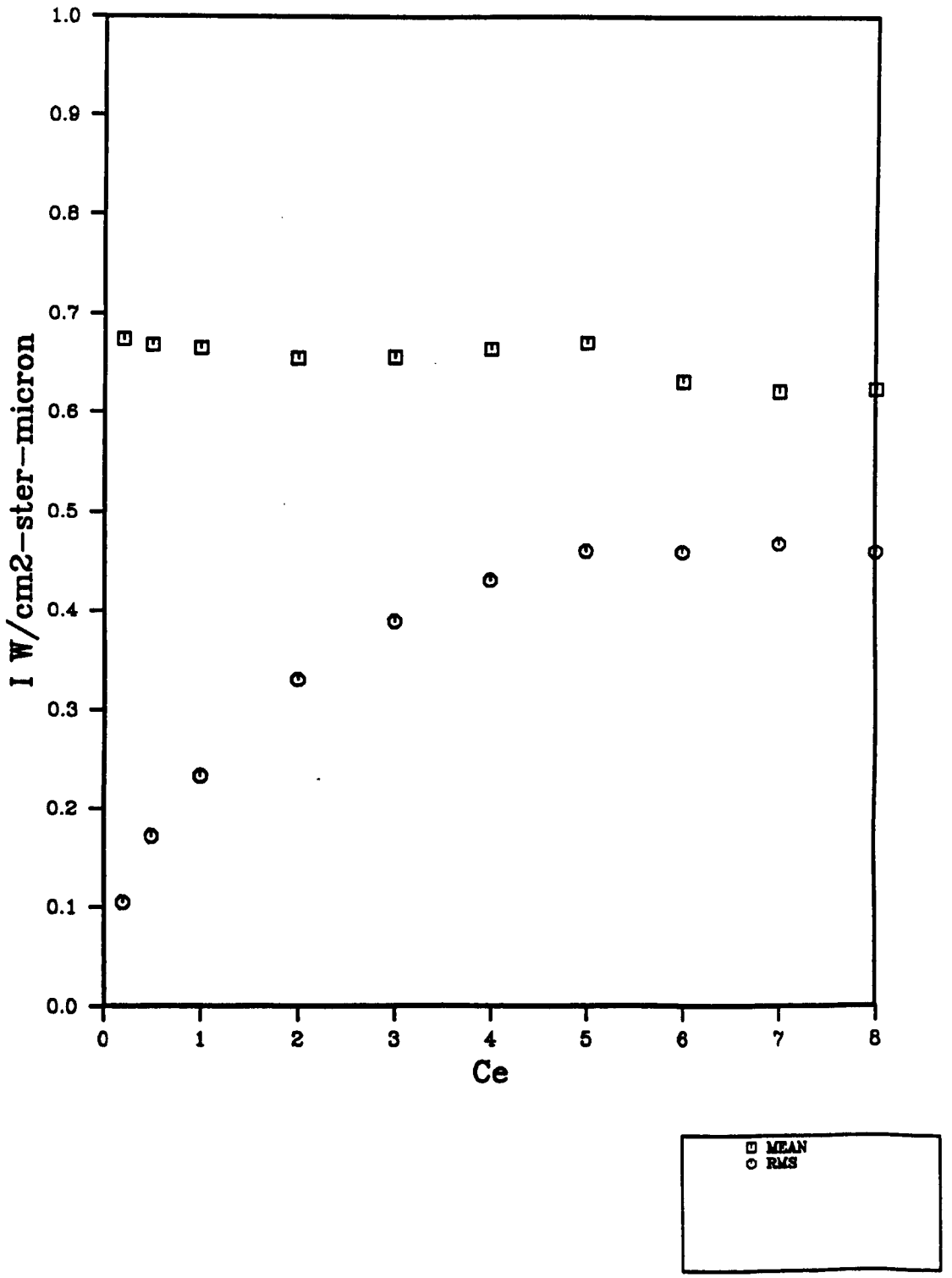

Spectral intensity at 4.3 microns obtained through stochastic approach. Path properties are for line of sight 30cm above burner. Graph shows the effect of characteristic eddy length on mean and rms intensity.

Figure 6.1

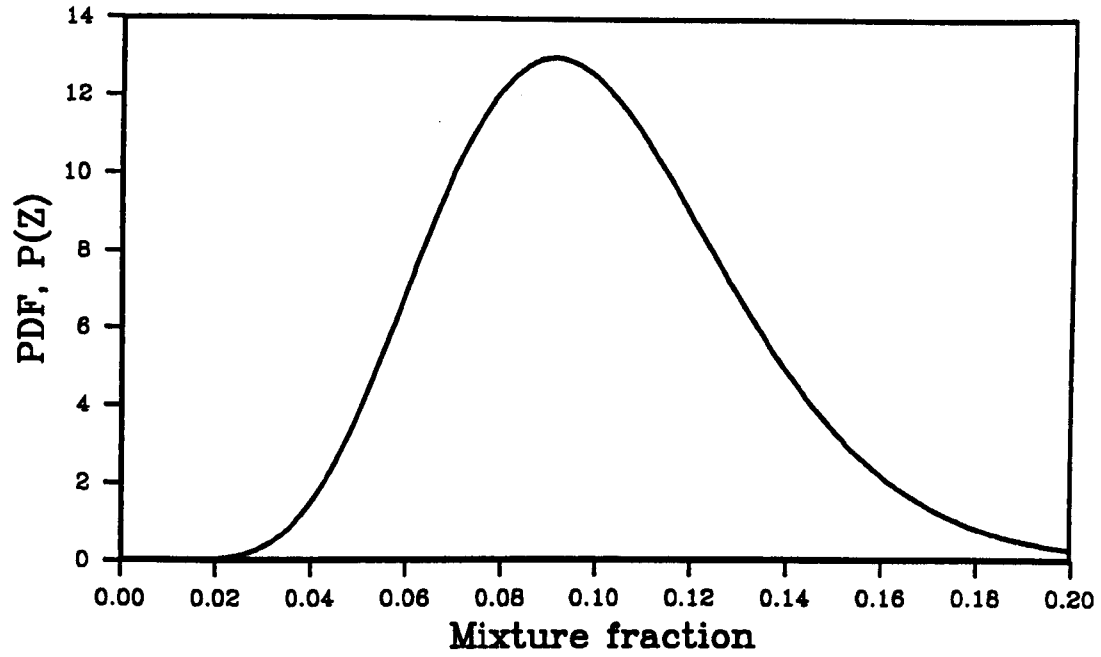

(a)

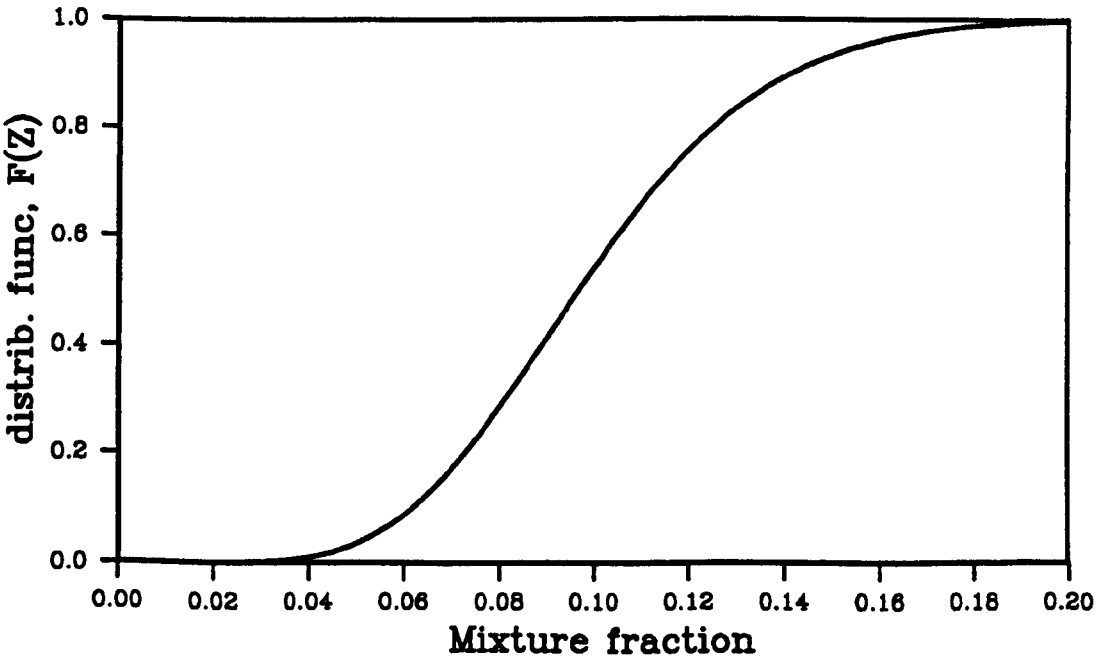

(b)

Probability density function and cumulative distribution function. Beta function specification for PDF with mean and variance 0.1 and 0.001 respectively.

Figure 6.2

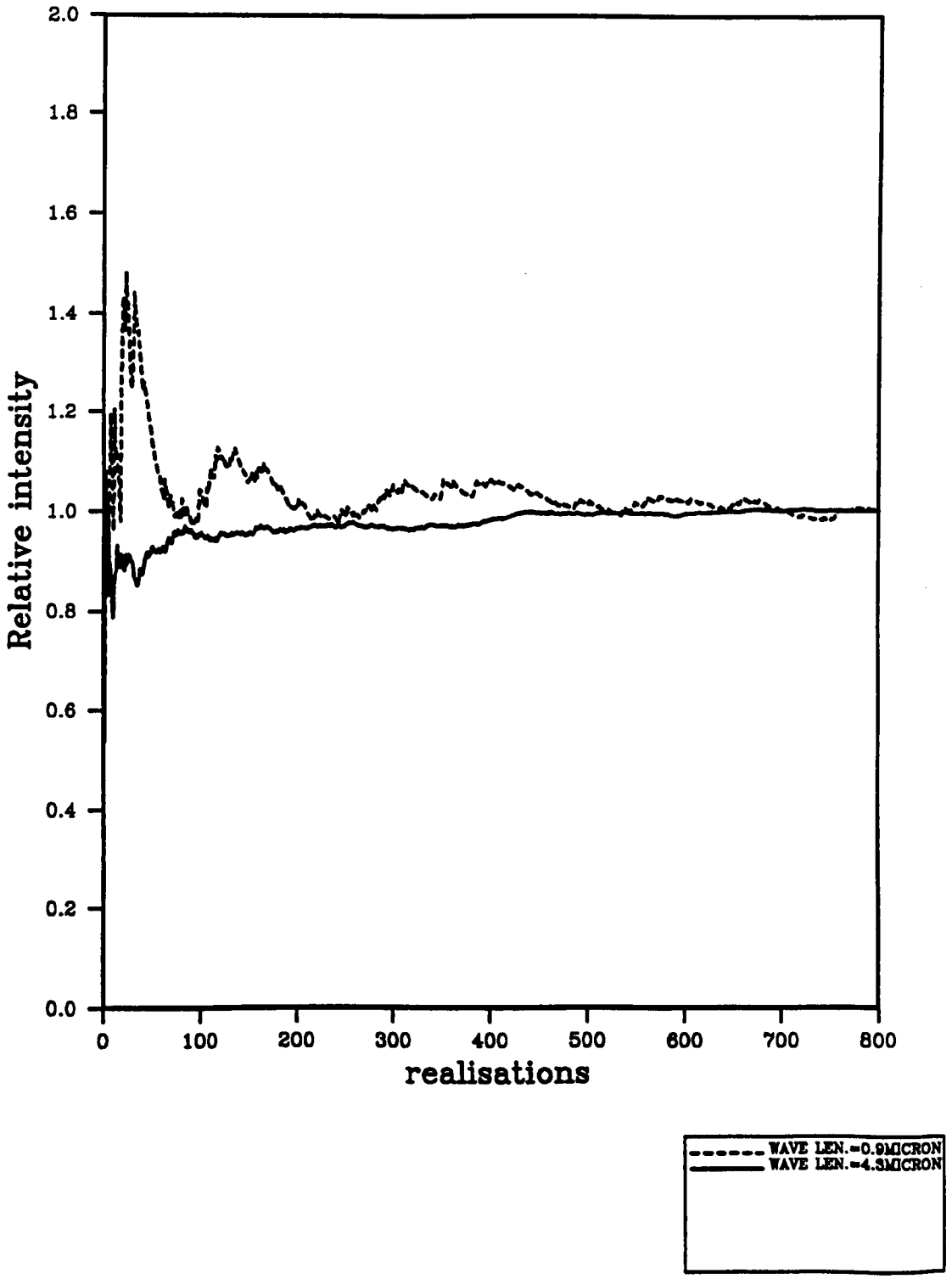

Relative mean spectral intensity variation with number of instantaneous realizations. Intensity is normalised by intensity at 800 realizations.
Height = 14cm in fire of Crauford (1984).

Figure 6.3

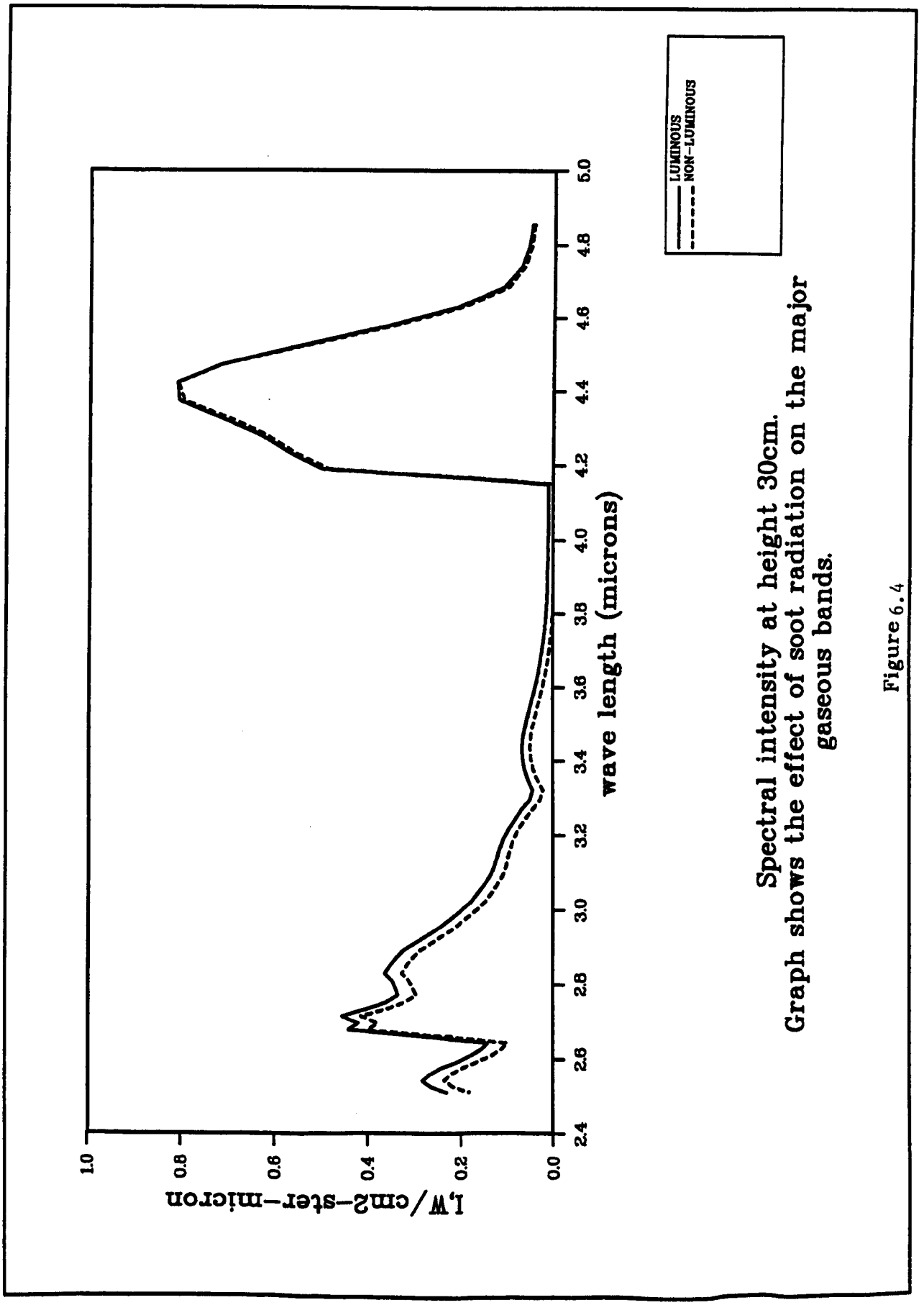

Spectral intensity at height 30cm.
Graph shows the effect of soot radiation on the major gaseous bands.

Figure 6.4

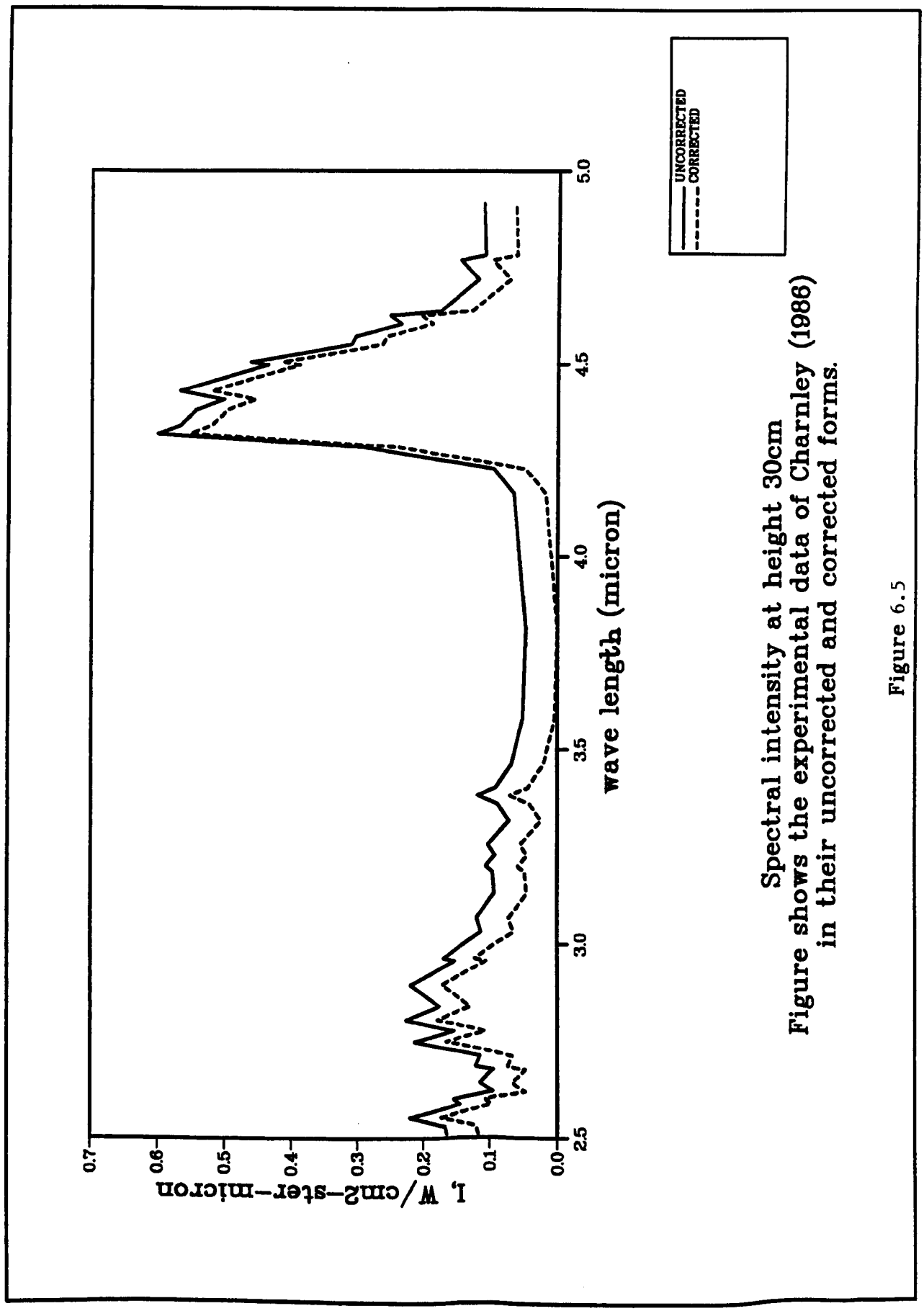

Spectral intensity at height 30cm
Figure shows the experimental data of Charnley (1986)
in their uncorrected and corrected forms.

Figure 6.5

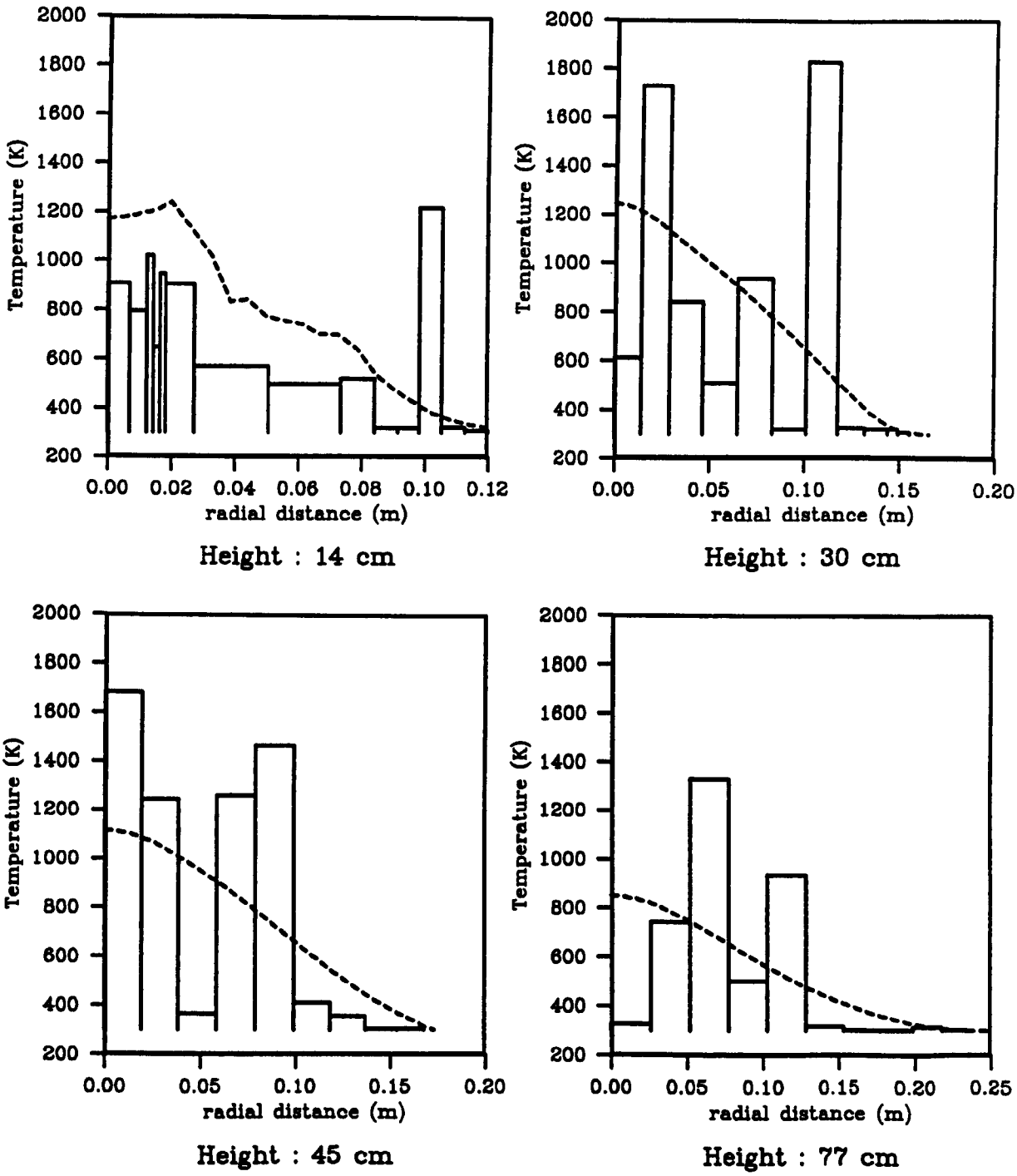

Profiles of Temperature
The histograms show typical realisations of temperature obtained through sampling the Reynolds PDF of mixture fraction. The dashed lines show the mean temperatures

Figure 6.6

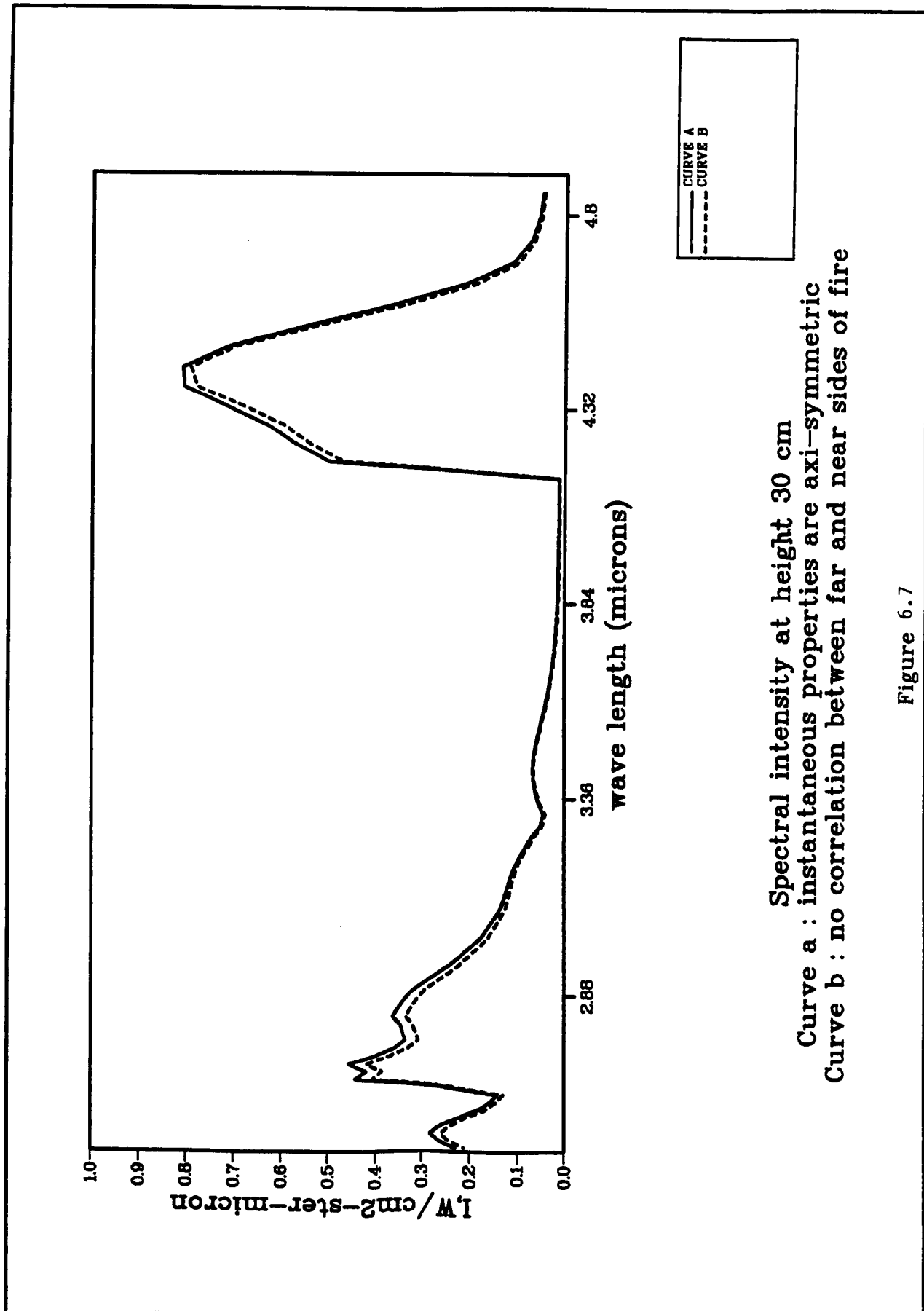

Spectral intensity at height 30 cm
Curve a : instantaneous properties are axi-symmetric
Curve b : no correlation between far and near sides of fire

Figure 6.7

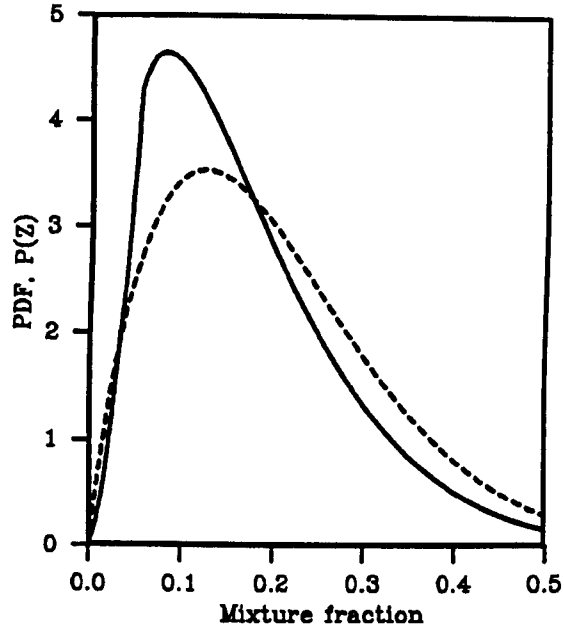

Height : 14 cm

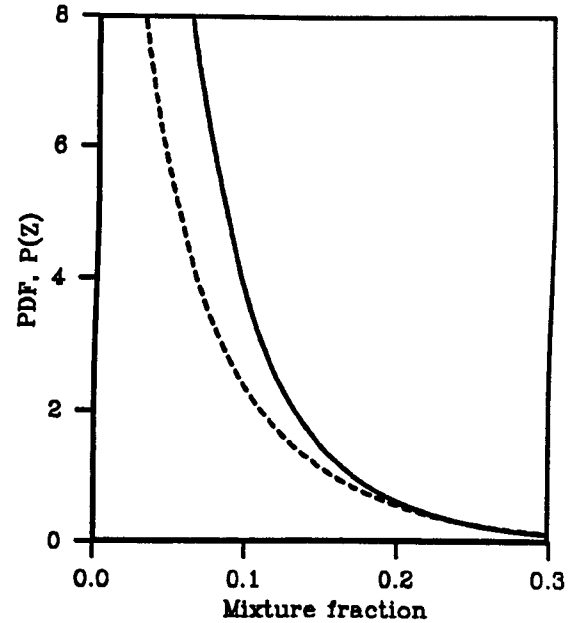

Height : 30 cm

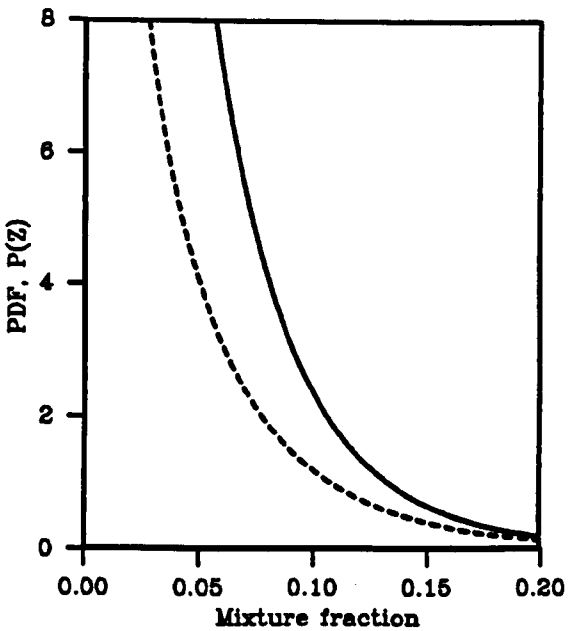

Height : 45 cm

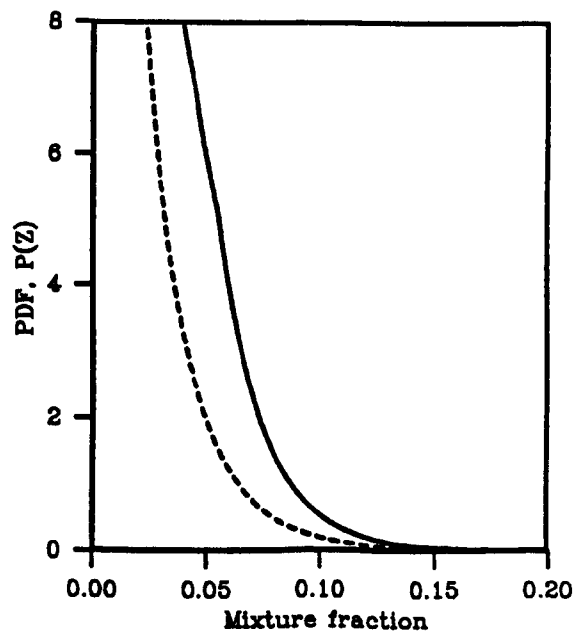

Height : 77 cm

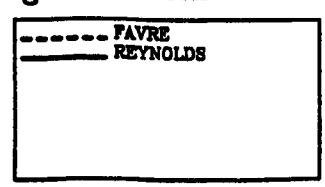

Predicted centre line PDFs
Figure compares predictions of Favre and Reynolds PDFs
Beta function form is assumed.

Figure 6.8

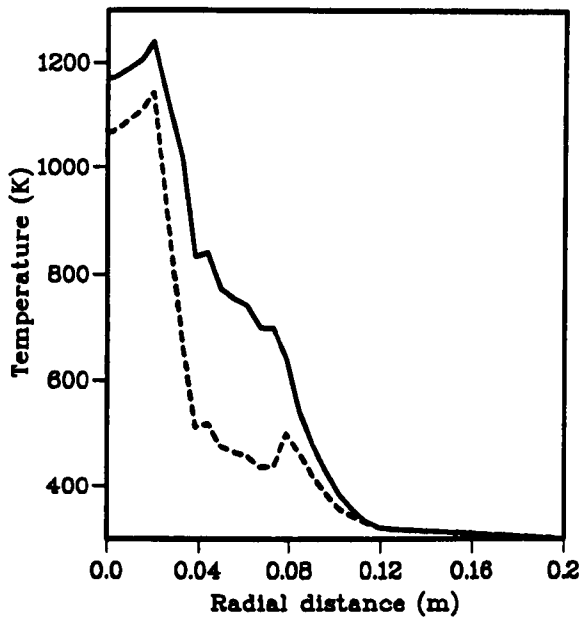

Height : 45 cm

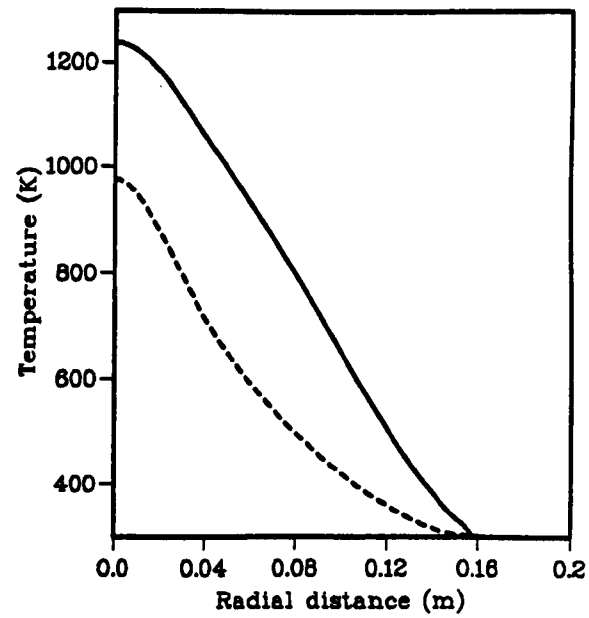

Height : 30 cm

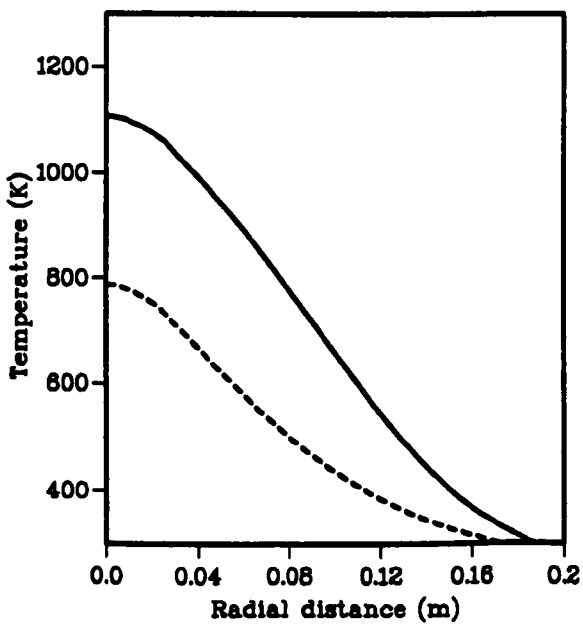

Height : 45 cm

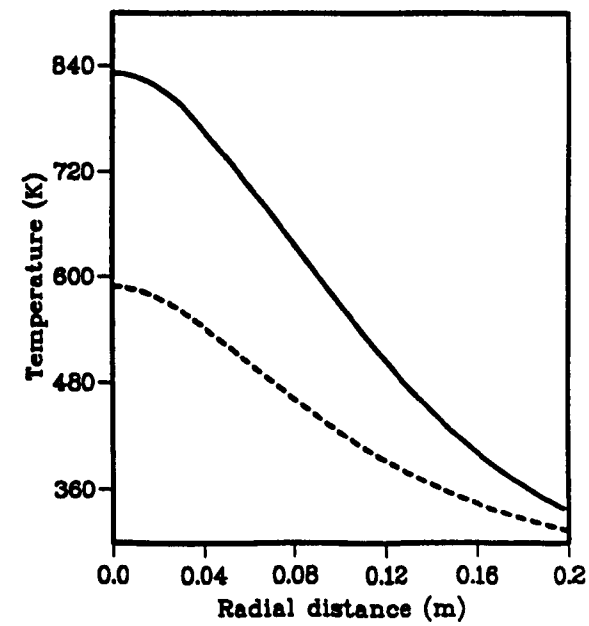

Height : 77 cm

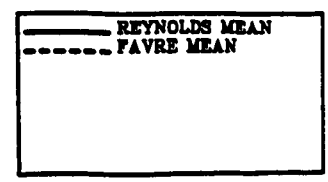

Comparison between predicted Reynolds and Favre mean temperatures.

Figure 6.9

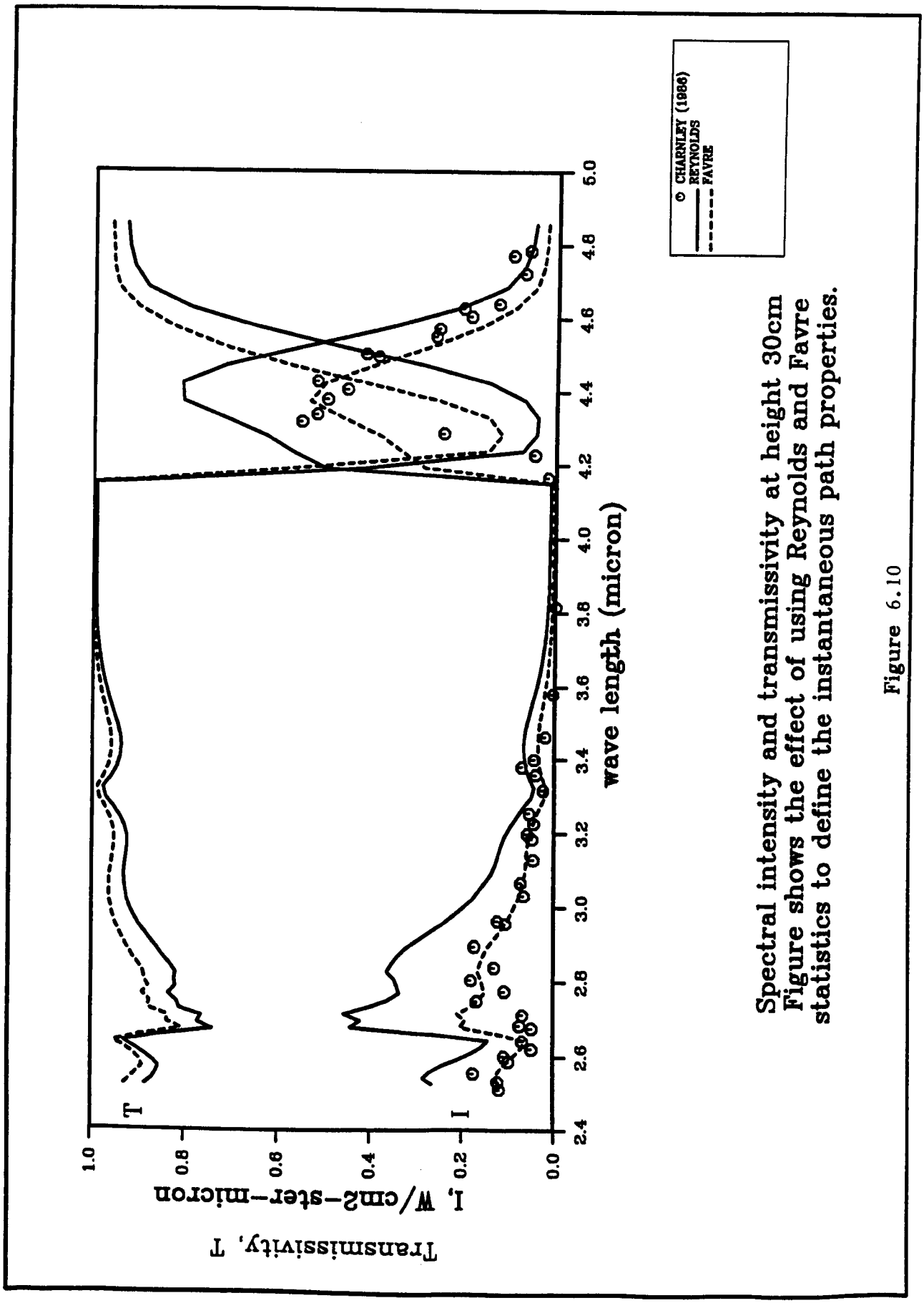

Spectral intensity and transmissivity at height 30cm
Figure shows the effect of using Reynolds and Favre
statistics to define the instantaneous path properties.

Figure 6.10

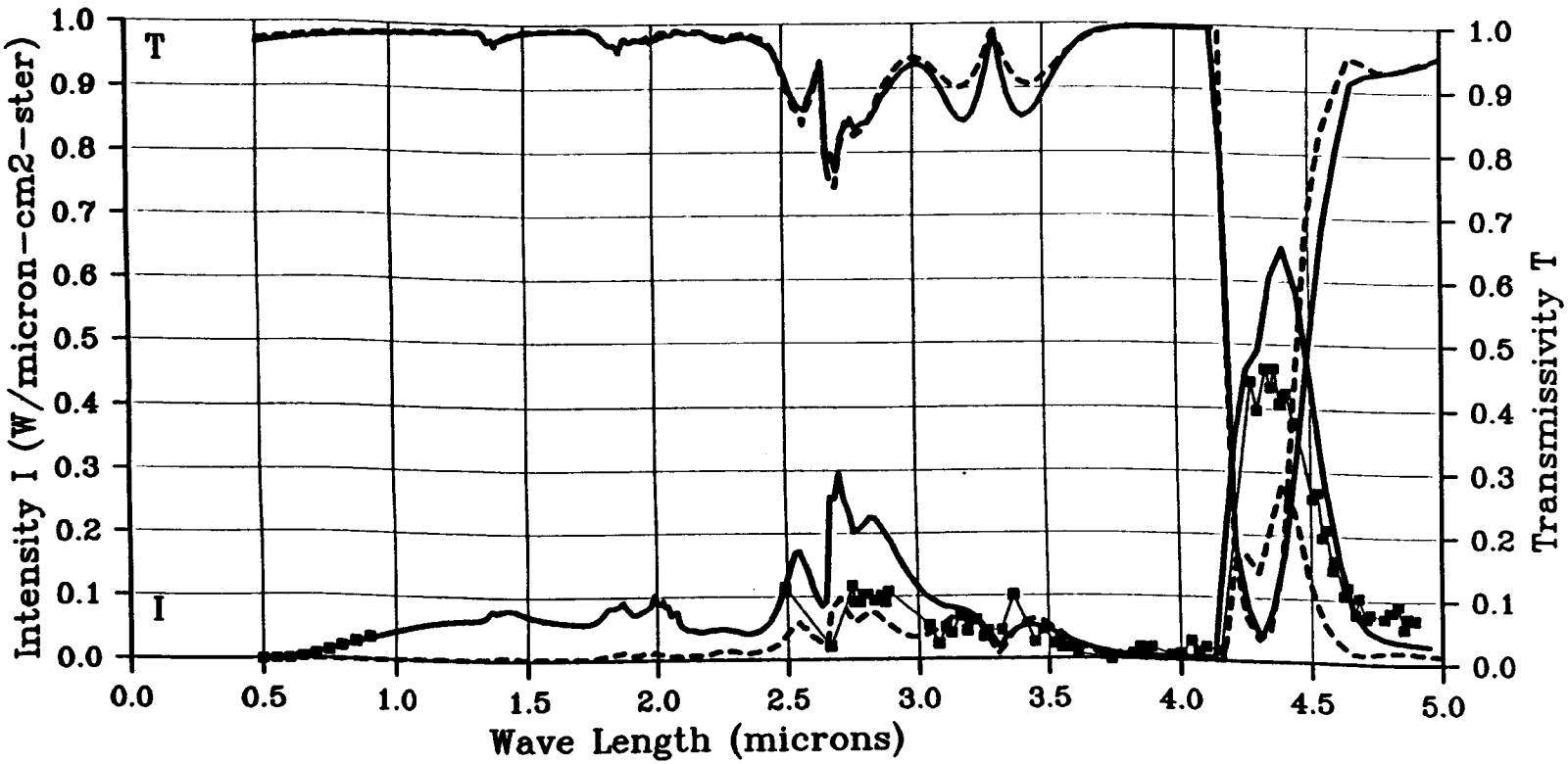

Spectral Transmissivity and Intensity

Height : 14cm

------- : MEAN PROPERTIES

——— : STOCHASTIC

—■— : EXPERIMENT

Figure 6.11

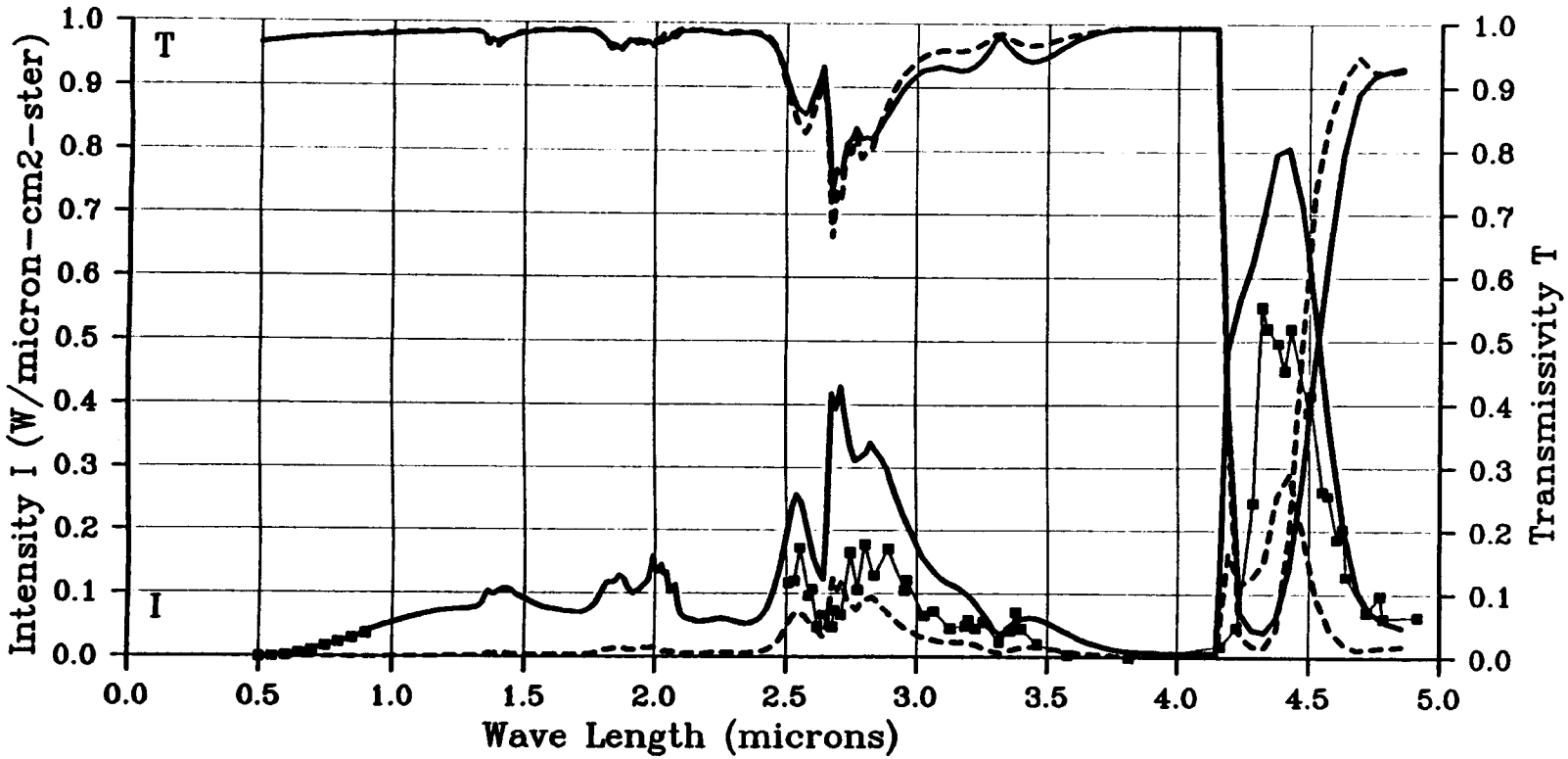

Spectral Transmissivity and Intensity

Height : 30cm

------- : MEAN PROPERTIES

——— : STOCHASTIC

—■— : EXPERIMENT

Figure 6.12

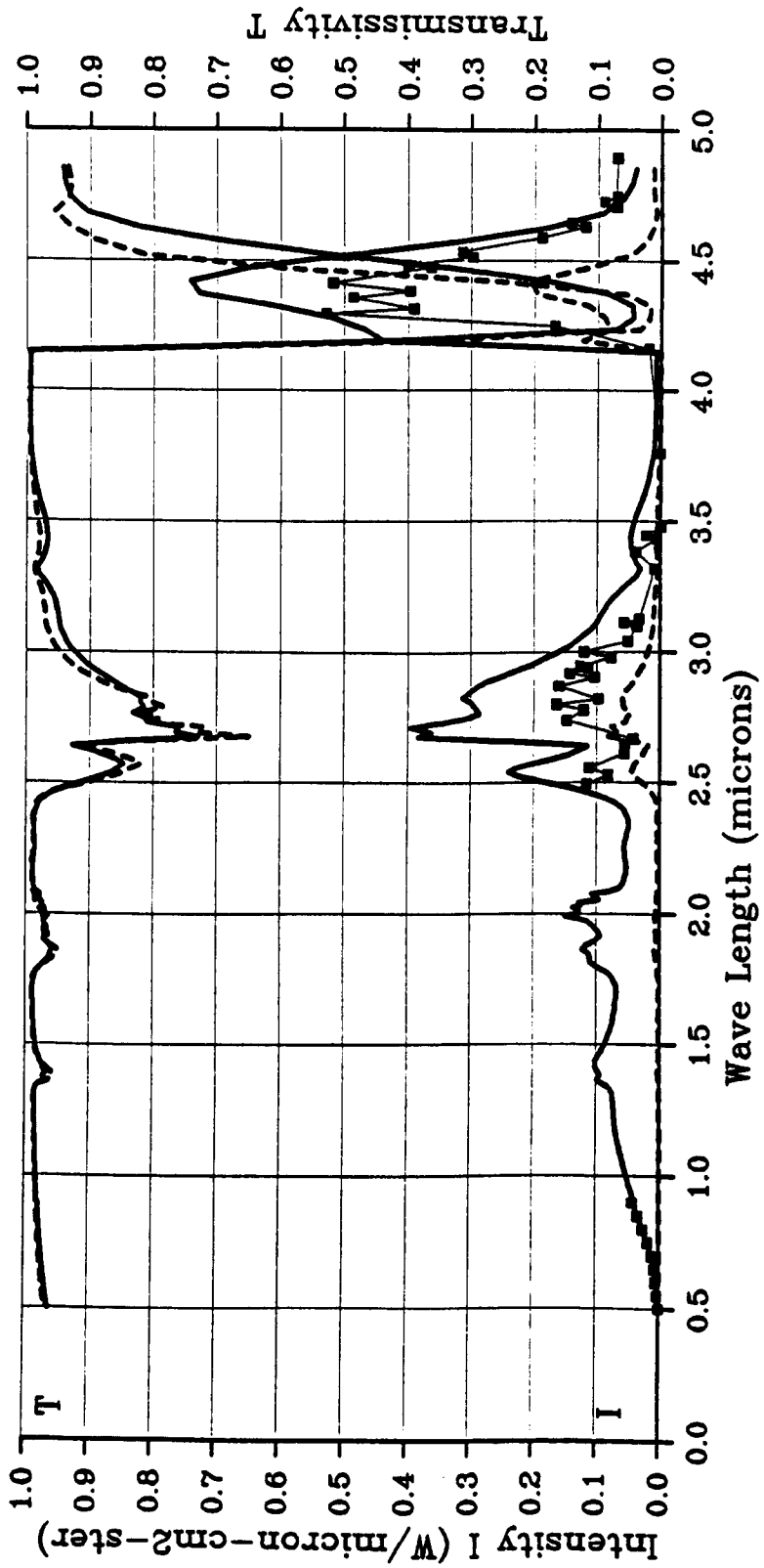

Spectral Transmissivity and Intensity

Height : 45cm

: MEAN PROPERTIES
: STOCHASTIC
: EXPERIMENT

Figure 6.13

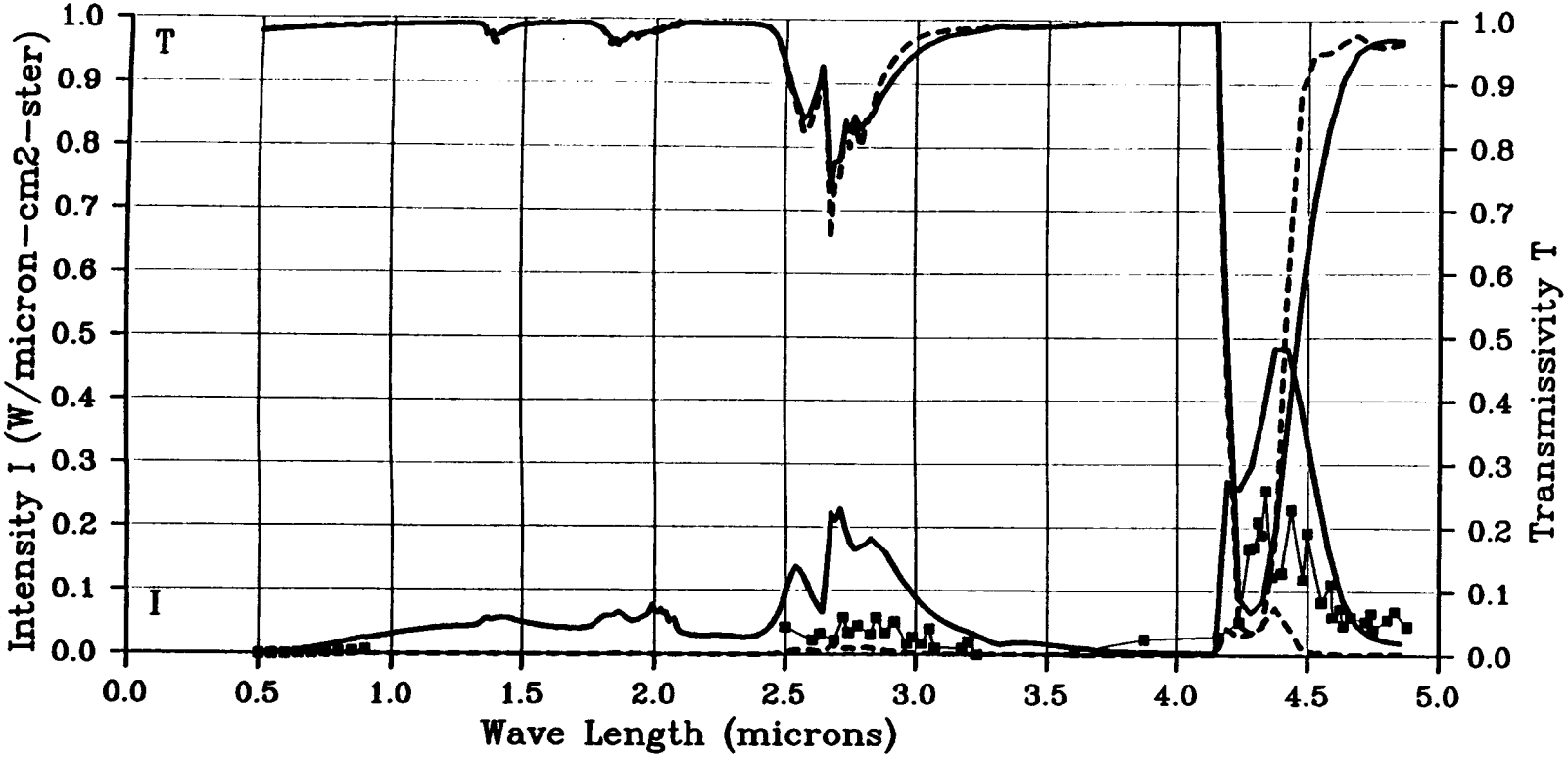

Spectral Transmissivity and Intensity

Height : 77cm

------- : MEAN PROPERTIES

——— : STOCHASTIC

—■— : EXPERIMENT

Figure 6.14

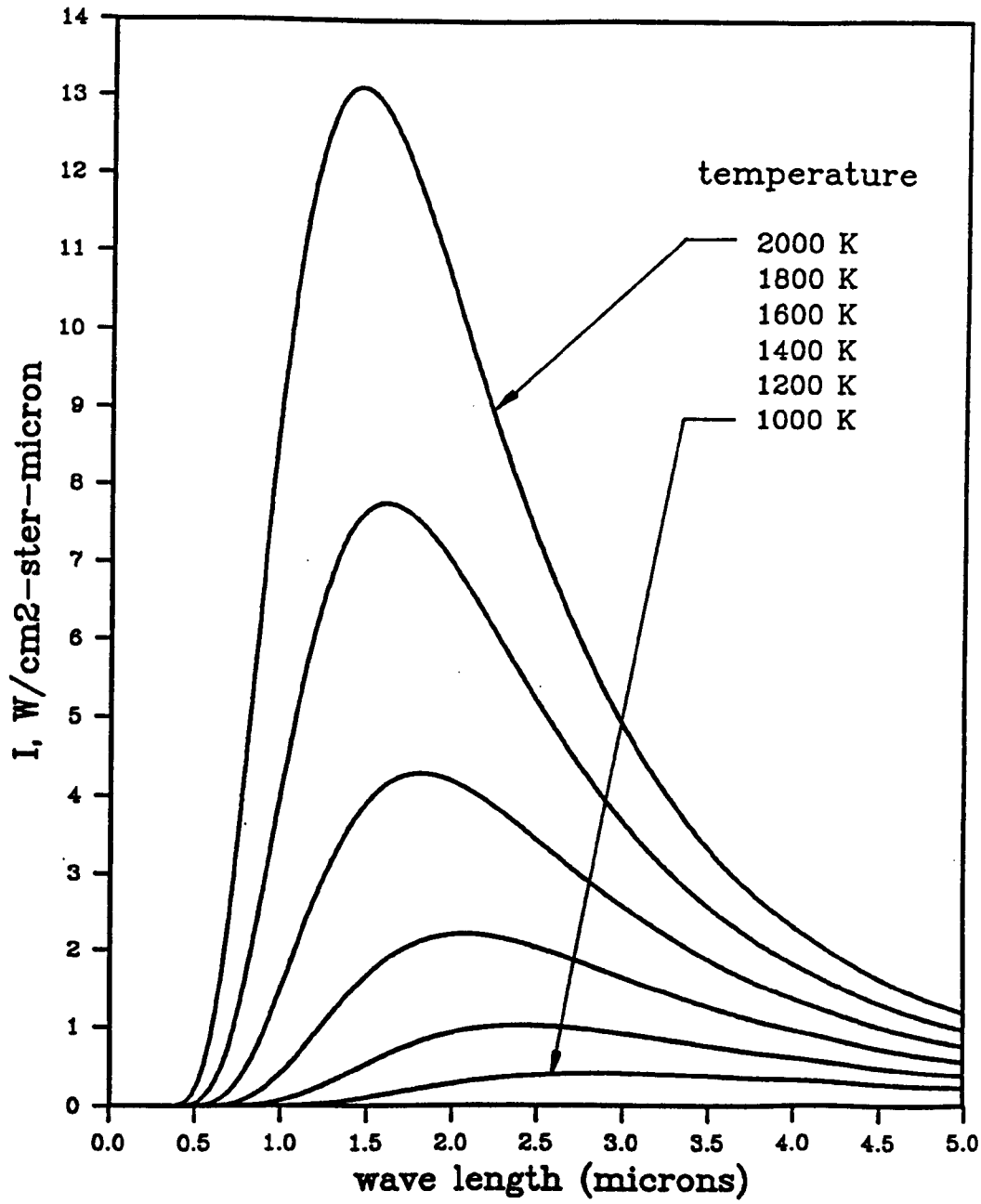

Blackbody radiative intensity

Figure 6.15

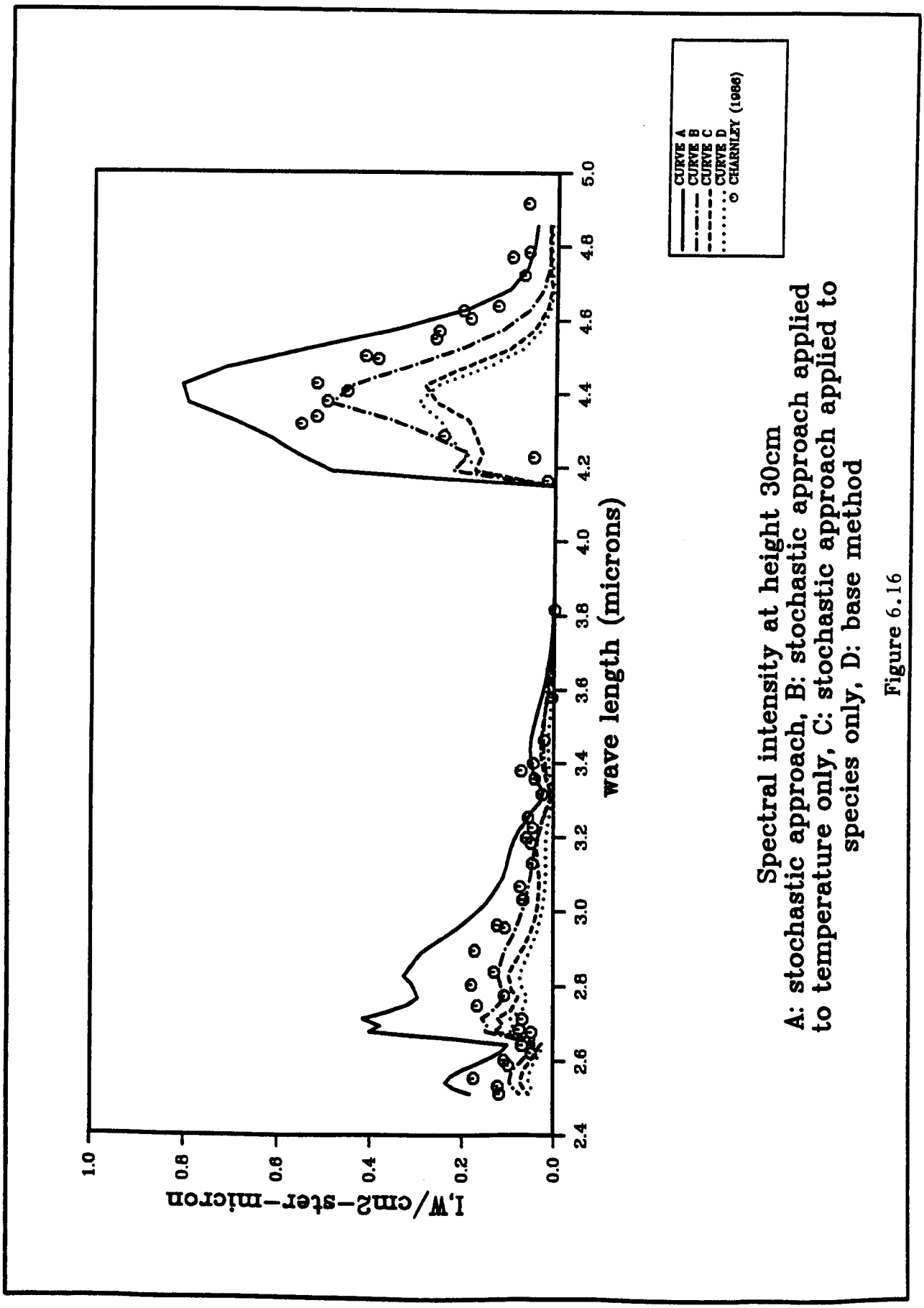

Spectral intensity at height 30cm
A: stochastic approach, B: stochastic approach applied to temperature only, C: stochastic approach applied to species only, D: base method

Figure 6.16

CHAPTER 7

Conclusions and recommendations for future work

This final chapter provides firstly a summary of the important features of all previous chapters, and then draws some overall conclusions. Subsequently a few key areas for further research are proposed.

Chapter 3 described a two-step two-parameter model for soot formation which incorporates, in an approximate manner, the processes of soot particle nucleation, coagulation and surface growth. The model is seen to reproduce the major features observed in a laminar flame experiment, in particular, the dependence of surface growth rate on particle surface area - a link that cannot be explicitly realised by single-step models. The soot formation rate is deduced from the experimental soot concentration data by detailed numerical simulation of the flame which allows the isolation of the source term appearing in conservation equations for the soot number density and mass concentration. A key feature of the model is that the soot formation rate is related explicitly to mixture fraction, in such a form that the model may be extended to turbulent flame prediction.

Chapter 4 grafts the soot formation model onto the flowfield prediction of a turbulent jet diffusion flame, where closure is achieved using the laminar flamelet approach and the two-equation k-ε turbulence model. Soot modelling entails the addition of mean balance equations for the soot number density and mass concentration, the source terms of which are related to mixture fraction. Their turbulent closure is then readily accomplished since the PDF of mixture fraction is a computed parameter. Soot particle coagulation is dependent on

particle number density whilst surface growth is dependent on the total soot surface area. This introduces correlations between these properties and mixture fraction within the soot source terms. Given the present modelling, however, such correlations are inaccessible and have therefore been neglected. The consequences of this simplification are shown to be of little significance and more important is the specification of the more highly non-linear terms which are dependent solely on mixture fraction. Soot concentration-mixture fraction correlations are, however, a major concern in soot oxidation, which is believed to result from the highly intermittent nature of this process. The accurate prediction of soot burnout rates would therefore require the computation of the joint PDF of soot concentration and mixture fraction.

Chapter 5 describes the prediction of a simulated buoyant fire for which Crauford (1984) has provided detailed velocity and temperature measurements that allow assessment of the predictions. As in chapter 4, turbulent closure is achieved using the laminar flamelet approach and the two equation k-ε turbulence model. Comparison with experimental data suggests that the gas phase is reasonably well predicted. There are, however, no direct soot measurements with which predicted values may be compared.

Chapter 6 uses the scalar field predicted in chapter 5 to calculate line-of-sight spectrally-resolved radiative intensities, which are subsequently compared with the data of Charnley (1986). The incorporation of turbulence interaction in the radiation calculation is shown to be essential. Some measure of its effect is achieved using the stochastic approach of Faeth et al (1986), which capitalises on the link between all scalars and mixture fraction to describe joint scalar statistics. Soot does not readily fall into this scheme since it cannot be unambiguously related to mixture fraction. A method is described by which locally-applicable soot state relationships may be derived. Such a treatment is essential since soot is generally strongly correlated with peak temperature zones. Radiation is a path-integral phenomenon and results in the appearance of multi-point

statistics which cannot be addressed by the moment closures presently used in turbulent flowfield modelling. The importance of multi-point statistics is believed to increase with optical depth. The presently used stochastic approach tends to overpredict radiative intensities which is thought to result from the overestimate of path lengths through instantaneous burning zones.

More generally, the present study has sought to propose and validate a soot formation model for the comprehensive prediction of soot and thermal radiation in turbulent buoyant fires. The strategy described is tractable in that it represents a relatively simple extension to the traditional laminar flamelet approach - only two further balance equations are required. Soot burnout remains a difficult area owing to the highly intermittent nature of this process and arguably requires a detailed description of the joint statistics of soot concentration and mixture fraction.

An estimate of turbulence-radiation interaction in the thermal emission from buoyancy-driven fires is essential. In the present case this results mainly from the non-linear dependence of blackbody radiation on temperature. Also important is the link between highly absorbing species and temperature. Turbulence interaction is most significant for luminous soot radiation since soot is contained in relatively thin sheets that are, typically, strongly related to high temperature zones. Moreover, soot radiation is most significant at shorter wavelengths where the temperature sensitivity of blackbody radiation is greatest.

Further development of the present work would require more specific investigation of soot oxidation in turbulent combustion. This entails the definition of a suitable instantaneous oxidation rate - at present it is not entirely clear which are the important oxidising species. In addition the intermittent nature of soot oxidation in turbulent non-premixed flames should be investigated. This might require the computation of the joint PDF of mixture fraction and soot

concentration, which should ideally be accompanied by detailed measurements of such correlations.

The better estimate of turbulence-radiation interaction will require the investigation of suitable length scales for burning zones.

REFERENCES

Abbas,A.S. and Lockwood,F.C. (1985) Prediction of soot concentrations in turbulent diffusion flames, J. Inst. Energy, pp.112-115.

Abramovitz,M. and Stegun,I.A. (1968) Handbook of mathematical functions, Dover Publications Inc., New York.

Appleton,J.P. (1973) Soot oxidation kinetics at combustion temperatures, AGARD-CP-125, Atmospheric Pollution by Aircraft Engines, paper 20.

Askari-Sardhai,A. (1987) Laminar flamelet modelling of turbulent combustion chemistry for practical fuels, Ph.D. thesis, Cranfield Institute of Technology.

Ballantyne,A., Boon,D.J. and Moss,J.B. (1976) Measurements of fluctuating temperature in open diffusion flames employing fine wire thermocouples, University of Southampton AASU Memo No.76/3.

Bilger,R.W. (1975) A note on Favre averaging, Comb. Sci. and Tech., 11, pp.215-217.

Bilger,R.W. (1976a) Turbulent jet diffusion flames, Prog. Energy and Comb. Sci., 1, pp.87-109.

Bilger,R.W. (1976b) Reaction zone thickness and formation of nitric oxide in turbulent diffusion flames, Comb. Flame, 26, pp.115-123.

Bilger,R.W. (1988) The structure of turbulent nonpremixed flames, 22nd Symp. (Int.) Comb., The Combustion Institute, pp.475-488.

Bockhorn,H., Fetting,F., Heddrich,A. and Wannemacher,G. (1984) Investigation of the surface growth of soot in flat low pressure hydrocarbon oxygen flames, 20th Symp. (Int.) Comb., The Combustion Institute, pp.979-988.

Borghi,R. (1975) Computational studies of turbulent flows with chemical reactions, in: Turbulent mixing in non-reactive and reactive flows, Murthy, S.N.B. (Ed.), Plenum Press, New York, pp.163-188.

Bray,K.N.C. (1973) Equations of turbulent combustion I: Fundamental equations of reacting turbulent flow, Univ. Southampton Report AASU Rept. no. 330.

Calcote,H.F. (1981) Mechanisms of soot nucleation in flames - a critical review, Comb. Flame, 42, pp.215-242.

Charnley,D. (1986) Radiating flamelet models of turbulent buoyant diffusion flames, Ph.D. thesis, Southampton University.

Chen,C.J. and Rodi,W. (1975) A mathematical model for turbulent stratified flow and its application to buoyant jets, 11th IAHR Congress, Sao Paulo, Brazil.

Chen,C.J. and Chen,C.H. (1979) On prediction and unified correlation for decay of vertical buoyant jets, J. Heat Transfer, 101, pp.532-537.

Chen,J-Y, Kollmann,W. and Dibble,R.W. (1989) PDF modelling of turbulent non-premixed methane jet flames, Comb. Sci. and Tech., 64, pp.315-346.

Cox,G. (1977) On radiant heat transfer from turbulent flames, Comb. Sci. and Tech., 17, p.75-78.

Cox,G. and Kumar,S. (1986) Field modelling of fire in forced ventilated enclosures, Comb. Sci. and Tech., 52, p.7-23.

Cox,G. and Kumar,S. (1987) A numerical model of fire in road tunnels. Tunnels and Tunnelling, pp.55-60 (March 1987).

Crauford,N.L. (1984) The structure of an unconfined buoyant turbulent diffusion flame, Ph.D. thesis, Southampton University.

Crauford,N.L., Liew,S.K. and Moss,J.B. (1985) Experimental and numerical investigation of a buoyant fire, Comb. Flame,61, pp.63-77.

Dalzall,W.H. and Sarofim,A.F. (1969) Optical constants of soot and their application to heat flux calculations, J. Heat Trans., 91, p. 100-104.

De Ris,J. (1979) Fire radiation -a review, 17th Symp. (Int.) Comb., The Combustion Institute, pp.1003-1016.

Dibble,R.W., Kollmann,W., Farshchi,M. and Scheffer,R.W. (1986) Second order closure for turbulent nonpremixed flames: scalar dissipation and heat release effects, 21st Symp. (Int.) Comb., The Combustion Institute, pp.1329-1340.

Dixon-Lewis,G., Goldsworthy,F.A. and Greenberg,J.B. (1975) Flame structure and flame reaction kinetics IX. Calculation of properties of multi-radical premixed flames, Proc. Roy. Soc., London A, 346, pp.261-278.

Dixon-Lewis,G. and Missaghi,M. (1988) Structure and extinction limits of counterflow diffusion flames of hydrogen-nitrogen mixtures in air, 22nd Symp. (Int.) Comb., The Combustion Institute, pp.1461-1470.

Dugwell,R. and Foster,P.J. (1973) Carbon formation from methane in combustion products, Carbon, 11, pp.455-467.

Edelman,R.B., Fortune,O. and Weilerstein,G. (1972) Some observations on flows described by coupled mixing and kinetics, Symp. on Emissions from Continuous Combustion Systems, pp.55-90, Cornelius,W. and Agnew,W.G. (Eds.), Plenum Press.

Edwards,D.K. and Menard,W.A. (1964) Correlations for absorption by methane and carbon dioxide, Appl. Optics., 3, pp.847-852.

Edwards,D.K. and Balakrishnan,A. (1973) Thermal radiation by combustion gases, Int. J. Heat Mass Trans., 16, pp.25-40.

Edwards,D.K. (1975) Advances in heat transfer, Irvine, T.F. and Hartnett, J.P. (Eds.), vol. 12, Academic Press, New York, pp.115-193

Emmons,H.W. (1979) The prediction of fires in buildings, 17th Symp. (Int.) Comb., The Combustion Institute, pp.1101-1111.

Faeth,G.M., Jeng,S.M. and Gore, J.P. (1986) Radiation from fires, in: Heat Transfer in Fire and Combustion Systems, Law, C.K. et al (Eds.), HTD, vol.45, ASME, pp.137-151.

Felske,J.D. and Tien,C.L. (1977) The use of the Milne-Eddington absorption coefficient for radiative heat transfer in combustion systems, Heat Transfer, 99, pp.458-465.

Frenklach,M., Clary,D.W., Gardiner,W.C. and Stein,S.E. (1985) Detailed kinetic modelling of soot formation in shock-tube pyrolysis of acetylene, 20th Symp. (Int.) Comb., The Combustion Institute, pp.887-901.

Frenklach,M., Clary,D.W. and Yuan,T. (1986) Mechanism of soot formation in acetylene-oxygen mixtures, Comb. Sci. and Tech., 50, pp.79-115.

Fristrom,R.M. and Westenberg,A.A. (1965) Flame structure, McGraw-Hill.

Fuchs, N.A. (1964) The mechanics of aerosols, Pergamon Press.

Gaydon,A.G. and Wolfhard,H.G. (1979) Flames: their structure, radiation and temperature, 4th Ed., Richard Clay Ltd.

Gengembre,E., Cambray,P., Karmed,D. and Bellett,J.C. (1984) Turbulent diffusion flames with large buoyancy effects, Comb. Sci. and Tech., 41, pp.55-67.

Gibson,M.M. and Launder,B.E. (1976) On the calculation of horizontal, turbulent free shear flows under gravitational influence, ASME J. of Heat Transfer, 98, pp.81-87.

Gilyazetdinov,L.P.(1972) The kinetics and formation mechanism of carbon black during the thermal decomposition of hydrocarbons in the gas phase, Khim. Tverd. Topl., 3, pp.103-111.

Givi,P. (1989) Model-free simulations of turbulent reactive flows, Prog. Energy and Comb. Sci., 15, pp.1-107.

Glassman,I. (1988) Soot formation in combustion processes, 22nd Symp. (Int.) Comb., The Combustion Institute, pp.295-311.

Goody,R.M. (1964) Atmospheric radiation, Clarendon Press.

Gordon,S. and McBride,B.J. (1971) Computer program for calculation of complex chemical equilibrium compositions, rocket performance, incident and reflected shocks and Chapman-Jouget detonations, NASA-SP-273.

Gore,J.P. and Faeth,G.M. (1986) Structure and spectral radiation properties of turbulent ethylene/air diffusion flames, 21st Symp. (Int.) Comb., The Combustion Institute, pp.1521-1531.

Gore,J.P. and Faeth,G.M. (1988) Structure and radiation properties of luminous turbulent acetylene/air diffusion flames, J. Heat. Transfer, 110, pp.173-181.

Gosman,A.D. and Ioannides,E. (1981) Aspects of computer simulation of liquid-fuelled combustors, AIAA 19th Aerospace Science Meeting.

Graham,S.C., Horner,J.B. and Rosenfeld,J.L.J. (1975) The formation and coagulation of soot aerosols generated by the pyrolysis of aromatic hydrocarbons, Proc. Royal Soc. London, 344, pp.259-285.

Gray,L.P. and Penner,S.S. (1965) Approximate band absorption calculations for methane, J. Quant. Spec. Rad. Transfer, 5., pp.611-620

Grosshandler,W.L. (1979) Radiation from non-homogeneous fires, Factory Mutual Research Corp. RC79-BT-9.

Grosshandler,W.L. (1980) Radiative heat transfer in nonhomogeneous gases: a simplified approach, J. Heat Mass Trans., 23, pp.1447-1459.

Grosshandler,W.L. (1985) The effect of large scale fluctuation on flame radiation, paper presented at the 10th ICODERS, Berkley, Aug. 1985.

Haynes,B.S. and Wagner,H. Gg. (1981) Soot formation, Prog. Energy and Comb. Sci., 7, pp.229-273.

Hisrschfelder,J.O., Curtis,C.F. and Bird,R.B. (1967) Molecular theory of gas and liquids, Wiley and Sons.

Hottel,H.C. and Sarofim,A. F. (1967) Radiative transfer, McGraw-Hill.

Janicka,J. and Kollmann,W. (1979) A two-variable formalism for the treatment of chemical reaction in turbulent H2-air diffusion flames, 17th Symp. (Int.) Comb., The Combustion Institute, pp.421-430.

Janicka,J. (1981) The application of partial equilibrium assumptions for the prediction of diffusion flames, J. Non-equilib. Thermodyn., 6, pp.367-386.

Jeng,S-M, Chen,L-D and Faeth,G.M. (1982) The structure of buoyant methane and propane diffusion flames, 19th Symp. (Int.) Comb., The Combustion Institute, pp.348-358.

Jeng,S-M, Lai,M-S and Faeth,G.M. (1984) Nonluminous radiation in turbulent buoyant axi-symmetric flames, Comb. Sci. and Tech., 40, pp. 41-53.

Jones,W.P. and Launder,B.E. (1972) The prediction of laminarization with a two-equation model of turbulence, Int. J. Heat and Mass Transfer, 15, pp.301-314.

Jones,W.P. and Priddin,C. (1979) Prediction of the flowfield and local gas composition in gas turbine combustors, 17th Symp. (Int.) Comb., The Combustion Institute, pp.399-409.

Jones,W.P. (1980) Models for turbulent flows with variable density, VKI lecture series 1979-2, in: Prediction Methods For Turbulent Flows, Kollmann,W. (Ed.), Hemisphere Pub. Corp.

Jones,W.P. and Whitelaw,J.H. (1981) Calculation methods for reacting turbulent flows, in: Prediction of turbulent reacting flows in practical systems, presented at the fluid engineering conference, Boulder, Colorado.

Jones,W.P. and Lindstedt,R.P. (1988) Global reaction schemes for hydrocarbon combustion, Comb. and Flame, 73, pp.233-249.

Kaye,G.W.C. and Laby,T.H. (1971) Tables of physical and chemical constants and some mathematical functions, Longmans, London.

Kennedy,I. and Kollmann,W. (1990) Prediction of soot in laminar diffusion flames, AIAA 90-0459, 28th Aerospace meeting, Reno, Nevada.

Kent,J.H. and Bilger,R.W. (1977) The prediction of turbulent diffusion flame fields and nitric oxide formation, 16th Symp. (Int.) Comb., The Combustion Institute, pp.1643-1656.

Kent,J.H., Jander,H. and Wagner,H.G. (1981) Soot formation in a laminar diffusion flame, 18th Symp. (Int.) on Combustion, The Combustion Institute.

Kent,J.H. and Wagner,H.Gg. (1984) Why do diffusion flames emit smoke? Comb. Sci. and Tech., 41, pp.245-269.

Kent,J.H. and Honnery,D. (1987) Soot and mixture fraction in turbulent diffusion flames, Comb. Sci. and Tech., 54, pp.383-397.

Kerker,M. (1969) The scattering of light and other electromagnetic radiation, Academic Press, New York.

Khan,I.M. and Greeves,G. (1974) A method for calculating the formation and combustion of soot in diesel engines, Heat transfer in flames, Afgan,N.H. and Beer,J.M. (Eds.), Scripta Book Co.

Kounalakis,M.E., Gore,J.P. and Faeth,G.M. (1988) Turbulence/radiation interaction in nonpremixed hydrogen/air flames, 22nd Symp. (Int.) Comb., The Combustion Institute, pp.1281-1290.

Launder,B.E. and Spalding,D.B. (1972) Mathematical models of turbulence, Academic Press.

Launder,B.E., Morse,A.P., Rodi,W. and Spalding,D.B. (1972) The prediction of free shear flows - a comparison of six turbulence models, NASA SP-311.

Launder,B.E., Reece,G.J. and Rodi,W. (1975) progress in the development of a Reynolds-stress turbulence closure, J. Fluid Mech., vol.68, part 3, pp.537-566.

Leckner,B. (1972) Spectral and total emissivity of water vapour and carbon dioxide, Comb. and Flame, 19, pp.33-48.

Lee,P.A., Thring,M.W. and Beer,J.M. (1962) On the rate of combustion of soot in laminar soot flames, Comb. Flame, 6, pp.137-145.

Lee,S.C. and Tien,C.L. (1981) Optical constants of soot in hydrocarbon flames, 18th Symp. (Int.) Comb., The Combustion Institute, pp.1159-1166.

Libby,P.A. (1975) On the prediction of intermittent turbulent flows, J. Fluid Mech., vol.68, part 2, pp.273-295.

Libby,P.A. and Williams,F.A. (1980) Fundamental aspects, in: Turbulent Reacting Flows, Libby,P.A. and Williams,F.A. (Ed.), Topics in Applied Physics, vol. 44, Springer-Verlag.

Liew,S.K., Bray,K.N.C. and Moss,J.B. (1981) A flamelet model of turbulent non-premixed combustion, Comb. Sci. and Tech., 27, pp.69-73.

Liew,S.K. (1983) Flamelet models of turbulent non-premixed combustion, Ph.D. thesis, University of Southampton.

Liew,S.K., Bray,K.N.C. and Moss,J.B. (1984) A stretched laminar flamelet model of turbulent nonpremixed combustion, Comb. and Flame, 56, pp.199-213.

Ljuboja,M. and Rodi,W. (1981) Prediction of horizontal and vertical turbulent buoyant wall jets, J. Heat Transfer, 103, pp.343-349.

Lockwood,F. and Naguib,A.S. (1975) The prediction of the fluctuations in the properties of free, round-jet turbulent diffusion flames, Comb. and Flame., 24, pp.109-124.

Lockwood,F.C. and Moneib,H.A. (1981) Fluctuating temperature measurements in turbulent jet diffusion flames, report, Mech. Eng. Dept., Imperial College of Science and Technology, May 1981.

Lockwood,F.C. and Shah,N.G. (1981) A new radiation solution method for incorporation in general combustion prediction procedures, 18th Symp. (Int.) Comb., The Combustion Institute, pp.1405-1414.

Ludwig,C.B., Malkmus,W., Reardon,J.E. and Thompson,J.A.L. (1973) Handbook of infrared radiation from combustion gases, NASA SP-3080.

Lundgren,T.S. (1969) Model equation for nonhomogeneous turbulence, Phys. Fluids, 12, pp.485-497.

Magnussen,B.F., Hjertager,B.H. (1976) On mathematical modelling of turbulent combustion with special emphasis on soot formation and combustion, 16th Symp. (Int.) Comb., The Combustion Institute, pp.719-729.

Magnussen,B.F., Hjertager,B.H., Olsen,J.G. and Bhaduri,D. (1979) Effects of turbulent structure and local concentrations on soot formation and combustion in C2H2 diffusion flames, 17th Symp. (Int.) Comb., The Combustion Institute, pp.1383-1393.

Malkmus,W. and Thomson,A. (1961) Infrared emissivity of diatomic gases for the anharmonic vibrating-rotator model, J. Quant. Spec. Rad. Trans., 2, pp.17-39.

Malkmus,W. (1963a) Infrared emissivity of carbon dioxide (2.7μm band), General Dynamics/Astronautics AE63-0047.

Malkmus,W. (1963b) Infrared emissivity of carbon dioxide (4.3μm band), J. Opt. Soc. America, 53, p.951.

Markatos,N.C., Malin,M.R. and Cox,G. (1982) Mathematical modelling of buoyancy-induced smoke flow in enclosures, Int. J. Heat and Mass Transfer, 25 (1), pp.63-75.

McGuirk,J.J. and Rodi,W. (1977) The calculation of three-dimensional free jets, Symposium on turbulent shear flows, Pennsylvania State University, April,1977.

Megaridis,C.M. and Dobbins,R.A. (1989) Comparison of soot growth and oxidation in smoking and non-smoking ethylene diffusion flames, Comb. Sci. and Tech., 66, pp.1-16.

Mitchell,R.E., Sarofim,A.F. and Clomburg,L.A. (1980) Experimental and numerical investigation of confined laminar diffusion flames, Comb. and Flame, 37, pp.227-244.

Morse,A.P. (1977) The prediction of free turbulent boundary layers by use of a two-equation model of turbulence, Ph.D. thesis, University of London.

Mullins,J. and Williams,A. (1987) The optical properties of soot: a comparison between experimental and theoretical values, Fuel, 66, pp.277-280.

Mullins,J., Simmons,B. and Williams,A. (1987) Rate of formation of soot from hydrocarbon flames and its destruction, AGARD CP-422, Combustion and Fuels in Gas Turbine Engines.

Moss,J.B., Stewart,C.D. and Syed,K.J. (1987) Flamelet chemistry modelling of soot formation for radiation prediction in combustor flowfields, AGARD CP-422, Combustion and Fuels in Gas Turbine Engines.

Moss,J.B., Stewart,C.D. and Syed,K.J. (1988) Flowfield modelling of soot formation at elevated pressure, 22nd Symp. (Int.) Comb., The Combustion Institute, p.413-423.

Nagle,J. and Strickland-Constable,R.F. (1962) Oxidation of carbon between 1000-2000°C, Proc. 5th Carbon Conference, Vol. 1, pp.154-164.

Neoh,K.G., Howard,J.B. and Sarofim,A.F. (1984) Effect of oxidation on the physical structure of soot, 20th Symp. (Int.) on Combustion, The Combustion Institute, pp.951-957.

Oran,E.S. and Boris,J.P. (1981) Detailed modelling of combustion systems, Prog. Energy and Comb. Sci., 7, pp.1-72.

Paczko,G., Lefdal,P.M. and Peters,N. (1986) Reduced reaction schemes for methane, methanol and propane flames, 21st Symp. (Int.) Comb., The Combustion Institute, pp.739-748.

Palmer,H.B. and Cullis,C.F. (1965) The formation of carbon from gases, in: Chemistry and Physics of Carbon, 1, Walker, P.L. (Ed.), Marcel Dekker Inc., pp.265-325.

Patankar,S.V. (1980) Numerical heat transfer and fluid flow, McGraw-Hill.

Patel,V.C., Rodi,W. and Scheuerer,G. (1985) Turbulence models for near-wall and low Reynolds number flows: a review, AIAA journal, 23, no.9, pp.1308-1319.

Pericleous,K.A., Worthington,D.R.E. and Cox,G. (1988) The field modelling of fire on an air-supported structure, 2nd Int. Symp. on Fire Safety Science, Tokyo.

Peters,N. (1984) Laminar diffusion flamelet models in non-premixed turbulent combustion, Prog. Energy Comb. Sci., 10, pp.319-339.

Pope,S.B. (1978) An explanation of the turbulent Round-jet/plane-jet anomaly, AIAA Journal., vol.16, no.3, pp.279-281.

Pope,S.B. (1981) A Monte Carlo method for the PDF equations of turbulent reactive flow, Comb. Sci. and Technol., 25, pp.159-174.

Pope,S.B. (1985) PDF methods for turbulent reactive flows, Prog. Energy and Comb. Sci., 11, pp.119-192.

Pope,S.B. (1990) Computation of turbulent combustion: progress and challenges, 23rd Symp. (Int.) Comb., Orleans.

Powell,M.J.D. (1970) A FORTRAN subroutine for solving systems of nonlinear algebraic equations, in: Numerical methods for nonlinear algebraic equations, Rabinowitz, P. (Ed.), Gordon and Breach Science Publishers.

Pratt,D.T. (1977) Calculation of chemically reacting flows with complex chemistry, In: Studies in Convection, 2, Launder,B.E. (Ed.), Academic Press.

Raine,R.R. (1977) A modelling study of soot and nitric oxide formation in diesel engines, Ph.D. thesis, Southampton university.

Reid,R.C., Dausnitz,J.M. and Sherwood,T.K. (1977) The properties of gases and liquids, 3rd Ed., McGraw-Hill Book Co.

Rodi,W. (1976) A new algebraic relation for calculating the Reynolds stresses, Z. Agnew. Math. Mech., 56, pp.219-221.

Rogg,B. and Williams,F.A. (1988) Structure of wet CO flames with full and reduced kinetic mechanisms, 22nd Symp. (Int.) Comb., The Combustion Institute, pp.1441-1451.

Roquemore,W.M., Chen,L.D., Goss,L.P. and Lynn,W.F. (1989) The structure of jet diffusion flames, in: Turbulent Reacting Flows, p.49 Borghi,R. and Murthy,S.N.B. (Eds.), Springer-Verlag.

Sarofim,A.F. (1986) Radiative heat transfer in combustion: friend or foe, 21st Symp. (Int.) Comb., The Combustion Institute, pp.1-23.

Schumann,U., Grotzbach,G. and Kleiser,L. (1980) Direct numerical simulation of turbulence, in: Prediction Methods for Turbulent Flows, Kollmann, W. (Ed.), Hemisphere Publishing Corp.

Schumann,U. and Friedrich,R. (Eds.) (1986) Direct and large eddy simulations of turbulence, Proc. EUROMECH Coll., no. 199, Viewig, Braunschweig.

Shepp,L.A. and Logan,B.F. (1974) The Fourier reconstruction of a head section, I.E.E.E. transactions on Nuclear Science, NS-21.

Siegel,R. and Howell,J.P. (1972) Thermal radiation heat transfer, McGraw-Hill, New York.

Smyth,K.C., Miller,J.H., Dorfman,R.C., Mallard,W.G. and Santoro,R.J. (1985) Soot inception in a methane/air diffusion flame as characterized by detailed species profiles, Comb. and Flame, 62, pp.157-181.

Spalding,D.B. (1971a) Mixing and chemical reaction in steady confined turbulent flames, 13th Symp. (Int.) Comb., The Combustion Institute, Pittsburgh, pp.649-657.

Spalding,D.B. (1971b) Concentration fluctuations in a round turbulent jet, Chem. Eng. Sci., 110, pp.173-181.

Spalding,D.B. (1977) GENMIX - A general program for two-dimensional parabolic phenomena, Pergamon Press.

Spalding,D.B. and Afgan, N. (Ed.) (1977) Heat transfer and turbulent buoyant convection, vols. 1 and 2, Hemisphere Pub. Corp.

Spalding,D.B. (1979) Combustion and mass transfer, Pergamon Press.

Speziale,C.G. (1987) On nonlinear k-l and k-ε models of turbulence, J. Fluid Mech., 178, pp.459-475.

Stewart,C.D. (1990) PH.D. thesis, Cranfield Institute of Technology.

Stewart,C.D., Syed,K.J. and Moss,J.B. (1990) Modelling soot formation in non-premixed kerosine-air flames, Submitted to Comb. Sci. and Tech.

Tennekes,H. and Lumley,J.L. (1972) A first course in turbulence, MIT Press.

Tesner,P.A. (1959) Formation of dispersed carbon by thermal decomposition of hydrocarbons, 7th Symp. (Int.) Comb., The Combustion Institute, pp.546-553.

Tesner,P.A., Snegiriova,T.D. and Knorre,V.G. (1971) Kinetics of dispersed carbon formation, Comb. and Flame, 17, pp.253-260.

Thomas, P.H. (1963) The size of flames from natural fires, 9th Symp. (Int.) Comb., The Combustion Institute, pp.844-859.

Tien,C.L. and Lee,S.C. (1982) Flame radiation, Prog. Energy and Comb. Sci., 8, pp.41-59.

Tsuji,H. and Yamaoka,I. (1969) The counterflow diffusion flame in the forward stagnation region of a porous cylinder, 12th Symp. (Int.) Comb., The Combustion Institute, pp.997-1005.

Vachon,M. and Champion,M. (1986) Integral model of flame with large buoyancy effects, Comb. and Flame, 63, pp.269-278.

Viskanta,R. and Menguc,M.P. (1987) Radiation heat transfer in combustion systems, Prog. Energy and Comb. Sci., 13, pp.97-160.

Warnatz,J. (1981) The structure of laminar alkane-, alkene- and acetylene flames, 18th Symp. (Int.) Comb., The Combustion Institute, pp.369-384.

Weckman,E.J. and Sobiesiak,A. (1988) The oscillatory behaviour of medium-scale pool fires, 22nd Symp. (Int.) Comb., The Combustion Institute, pp.1299-1310.

Weissman,W. and Benson,S.W. (1989) Mechanism of soot initiation in methane systems, Prog. Energy and Comb. Sci., 15, pp.273-285.

Williams,F.A. (1985) Combustion theory, 2nd ed., The Benjamin/ Cummings Publishing Company.

Wolfhard,H.G. and Parker,W.G. (1949) A new technique for the spectroscopic examination of flames at normal pressure, The Proceedings of the Physical Society, Sect. A, Vol. 62.

Zeman,O. and Lumley,J.L. (1977) A second order model for buoyancy driven mixing layers, in: heat transfer and turbulent buoyant convection, Spalding,D.B. and Afgan,N.H. (Eds.), Hemisphere Pub. Corp., pp.66-75.

Appendix A

FAVRE AVERAGED GOVERNING EQUATIONS - HIGH REYNOLDS NUMBER FORM

Mass continuity

$$\frac{\partial \bar{\rho}}{\partial t} + \frac{\partial}{\partial x_i}(\bar{\rho}\,\tilde{u}) = 0 \qquad \ldots (A.1)$$

Momentum conservation

$$\frac{\partial}{\partial t}(\bar{\rho}\,\tilde{u}_i) + \frac{\partial}{\partial x_j}(\bar{\rho}\,\tilde{u}_i\tilde{u}_j) = \bar{\rho}g_i - \frac{\partial \bar{P}}{\partial x_i} - \frac{\partial}{\partial x_j}(\bar{\rho}\,\widetilde{u_i''u_j''}) \qquad \ldots (A.2)$$

Conservation of a scalar property

$$\frac{\partial}{\partial t}(\bar{\rho}\,\tilde{\phi}) + \frac{\partial}{\partial x_i}(\bar{\rho}\,\tilde{u}_i\tilde{\phi}) = -\frac{\partial}{\partial x_i}(\bar{\rho}\,\widetilde{u_i''\phi''}) + \bar{S}_\phi \qquad \ldots (A.3)$$

Where S_ϕ is the volumetric source term.

Use of the two-equation k-ε turbulence model results in the following representation of the Reynolds stresses and turbulent scalar fluxes:

$$\bar{\rho}\,\widetilde{u_i''u_j''} = \frac{2}{3}\delta_{ij}\left(\bar{\rho}\,k + \mu_t\frac{\partial \tilde{u}_k}{\partial x_k}\right) - \mu_t\left(\frac{\partial \tilde{u}_i}{\partial x_j} + \frac{\partial \tilde{u}_j}{\partial x_i}\right) \qquad \ldots (A.4)$$

$$\bar{\rho}\,\widetilde{u_j''\phi''} = -\frac{\mu_t}{\sigma_t}\frac{\partial \tilde{\phi}}{\partial x_j} \qquad \ldots (A.5)$$

where the eddy viscosity is given by

$$\mu_t = C_\mu\,\bar{\rho}\,k^2/\varepsilon \qquad \ldots (A.6)$$

where $C_\mu = 0.09$.

k equation

$$\frac{\partial}{\partial t}(\bar{\rho}\, k) + \frac{\partial}{\partial x_i}(\bar{\rho}\, \tilde{u}_i k) = \frac{\partial}{\partial x_i}\left(\frac{\mu_t}{\sigma_k}\frac{\partial k}{\partial x_i}\right)$$

$$- \bar{\rho}\, \widetilde{u_i'' u_j''}\frac{\partial \tilde{u}_i}{\partial x_j} - (\mu_t/\bar{\rho}^2)\frac{\partial \bar{\rho}}{\partial x_i}\frac{\partial \bar{P}}{\partial x_i} - \bar{\rho}\,\varepsilon \qquad \ldots \text{(A.7)}$$

ε equation

$$\frac{\partial}{\partial t}(\bar{\rho}\,\varepsilon) + \frac{\partial}{\partial x_i}(\bar{\rho}\,\tilde{u}_i\varepsilon) = \frac{\partial}{\partial x_i}\left(\frac{\mu_t}{\sigma_\varepsilon}\frac{\partial \varepsilon}{\partial x_i}\right)$$

$$- C_{\varepsilon 1}\frac{\varepsilon}{k}\left(\bar{\rho}\,\widetilde{u_i'' u_j''}\frac{\partial \tilde{u}_i}{\partial x_j} - (\mu_t/\bar{\rho}^2)\frac{\partial \bar{\rho}}{\partial x_i}\frac{\partial \bar{P}}{\partial x_i}\right) - C_{\varepsilon 2}\bar{\rho}\frac{\varepsilon^2}{k} \qquad \ldots \text{(A.8)}$$

Balance equation for the fluctuation of a conserved scalar

$$\frac{\partial}{\partial t}(\bar{\rho}\,\widetilde{\xi''^2}) + \frac{\partial}{\partial x_i}(\bar{\rho}\,\tilde{u}_i\widetilde{\xi''^2}) = \frac{\partial}{\partial x_i}\left(\frac{\mu_t}{\sigma_t}\frac{\partial \widetilde{\xi''^2}}{\partial x_i}\right)$$

$$+ C_{g1}\frac{\mu_t}{\sigma_t}\left(\frac{\partial \tilde{\xi}}{\partial x_i}\right)^2 - C_{g2}\,\bar{\rho}\frac{\varepsilon}{k}\widetilde{\xi''^2} \qquad \ldots \text{(A.9)}$$

Appendix B

CALCULATION OF MIXTURE FRACTION

This appendix describes the calculation of mixture fraction from the mass spectrometer data which consists of the molar ratio of CO_2 to N_2. The former is obtained through complete oxidation of the fuel (CH_4) and the latter is assumed to be inert.

Mixture fraction may be expressed in terms of fuel to air mass ratio, cf.

$$\xi = (Y_f/Y_a)/(1+Y_f/Y_a) \qquad \ldots (B.1)$$

The fuel to air ratio may be expressed in terms of the CO_2 to N_2 mass ratio, noting that air contains 77% N_2 by mass and that complete combustion of 1kg of CH_4 produces (44/16)kg of CO_2, cf.

$$(Y_f/Y_a) = (Y_{CO2}/Y_{N2})x(16/44)x(.77) \qquad \ldots (B.2)$$

The ratio of mass fractions may be converted into the ratio of mole fraction, by dividing by the ratio of the molecular mass. Eqn. B.2 then becomes

$$\begin{aligned}(Y_f/Y_a) &= (\chi_{CO2}/\chi_{N2})x(16/44)x(.77)x(44/28) \\ &= 0.44(\chi_{CO2}/\chi_{N2}) \qquad \ldots (B.3)\end{aligned}$$

where (χ_{CO2}/χ_{N2}) is measured by the mass spectrometer.

The mixture fraction is then found through substitution of equation B.3 into B.1

Appendix C

KINETIC SCHEME FOR $CO-O_2-H_2$ SYSTEM

C.1 REACTION MECHANISM

1.		1.0 O	+	1.0 H_2O	=	1.0 OH	+	1.0 OH	
2.	M	+ 1.0 H	+	1.0 H	=	1.0 H_2			+ M
3.	M	+ 1.0 O	+	1.0 O	=	1.0 O_2			+ M
4.	M	+ 1.0 H	+	1.0 OH	=	1.0 H_2O			+ M
5.		1.0 H	+	1.0 O_2	=	1.0 OH	+	1.0 O	
6.		1.0 O	+	1.0 H_2	=	1.0 OH	+	1.0 H	
7.	M	+ 1.0 O_2	+	1.0 H	=	1.0 HO_2			+ M
8.		1.0 H	+	1.0 HO_2	=	1.0 OH	+	1.0 OH	
9.		1.0 CO	+	1.0 OH	=	1.0 CO_2	+	1.0 H	
10.		1.0 H_2	+	1.0 OH	=	1.0 H_2O	+	1.0 H	
11.	M	+ 1.0 CO	+	1.0 O	=	1.0 CO_2			+ M
12.	M	+ 1.0 H	+	1.0 O	=	1.0 OH			+ M

C.2 Kinetic Constants Values

Rate Coefficient(k) = A*T**B*EXP(-TACT/T) (m**3/kg-mole.s)

	FORWARD RATE			BACKWARD RATE		
	A	B	TACT	A	B	TACT
1.	1.760E+10	-2.000E-02	8.420E+03	1.550E+09	0.000E+00	0.000E+00
2.	1.000E+12	-1.000E+00	0.000E+00	7.150E+04	-8.200E-01	5.195E+04
3.	6.000E+02	0.000E+00	0.000E+00	5.830E+10	-1.000E+00	6.025E+04
4.	2.000E+17	-2.000E+00	0.000E+00	2.200E+13	0.000E+00	5.290E+04
5.	2.000E+11	0.000E+00	8.379E+03	1.650E+09	2.700E-01	0.000E+00
6.	6.000E+10	0.000E+00	5.032E+03	1.940E+10	-3.000E-02	4.052E+03
7.	1.500E+09	0.000E+00	5.000E+02	2.100E+12	0.000E+00	2.315E+04
8.	1.590E+11	0.000E+00	5.430E+02	1.260E+10	0.000E+00	2.005E+04
9.	1.500E+08	0.000E+00	5.030E+02	1.500E+10	0.000E+00	1.183E+04
10.	1.500E+10	0.000E+00	2.516E+03	5.550E+10	-1.000E-02	9.956E+03
11.	6.000E+07	0.000E+00	0.000E+00	1.310E+10	-5.800E-01	6.327E+04
12.	3.000E+08	0.000E+00	0.000E+00	6.960E+10	2.100E-01	5.097E+04

Appendix D

LINE BROADENING PARAMETERS

Collision half widths, γ_{stp}

colliding species	radiating species CO_2	H_2O	CH_4	CO
CO_2	.09	.12	.0	.07
H_2O	.07	.09	.0	.06
CH_4	.0	.0	.16	.0
CO	.06	.10	.0	.06
O_2	.055	.04	.0	.05
N_2	.07	.09	.0	.06
self resonant	.01	.44	.0	.0

η

The indices $\eta_{i,j}$ are all 0.5 and $\eta_{i,i}$ are 1.0.

The above values are taken from Ludwig et al (1973).